UNIVERSIDADE DE BRASÍLIA
INSTITUTO DE GEOCIÊNCIAS – IG
PROGRAMA DE PÓS-GRADUAÇÃO EM GEOLOGIA

GEOQUÍMICA ISOTÓPICA DO DEPÓSITO AURÍFERO DA BACIA DE JACOBINA E DOS SULFETOS DE METAIS BASE DO GREENSTONE BELT MUNDO NOVO, CRÁTON DO SÃO FRANCISCO, E SUAS IMPLICAÇÕES SOBRE O PALEOARQUEANO.

Guilherme dos Santos Teles

Tese de Doutorado N° 141

Brasília-DF
Outubro de 2017

UNIVERSIDADE DE BRASÍLIA- UnB
INSTITUTO DE GEOCIÊNCIAS – IG
PROGRAMA DE PÓS-GRADUAÇÃO EM GEOLOGIA

GEOQUÍMICA ISOTÓPICA DO DEPÓSITO AURÍFERO DA BACIA DE JACOBINA E DOS SULFETOS DE METAIS BASE DO GREENSTONE BELT MUNDO NOVO, CRÁTON DO SÃO FRANCISCO, E SUAS IMPLICAÇÕES SOBRE O PALEOARQUEANO.

Guilherme dos Santos Teles

Tese de Doutorado N° 141

Orientador: Prof. Dr. Farid Chemale Júnior

Banca Examinadora: Prof.ª Dra. Catarina Labouré Benfica Toledo (UnB)
Prof. Dr. Elson Paiva de Oliveira (UNICAMP)
Prof. Dr. Léo Afraneo Hartmann (UFRGS)

Suplente: Prof. Dr. Márcio Martins Pimentel (UnB)

Brasília-DF,
Outubro de 2017

Agradecimentos

Agradeço primeiramente ao meu orientador, Prof. Dr. Farid Chemale, pela paciência, conselhos e incentivos ao longo dos últimos anos, os quais foram fundamentais no decorrer no doutorado, e que estarão presentes ao longo de toda minha vida acadêmica.

Aos meus pais Francisca e Fernando, e meus irmãos Danilo e Gustavo, pelo apoio e incentivo durante toda minha vida.

À minha esposa Daniele, pelo suporte e apoio incondicional, e por embarcar comigo na aventura de morar no exterior.

Aos familiares e amigos de Brasília, especialmente meus tios Luís e Itania, meus primos Mayra, Moema e Uyrá, família Brito (Jorge, Graci, e Thalis), e Aldo, meu muito obrigado pelo acolhimento na cidade durante o período do doutorado.

Agradeço à Dra. Janaína Ávila, pela recepção e suporte para adaptação em Canberra, bem como por todas as conversas e tempo dedicado na realização das minhas análises, em especial as dos isótopos de enxofre no SHRIMP-SI.

Ao Prof. Dr. Trevor Ireland pela orientação, discussões, e por possibilitar a utilização de equipamentos diversos da *Research School of Earth Sciences* (RSES), na *Australian National University* (ANU).

Aos professores e funcionários do IG-UnB pelos conhecimentos compartilhados, e apoio durante os anos do doutorado. Ao *staff* e colegas da RSES, pela recepção, ajuda, e amizade, fundamentais para que eu me sentisse em casa durante o período de estágio sanduíche na Austrália.

À Yamana Gold, em especial os geólogos Sr. Anselmo, Pablo, e Cid, e demais funcionários que me auxiliaram nas atividades de campo e coleta de amostras em Jacobina. À Companhia Baiana de Pesquisa Mineral (CBPM) por permitir a coleta de amostras em furos de sonda do alvo Fazenda Coqueiro.

Ao CNPq pela concessão da bolsa de doutorado (processo 163459/2013-4), e pelo financiamento de meu estágio sanduíche na Austrália, por meio do programa *Ciências Sem Fronteiras* (processo 202267/2014-8).

Aos Drs. Marc Norman e Richard Armstrong por cederem padrões de sulfetos para análises isotópicas e de elementos-traço. Ao Dr. Charles Magee pelas discussões sobre a geologia da região de Jacobina, e pelo convite para coautoria em uma publicação no periódico *Geology*.

"Queremos buscar a verdade, não importa aonde ela nos leve. Mas para encontrá-la, precisaremos tanto de imaginação quanto de ceticismo. Não teremos medo de fazer especulações, mas teremos o cuidado de distinguir a especulação do fato"

Carl Sagan

Resumo

Guilherme dos Santos Teles, 2017. Geoquímica Isotópica do Depósito Aurífero da Bacia de Jacobina e dos Sulfetos de Metais Base do *Greenstone Belt* Mundo Novo, Cráton do São Francisco, e suas Implicações sobre o Paleoarqueano. Tese de Doutorado, Universidade de Brasília, 159 pp.
Orientador: Farid Chemale Júnior

Desvendar os processos que modelaram a superfície do planeta Terra é um papel fundamental da Geologia. Entretanto, devido à antiguidade do nosso planeta, parte considerável de sua história foi obliterada do registro geológico, ou em diversos casos encontra-se profundamente modificada, ou reduzida a exposições isoladas ao redor do globo. Essa premissa é verdadeira tratando-se do registro da primeira metade da existência do planeta, ao longo da qual ocorreram mudanças significativas, que permitiram dentre outras coisas o surgimento da vida e a melhoria das condições de habitabilidade na superfície.

O Estado da Bahia reúne em seu território algumas das rochas mais antigas do continente sul-americano, cuja história geológica se inicia no Paleoarqueano. Essas rochas estão localizadas na porção nordeste do Cráton do São Francisco e compreendem o embasamento Paleoarqueano do Bloco Gavião, o que torna essa unidade tectônica um interessante laboratório natural para avaliação dos processos e condições atuantes no planeta naquele período. Duas importantes sequências supracrustais do Bloco Gavião, o *Greenstone Belt* Mundo Novo e a Bacia de Jacobina, foram estudadas com o objetivo de investigar as condições paleoambientais vigentes durante a deposição dessas unidades (~ 3.3 Ga). Para tanto, foram utilizadas informações provenientes das análises *in-situ* dos múltiplos isótopos de enxofre (^{32}S, ^{33}S, ^{34}S e ^{36}S), e de elementos traço em sulfetos.

A Bacia de Jacobina hospeda um depósito Au-(U)-pirita em camadas de conglomerados, similares ao da Bacia de Witwatersrand. Observações petrográficas indicam a ocorrência de pirita de origem sedimentar, tanto nos conglomerados (continentais) quanto nas amostras da seção marinha de Jacobina. A composição dos múltiplos isótopos de enxofre, reportados pelos valores de $\delta^{34}S$, $\Delta^{33}S$ e $\Delta^{36}S$, sugerem que a atmosfera permaneceu empobrecida em O_2 durante a deposição da bacia, apesar das recentes evidências de oxidação no Cráton do São Francisco ao final do Paleoarqueano.

Entretanto, as amostras continentais e marinhas estudadas apresentam diferentes rotas para preservação das anomalias isotópicas $\Delta^{33}S$ e $\Delta^{36}S$ (MIF-S), evidenciando o controle ambiental na transferência dessas anomalias atmosféricas para a superfície. Além disso, os dados de elementos traço, em conjunto com as condições paleoambientais observadas na Bacia de Jacobina, sugerem acumulação singenética de ouro na bacia.

O *Greenstone Belt* Mundo Novo possui mineralizações de metais base associadas a sulfetos maciços vulcanogênicos (VMS), formadas num intervalo de tempo cuja ocorrência desse tipo de mineralização é escassa. Logo, essas ocorrências permitem a avaliação dos sistemas hidrotermais marinhos no Paleoarqueano (3.3 Ga). Os dados dos múltiplos isótopos de enxofre indicam a assimilação de S atmosférico nas células hidrotermais. Entretanto, as fontes de enxofre são distintas entre os segmentos setentrional e meridional do *greenstone*. Ao norte, os sulfetos possuem composição isotópica similar aos depósitos paleoarqueanos de barita na Australia e África do Sul ($\Delta^{33}S < 0$), o que sugere a circulação de sulfato oceânico em uma bacia restrita; enquanto que ao sul (depósito da Fazenda Coqueiro) os sulfetos apresentam $\Delta^{33}S > 0$, assinatura indicativa de fonte sedimentar para o S. A distribuição dos elementos traço nos sulfetos correlaciona-se bem com cada fase analisada, e se assemelha com a partição conhecida em outros depósitos. Os dados isotópicos obtidos neste estudo são particularmente distintos daqueles publicados em VMS arqueanos, o que pode ter forte implicação no tamanho e potencial econômico desses depósitos.

Palavras-chave: Sulfetos, Isótopos de Enxofre, Elementos Traço, Depósitos Minerais, Paleoarqueano, Bacia de Jacobina, Greenstone Belt Mundo Novo, e Cráton do São Francisco.

Abstract

Guilherme dos Santos Teles, 2017. Isotope Geochemistry of the Auriferous Deposit of Jacobina Basin and the Base Metals Sulfides from the Mundo Novo Greenstone Belt, São Francisco Craton, and their implications for the Paleoarchean. PhD Thesis, Universidade de Brasília, 159 pp.
Thesis Advisor: Farid Chemale Júnior.

Unraveling the processes that shaped the Earth's surface is a fundamental role of Geology. However, due to the antiquity of our planet, a considerable part of its history has been obliterated from the geological record, or in several cases has been deeply modified, or reduced to isolated exposures around the globe. This premise is true regarding to the record of the first half of our planet existence, during which significant changes took place and allowed, among other things, the emergence of life and the improvement of habitability conditions for the surficial environments.

Some of the oldest rocks of the South American continent are found in the Bahia State territory, whose geological history begins in the Paleoarchean. These rocks are in the northeast portion of the São Francisco Craton, and comprise the Paleoarchean basement of the Gavião Block, which makes this tectonic unit an interesting natural laboratory for evaluating the processes and conditions on Earth in that period. Two important supracrustal sequences of the Gavião Block, the Greenstone Belt Mundo Novo and the Jacobina Basin, were studied in order to investigate the paleoenvironmental conditions prevailing during the deposition of these units (~ 3.3 Ga). Therefore, we used information from in-situ analysis of multiple sulfur isotopes (^{32}S, ^{33}S, ^{34}S and ^{36}S), and trace elements in sulfides.

The Jacobine Basin hosts Au-(U)-pyrite mineralization in conglomerate beds, similarly to the Witwatersrand Basin. Petrographic observations indicate the occurrence of sedimentary pyrite in the continental conglomerates and in samples from the marine section of Jacobina Basin. The multiple sulfur isotopic compositions, reported by the $\delta^{34}S$, $\Delta^{33}S$ and $\Delta^{36}S$ values, suggest absence of atmospheric O_2 during the basin deposition, despite the recent evidence for oxidation at the São Francisco Craton in late Paleoarchean. However, the continental and marine samples present different routes for the preservation of $\Delta^{33}S$ and $\Delta^{36}S$ isotopic anomalies (MIF-S), evidencing environmental control in the

transfer of these atmospheric signals to surface. In addition, the trace elements data, together with the paleoenvironmental conditions observed, suggest syngeneic accumulation of gold in the Jacobina Basin.

The Mundo Novo Greenstone Belt has base metal mineralizations associated to volcanogenic massive sulfides (VMS) that were formed in a time interval characterized by the relative scarcity of these deposits. Thus, these occurrences allow the evaluation of Paleoarchean (3.3 Ga) marine hydrothermal systems. The multiple sulfur isotopes data indicate the assimilation of atmospheric sulfur in the hydrothermal cells. However, the S sources are distinct between the northern and southern segments of the greenstone belt. At north, the sulfides yield isotopic compositions similar to the Paleoarchean barite deposits in Australia and South Africa ($\Delta^{33}S < 0$), suggesting the circulation of oceanic sulfate in a restricted basin; while at south (Fazenda Coqueiro deposit) the sulfides present $\Delta^{33}S > 0$, a signature indicative of sedimentary source for S. The trace element distribution in sulfides correlates well with each phase analyzed, and resembles the known partition in other deposits. The isotopic data obtained in this study are particularly distinct from those published in Archean VMS, which may have a strong implication on the size and economic potential in these deposits.

Key-words: Sulfides, Sulfur Isotopes, Trace Elements, Mineral Deposits, Paleoarchean, Jacobina Basin, Mundo Novo Greenstone Belt, and São Francisco Craton.

Lista de Figuras

Lista de Tabelas

Sumário

CAPÍTULO 1

1.1. INTRODUÇÃO

A trajetória do nosso planeta é marcada por grandes eventos, que mudaram significativamente suas condições ambientais e de habitabilidade. Evidências geológicas sugerem que parte desses eventos ocorreram pouco após a constituição do planeta; dentre os quais destacam-se a formação dos primeiros fragmentos de crosta continental, em torno de 4.4 Ga (Valley et al., 2014), e o surgimento das primeiras formas de vida, possivelmente em 4.3 Ga (Dodd et al., 2017). Entretanto, as mudanças fundamentais, que modelaram o planeta para o estágio que conhecemos hoje, foram somente possíveis após o estabelecimento da tectônica de placas e a oxigenação da atmosfera, que transcorreram ao longo do Arqueano e início do Paleoproterozóico.

No entanto, decifrar e reconstituir a história desses eventos não é tarefa simples, uma vez que são raras as rochas desses períodos longínquos. A ocorrência dessas rochas está limitada às diversas áreas cratônicas ao redor do planeta, as quais constituem pequenos fragmentos de um grande "quebra-cabeças". Além disso, em função da sua antiguidade, essas rochas foram envolvidas em diversos eventos geológicos subsequentes, os quais podem ter modificado substancialmente as evidências dos eventos associados à sua formação. Dessa forma, os cientistas que estudam as rochas mais antigas do nosso planeta recorrem de diferentes ferramentas geoquímicas e isotópicas, que podem fornecer informações preciosas sobre o tempo e condições associados à formação da rocha, bem como sobre os processos posteriores à sua formação.

Neste contexto, depósitos minerais antigos (arqueanos) registram informações valiosas sobre a evolução da atmosfera, hidrosfera, além da vida em nosso planeta. Dentre esses depósitos, pode-se destacar os do tipo VMS (*Volcanogenic Massive Sulfide*), e de Au-U em conglomerados ricos em pirita (tipo Witwatersrand).

Estudos com isótopos de enxofre em ambientes exalativos da Formação Dresser (3.5 Ga, Cráton de Pilbara, Austrália) sugerem, por exemplo, a existência de uma das formas mais antigas de metabolismo (Philippot et al., 2007; Ueno et al., 2008; Shen et al., 2009). Outros estudos, relacionados a ambientes exalativos portadores mineralizações do tipo VMS estabeleceram uma estimativa da concentração do íon sulfato dissolvido nos

oceanos antigos, e seu papel na formação de depósitos VMS desde o Arqueano (Huston et al., 2001; Golding et al., 2011; Jamieson et al., 2013; Sharman et al., 2015).

Depósitos auríferos do tipo Witwatersrand tem sido objeto de debate na comunidade geológica, pois esse tipo de depósito seria um forte indicativo da condição anóxica da atmosfera até meados de 2.3 Ga, quando ocorreu o Evento Global de Oxigenação na Terra (Cattling, 2014 e demais referências). A partir desse evento, a atmosfera teve um aumento substancial de O_2 e diminuição drástica de CO_2 e CH_4 (até 10 vezes menos que no Arqueano e no início do Paleoproterozóico). A condição anóxica é suportada principalmente pela ocorrência de grãos detríticos de pirita e uraninita, os quais são minerais altamente instáveis, e podem ser rapidamente oxidados em contato com nossa atmosfera atual rica em oxigênio. Outra questão relevante associada a esse tipo de depósito, e principalmente ao seu exemplo mais conhecido (Witwatersrand), são os processos que levaram à gigantesca acumulação de ouro no depósito sul-africano. Estudos mais recentes, suportados por dados isotópicos de enxofre e elementos-traço em pirita, têm fornecido novas ideias sobre as condições ambientais favoráveis, e o papel de micro-organismos nos processos de formação desses depósitos.

Exemplares das rochas mais antigas da América do Sul são encontradas no Brasil, mais especificamente no Cráton do São Francisco, Estado da Bahia, os quais registram uma longa história evolutiva que se inicia no Paleoarqueano. Em associação com essas rochas mais antigas, ocorrem os depósitos de Jacobina e da Fazenda Coqueiro, ambos de idade supostamente paleoarqueana (~3.3 Ga). O depósito aurífero de Jacobina é um exemplo de mineralização do tipo Witwatersrand, com mineralizações de Au-(U) em horizontes de conglomerados ricos em pirita; enquanto que o depósito de Cu-Zn-Pb da Fazenda Coqueiro é um exemplar de mineralização do tipo VMS, associada à sequência vulcano-sedimentar do *Greenstone Belt* Mundo Novo.

Os depósitos de Jacobina e Fazenda Coqueiro representam uma importante chave para a compreensão das condições paleoambientais ao final do Paleoarqueano. Elementos relacionados à atmosfera, hidrosfera e biosfera, bem como os processos associados com as mineralizações de Jacobina e do *Greenstone Belt* Mundo Novo, são objeto de estudo nesta tese de doutorado.

1.2. OBJETIVOS

O escopo desta tese é a avaliação de diferentes aspectos relacionados à formação dos depósitos auríferos de Jacobina, e de metais-base da Fazenda Coqueiro, com o auxílio de dados isotópicos de enxofre e de elementos-traço em sulfetos, com enfoque para:

i) As condições paleoambientais dominantes ao final do Paleoarqueano (~3.3 Ga), associadas à deposição da Bacia de Jacobina e do *Greenstone Belt* Mundo Novo, e sua influência na formação dos depósitos auríferos e VMS correspondentes.

ii) A origem do ouro nos conglomerados da Bacia de Jacobina, e fonte dos metais-base no depósito da Fazenda Coqueiro, bem como os processos responsáveis pela acumulação desses metais nos depósitos.

iii) A comparação dos depósitos estudados com depósitos similares ao redor do planeta, de forma que se possa avaliar se os processos dominantes na porção estudada do Cráton do São Francisco tiveram correspondência em escala global, tanto ao final do Paleoarqueano (~3.3 Ga), quanto no restante do Arqueano.

1.3. CONTEXTO GEOTECTÔNICO

A Bacia de Jacobina e o *Greenstone Belt* Mundo Novo estão localizados no Cráton do São Francisco (CSF), porção centro-leste do Estado da Bahia (Figura 1.1). Estas unidades formam um alongado cinturão de rochas que afloram desde as proximidades do município de Mundo Novo, a sul, até a cidade de Juazeiro, a norte (Mascarenhas & Silva, 1994). Rochas do embasamento Arqueano e Paleoproterozóico do cráton afloram nessa região, dentre as quais algumas das mais antigas da América do Sul, cuja formação ocorreu no Paleoarqueano (Barbosa & Sabaté, 2004), no segmento crustal denominado Bloco Gavião (Figura 1.1).

O Bloco Gavião reúne TTG's (tonalito-trondhjemito-granodiorito), associações de rochas supracrustais, geradas entre 3.4 e 3.0 Ga, além de granitoides reciclados de 2.7 Ga (Nutman & Cordani, 1993; Martin *et al*., 1997; Peucat *et al*., 2002; Barbosa & Sabaté, 2004; Santos-Pinto *et al*., 2012; Cruz *et al*., 2012). Dados isotópicos em rocha-total (Sm-Nd), em zircões detríticos e magmáticos (U-Pb e Lu-Hf), indicam, entretanto, processo de geração e reciclagem de crosta mais antiga que 3.6 Ga (Barbosa & Sabaté, 2004; Santos-Pinto *et al*., 2012; Teles et al., 2015; Paquette et al., 2015).

Os outros segmentos crustais de idade arqueana que compõem o embasamento do CFS, em associação ao Bloco Gavião, são denominados de blocos Serrinha, Jequié e Itabuna-Salvador-Curaçá. O Bloco Serrinha é formado por migmatitos, gnaisses bandados, e ortognaisses de composição granodiorítica de idade mesoarqueana (3.2-2.9 Ga; Rios et al., 2008; Oliveira et al., 2010); diques máficos e complexos máfico-ultramáficos neoarqueanos (2.7-2.6 Ga; Oliveira et al., 2013); sequências supracrustais paleoproterozóicas, como as do Rio Itapicuru e Rio Capim (2.2-2.1 Ga; Silva, 1994; Oliveira et al., 2011); além de rochas graníticas contemporâneas às sequências supracrustais (Rios et al., 2008).

O Bloco Jequié é formado por rochas em fácies granulito, majoritariamente orto e paraderivadas, rochas enderbíticas, charnoenderbíticas, e charnockíticas de idade neoarqueana (2.7-2.6 Ga; Barbosa & Sabaté, 2004).

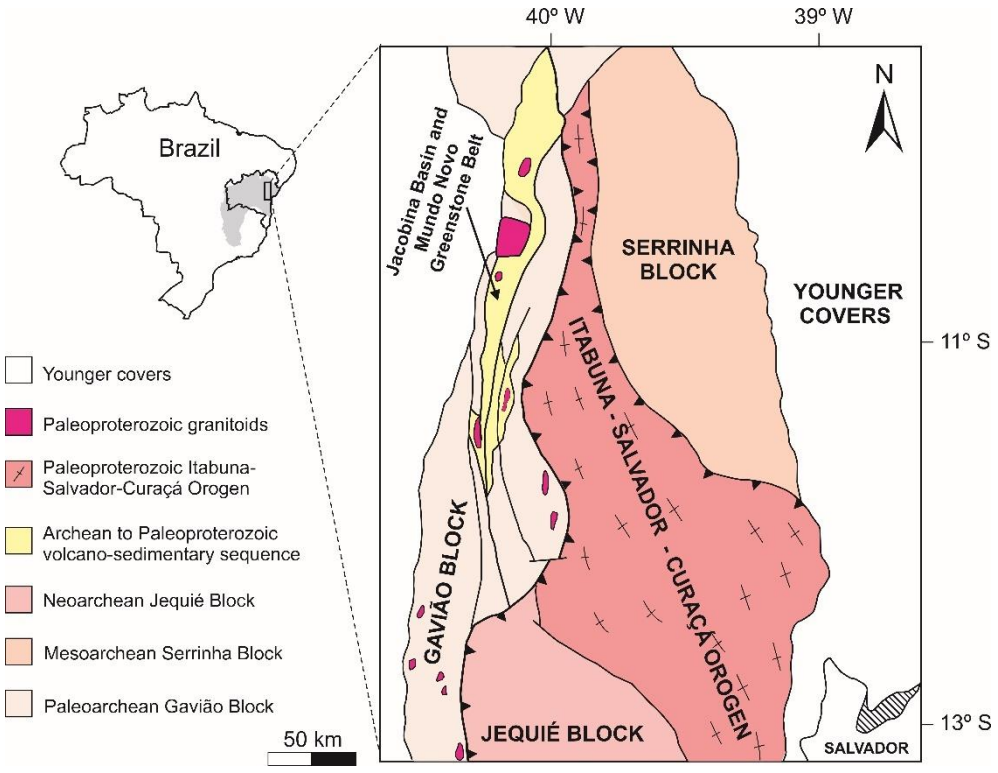

Figura 1.1. Esboço geotectônico das unidades do embasamento Arqueano e Paleoproterozóico na porção centro-leste do Cráton do São Francisco (modificado de Teles, 2013).

O último bloco fundamental do segmento baiano do CSF corresponde ao Itabuna-Salvador-Curaçá (ISC). Esse bloco é dominado por rochas em fácies granulito, dentre as quais predominam ortognaisses, granulitos máficos, e granulitos para-derivados (Barbosa

& Sabaté, 2004; Oliveira et al., 2010). Parte dessas rochas foi formada ao final do Neoarqueano, com metamorfismo de alto grau no Paleoproterozóico (Oliveira et al., 2010). Segundo Barbosa & Sabaté (2004), o ISC constituiu uma importante cadeia de montanhas, formada pela colisão continente-continente entre os blocos arqueanos do CSF na Bahia, cujos protólitos envolvidos foram formados em ambientes de arco de ilhas, bacias de *back-arc* e zonas de subducção.

Essa orogenia paleoproterozóica (2.2-1.9 Ga), também conhecida como ciclo Transamazônico-Eburneano (Ledru et al., 1994), foi responsável por importante magmatismo granítico a sienítico ao longo dos blocos arqueanos. Ao longo da borda leste do Bloco Gavião, por exemplo, formou-se um extenso lineamento, conhecido como Jacobina-Contendas-Mirante (Sabaté *et al*., 1990). Esse lineamento, que se estende por mais de 600 km, marca a zona de sutura da tectônica paleoproterozóica, onde se observam estruturas de cavalgamento, com movimentação de leste para oeste, além de intrusões graníticas peraluminosas sin- a tardi-tectônicas (Figura 1.1), com idades entre 1974 ± 36 e 1883 ± 87 Ma (Sabaté *et al*., 1990).

1.3.1. Geologia da Bacia de Jacobina

A Bacia de Jacobina compõe um conjunto de serras que totalizam quase 200 km de extensão, ao longo de um *trend* NNE-SSW (Figura 1.2). As rochas siliciclásticas da bacia estão em fácies xisto-verde, e preservam feições primárias como acamamento e estruturas sedimentares. Os padrões estratigráficos indicam deposição em contexto rifte (Mascarenhas et al., 1992; Pearson et al., 2005; Teles et al., 2015), embora alguns autores sugiram que Jacobina representa uma bacia *foreland* (Ledru et al., 1997; Milesi et al., 2002).

A estratigrafia da bacia é composta, da base para o topo, pelos depósitos aluviais da Formação Serra do Córrego, seguidos por quartzitos transgressivos da Formação Rio do Ouro, e pelos quartzitos marinhos intercalados com andalusita-xistos e conglomerados subordinados da Formação Serra da Paciência (Mascarenhas et al., 1992; Pearson et al., 2005; Teles et al., 2015). Estudos recentes de Teles et al., (2015) e Magee et al., (2016), ambos baseados em idades U-Pb em zircão detrítico, mostram que rochas paleoarqueanas (3.3 a 3.6 Ga) foram as únicas fontes de sedimentos à bacia, e sugerem que a deposição deve ter ocorrido ao final do Paleoarqueano (~3.3 Ga).

A Formação Serra do Córrego aflora na borda oeste da serra de Jacobina, e possui espessura que varia entre 500 e 1000 m (Pearson *et al*., 2005). Esta formação é constituída por dois horizontes de conglomerados, hospedeiros das mineralizações em Au-(U)-Py, separados por um espesso pacote de quartzitos. Os conglomerados variam quanto à seleção e arredondamento dos seixos, empacotamento, teores de ouro, presença de sulfetos, ou ao grau de oxidação. Porém, eles são essencialmente oligomíticos, com seixos de quartzo, e mais raramente *chert*. Os quartzitos da unidade são geralmente de granulação grossa; variam entre a coloração branca, esverdeada ou avermelhada, dependendo do teor de fuchsita ou grau de oxidação; e possuem mineralogia semelhante à dos conglomerados, com exceção aos teores de ouro e presença de pirita.

A deposição dessa unidade é associada a um sistema aluvial, onde leques aluviais evoluíam para canais fluviais entrelaçados, cujas paleocorrentes indicam transporte principal de leste para oeste (Teles et al., 2015).

A Formação Rio do Ouro aflora na porção central da Serra de Jacobina (Figura 1.2), constitui-se principalmente por quartzitos puros, finos a médios, de coloração branca, cinza e por vezes esverdeada. Níveis descontínuos de conglomerados ocorrem na base (Mascarenhas et al., 1998), marcando a transição com a unidade inferior (Serra do Córrego). Intercalações de camadas descontínuas de metapelitos carbonosos ocorrem associadas aos quartzitos (Ledru et al., 1997).

A deposição dessa unidade representa uma transgressão contínua na bacia, que marca a passagem de um regime de sedimentação aluvial para um sistema marinho raso dominado por marés (Teles et al., 2015 e demais referências). Quartzitos com marcas de ondas, estratificações cruzadas de pequeno porte, e estratificações cruzadas do tipo espinha de peixe são indicativos da mudança no ambiente de sedimentação, assim como a inversão do padrão de paleocorrentes.

A Formação Serra da Paciência está exposta na margem leste da serra (Figura 1.2), e representa uma porção mais profunda da bacia, uma plataforma dominada por marés (Mascarenhas et al., 1992). Consiste de espessos pacotes de quartzitos finos a grossos, quartzitos conglomeráticos, e lentes subordinadas de conglomerados auríferos, as quais podem ser interpretadas como pulsos distais dos canais fluviais da Formação Serra do Córrego. Fácies associadas à lâmina d'água mais profunda são representadas por intercalações de quartzitos com andalusita- grafita- xistos.

Diques e *sills* de rochas máficas-ultramáficas, metamorfizados e alterados hidrotermalmente, representam um importante evento magmático, de idade ainda

desconhecida na região de Jacobina. As rochas ultramáficas tem orientação N-S, e seus protólitos são classificados como metaperidotitos e metapiroxenitos de afinidade komatiitica (Teixeira et al., 2001). As rochas máficas são compostas por metagabros e metadioritos que preenchem um sistema de falhas *en echelon* de orientação E-W. Essas intrusões comumente assimilam os sedimentos encaixantes, e podem apresentar teores de ouro anômalos de forma errática.

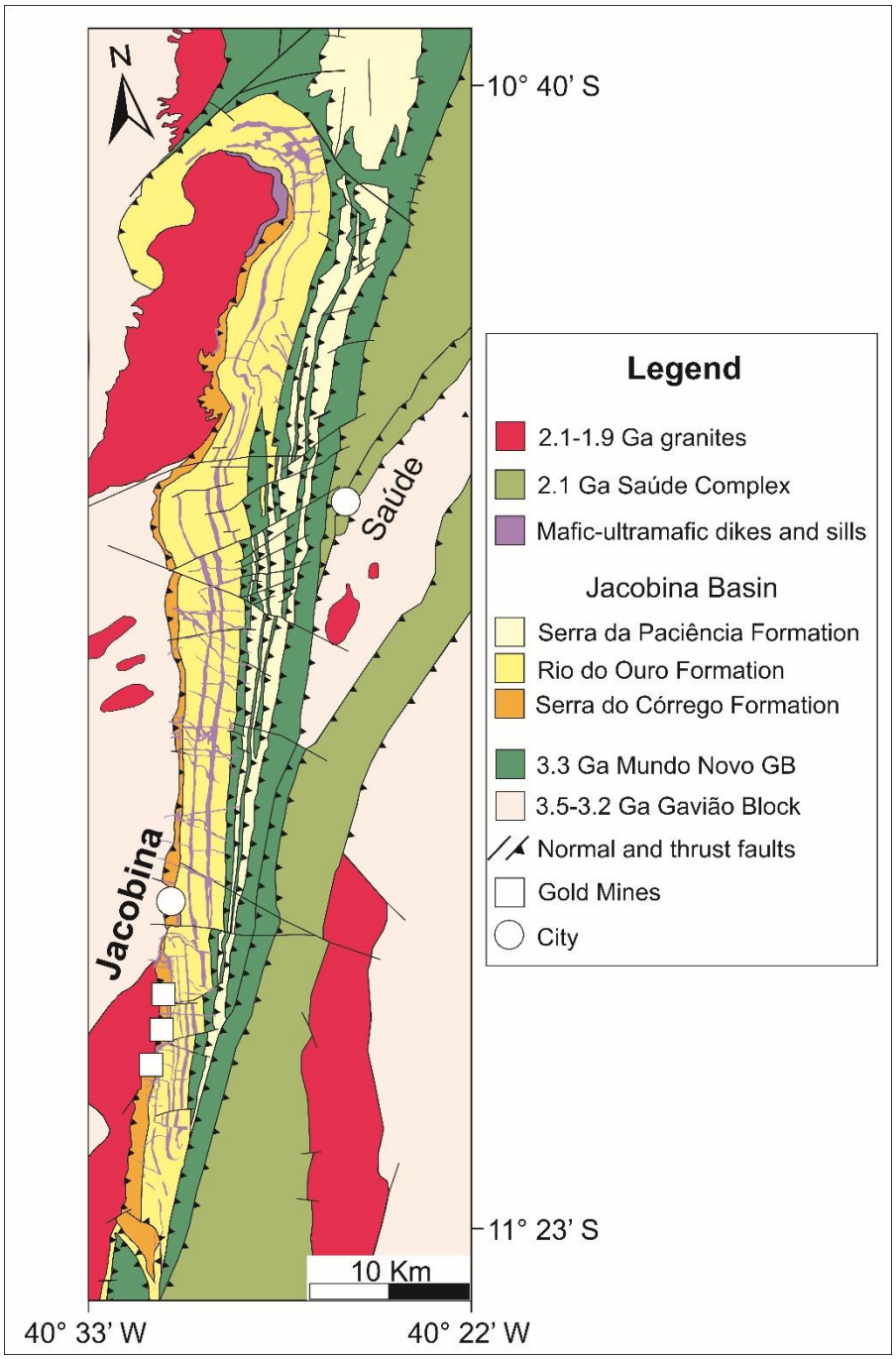

Figura 1.2. Mapa geológico da Bacia de Jacobina (modificado de Teles et al., 2015).

1.3.2. Geologia do Greenstone Belt Mundo Novo

O *Greenstone Belt* Mundo Novo, definido por Mascarenhas & Silva (1994), consiste de uma associação vulcano-sedimentar metamorfizada em fácies xisto-verde. Limita-se a oeste com a Bacia de Jacobina, através da falha de Pindobaçu, e a leste com as rochas em grau anfibolito dos Complexos Saúde e Mairi (figuras 1.2 e 1.3).

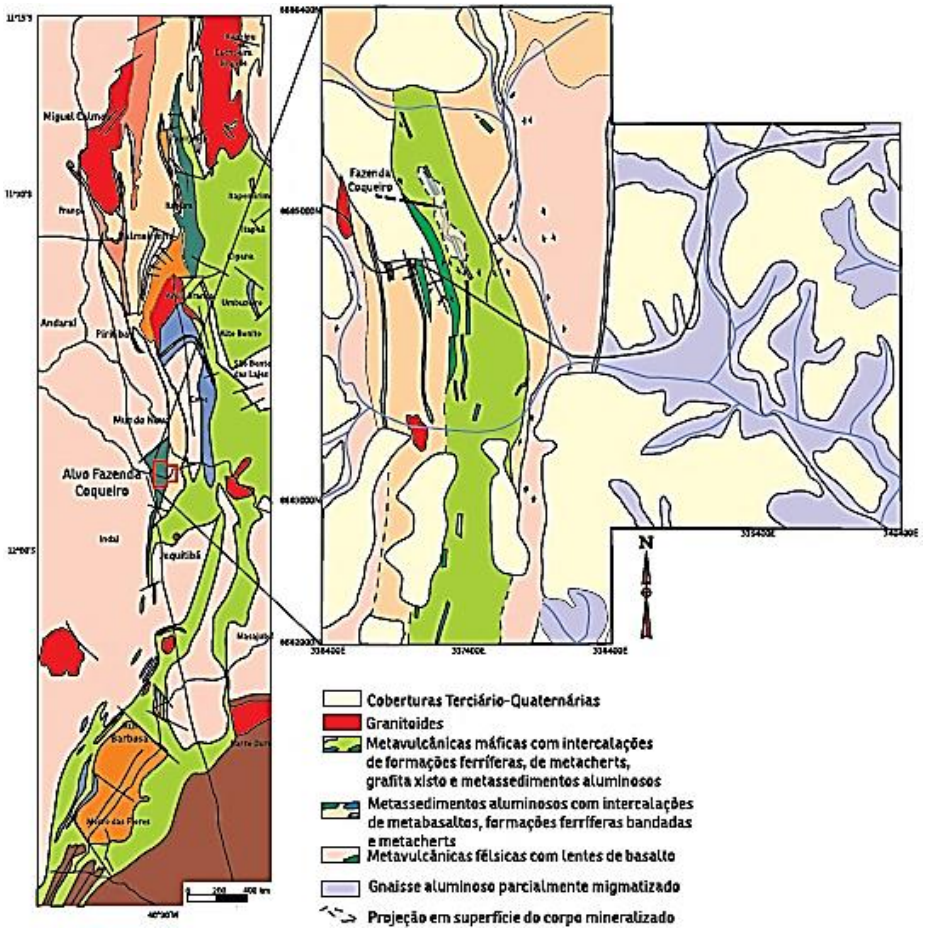

Figura 1.3. Mapa geológico simplificado da porção sul do *Greenstone Belt* Mundo Novo, com detalhe para o depósito do tipo VMS da Fazenda Coqueiro (Cunha et al., 2012).

A sequência do *greenstone* é composta por rochas metavulcânicas máficas (basaltos, alguns com estrutura do tipo *pillow-lava*), intermediárias (andesitos e dacitos), félsicas (riolitos); as quais se associam às rochas metassedimentares químicas (formação ferrífera bandada e *cherts*) e clásticas (xistos carbonos e metapelitos). Dados geoquímicos das rochas vulcânicas máficas indicam afinidade com magmas toleíticos, gerados em ambiente do tipo *back-arc* extensional (Mascarenhas & Silva, 1994).

A idade do *greenstone belt* foi determinada pelo método U-Pb em zircão, em uma amostra de metadacito aflorante nas proximidades do município de Mundo Novo. A idade obtida foi de 3305 ± 9 Ma (Peucat et al., 2002). Em trabalho recente, Zincone et al., (2016) dataram uma amostra de riolito aflorante na porção sul do mesmo *greenstone*, e obtiveram idade semelhante (3303 ± 7 Ma) à anterior.

O depósito de Zn-Cu-Pb do tipo VMS da Fazenda Coqueiro ocorre no segmento sul do *Greenstone Belt* Mundo Novo (Figura 1.3). A mineralização de sulfeto maciço ocorre na unidade metavulcânica máfica, composta dominantemente por metabasaltos intercalados com formação ferrífera bandada, *metacherts* e mica-xistos (que localmente contém grafita). Rochas metavulcânicas félsicas ocorrem associadas, incluindo o metadacito datado por Peucat et al., (2002). A mineralização principal, definida por furos de sonda, é constituída por lentes de sulfeto maciço com cerca de 8 m de espessura, 400 m de extensão ao longo do *strike* (N-S), e à 300 m de profundidade. Os teores médios nesse intervalo são de 6,2% de Zn, 0,7% de Pb, 498 ppm de Cu, 35 g/t de Ag e 103 ppb de Au (Souza et al., 2002).

1.4. ESTRUTURA DA TESE

Após este capítulo introdutório, no **Capítulo 2** é apresentada uma breve revisão sobre os depósitos auríferos do tipo Witwatersrand, e de metais-base do tipo VMS, ambos geneticamente relacionados às mineralizações encontradas na Bacia de Jacobina e *Greenstone Belt* Mundo Novo. Adicionalmente, a geoquímica dos isótopos de enxofre também é abordada no **Capítulo 2**. Os materiais e métodos empregados no desenvolvimento deste estudo, com detalhes para as análises *in-situ* de isótopos de enxofre e de elementos traço em sulfetos, são apresentados no **Capítulo 3**. Em seguida, estão listadas as referências bibliográficas citadas nesses três primeiros capítulos.

Os resultados da tese estão redigidos no formato de artigos para divulgação em periódicos internacionais. Dessa forma, o **Capítulo 4** apresenta o artigo científico submetido ao periódico *Geology*, intitulado "*Contrasting preservation of MIF-S in the Jacobina Basin, São Francisco Craton: implications for atmospheric conditions and formation of Au-(U)-Py deposits*". Esse estudo baseou-se na análise dos múltiplos isótopos de enxofre, e elementos-traço, em diferentes fases de pirita encontradas em amostras das seções emersa e marinha da Bacia de Jacobina. Com base nesses dados, são avaliadas as condições ambientais existentes durante a deposição da bacia. Além disso, propõem-se um processo

alternativo à acumulação de ouro nos conglomerados aluviais de Jacobina, o qual estaria associado à formação de pirita sedimentar; em consonância com estudos recentes realizados em Witwatersrand.

O **Capítulo 5** apresenta o artigo científico a ser submetido à revista *Earth and Planetary Science Letters*, intitulado "*Multiple sulfur isotopes and trace elements geochemistry of sulfides from the Paleoarchean (3.3 Ga) Mundo Novo Greenstone Belt, São Francisco Craton, Brazil: clues on S and metal sources in ancient hydrothermal systems*". Nesse estudo, foram determinadas as composições isotópicas do enxofre, e conteúdo de elementos-traço em diferentes tipos de sulfetos associados ao depósito VMS da Fazenda Coqueiro, *Greenstone Belt* Mundo Novo. A partir dessas informações, são avaliadas as prováveis fontes e tipos de fluidos envolvidos na mineralização dos metais-base. Por fim, são consideradas as condições paleoambientais durante a formação do depósito (ao final do Paleoarqueano), e se elas possuem amplitude global, comparando-se com depósitos de idades e gênese semelhantes, em diferentes crátons ao redor do planeta.

O **Capítulo 6** apresenta as considerações finais da tese, enquanto que no **Capítulo 7** encontram-se os Apêndices (materiais suplementares) referentes aos artigos dos **Capítulos 4** e **5**. Além disso, ao final dos Apêndices (Item 7.3) é apresentada uma cópia do artigo intitulado "*Uranium irradiation history of carbonado diamond; implications for Paleoarchean oxidation in the São Francisco craton*", publicado na *Geology* em 2016, e do qual o autor desta tese é 2° autor. Esse trabalho foi desenvolvido como parte da presente tese de doutorado e tem como base a tese de doutorado de Magee (2001), sobre a origem dos diamantes carbonados; e trabalhos recentes, resultantes de estudos geocronológicos na Bacia de Jacobina (Teles et al., 2015) e na Formação Tombador (Guadagnin et al., 2015); os quais forneceram o arcabouço geocronológico e geoquímico para o modelo proposto por Magee et al., (2016), que sugere o enriquecimento em urânio nos diamantes carbonados ao final do Paleoarqueano. Esse trabalho corrobora, por evidências diferentes, com a ideia de que a produção de oxigênio na superfície do planeta ocorreu muito antes do que era anteriormente considerado; sem que, no entanto, essa oxigenação modifique a baixa concentração de O_2 na atmosfera arqueana, mudança que ocorreria somente em torno de 2.3 Ga durante o *Great Oxidation Event* (GOE). Por fim, a produção de oxigênio ao final do Paleoarqueano, no Cráton do São Francisco, teria importante implicação na mineralização aurífera da Bacia de Jacobina (**Capítulo 4**).

CAPÍTULO 2

2.1. DEPÓSITOS AURÍFEROS DO TIPO WITWATERSRAND

O ouro é historicamente um dos metais mais cobiçados pela humanidade. A procura incessante por esse metal levou à descoberta da província aurífera de Witwatersand na África do Sul. Após a descoberta desse depósito no século XIX, cerca de 32% de todo ouro já minerado no planeta (> 52.000 toneladas) seria proveniente dessa província mesoarqueana (Frimmel & Hennigh, 2015). A acumulação gigantesca de ouro nesse depósito ocorre em camadas de conglomerados, onde o metal associa-se comumente a pirita, minerais de urânio, e matéria orgânica. Depósitos auríferos semelhantes ocorrem em diversos países ao redor do globo, dentre os quais o Brasil, Canadá, Índia e Austrália. Em geral, essas mineralizações situam-se em bacias sedimentares antigas, em diferentes áreas cratônicas, cujas idades abrangem boa parte do Arqueano e início do Paleoproterozóico (Frimmel, 2014).

A origem, e o imenso volume de ouro encontrado em Witwatersrand foram importantes temas de debate na Geologia Econômica no último século. Boa parte da discussão se concentrou em duas linhas de hipóteses (ou modelos): o modelo de *paleoplacer* e o modelo hidrotermal. O modelo de *paleoplacer* sugere que o ouro acumulado na Bacia de Witwatersrand foi erodido de fontes ricas no metal; transportado por rios entrelaçados, juntamente com sedimentos rudáceos e pirita, e depositados mecanicamente (por densidade) nas camadas de conglomerado (ex.: Kirk et al., 2003; Figura 2.1). A hipótese hidrotermal sugere que o ouro foi acumulado na bacia após a litificação dos sedimentos. Nesse modelo, fluidos hidrotermais formados em grande profundidade na crosta seriam responsáveis por transportar o ouro, ao longo de falhas e fraturas, para os níveis mais rasos, onde o metal é posteriormente precipitado nos conglomerados (ex.: Barnicoat et al., 1997; Law & Phillips, 2000; Figura 2.1).

No entanto, evidências que corroboram ambas as hipóteses são encontradas nos conglomerados auríferos de Witwatersrand. Por exemplo, partículas de ouro e pirita arredondadas (detríticas), bem como pirita e ouro com morfologias que indicam recristalização (hidrotermais), podem ocorrer conjuntamente numa mesma amostra. Dessa forma, com base nessas evidências, estabeleceu-se um terceiro modelo: o *paleoplacer* modificado (ex.: Frimmel, 2005), que sugere uma origem detrítica para as

partículas de ouro e pirita, as quais seriam recristalizadas durante o metamorfismo nos conglomerados, mas sem a interação de fluidos hidrotermais externos à bacia sedimentar.

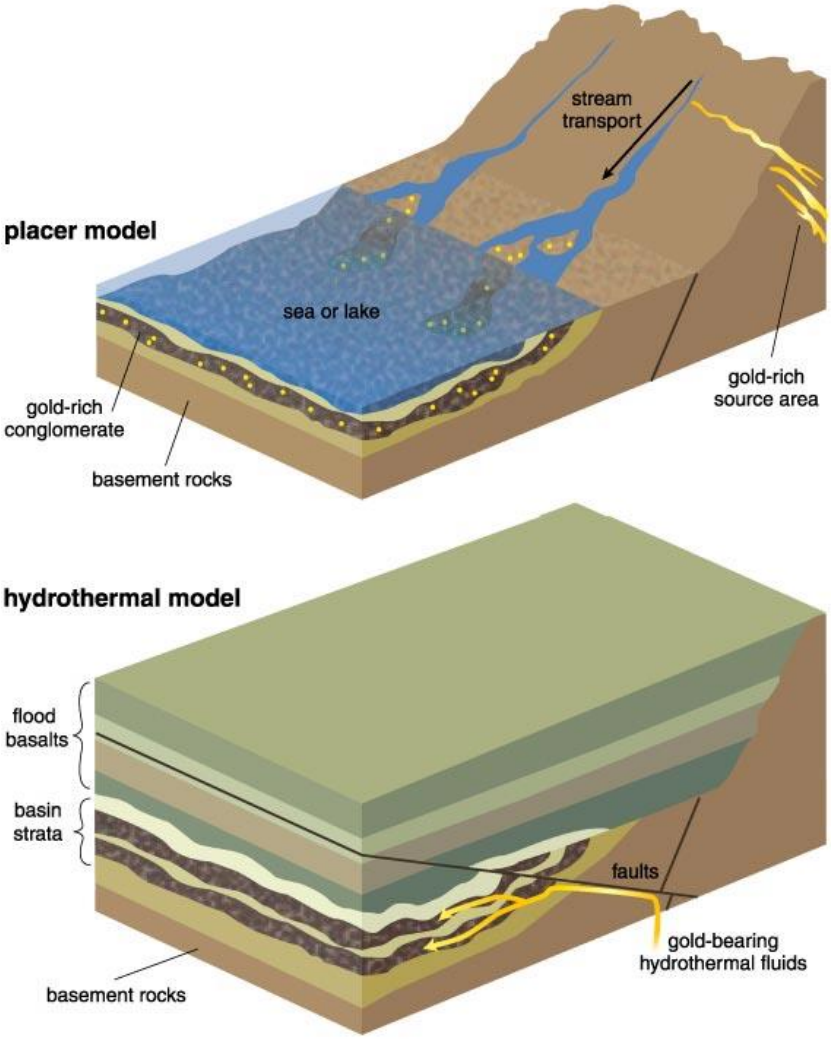

Figura 2.1. Representação das principais hipóteses para gênese do depósito aurífero de Witwatersrand, o modelo de *paleoplacer* e o hidrotermal. Ambas as representações foram tema de debate por mais de um século (Kirk et al., 2003).

Novas ideias sobre a formação do depósito Witwatersrand tem surgido recentemente na literatura, dentre as quais se destacam a acumulação singenética do ouro, associada à formação de pirita sedimentar na bacia, e atividade microbial (ex.: Horscroft et al., 2011; Large et al., 2013; Guy et al., 2014; Agangi et al., 2015; Frimmel & Hennigh, 2015; Heinrich, 2015). A figura 2.2 apresenta de forma resumida os processos relacionados a essa nova proposição, que de certa forma, concilia as evidências de processos hidrotermais e sedimentares (tema de debate por diversos anos).

Segundo o modelo mais recente, o ouro seria lixiviado das áreas fontes da bacia pela ação do intenso intemperismo químico (predominante no Arqueano); a atmosfera arqueana, anóxica e rica em enxofre, permitiria uma grande concentração de ouro dissolvido nas águas superficiais; que dessa forma, seria transportado em solução complexado ao enxofre; e em corpos d'água maiores (de menor energia), favoráveis à proliferação de cianobactérias, o ouro se precipitaria graças à produção local de oxigênio por esses organismos. Por fim, os sedimentos formados nesses ambientes - incluindo pirita singenética (rica em ouro) e partículas de ouro - seriam eventualmente erodidos, retrabalhados juntamente com os sedimentos rudáceos, e posteriormente depositados como camadas de conglomerados ricos em ouro.

O depósito da Bacia de Witwatersrand é a principal referência para compreensão de depósitos semelhantes, sendo em termos de gênese, ou como modelo para exploração e mineração de ouro. Destarte, as considerações propostas, nesta tese, em relação ao depósito da Bacia de Jacobina serão substanciadas com a literatura sobre o depósito sul-africano.

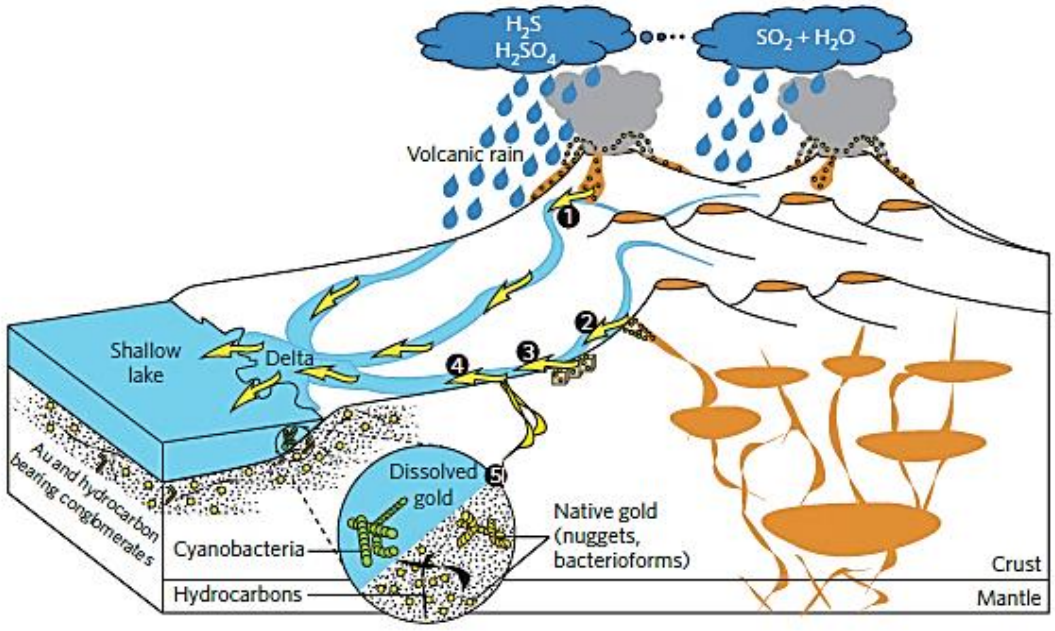

Figura 2.2. Modelo de formação do depósito de Witwatersrand, que envolve evidências da hipótese de *paleoplacer*, bem como do transporte hidrotermal do ouro da área fonte dos sedimentos para a bacia de deposição (Frimmel & Hennigh, 2015; Heinrich, 2015). A explicação completa da ilustração está disponível em Gaillard & Copard (2015).

2.2. DEPÓSITOS DO TIPO SULFETO MACIÇO VULCANOGÊNICO (VMS)

Os depósitos do tipo sulfeto maciço vulcanogênico ou *volcanogenic massive sulfide* (VMS) são praticamente únicos dentre as classes de depósitos minerais existentes; uma vez que eles são relativamente comuns, e abrangem mais que 75% da história do planeta. O exemplo conhecido mais antigo é o depósito da Formação Dresser, na Austrália, que data de cerca de 3.5 Ga (Huston et al., 2010).

Durante décadas, houve uma grande busca pelos correspondentes modernos dos depósitos VMS, que culminaram nas campanhas de pesquisa dos leitos oceânicos. Nessas investigações, ocorridas em diferentes oceanos, foram descobertas as fumarolas exalativas (figuras 2.3 e 2.4), que corresponderiam ao melhor análogo para compreensão dos depósitos VMS de diferentes idades (Hannington et al., 2005). Feições semelhantes às fumarolas atuais foram encontradas, por exemplo, no depósito paleoarqueano (3.26 Ga) do *Greenstone Belt* Strelley, situado no Cráton de Pilbara, Austrália (Vearncombe et al., 1995).

Depósitos do tipo VMS ocorrem tipicamente como lentes massivas de sulfetos polimetálicos, que se formam sob ou próximos ao leito oceânico, em ambientes de vulcanismo submarino, por meio de focos de descarga de fluidos hidrotermais ricos em metais (Franklin et al., 2005; Galley et al., 2007; Hannington et al., 2014). Por essa razão, os depósitos VMS pertencem a uma classe de depósito mais abrangente, os depósitos exalativos, que também incluem os depósitos sedimentares-exalativos (SEDEX). Além disso, depósitos vulcanogênicos correspondem a importantes fontes de uma vasta gama de metais, dentre os quais destacam-se Zn, Cu, Pb, Ag e Au (Galley et al., 2007).

As mineralizações formadas são do tipo *stratabound*, possuem geometria de montículo ou tabular (Figura 2.3); e são compostas principalmente por sulfetos maciços (>40%), quartzo, e de forma subordinada, por filossilicatos e óxidos de ferro (Galley et al., 2007). Esses corpos mineralizados recobrem uma rede de veios (tipo *stockwork)* e sulfetos disseminados, que são envolvidos por distintos halos de alteração (*alteration pipe*; Figura 2.3), e podem constituir concentrações relevantes de minério (mineralização do tipo *stringer*).

A Figura 2.4 sintetiza o funcionamento de um sistema hidrotermal em ambiente marinho, responsável pela formação de um depósito VMS. De maneira geral, fluidos hidrotermais gerados nas proximidades de uma intrusão ígnea são transportados por falhas sinvulcânicas, e descarregados no leito marinho ou em um estrato permeável. A

precipitação dos sulfetos e minerais de ganga ocorre em função do resfriamento do fluido, mistura com água marinha, reação com as rochas encaixantes, e mudanças de pH. Diferentes cenários são possíveis tratando-se da descarga dos fluidos hidrotermais, o que em última instância, pode gerar diferentes tipos de depósitos, a depender das temperaturas, densidade e salinidade das soluções mineralizadoras (Hannington et al., 2014; Tornos et al., 2015).

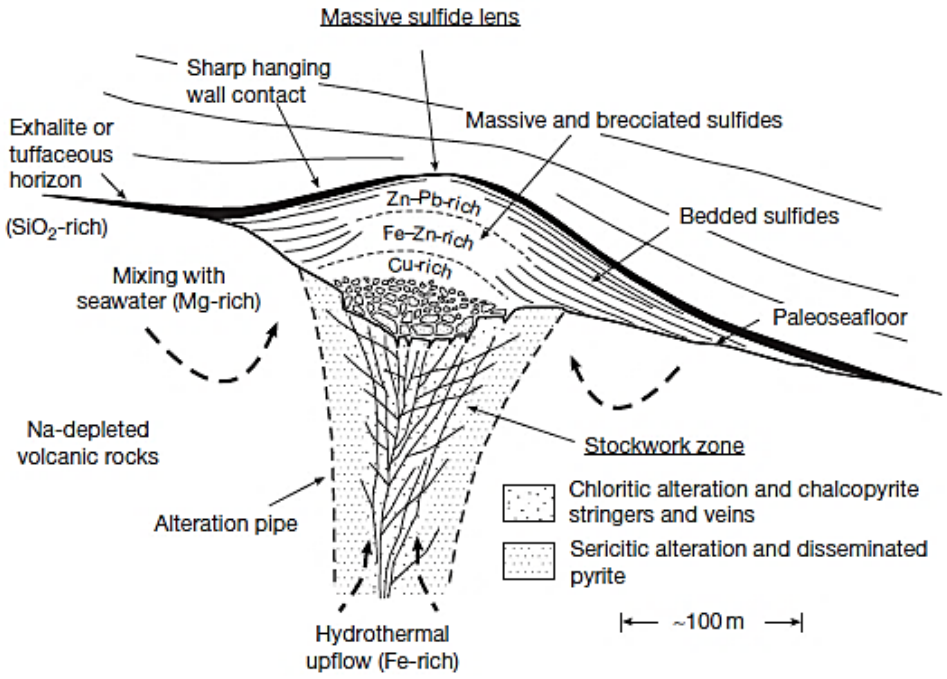

Figura 2.3. Seção esquemática de um típico depósito VMS (Hannington, 2014).

Existe, entretanto, discussão na literatura sobre as fontes dos metais e enxofre envolvidos no sistema mineralizante, bem como do envolvimento efetivo de água marinha nas células hidrotermais. Os fluidos que formam os depósitos VMS, tem sido interpretado como água marinha e/ou fluidos magmáticos hidrotermais. Como consequência, mudanças seculares na composição da água marinha contemporânea podem ter forte influência nas características dos fluidos hidrotermais que formam os depósitos VMS (Huston et al., 2010; Farquhar et al., 2010; Hannington et al., 2014). Alguns estudos demostram que os metais e enxofre foram lixiviados das rochas nas porções mais profundas em alguns depósitos, como no exemplo do depósito de Panorama na Austrália, onde cálculos de balanço de massa indicam que a quantidade de metal lixiviado supera a concentração conhecida no depósito (Huston et al., 2001). Por outro lado, existem evidências de depósitos formados pelo aporte efetivo de metais e enxofre

através de fluidos magmáticos/hidrotermal, com mínimo envolvimento de água marinha; o que demonstra ser uma explicação convincente para alguns depósitos ricos em ouro (Huston et al., 2011).

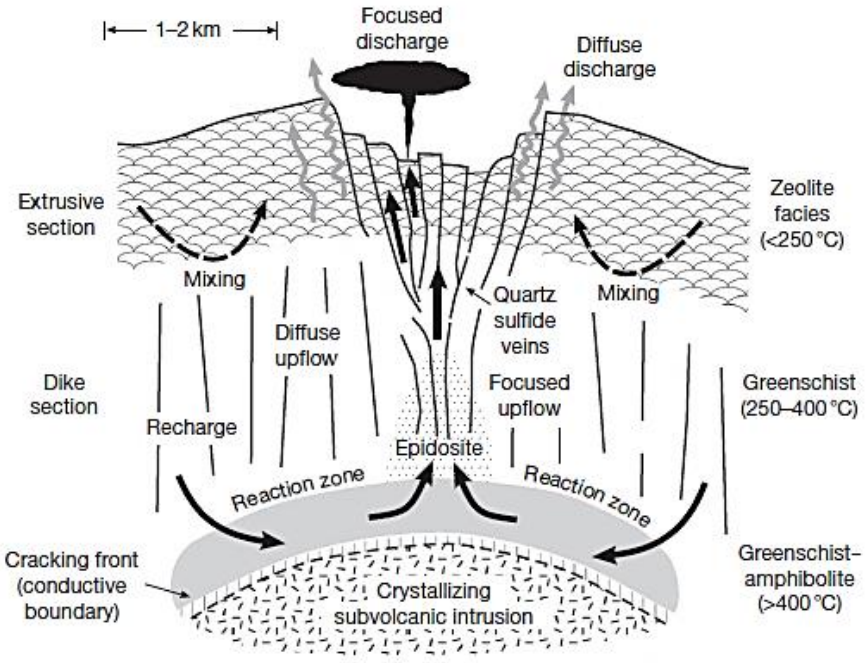

Figura 2.4. Modelo de funcionamento de um sistema hidrotermal marinho (Hannington, 2014).

Os depósitos VMS podem ser classificados por diferentes critérios, mas que de maneira geral estão associados à composição das rochas hospedeiras do depósito, dentre os quais destacam-se:

i. A classificação baseada no conteúdo de metais-base nos depósitos, dividindo-os em função da proporção entre Cu, Zn e Pb (ver Galley et al., 2007 para revisão).
ii. A divisão fundamentada na concentração de ouro nos depósitos, separando-os em dois grupos, os normais e os ricos em ouro.
iii. O sistema de classificação proposto por Barrie & Hannington (1999), posteriormente refinado por Franklin et al., (2005), que considera a sucessão litoestratigráfica hospedeira do depósito, e define cinco classes: bimodal-máfico, máfico-retroarco, pelítico-máfico, bimodal-félsico, e félsico-siliciclástico.

Nota-se que o contexto geodinâmico representa um controle fundamental ao tipo de depósito VMS formado. Nesse sentido, os depósitos VMS possuem como

característica comum sua formação em ambientes extensionais; apesar de que, em diversos casos, o contexto tectônico seja convergente de maneira mais ampla. Os ambientes de formação desses depósitos incluem: dorsais meso-oceânicas e ambientes de arco (arcos nascentes oceânicos e continentais, arcos rifteados, e *back-arcs*).

2.3. GEOQUÍMICA DOS ISÓTOPOS DE ENXOFRE

Isótopos estáveis são variedades não-radioativas de um elemento químico com o mesmo número de prótons, mas com diferente número de nêutrons em seus núcleos. O elemento enxofre (S) possui quatro isótopos estáveis, ^{32}S, ^{33}S, ^{34}S e ^{36}S, os quais possuem abundância relativa de 95,04%, 0,749%, 4,197% e 0,015%, respectivamente (Ding et al., 2001). A abundância relativa entre esses isótopos (ex. $^{34}S/^{32}S$) pode variar em diferentes materiais, em função de reações químicas e biológicas, num processo conhecido como fracionamento isotópico.

A magnitude desse fracionamento é expressa em relação a um padrão conhecido, em per mil (‰), utilizando a notação delta (δ):

$$\delta^{3x}S = \left[\frac{\left(^{3x}S/^{32}S\right)_{amostra} - \left(^{3x}S/^{32}S\right)_{padrão}}{\left(^{3x}S/^{32}S\right)_{padrão}}\right] \times 1000$$

Onde x pode assumir os valores 3, 4 e 6, correspondendo aos isótopos ^{33}S, ^{34}S e ^{36}S. O padrão conhecido, anunciado na equação, é o *Vienna – Canyon Diablo Troillite* (V-CDT), representativo da composição global do reservatório terrestre de enxofre.

Tradicionalmente, investigações sobre a composição isotópica do enxofre em diferentes materiais geológicos estiveram restritas à análise dos dois isótopos mais abundantes (^{32}S e ^{34}S). Isso é explicado, em parte, pelas limitações das técnicas analíticas; mas também em função de observações preliminares. Essas observações demostraram que o fracionamento dos isótopos de enxofre segue uma proporção fixa (Hulston & Thode, 1965), estabelecendo uma relação linear entre $\delta^{33}S$, $\delta^{34}S$ e $\delta^{36}S$, dependente da massa dos isótopos – ou fracionamento dependente da massa (Figura 2.5); o que levou à concepção de que nenhuma informação adicional seria suprida pela análise dos isótopos menos abundantes.

No entanto, Farquhar et al., (2000) ao analisarem os isótopos ^{33}S e ^{36}S em amostras de rochas sedimentares arqueanas, perceberam que essas apresentavam fracionamentos

com proporções distintas, que desviavam da relação linear conhecida; ou seja, com fracionamento independente da massa. Esses desvios (Figura 2.5), ou anomalias isotópicas, são representados na forma de $\Delta^{33}S$ e $\Delta^{36}S$:

$$\Delta^{33}S = \delta^{33}S - 1000 \times \left[\left(1 + \frac{\delta^{34}S}{1000}\right)^{0.515} - 1\right]$$

$$\Delta^{36}S = \delta^{36}S - 1000 \times \left[\left(1 + \frac{\delta^{34}S}{1000}\right)^{1.91} - 1\right]$$

Os mecanismos responsáveis pela geração dessas anomalias isotópicas ainda são motivo de discussão. Entretanto, a hipótese atualmente mais aceita, sugere que o fracionamento independente da massa ocorre através da foto-dissociação do SO_2 pela incidência de radiação ultravioleta (UV) de comprimento de onda curto (<220 nm; Farquhar et al., 2001). Essa reação ocorre nos dias atuais nas camadas mais externas da atmosfera; onde a concentração de oxigênio, e consequentemente de ozônio, é diminuta; permitindo a absorção de parte do espectro UV, o que permite a foto-dissociação do SO_2.

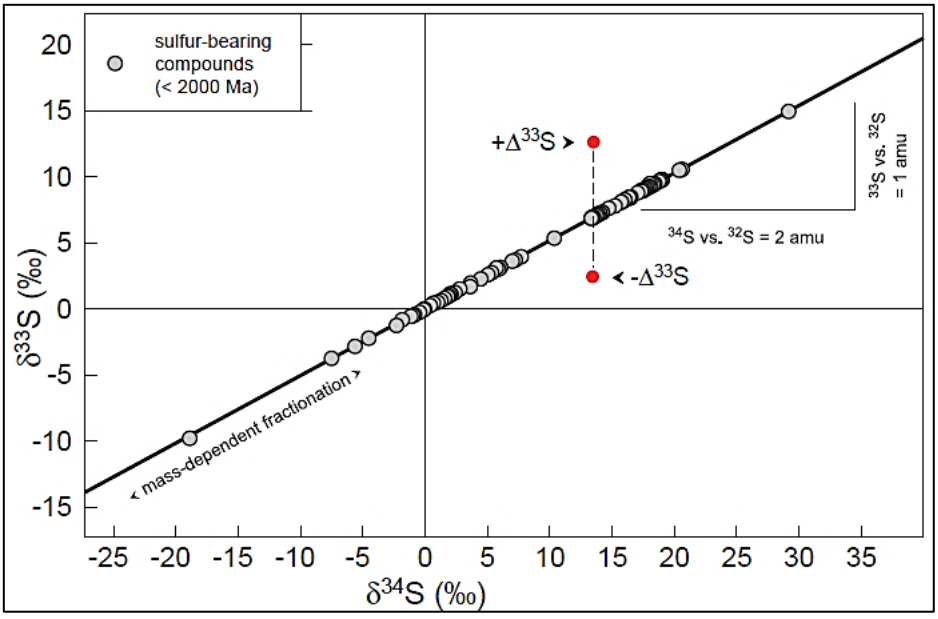

Figura 2.5. Relação linear que representa o fracionamento dependente da massa, dominante em materiais mais novos que 2.0 Ga. Os pontos em vermelho indicam as assinaturas anômalas, ou fracionamento independente da massa, indicado por $\Delta^{33}S$; que representa o desvio de amostras mais antigas em relação à linha do fracionamento terrestre (Farquhar & Wing, 2003).

O fator principal para o sucesso dessa reação fotoquímica (a ausência de O_2 atmosférico) foi repetido em experimentos de laboratório, nos quais as anomalias isotópicas foram reproduzidas (Farquhar et al., 2001). Este *link* com as concentrações de oxigênio, e as anomalias isotópicas medidas por Farquhar et al., (2000), em amostras restritas ao Arqueano; representam um forte indício da baixa concentração de oxigênio na atmosfera até ~2.4 Ga (Farquhar et al., 2000; Farquhar & Wing, 2003; Farquhar et al.,2014), com modelos que indicam concentração em torno de ~1 ppm, ou $<10^{-5}$ *PAL* (*Present Atmospheric Level*; Pavlov & Kasting, 2002).

2.3.1. O Ciclo do Enxofre no Arqueano

Diversas evidências geológicas e geoquímicas sustentam a ideia da concentração limitada de oxigênio livre (O_2) na atmosfera durante o Arqueano (Farquhar et al., 2014), e, portanto, da ausência de uma camada de ozônio capaz de proteger a superfície do planeta da incidência da radiação ultravioleta.

Dessa forma, a formação do fracionamento independente da massa dos isótopos de enxofre ocorreria pela interação da radiação UV com compostos de enxofre liberados por vulcões. Em uma atmosfera rica em oxigênio, como a atual, essas reações ocorrem em suas camadas mais superiores, mas as assinaturas anômalas são rapidamente homogeneizadas graças à oxidação dos compostos de enxofre (Farquhar & Wing, 2003).

Na atmosfera anóxica do Arqueano, gases vulcânicos (ex. H_2S e SO_2) reagem com a radiação UV, e produzem aerossóis de enxofre elementar (ex. S_8) e de enxofre oxidado (ex. H_2SO_4); os quais carregam, respectivamente, as anomalias positivas e negativas do $\Delta^{33}S$ (Farquhar & Wing, 2003; Figura 2.6).

Ambas as anomalias são transferidas para a superfície por dois canais principais (Figura 2.6). O primeiro, correspondente ao sulfato produzido pelas reações na atmosfera, se acumula nos oceanos na forma de íon dissolvido, preservando os valores negativos do $\Delta^{33}S$ (Halevy et al., 2010). Essa premissa é suportada pelos valores negativos do $\Delta^{33}S$ em diferentes depósitos de barita encontrados na Índia, Austrália e África do Sul (Farquhar et al., 2000; Huston & Logan, 2004; Philippot et al., 2007; Ueno et al., 2008; Shen et al., 2009; Philippot et al., 2012; Roerdink et al., 2012; Montinaro et al., 2015; Muller et al., 2017); bem como em sulfetos em depósitos do tipo VMS (Bekker et al., 2009; Jamieson et al., 2013; Sharman et al., 2015; Chen et al., 2015). O segundo canal, correspondente ao do enxofre reduzido ou elementar; que por ser insolúvel na coluna d'água, é acumulado

no leito dos oceanos, onde rapidamente reage com ferro disponível para formar pirita sedimentar com valores positivos do $\Delta^{33}S$; e que é fato comum em diversas sequências sedimentares arqueanas (Farquhar & Wing, 2003; Ono et al., 2003; Halevy et al., 2010).

O registro das anomalias de enxofre ao longo do tempo geológico pode ser dividido em pelo menos três fases (Figura 2.7). A primeira, pré-2.45 Ga, apresenta anomalias variadas e proeminentes. A segunda, entre 2.45 e 2.0 Ga, possui anomalias menos expressivas; e a terceira, pós-2.0 Ga, onde as anomalias deixam de existir e o fracionamento dependente da massa passa a dominar nos diversos ambientes do planeta (Farquhar & Wing, 2003).

Apesar da variabilidade das anomalias isotópicas pré-2.45 Ga, considerada por alguns autores como um indício de oxigenação da atmosfera (ex.: Ohmoto et al., 2006); notou-se uma consistente relação entre as anomalias ($\Delta^{36}S/\Delta^{33}S \sim -1.0$), para o Paleoarqueano e Neoarqueano, sendo isso um reflexo das reações fotoquímicas numa atmosfera anóxica (Farquhar et al., 2000; Kaufman et al., 2007; Thomassot et al., 2015). Para essa relação, deu-se o nome de *Archean Array* ($\Delta^{36}S/\Delta^{33}S \approx -1$). A exceção para esse comportamento ocorre durante o Mesoarqueano, quando a magnitude das anomalias do $\Delta^{33}S$ diminuiu significativamente. Para esse intervalo, considera-se que mudanças na composição química da atmosfera, ou o aumento da concentração de gases que inibem a fotólise do SO_2 (ex.CH_4), seriam responsáveis pela diminuição dos valores do $\Delta^{33}S$, mas sem nenhuma relação com um aumento do O_2 livre na atmosfera (Farquhar et al., 2007).

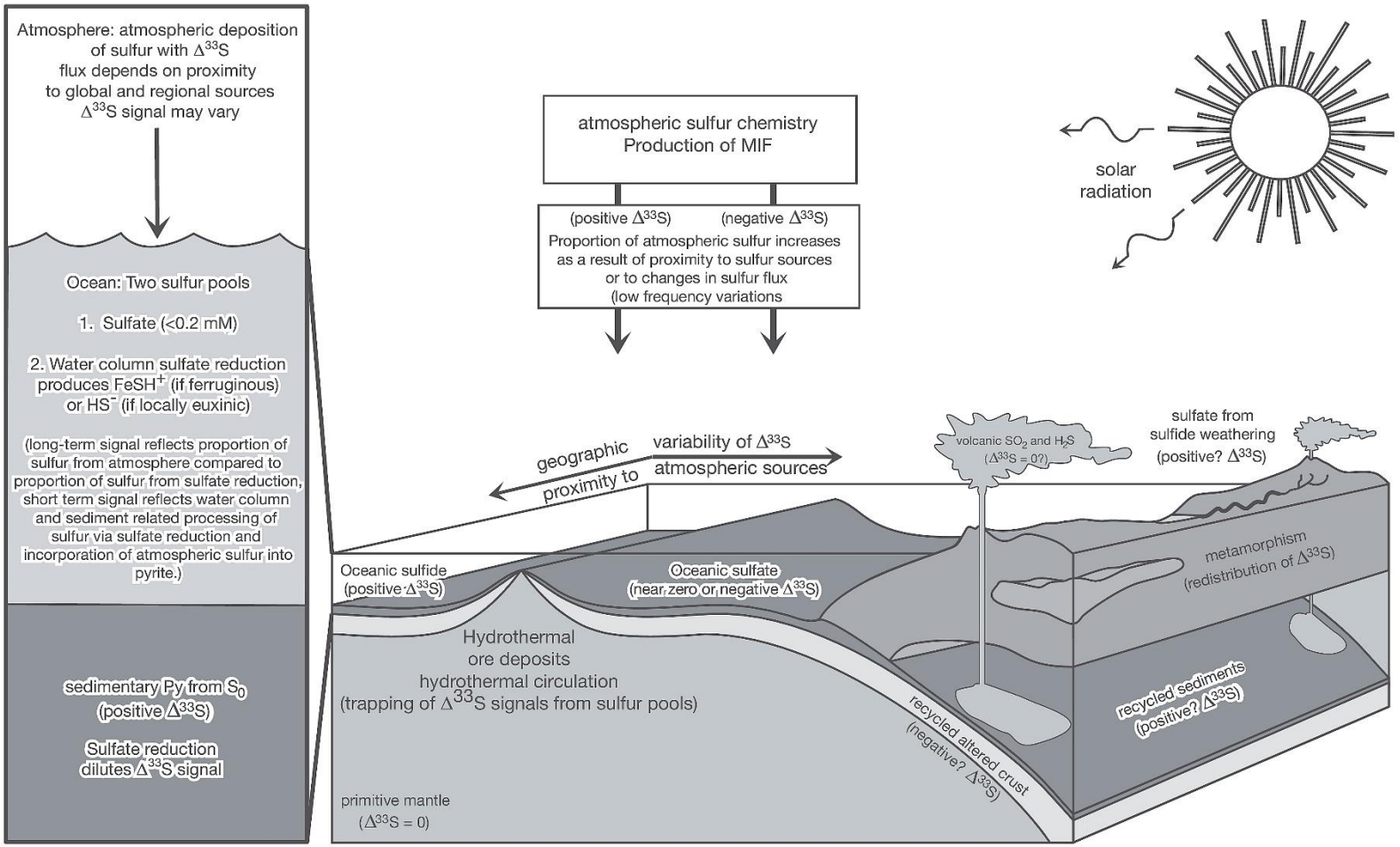

Figura 2.6. Diagrama ilustrativo do ciclo do enxofre no Arqueano, com os valores correspondentes do $\Delta^{33}S$ em diferentes reservatórios terrestres, e indicação dos diferentes caminhos de transferência das assinaturas anômalas da atmosfera para a superfície terrestre (Farquhar & Wing, 2003).

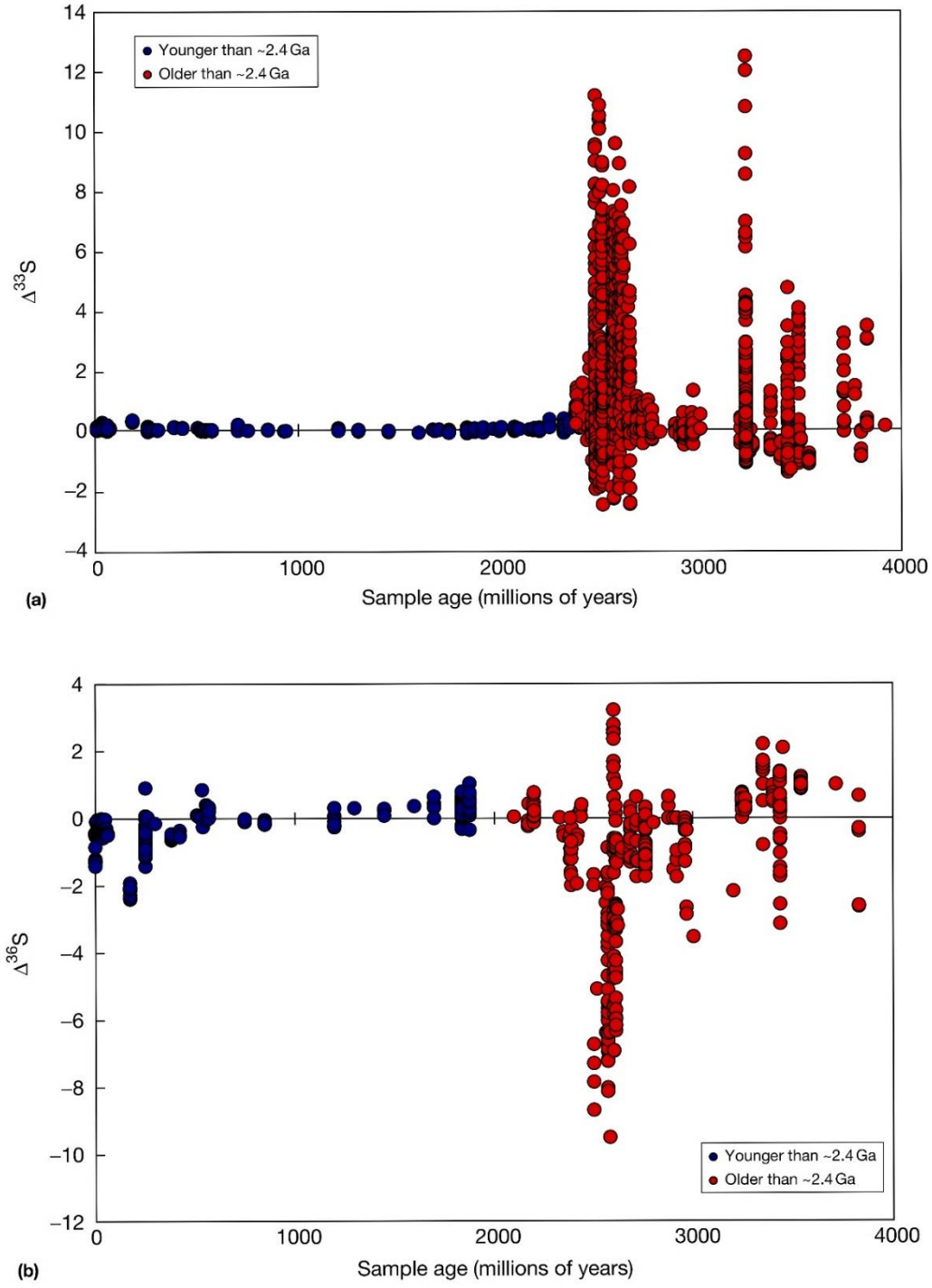

Figura 2.7. Variação das anomalias isotópicas do enxofre ao longo do tempo geológico (Farquhar et al., 2014). (a) Gráfico dos valores do $\Delta^{33}S$ em relação à idade da amostra. (b) *Plot* dos valores do $\Delta^{36}S$ vs. idade da amostra. Os símbolos em vermelho correspondem a amostras mais antigas que 2.4 Ga, enquanto que os azuis representam amostras mais novas que 2.4 Ga.

2.3.2. Aplicação dos Múltiplos Isótopos de Enxofre no Estudo de Depósitos Minerais

A descoberta do fracionamento independente da massa dos isótopos de enxofre, em amostras mais antigas que 2.4 Ga, trouxeram uma nova percepção sobre os mecanismos de formação de diferentes tipos de depósitos minerais no Arqueano. Não somente em função das fontes do enxofre e de metais no sistema mineralizante, mas também em relação à química da hidrosfera e atmosfera no momento de formação dos depósitos.

Ademais, a identificação dessas anomalias em depósitos minerais é um complemento para as informações, geralmente limitadas, fornecidas pelo $\delta^{34}S$ - valor tradicionalmente determinado nas análises isotópicas de enxofre. Um exemplo disso ocorre em depósitos do tipo VMS.

Devido à condição anóxica da atmosfera durante o Arqueano, considera-se que os oceanos desse período possuíam baixa concentração em sulfato dissolvido; uma vez que a principal fonte desse íon está associada ao intemperismo oxidativo nos continentes. Dessa forma, acreditava-se que o sulfato dissolvido nos oceanos não seria um componente fundamental na formação dos depósitos VMS arqueanos, ao contrário daqueles formados no Fanerozóico. Essa premissa, corroborada pelos valores limitados do $\delta^{34}S$ em depósitos arqueanos (entre -2.0 a +2.0‰; Huston & Logan, 2004), os quais sugerem fontes magmáticas para esses depósitos. Todavia, trabalhos recentes têm demonstrado, através da análise adicional do isótopo ^{33}S, que o íon sulfato estaria envolvido nos sistemas hidrotermais formadores dos depósitos VMS no Arqueano. A prova disso são os valores negativos do $\Delta^{33}S$ nos sulfetos desses depósitos (ex.: Bekker et al., 2009; Golding et al., 2011; Jamieson et al., 2013; Sharman et al., 2015; Chen et al., 2015). Entretanto, a origem desse sulfato seria fotoquímica, conforme explanado anteriormente.

Além dos depósitos VMS, a análise dos múltiplos isótopos de enxofre tem auxiliado na compreensão de diversos depósitos minerais antigos, dentre os quais podem ser destacados: os depósitos auríferos do tipo Witwatersrand (ex.: Hofmman et al., 2009; Ulrich et al., 2011; Guy et al., 2014; Agangi et al., 2015), do tipo *lode* (ex.: Xue et al., 2013), e depósitos de níquel associados a komatiitos (ex.: Bekker et al., 2009).

CAPÍTULO 3

3.1. MATERIAIS E MÉTODOS

3.1.1. Amostras

As amostras estudadas neste trabalho foram coletadas nos anos de 2014 e 2015, e são provenientes tanto de afloramentos quanto de furos de sonda. As amostras de afloramentos foram coletadas na porção setentrional do cinturão composto pelas rochas da Bacia de Jacobina e do *Greenstone Belt* Mundo Novo; estando geograficamente localizadas entre os municípios de Jacobina e Pindobaçu (vide mapas de localização nos capítulos 4 e 5).

Na região entre Jacobina e Pindobaçu é possível observar as relações de contato entre os sedimentos da bacia, e as rochas do *greenstone belt*. Nessa localidade foram amostradas rochas correspondentes às fácies meta-vulcânicas máficas, químicas (*cherts* e formação ferrífera), e sedimentares (xistos carbonosos) do *greenstone*. Em relação à Bacia de Jacobina, foi amostrado o intervalo representativo da porção superior da bacia, correspondente à Formação Serra da Paciência, cujas rochas indicam deposição predominantemente em ambiente marinho.

O intervalo basal da bacia foi amostrado em três furos de sonda, gentilmente cedidos pela exploração da Jacobina Mineração e Comércio (JMC), pertencente ao grupo canadense Yamana Gold. Esses furos interceptam os diferentes *reefs* (conglomerados) mineralizados que caracterizam a Formação Serra do Córrego, na qual se concentra a extração de ouro na região. As amostras foram coletadas de maneira a representar, nos três furos, os diferentes níveis estratigráficos da formação (vide Capítulo 4); desde o contato com o embasamento, até sua transição para a Formação Rio do Ouro; com preferência aos intervalos contendo pirita preservada.

Em função da escassez de afloramentos do *Greenstone Belt* Mundo Novo em sua porção meridional, nas proximidades do município de Mundo Novo; somente amostras provenientes de furos de sonda foram estudadas. As amostras de testemunho foram cedidas pela Companhia Baiana de Pesquisa Mineral (CBPM), a qual desenvolveu diversas campanhas de sondagem para pesquisa do depósito de Zn-Cu-Pb associado aos sulfetos vulcanogênicos da Fazenda Coqueiro. As amostras obtidas dessa localidade abrangem diferentes níveis do depósito, dentre os quais, o *footwall*, o *hangingwall*; o

principal intervalo mineralizado (sulfeto maciço), bem como mineralizações associadas ao *stringer*. Os litotipos correspondentes são metabasaltos, tremolititos, *cherts*, mica-xistos, e sulfeto maciço.

Após a obtenção das amostras, estas foram descritas macroscopicamente, e suas porções de interesse foram selecionadas para confecção de lâminas e seções polidas. Posteriormente, essas amostras foram observadas ao microscópio petrográfico, para descrição das texturas dos sulfetos e sua paragênese. Nesta etapa, utilizou-se de hipoclorito de sódio (NaOCl), substância que produz uma leve oxidação na superfície dos sulfetos (principalmente pirita), produzindo um efeito semelhante à técnica de *etching* tradicional, realizada com ácidos. Dessa forma, o *etching* com NaOCl revela possíveis variações composicionais na superfície dos sulfetos, as quais, em alguns casos, são difíceis de detectar mesmo com auxílio de técnicas mais sofisticadas, como o microscópio eletrônico de varredura (MEV), por exemplo (Figura 3.1). Contudo, esse procedimento não altera as composições química e isotópicas do sulfeto; além de que a superfície oxidada pode ser facilmente removida com polimento.

Por fim, ao final da observação mais detalhada das amostras, e descrição das possíveis variações texturais dos sulfetos, foram selecionados os locais para as análises *in-situ*, tanto isotópicas (SHRIMP-SI), quanto de elementos-traço (LA-ICP-MS), cujos procedimentos analíticos são descritos nos itens subsequentes.

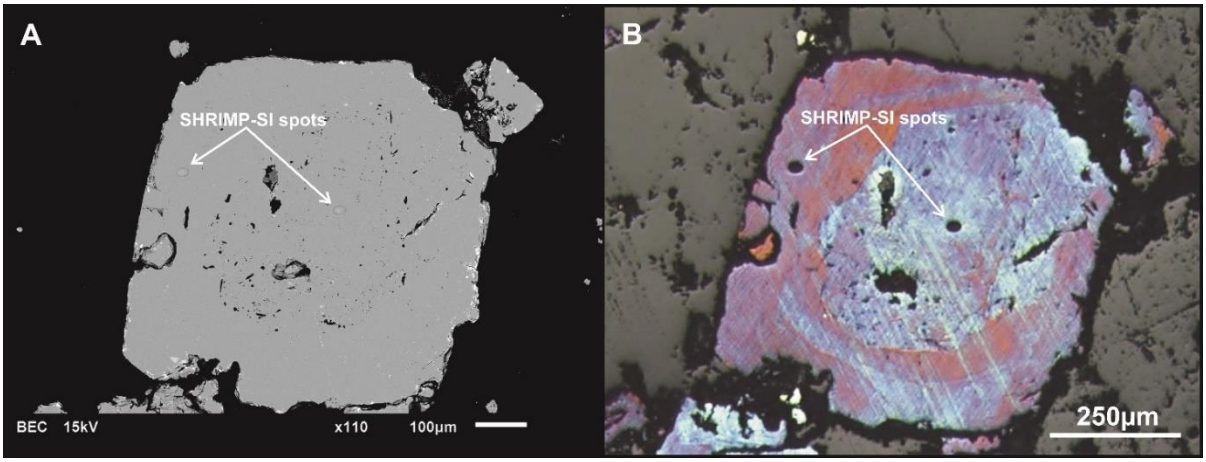

Figura 3.1. Comparação entre imagens de elétrons retroespalhados (A) e fotomicrografia à luz refletida (B) do mesmo grão de pirita. Nota-se, no segundo exemplo, que o grão possui diferentes zonas composicionais, dificilmente perceptíveis com o uso do MEV, mas facilmente distinguíveis após o *etching* com NaOCl.

3.1.2. Sensitive High-Resolution Ion Microprobe - Stable Isotopes (SHRIMP-SI)

Diagênese, metamorfismo e hidrotermalismo são processos que podem facilmente alterar a composição original de uma rocha. No caso de rochas muito antigas, dentre as quais as formadas no Arqueano, a possibilidade de atuação de pelo menos um desses processos é grande. Essa constatação é válida, por exemplo, quando se trata da composição isotópica do enxofre em amostras muito antigas, cuja composição inicial pode ter sido mascarada, modificada ou mesmo obliterada. Nesse sentido, o registro isotópico do enxofre (pré-GOE) deve ser avaliado com cautela, uma vez que processos posteriores podem ter modificado a assinatura original da atmosfera, hidrosfera e biosfera primitivas.

Dessa maneira, o SHRIMP-SI (*Sensitive High-Resolution Ion Microprobe - Stable Isotopes*) foi desenvolvido para permitir a análise dos múltiplos isótopos de enxofre com alta precisão analítica; em sulfetos que requerem a avaliação de heterogeneidades em microescala, em função dos diferentes registros que um único grão pode conter. Esse equipamento é bastante similar aos modelos já consagrados do SHRIMP, os quais são amplamente utilizados para datação U-Pb em zircão, por exemplo. De maneira similar às análises de oxigênio nos modelos mais antigos, o SHRIMP-SI utiliza de um feixe de íons de césio (Cs^+) para extrair o enxofre da amostra, na forma de íons secundários com carga negativa (Figura 3.2). O feixe de íons Cs^+, neste caso, foi focalizado para analisar *spots* com áreas de aproximadamente 25 µm na superfície dos sulfetos.

A geometria do SHRIMP-SI é semelhante à utilizada no SHRIMP-II (Ireland et al., 2014), o que permite elevada resolução de massa, mantendo alta sensibilidade através do espectrômetro. O *design* do equipamento inclui multi-coletores (copos de Faraday) que podem ser configurados de acordo com o objetivo da análise. Na configuração para mensuração dos quatro isótopos de enxofre, o equipamento é capaz de obter medidas do $\Delta^{33}S$ com erros internos melhores que 0.05‰ (2SE), e reprodutibilidade tipicamente de 0.1‰ (2σ). Medidas do tipo *charge mode* (Ireland et al., 2014) do $^{36}S^-$ geram valores do $\Delta^{36}S$ com precisão interna de $\pm$ 0.25‰ (2SE) e reprodutibilidade melhor que 0.5‰ (2σ). A determinação das composições isotópicas, bem como a avaliação da acurácia das medidas ($\delta^{33}S$, $\delta^{34}S$, $\delta^{36}S$, $\Delta^{33}S$ e $\Delta^{36}S$) ocorre pela análise de padrões de referência de sulfetos, realizada no início e fim de cada sessão analítica, bem como entre as análises das amostras.

A figura 3.2 apresenta uma visão geral do SHRIMP-SI, da geometria dos coletores utilizada na análise dos quatro isótopos de enxofre, bem como das condições analíticas empregadas. Detalhes sobre alguns dos procedimentos prévios e aplicados durante as análises, padrões de sulfetos utilizados, além do conjunto de dados obtidos para as amostras e padrões, podem ser observados nos capítulos 4. 5, e nos Apêndices desta tese.

3.1.3. Laser Ablation Inductive Coupled Plasma Mass Spectometry (LA-ICP-MS)

A técnica de LA-ICP-MS (*Laser Ablation Inductive Coupled Plasma Mass Spectometry*) é uma das mais difundidas nas geociências, pois serve para diversas aplicações, e permite a análise de uma grande variedade de materiais geológicos.

Devido à sua praticidade, a técnica tem sido cada vez mais utilizada para estudos de depósitos minerais, pois ela permite a análise de praticamente toda a tabela periódica, de forma rápida, barata, e com limites de detecção muito baixos para a maioria dos elementos químicos (Norman et al., 2003; Danyushevsky et al., 2011, Gregory et al., 2015). Além desses aspectos, a técnica de LA-ICP-MS permite análises com elevada resolução espacial e temporal, que permite a detecção de fases minerais distintas, bem como a produção de mapas composicionais (ex: Large et al., 2009). Os dados obtidos por essa técnica permitem, portanto: 1) observar a distribuição de elementos-traço em minerais e minérios associados, informação que pode ser utilizada como indicadores (vetores) da distribuição de metais-base e preciosos; 2) indicar as condições físico-químicas que controlam a deposição do minério; e 3) investigar as fontes dos metais.

Neste trabalho, um conjunto de elementos de interesse foram analisados em diferentes sulfetos, nas amostras do depósito aurífero de Jacobina, e em exemplares das mineralizações sulfetadas do *Greenstone Belt* Mundo Novo. Os dados obtidos são discutidos nos capítulos 4 e 5, e disponibilizados nos Apêndices desta tese.

As análises foram realizadas na *Research School of Earth Sciences* (RSES), *Australian National University* (ANU). As amostras de sulfetos foram analisadas por um sistema de ablação *Lambda Physic Laser*, operando em 193 nm, com uma energia de 45 mJ. Após a ablação, o material foi carregado por uma mistura de H-He-Ar para o ICP-MS, neste caso um quadrupolo da séria 7700 da *Agilent Technology*.

A ablação dos sulfetos ocorreu na forma de *spots*, dependendo do tamanho e da complexidade textural dos grãos (observada após o *etching* das amostras). Nessas análises, o feixe do *laser* variou entre13 e 27 µm; a coleta de dados foi programada para

65 segundos, sendo 20 deles dedicados à aquisição do *background* (*laser* desligado), e 45 segundos para ablação e aquisição dos elementos de interesse (Figura 3.3).

Os padrões de sulfeto MASS-1 (Wilson et al., 2002) e STDGL-1 (Norman et al., 2003), além dos padrões NIST-610 e NIST-612 foram utilizados ao longo das sessões analíticas, intercalados com as análises das amostras. A redução dos dados e integração dos sinais seguiram os procedimentos descritos por Longerich et al., (1996), e realizadas com o uso do *software* Iolite (Paton et al., 2011), de forma a minimizar erros durante o processamento, e normalizar as amostras desconhecidas aos valores dos padrões utilizados. Análises adicionais, no padrão RTS-4 (Norman et al., 2003), foram realizadas e tratadas juntamente com as amostras desconhecidas, com o objetivo de assegurar a qualidade dos dados obtidos.

Inclusões de fases distintas às dos sulfetos em questão foram identificadas durante a redução dos dados. Essas fases estão associadas a "saltos" no sinal dos elementos que as compõem, sem que haja o mesmo comportamento para os principais constituintes do sulfeto. Por exemplo, na figura 3.3A, ocorre uma inclusão de galena (vide pico do Pb). Dentro do possível, os intervalos associados a esses picos (fases minerais distintas) foram evitados durante a redução dos dados.

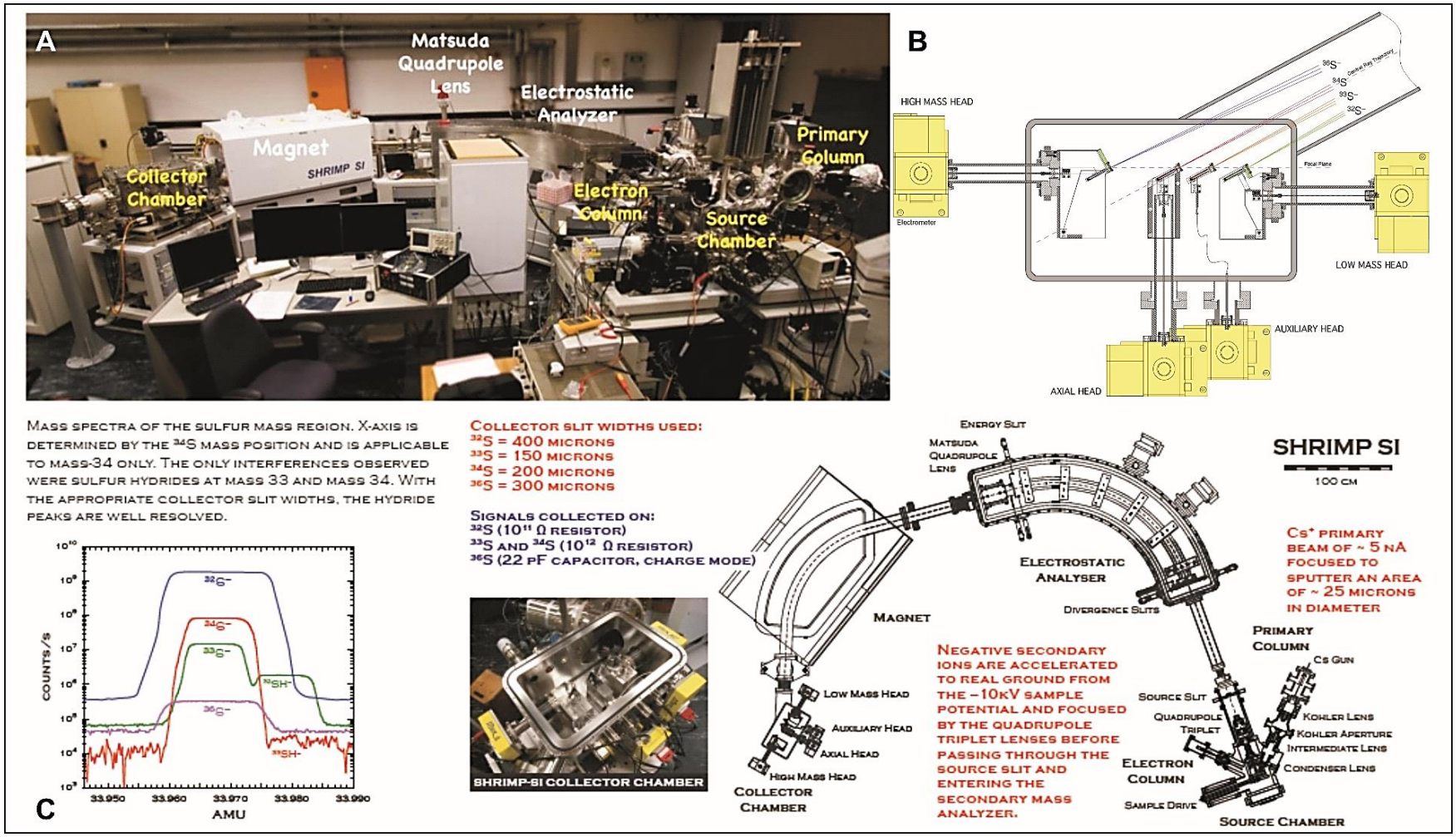

Figura 3.2. (A) SHRIMP-SI e seus principais componentes. (B) Geometria dos coletores utilizada na análise dos quatro isótopos de enxofre. (C) Condições analíticas empregadas durante a aquisição dos dados isotópicos.

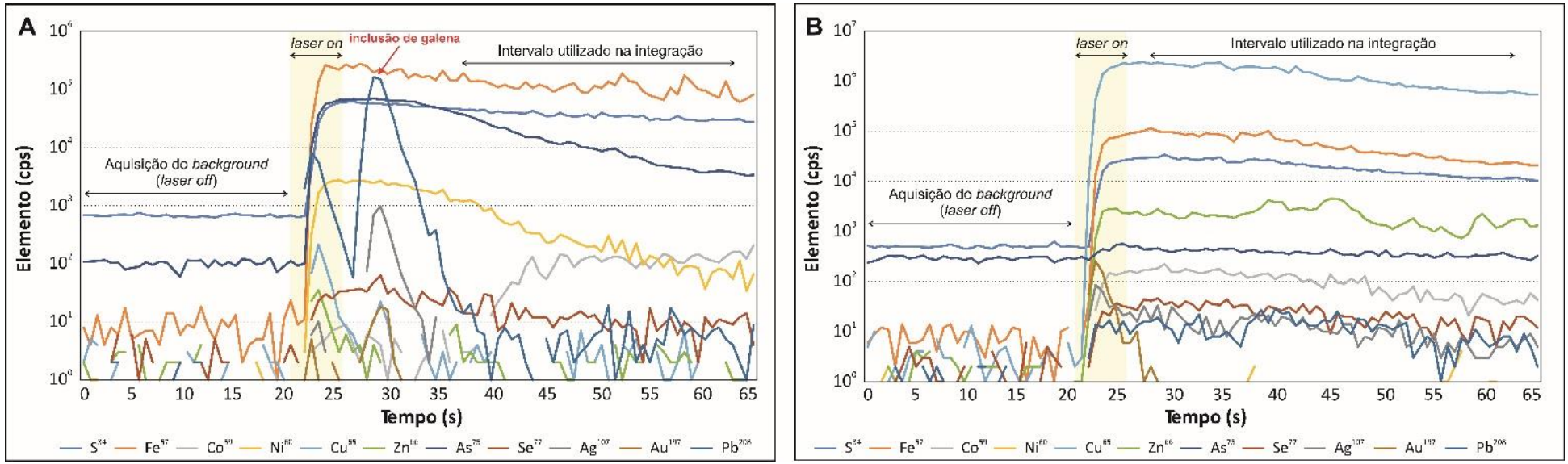

Figura 3.3. Exemplos de análises de sulfetos com LA-ICP-MS, com demonstração de alguns elementos analisados. (A) Análise de pirita, com indicação de inclusão de galena (pico no sinal do ^{208}Pb). (B) Análise em calcopirita. Os intervalos considerados para aquisição do *background*, e para o cálculo das concentrações dos elementos estão indicados.

REFERÊNCIAS BIBLIOGRÁFICAS

Agangi, A., Hofmann, A., Rollion-Bard, C., Marin-Carbonne, J., Cavalazzi, B., Large, R., Meffre, S., 2015. Gold accumulation in the Archaean Witwatersrand Basin, South Africa – Evidence from concentrically laminated pyrite. Earth-Science Reviews 140, p. 27-53.

Barbosa, J.S.F., Sabaté, P., 2004. Archean and Paleoproterozoic crust of the São Francisco Craton, Bahia, Brazil: geodynamic features. Precambrian Research 133, p. 1-27.

Barnicoat, A.C., et al., 1997. Hydrothermal gold mineralization in the Witwatersrand basin. Nature 386, p. 820-824.

Barrie, C.T., Hannington, M.D., 1999. Classification of volcanic-associated massive sulphide deposits based on host-rock compositions. Reviews in Economic Geology 8, p. 1-11.

Bekker, A., Barley, M.E., Fiorentini, M.L., Rouxel, O.J., Rumble, D., Beresford, S.W., 2009. Atmospheric Sulfur in Archean Komatiite-Hosted Nickel Deposits. Science 326, p. 1086-1089.

Cattling, D.C. 2014. The Great Oxidation Event Transition. *In*: Holland, H., Turekian, K., (eds.), Treatise on Geochemistry 2nd Edition: Amsterdam, Elservier, p. 177-195.

Chen, M., Campbell, I.H., Xue, Y., Tian, W., Ireland, T.R., Holden, P., Cas, R.A.F., Hayman, P.C., Das, R., 2015. Multiple Sulfur Isotope Analyses Support a Magmatic Model for the Volcanogenic Massive Sulfide Deposits of the Teuctonic Bore Volcanic Complex, Yilgarn Craton, Western Australia. Economic Geology 110, p. 1411-1423.

Cruz, S.C.P., *et al*., 2012. The Caraguataí syenitic suite, a ca. 2.7 Ga-old alkaline magmatism (petrology, geochemistry and U-Pb zircon ages). Southern Gavião block (São Francisco Craton), Brazil. Journal of South American Earth Sciences 37, p. 95-112.

Cunha, J.C., Barbosa, J.S., Mascarenhas, J.F., 2012. *Greenstone Belts* e Sequências Similares. *In*: Barbosa, J.S.F., Mascarenhas, J.F., Gomes, L.C.C., Dominguez, J.M.L., Souza, J.S., (eds.), Geologia da Bahia: pesquisa e atualização: Salvador, CBPM, p. 203-325.

Danyushevsky, L., Robinson, P., Gilbert, S., Norman, M., Large, R., McGoldrick, P., Shelley, M., 2011. Routine quantitative multi-element analysis of sulphide minerals by laser ablation ICP-MS: Standard development and consideration of matrix effects. Geochemistry: Exploration, Environment, Analysis 11, p. 51-60.

Ding, T., Valkiers, S., Kipphardt, H., De Bièvre, P., Taylor, P.D.P., Gonfiantini, R., Krouse, R., 2001. Calibrated sulfur isotope abundance ratios of three IAEA sulfur isotope reference materials and V-CDT with a reassessment of the atomic weight of sulfur. Geochimica et Cosmochimica Acta 65 (15), p. 2433-2437.

Dodd, M.S., Papineau, D., Grenne T., Slack, J.F., Rittner, M., Pirajno, F., O'Neil, J., Little, C.T.S., 2017. Evidence for early life in Earth's oldest hydrothermal vent precipitates. Nature 543, p. 60-64.

Farquhar, J., Bao, H., Thiemens, M., 2000. Atmospheric Influence of Earth's Earliest Sulfur Cycle. Science 289, p. 756-758.

Farquhar, J., Savarino, J., Airieau, S., Thiemens, M., 2001. Observation of wavelength-sensitive mass-independent súlfur isotope effects during SO_2 photolysis: Implications for the early atmosphere. Journal of Geophysical Research 106, p 32829-32839.

Farquhar, J., Wing, B.A., 2003. Multiple sulfur isotopes and the evolution of the atmosphere. Earth and Planetary Science Letters 213, p. 1-13.

Farquhar, J., Peters, M., Johnston, D.T., Strauss, H., Masterson, A., Wiechert, U., Kaufman, A.J., 2007. Isotopic evidence for Mesoarchean anoxia and changing atmospheric sulphur chemistry. Nature 449, p. 706-709

Farquhar, J., Wu, N., Canfield, D.E., Oduro, H., 2010. Connections between Sulfur Cycle Evolution, Sulfur Isotopes, Sediments, and Base Metal Sulfide Deposits. Economic Geology 105, p. 509-533.

Farquhar, J., Zerkle, A.L., Bekker, A., 2014. Geologic and Geochemical Constraints on Earth's Early Atmosphere. *In*: Holland, H., Turekian, K., (eds.), Treatise on Geochemistry 2nd Edition: Amsterdam, Elservier, p. 91-129.

Franklin, J.M., Gibson, H.L., Jonasson, I.R., Galley, A.G., 2005. Volcanogenic massive sulfide deposits. *In*: Hedenquist, J.W., Thompson, J.F.H., Goldfarb, R.J., Richards, J.P., (eds.), 100th Anniversary Volume of Economic Geology, p. 523-560.

Frimmel, H.E., 2005. Archaean atmospheric evolution: evidence from the Witwatersrand gold fields, South Africa. Earth Science Reviews 70, p. 1-46.

Frimmel, H.E., 2014. A Giant Mesoarchean Crustal Gold-Enrichment Episode: Possible Causes and Consequences for Exploration. Society of Economic Geologists, Special Publication 18, p. 209-234.

Frimmel, H.E., Hennigh, Q., 2015. First whiffs of atmospheric oxygen triggered onset of crustal gold cycle. Mineralium Deposita 50, p. 5-23.

Gaillard, F., Copard, Y., 2015. Gold buried by oxygen. Nature Geoscience 8, p. 1-2.

Galley, A.G., Hannington, M.D., Jonasson, I.R., 2007. Volcanogenic massive sulphide deposits. *In*: Goodfellow, W.D., (ed.), Mineral Deposits of Canada: A Synthesis of Major Deposit-Types, District Metallogeny, the Evolution of Geological Provinces, and Exploration Methods. Geological Association of Canada, Special Publication 5, p. 141-161.

Golding, S.D., Duck, L.J., Young, E., Baublys, K.A., Glikson, M., Kamber, B.S., 2011. Earliest seafloor hydrothermal systems on Earth: comparisons with modern analogues. *In*: Golding, S.D., (eds.), Earliest life on Earth:habitats, environments and methods of detection: Dordrecht, Springer, p. 15-49.

Gregory, D.D., Large, R.R., Halpin, J.A., Baturina, E.L., Lyons, T.W., Wu, S., Danyushevsky, L., Sack, P.J., Chappaz, A., Maslennikov, V.V., Bull, S.W., 2015. Trace Element Content of Sedimentary Pyrite in Black Shales. Economic Geology 110, p. 1389-1410.

Guadagnin, F., Chemale Jr., F., Magalhães, A.J.C., Santana, A., Dussin, I., Takehara, L., 2015. Age constraints on crystal-tuff from the Espinhaço Supergroup – Insight into the Paleoproterozoic to Mesoproterozoic intracratonic basin cycles of the Congo-São Francisco Craton. Gondwana Research 27, p. 363-376.

Guy, B.M., Ono, S., Gutzmer, J., Lin, Y., Beukes, N.J., 2014. Sulfur sources of sedimentar “buckshot” pyrite in the Auriferous Conglomerates of the Mesoarchean Witwatersrand and Vetersdorp Supergroups, Kaapvaal Craton, South Africa. Mineralium Deposita 49, p. 751-775.

Halevy, I., Johnston, D. T., and Schrag, D. P., 2010. Explaining the Structure of the Archean Mass-Independent Sulfur Isotope Record. Science 329, p. 204-207.

Hannington, M.D., de Ronde, C.E.J., Peterson, S., 2005. Sea-floor tectonics and submarine hydrothermal systems. *In*: Hedenquist, J.W., Thompson, J.F.H., Goldfarb, R.J., Richards, J.P., (eds.), 100th Anniversary Volume of Economic Geology, p.111-141.

Hannington, M.D., 2014. Volcanogenic Massive Sulfide Deposits. *In*: Holland, H., Turekian, K., (eds.), Treatise on Geochemistry 2nd Edition: Amsterdam, Elsevier, p. 463-488.

Heinrich, C.A., 2015. Witwatersrand gold deposits formed by volcanic rain, anoxic rivers and Archaean life. Nature Geoscience 8, p. 206-209.

Horscroft, F.D.M., Mossman, D.J., Reimer, T.O., 2011. Witwatersrand metallogenesis: the case for (modified) syngenesis. SEPM Special Publications 101, p. 75-95.

Hofmann, A., Bekker, A., Rouxel, O., Rumble, D., Master, S., 2009. Multiple sulphur and iron isotope composition of detrital pyrite in Archaean sedimentary rocks: A new tool for provenance analysis. Earth and Planetary Science Letters 286, p. 436-445.

Hulston, J.R., Thode, H.G., 1965. Cosmic-Ray-Produced S36 and S33in Metallic Phase of Iron Meteorites. Journal of Geophysical Research 70 (18), p. 4435.

Huston, D.L., Brauhart, C.W., Drieberg, S.L., Davidson, G.J., Groves, D.I., 2001. Metal leaching and inorganic sulfate reduction in volcanic-hosted massive sulfide mineral systems: Evidence from the paleo-Archean Panorama district, western Australia. Geology 29 (8), p. 687-690.

Huston, D.L., Logan, G.A., 2004. Barite, BIFs and bugs: evidence for the evolution of the Earth's early hydrosphere. Earth and Planetary Science Letters 220, p. 41-55.

Huston, D.L., Pehrsson, S., Eglington, B.M., Zaw, K., 2010. The Geology and Metallogeny of Volcanic-Hosted Massive Sulfide Deposits: Variations through Geologic Time and with Tectonic Setting. Economic Geology 106, p. 571-591.

Huston, D.L., Relvas, J.M.R.S., Gemmell, J.B., Drieberg, S., 2011. The role of granites in volcanic-hosted massive sulphide ore-forming systems: an assessment of magmatic-hydrothermal contributions. Mineralium Deposita 46, 473-507.

Ireland, T.R., Schram, N., Holden, P., Lanc, P., Ávila, J., Armstrong, R., Amelin, Y., Latimore, A., Corrigan, D., Clement, S., Foster, J.J., Compston, W., 2014. Charge-mode electrometer measurements of S-isotopic compositions on SHRIMP-SI. International Journal of Mass Spectrometry 359, p. 26-37.

Jamieson, J.W., Wing, B.A., Farquhar, J., Hannington, M.D., 2013. Neoarchaean seawater sulphate concentrations from Sulphur isotopes in massive ore. Nature Geoscience 6, p. 61-64.

Johnston, D.T., 2011. Multiple sulfur isotopes and the evolution of Earth's surface sulfur cycle. Earth-Science Reviews 106, p. 161-183.

Kaufman, A.J., Johnston, D.T., Farquhar, J., Masterson, A.L., Lyons, T.W., Bates, S., Anbar, A.D., Arnold, G.L., Garvin, J., Buick, R., 2007. Late Archean biospheric oxygenation and atmospheric evolution. Science 317, p. 1900-1903.

Kirk, J., Ruiz, J., Chesley, J., Titley, S., 2003. The Origin of Gold in South Africa. American Scientist 91, p. 534-541.

Large, R.R., Danyushevsky, L., Hollit, C., Maslennikov, V.V., Meffre, S., Gilbert, S., Bull, S., Scott, R., Emsbo, P., Thomas, H., Singh, B., Foster, J., 2009. Gold and Trace Element Zonation in Pyrite Using a Laser Imaging Technique: Implications for the Timing of Gold in Orogenic and Carlin-Style Sediment-Hosted Deposits. Economic Geology 104, p. 635-668.

Large, R.R., Meffre, S., Burnett, R., Guy, B., Bull, S., Gilbert, S., Goemann, K., Danyushevsky, L., 2013. Evidence for an intrabasinal source and multiple concentration processes in the formation of the Carbon Leader Reef, Witwatersrand Supergroup, South Africa. Economic Geology 108, p. 1215-1241.

Ledru, P., Johan, V., Milési, J.P., Tegyey, M., 1994. Markers of the last stages of the Palaeoproterozoic collision: evidence for a 2 Ga continent involving circum–South Atlantic provinces. Precambrian Research 69, p. 169-191.

Longerich, H.P., Jackson, S.E., Günther, D., 1996. Laser Ablation Inductively Coupled Plasma Mass Spectrometric Transient Signal Data Acquisition and Analyte Concentration Calculation. Journal of Analytical Atomic Spectrometry 11, p. 899-904.

Magee, C.W., 2001. Geologic, Microstructural, and Spectroscopic Constraints on the Origin and History of Carbonado Diamond. PhD Thesis, The Australian National University, 272 pp.

Magee, C.W., Teles, G., Vicenzi, E.P., Taylor, W., Heaney, P., Uranium irradiation history of carbonado diamond; implications for Paleoarchean oxidation in the São Francisco craton. Geology 44, p. 527-530.

Martin, H., Peucat, J.J., Sabaté, P., Cunha, J.C., 1997. Crustal Evolution in the early Archaean of South America: example of the Sete Voltas Massif, Bahia State, Brazil. Precambrian Research 82, p. 35-62.

Mascarenhas, J.F., Filho, V.M.C., Griffon, J.C, 1992, Contribuição à Geologia do Grupo Jacobina na Região Jacobina/Pindobaçu: 37° Congresso Brasileiro de Geologia, São Paulo, SP, Boletim de Resumos Expandidos, v. 2, p. 141-142.

Mascarenhas, J.F., Silva, E.F.A., 1994. *Greenstone Belt* de Mundo Novo: caracterização e implicações metalogenéticas e geotectônicas no Cráton do São Francisco. Companhia Baiana de Pesquisa Mineral, Salvador. Série Arquivos Abertos 5, 32 pp.

Mascarenhas, J.F., Ledru, P., Souza, S.L., Conceição Filho, V.M., Melo, L.F.A., Lorenzo, C.L., Milesi J.P., 1998. Geologia e recursos minerais do Grupo Jacobina e da parte sul do Greenstone Belt de Mundo Novo. Companhia Baiana de Pesquisa Mineral, Salvador. Série Arquivos Abertos 13, 58 pp.

Montinaro, A., Strauss, H., Mason, P.R.D., Roerdink, D., Münker, C., Schwarz-Schampera, U., Arndt, N.T., Farquhar, J., Beukes, N.J., Gutzmer, J., Peters, M., 2015. Paleoarchean sulfur cycling: Multiple súlfur isotope constraints from the Barberton Greenstone Belt, South Africa. Precambrian Research 267, p. 311-322.

Muller, E., Philippot, P., Rollion-Bard, C., Cartigny, P., Assayag, N., Marin-Carbonne, J., Mohan, M.R., Sarma, D.S., 2017. Primary sulfur isotope signatures preserved in high-grade Archean barite deposits of the Sargur Group, Dharwar Craton, India. Precambrian Research 295, p. 38-47.

Norman, M., Robinson, P., Clarck, D., 2003. Major and Trace-Element Analysis of Sulfide Ores by Laser-Ablation ICP-MS, Solution ICP-MS, and XRF: New Data on International Reference Materials. The Canadian Mineralogist 41, p. 293-305.

Nutman, A.P., Cordani, U.G., 1993. SHRIMP U-Pb zircon geochronology of Archean granitoids from the Contendas-Mirante area of the São Francisco Craton, Bahia, Brazil. Precambrian Research 63, p. 179-188.

Ohmoto, H., Watanabe, Y., Ikemi, H., Poulson, S.R., Taylor, B.E., 2006. Suphur isotope evidence for na oxic Archaean atmosphere. Nature 442, p. 908-911.

Oliveira, E.P., McNaughton, N.J., Armstrong, R., 2010. Mesoarchaean to Paleoproterozoic growth of the northern segment of the Itabuna-Salvador-Curaçá orogen, São Francisco craton, Brazil. *In*: Kusky, T.M., Zhai, M.G., Xiao, W. (eds.), The Evolving Continents: Understanding Processes of Continental Growth: London, Geological Society Special Publications 338, p. 263-286.

Oliveira, E.P., Souza, Z.S., McNaughton, N.J., Lafon, J.-M., Costa, F.G., Figueiredo, A.M., 2011. The Rio Capim volcanic-plutonic-sedimentary belt, São Francisco Craton, Brazil: Geological, geochemical and isotopic evidence for oceanic arc accretion during Palaeoproterozoic continental collision. Gondwana Research 19, p. 735-750.

Oliveira, E.P., Silveira, E.M., Söderlund, U., Ernst, R.E., 2013. U-Pb ages and geochemistry of mafic dykes swarms from the Uauá Block, São Francisco craton, Brazil: LIPS remnants relevant for Late Archaean break-up of a supercraton. Lithos 174, p. 308-322.

Ono, S., Eigendrode, J.L, Pavlov, A.A., Kharecha, P., Rumble III, D., Kasting, J.F., Freeman, K.H., 2003. New insights into Archean sulfur cycle from mass-independent sulfur isotope records from the Hamersley Basin, Australia. Earth and Planetary Science Letters 213, p. 15-30.

Paquette, J.L., Barbosa, J.S.F., Rohais, Cruz, S.C.P., Goncalves, P., Peucat, J.J., Leal, A.B.M., Santos-Pinto, M., Martin, H., 2015. The geological roots of South America: 4.1 Ga and 3.7 Ga zircon crystals discovered in NE Brazil and NW Argentina. Precambrian Research 271, p. 49-55.

Paton, C., Hellstrom, J., Paul, B., Woodhead, J., Hergt, J., 2011. Iolite: Freeware for the visualisation and processing of mass spectrometric data. Journal of Analytical Atomic Spectrometry 26, p. 2508-2518.

Pavlov, A.A., Kasting, J.F., 2002. Mass-independent fractionation of sulfur isotopes in Archean sediments: Strong evidence for an anoxic Archean atmosphere. Astrobiology 2, p. 27–41.

Pearson, W., Macêdo, P.M., Rúbio, A., Lorenzo, C.L., Karpeta, P., 2005. Geology and gold mineralization of the Jacobina Mine and Bahia Gold Belt, Bahia, Brazil and comparison to Tarkwa and Witwatersrand. *In*: Rhoden, H.N., Steininger, R.C., Vikre, P.G. (eds.). Geological Society of Nevada Symposium, 29 pp.

Peucat, J.J., Mascarenhas, J.F., Barbosa, J.S.F., Souza, S.L., Marinho, M.M., Fanning, C.M., Leite, C.M.M., 2002. 3.3 Ga SHRIMP U–Pb zircon age of a felsic metavolcanic rock from the Mundo Novo greenstone belt in the São Francisco Craton, Bahia (NE Brazil). Journal of South American Earth Sciences 15, p. 363-373.

Philippot, P., Van Zuilen, M., Lepot, K., Thomazo, C., Farquhar, J., Van Kranendonk, M. J., 2007. Early Archaean Microorganisms Preferred Elemental Sulfur, Not Sulfate. Science 317, p. 1534-1537.

Philippot, P., van Zuilen, M., Rollion-Board, C., 2012. Variations in atmospheric sulphur chemistry on early Earth linked to volcanic activity. Nature Geoscience 5, p. 668-674.

Phillips, G.N., Law, J.D.M., 2000. Witwatersrand gold fields: Geology, genesis and exploration. Society of Economic Geologists Reviews 13, 439-500.

Rios, D.C., Davis, D.W., Conceição, H., Rosa, M.L.S., Davis, W.J., Dickin, A.P., Marinho, M.M., Stern, R., 2008. 3.65-210 Ga history of crust formation from zircon geochronology and isotope geochemistry of the Quijingue and Euclides plutons, Serrinha nucleus, Brazil. Precambrian Research 167, 53-70.

Roerdink, D.L., Mason, P.R.D., Farquhar, J., Reimer, T., 2012. Multiple sulfur isotopes in Paleoarchean barites indentify an important role for microbial sulfate reduction in the early marine environment. Earth and Planetary Science Letters 331-332, p. 177-186.

Santos-Pinto, M., Peucat, J.J., Martin, H., Barbosa, J.S.F., Fanning, C.M., Cocherie, A., Paquette, J.L., 2012. Crustal evolution between 2.0 and 3.5 GA in the southern Gavião block (Umburanas-Brumado-Aracatu region), São Francisco Craton, Brazil: A 3.5-3.8 Ga proto-crust in the Gavião block? Journal of South American Earth Sciences 40, p. 129-142.

Sharman, E.R., Taylor, B.E., Minarik, W.G., Dubé, B., Wing, B.A., 2015. Sulfur and trace element data from ore sulphides in the Noranda district (Abitibi, Canada): implications for volcanogenic massive sulfide deposit genesis. Mineralium Deposita 50, p. 591-606.

Shen, Y., Farquhar, J., Masterson, A., Kaufman, A. J., Buick, R., 2009. Evaluating the role of microbial sulfate reduction in the early Archean using quadruple isotope systematics. Earth and Planetary Science Letters 279, p. 383-391.

Silva, M.G., 1994. Greenstone Belt do Rio Itapicuru: Uma Bacia do Tipo Back Arc Fóssil. Revista Brasileira de Geociências 22, 157-166.

Souza, S., et al., 2002. Projeto *greenstone belt* de Mundo Novo: escala 1:100.000. Salvador, CBPM.

Teixeira, J.B.G., Souza, J.A.B., Silva, M.G., Leite, C.M.M., Barbosa, J.Q.F., Coelho, C.E.S., Abram, M.B., Conceição Filho, V.M., Iyer, S.S.S., 2001. Gold mineralization in the Serra de Jacobina region, Bahia Brazil: tectonic framework and metallogenesis. Mineralium Deposita 36, p. 332-344.

Teles, G.S., 2013. Proveniência e idades de deposição dos sedimentos auríferos da Bacia de Jacobina: implicações sobre a evolução da bacia durante o Paleoarqueano e a gênese da mineralização. Dissertação de Mestrado, Universidade de Brasília, 122 pp.

Teles, G., Chemale Jr., F., Oliveira, C.G., 2015. Paleoarchean record of the detrital pyrite-bearing, Jacobina Au–U deposits, Bahia, Brazil. Precambrian Research 258, p. 289-313.

Thomassot, E., O'Neil, J., Francis, D., Cartigny, P., Wing, B.A., 2015. Atmospheric record in the Hadean Eon from multiple sulfur isotope measurements in Nuvvuagittuq Greenstone Belt (Nunavik, Quebec). Proceedings of the National Academy of Sciences 112 (3), p. 707-712.

Tornos, F., Peter, J.M., Allen, R., Conde, C., 2015. Controls on the siting and style of volcanogenic massive sulphide deposits. Ore Geology Reviews 68, p. 143-163.

Ueno, Y., Ono, S., Rumble, D., Maruyama, S., 2008. Quadruple sulfur isotope analysis of ca. 3.5Ga Dresser Formation: New evidence for microbial sulfate reduction in the early Archean. Geochimica et Cosmochimica Acta 72, p. 5675-5691.

Ulrich, T., Long, D.G.F., Kamber, B.S., Whitehouse, M.J., 2011. In situ trace element and sulfur isotope analysis of pyrite in a Paleoproterozoic Gold Placer Deposit, Pardo and Clement Townships, Ontario, Canada. Economic Geology 106, p. 667-686.

Valley, J.W., Cavosie, A.J., Ushikubo, T., Reinhard, D.A., Lawrence, D.F., Larson, D.J., Clifton, P.H., Kelly, T.F., Wilde, S.A., Moser, D.E., Spicuzza, M.J., 2014. Hadean age for a post-magma-ocean zircon confirmed by atom-probe tomography. Nature Geoscience 7, p. 219-223.

Vearncombe, S., Barley, M.E., Groves, D.I., McNaughton, N.J., Mikucki, E.J., Vearncombe, J.R., 1995. 3.26 Ga black smoker-type mineralization in the Strelley Belt, Pilbara Craton, Western Australia. Journal of the Geological Society 152, p. 587-590.

Wilson, S.A., Ridley, W.I., Koenig, A.E., 2002. Development of sulphide calibration standards for the laser ablation inductively-coupled plasma mass spectrometry technique. Journal of Analytical Atomic Spectrometry 17, p. 406-409.

Xue, Y., Campbell, I., Ireland, T.R., Holden, P., Armstrong, R., 2013. No mass-independent sulfur isotope fractionation in auriferous fluids supports a magmatic origin for Archean gold deposits. Geology 41, p. 791-794.

Zincone, S.A., Oliveira, E.P., Laurent, O., Zhang, H., Zhai, M., 2016. 3.30 Ga high-silica intraplate volcanic-plutonic system of the Gavião Block, São Francisco Craton, Brazil: Evidence of an intracontinental rift following the creation of insulating continental crust. Lithos 266-267, p. 414-434.

CAPÍTULO 4

Contrasting preservation of MIF-S in the Jacobina Basin, São Francisco Craton: implications for atmospheric conditions and formation of Au-(U)-Py deposits.

Guilherme S. Teles[1], Farid Chemale Jr.[1,2], Janaína N. Ávila[3] and Trevor R. Ireland[3]

[1]*Instituto de Geociências, Universidade de Brasília, Brasília, Brasil*

[2]*Programa de Pós-Graduação em Geologia, Universidade do Vale do Rio dos Sinos, São Leopoldo, Brasil*

[3]*Research School of Earth Sciences, The Australian National University, Canberra ACT 2601, Australia*

ABSTRACT

The late Paleoarchean Jacobina Basin has a well-preserved sedimentary record, including continental and marine deposits, and hosts Au-(U)-Py mineralization in conglomerate beds similar to the Witwatersrand gold province. Based on petrographic observations, and in situ multiple sulfur isotope analyses (^{32}S, ^{33}S, ^{34}S, and ^{36}S) of pyrite from alluvial and marine facies, distinct generations of pyrite can be recognized. Pyrite associated with terrestrial sediments shows a wide range in $\delta^{34}S$ but quite restricted ranges in $\Delta^{33}S$ and $\Delta^{36}S$. Pyrite associated with the marine sedimentary rocks shows only limited $\delta^{34}S$, but a wide range in $\Delta^{33}S$ and correlated $\Delta^{36}S$ close to the Archean array. This data suggests distinct preservation routes for MIF-S from atmospheric SO_2 and S_8 in terrestrial and marine environments. Conditions on the terrestrial surface resulted in re-equilibration of SO_2 and S_8 removing much of the Archean atmospheric signal. In contrast, SO_2 dissolved in shallow marine settings while S_8 settled to the floor favors preservation of MIF-S isotopic signatures. Such processing may also explain the apparent differences in interpretations of atmospheric conditions derived from uncharacterized pyrites from Archean sources. Our data suggest that the Earth's atmosphere remained anoxic and terrestrial conditions were such to allow syngenetic accumulation of gold, as has been recently proposed for Witwatersrand.

4.1. INTRODUCTION

It is generally accepted that the Archean atmosphere had lower O_2 levels than the present-day atmosphere, and several geological and geochemical line of evidence support this interpretation (e.g., Farquhar et al., 2014). The occurrence of oxygen-sensitive detrital minerals as well as the anomalous mass-independent fractionation of sulfur isotopes (MIF-S) in sulfides and barite in many Archean and early Paleoproterozoic successions provide the best constraints of the reduced state of the atmosphere during that time ($pO_2 < 10^{-5}$ PAL; Pavlov and Kasting, 2002; Farquhar et al., 2014). However, an increasing number of studies have interpreted Archean S-isotope data that indicate some molecular O_2 was present well before the Great Oxidation Event (GOE; see Lyons et al., 2014, for review). Most of these studies have focused on marine sedimentary sequences, with only a few examples of continental deposits. This approach may lead to potential bias in the interpretation of the Archean MIF-S record as well as conflicting interpretations of the nature of the "whiffs" of O_2 prior to the GOE.

Magee et al. (2016) presented indications of late Paleoarchean (3.32 Ga) oxidation in the São Francisco Craton, Brazil, based on the epigenetic uranium enrichment of carbonado diamonds. However, the occurrence of detrital pyrite and uraninite in the sedimentary rocks of Jacobina Basin (Teles et al., 2015), in a similar way to the Mesoarchean Witwatersrand Basin, is consistent with anoxic atmospheric conditions during deposition.

To explore the issues associated with preservation of MIF-S, and to better constrain the environmental and atmospheric redox conditions during the Jacobina Basin deposition, we determined the sulfur isotope abundances (^{32}S, ^{33}S, ^{34}S and ^{36}S) by *in situ* analyses of sedimentary pyrite grains formed and preserved in both continental and marine environments of the basin. These data can be used to address the role of atmospheric interaction with terrestrial fluvial sediments as opposed to preservation of MIF-S in marine settings. In addition, this information could indicate whether S isotope variability might reflect global or more local changes.

4.2. GEOLOGY OF THE JACOBINA BASIN

The Jacobina Basin is in the northeastern portion of the São Francisco Craton (Figure 7.1), and lies on the eastern edge of the Paleoarchean Gavião Block, one of the most ancient crustal segments of South America. (Barbosa and Sabaté, 2004 and

references therein). This region was affected by the Transamazonian-Eburnean Cycle, which resulted in thrust- folding deformation, and granite emplacement at the cratonic margin of the Gavião Block (Barbosa and Sabaté, 2004). Based on the nature of this tectonic event, it has been proposed that the Jacobina deposition occurred in a foreland basin developed between 2.1 and 1.9 Ga, and gold mineralization was emplaced by hydrothermal/epigenetic activity (e.g., Milesi et al., 2002). However, these authors disregard the previous descriptions of detrital pyrite, gold, and uraninite in the auriferous sediments (Hendrickson, 1984). Recent studies by Teles et al. (2015) and Magee et al. (2016), both based on U-Pb ages of detrital zircons, show that Paleoarchean (3.3 to 3.6 Ga) rocks were the exclusive sources for Jacobina sediments, and suggest that deposition occurred before the GOE, likely in the late Paleoarchean.

The sedimentary sequence of basin is suggestive of deposition in a rift setting (Chapter 7, Item 7.1), which is represented by the lower alluvial deposits of Serra do Córrego Formation, followed by transgressive high-maturity quartzites of Rio do Ouro Formation, and by marine quartzites interbedded with metapelites and minor conglomerates of Serra da Paciência Formation (Figure 4.1).

The Serra do Córrego Fm. hosts the Au-(U) and pyrite mineralization in conglomerate beds comprised of two horizons separated by a thick sequence of quartzite (Figure 4.1). The mineralized conglomerates are referred to as *reefs* because of their similarities with the Witwatersrand conglomerates. Similar pyritic quartz-pebble conglomerates also occur in the Serra da Paciência Fm. (Figures 4.1 and 7.3).

4.3. SAMPLES AND METHODS

The studied samples are conglomerates, quartzites, and metapelites that comprise the alluvial and marine intervals of Jacobina Basin (Figure 4.1), the Serra do Córrego and Serra da Paciência formations, respectively.

The *in situ* 4-sulfur isotope analysis of pyrite was carried out at The Australian National University, using the Sensitive High-Resolution Ion Microprobe for Stable Isotopes (SHRIMP-SI). Instrumental configuration and analytical procedures were similar to those described by Ireland et al., (2014). Details about samples, analytical procedures, and the complete data set are provided in the Data Repository. Typical internal precision (2σ) for $\delta^{34}S$, $\Delta^{33}S$, and $\Delta^{36}S$ measurements were 0.02‰, 0.1‰, and

0.4‰, respectively, with reproducibility (2SD) generally better than 0.4‰, 0.12‰, and 0.5‰ for $\delta^{34}S$, $\Delta^{33}S$, and $\Delta^{36}S$, respectively.

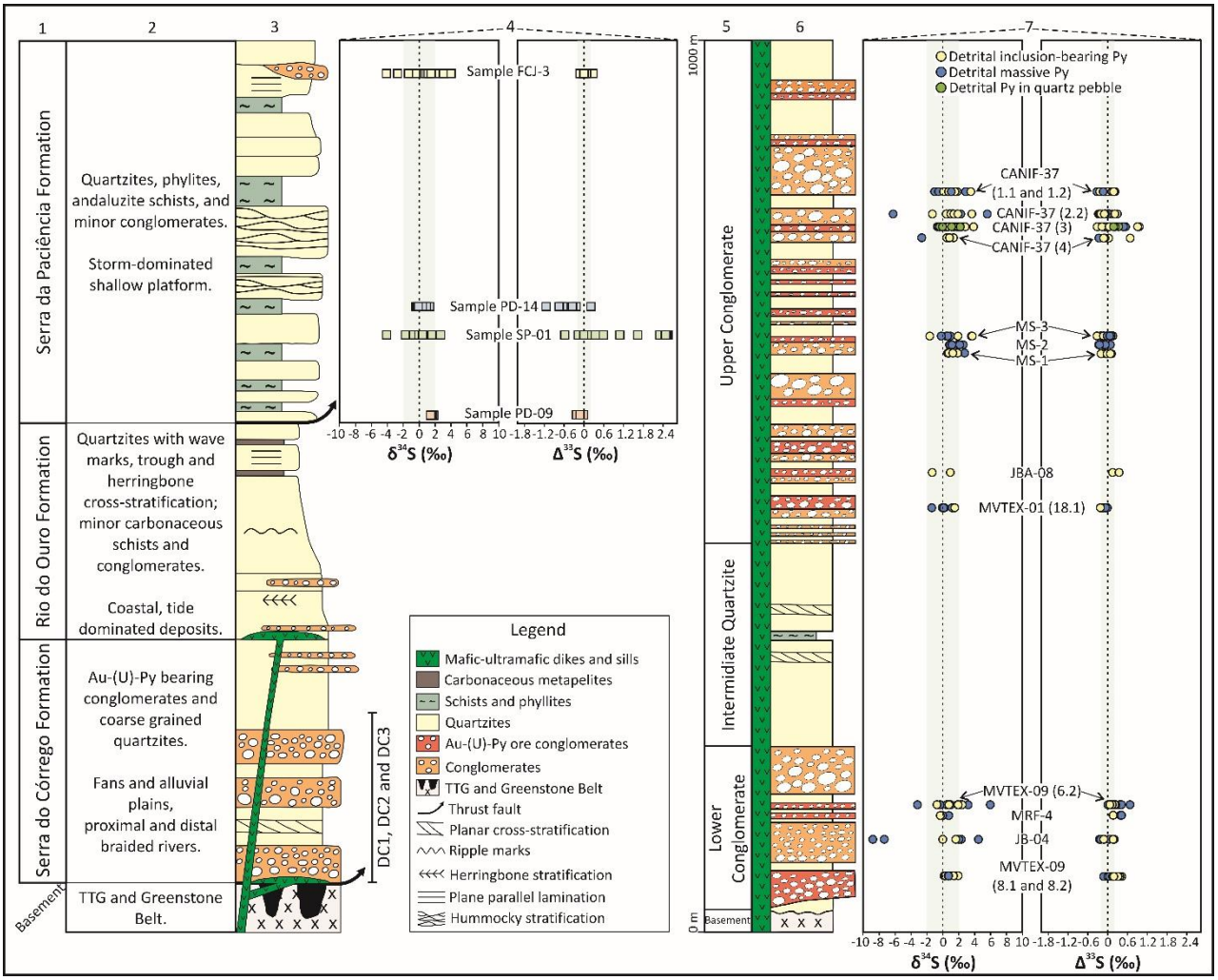

Figure 4.1. Stratigraphy of the Jacobina Basin with the samples positions, and their respective $\delta^{34}S$ and $\Delta^{33}S$ data. (1) Basin units; (2) Summarized description of units; (3) Stratigraphic column with indication of sampled intervals. DC1, DC2 and DC3 represent the the sampled drill-cores, whose related stratigraphy is shown in 5 and 6. (4) and (7) S data, respectively for the Serra da Paciência and Serra do Córrego Fms.

4.4. RESULTS

Pyrite grains from samples of Serra do Córrego Fm. show textural complexity that has not been described previously in the Jacobina deposit. After careful petrographic examination, four generations of pyrite were recognized. The first type of pyrite consists of detrital grains with rounded shapes, sometimes broken and fragmented, that host fine-grained inclusions of detrital quartz, muscovite, chlorite, fuchsite, apatite, and chromite (Figures 4.2A; 7.3B and C). This type of pyrite has been described as “porous” pyrite in

the Witwatersrand Basin, and is thought to be sedimentary in origin. The second group (detrital massive), have rounded or anhedral morphology, with or without inclusions, and are typically massive, although sometimes zoned as revealed by etching with NaOCl (Figures 4.2B; 7.3D and E). The third group of detrital pyrite was observed in only one sample. It comprises small euhedral grains (~50 µm), sometimes forming aggregates and were hosted in a single quartz pebble (Figure 4.2C). Finally, euhedral overgrowths of late pyrite are common, enclosing both inclusion-bearing (group 1) and massive (group 2) detrital pyrites, which comprise the fourth group (Figure 4.2A and B).

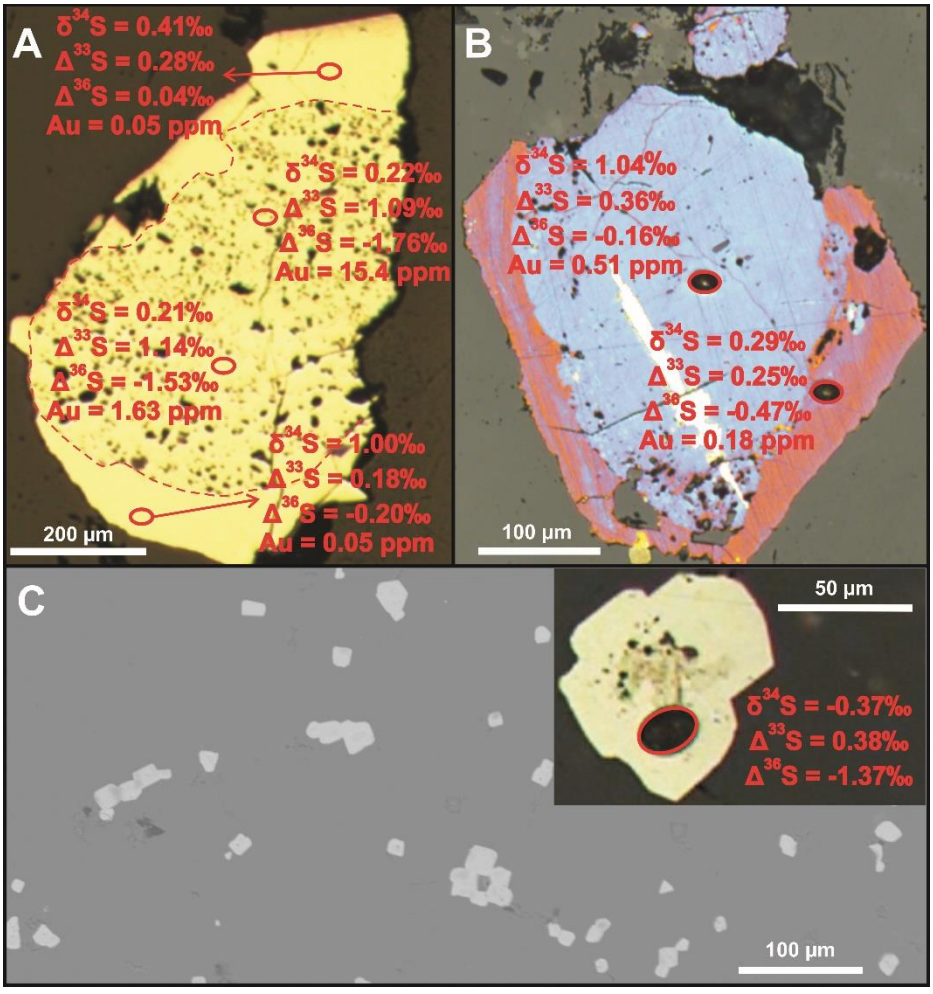

Figure 4.2. Examples of the detrital pyrite found in conglomerates of Serra do Córrego Fm. (A) Rounded inclusion-bearing pyrite with an overgrowth of late massive pyrite; (B) Etched pyrite grain showing a rounded massive core with a late euhedral rim; (C) Single and aggregate grains of small euhedral pyrite hosted by a quartz pebble. SHRIMP-SI spots (with $\delta^{34}S$, $\Delta^{33}S$ and $\Delta^{36}S$ data), and the corresponding gold content are noted.

The multiple S isotope compositions are very similar between the three groups of detrital pyrite (Figures 4.1; 4.3A and B; and 7.6A). The $\delta^{34}S$ values have a range of 15‰ (from -8.7 to +6.0‰) with a clustering between 0 and 2‰. Most of the $\Delta^{33}S$ values are restricted to a range defined by the absence of MIF-S (0 $\pm$ 0.2‰). However, some grains plot above this interval, showing positive MIF-S values up to 1.1‰ (Figure 4.3A). The $\Delta^{36}S$ values range from -1.8 to +0.7‰, with most of the data plotting around the origin of the $\Delta^{36}S$-$\Delta^{33}S$ diagram (0 $\pm$ 0.4‰; Figure 4.3A and B).

Detrital pyrite grains are also observed in samples of the marine interval. The conglomerate sample (FCJ-3) has massive detrital pyrites that comprise a lag of heavy minerals together with detrital chromite and zircon (Figure. 7.3A). These pyrites yield $\delta^{34}S$ comparable to the Serra do Córrego data (Figures 4.3B and 7.6B), but without any indication of MIF-S (mean $\Delta^{33}S$ = -0.01‰ $\pm$ 0.1). The same relationship is observed in analyses of detrital pyrites from the quartzite sample SP-01. It is possible that these grains were reworked from the continent into the marine environment (Figure 7.4).

On the other hand, euhedral pyrite and overgrowths on the detrital grains in sample SP-01 yield strongly positive $\Delta^{33}S$ values (up to +2.5‰) while $\delta^{34}S$ values are close to 0‰ (Figures 4.3C and 7.6B). The metapelite sample (PD-14) yields negative $\Delta^{33}S$ values (down to -1.2‰), except for one data point ($\Delta^{33}S$ = 0.2‰), but with the same restricted $\delta^{34}S$ values (Figures 4.3C and 7.6B). The texture and isotopic compositions of these latter pyrites (Figure 7.4) are indicative of diagenetic and syngenetic origins, respectively.

Sample PD-09, collected just above the contact with basalts of the Mundo Novo Greenstone Belt, contains large euhedral pyrite grains with no MIF-S (mean $\Delta^{33}S$ = -0.11‰ $\pm$ 0.1‰). We also recognize a single population of $\delta^{34}S$ values (Figure 7.6B), which suggests a hydrothermal origin for these grains.

There is a clear distinction between the data of the two studied units, and this is especially noteworthy in terms of the $\Delta^{36}S/\Delta^{33}S$ correlations (Figure 4.3). Regression of $\Delta^{36}S$ and $\Delta^{33}S$ data for detrital pyrite from Serra do Córrego Fm. yields a $\Delta^{36}S/\Delta^{33}S$ slope of -1.42 $\pm$ 0.24 (2σ). With reference to the textural type of detrital pyrites described in the conglomerate samples, the inclusion-bearing pyrites define a slope of -1.48 $\pm$ 0.27 (2σ), whereas the massive detrital and pyrite enclosed in quartz pebble yield a $\Delta^{36}S/\Delta^{33}S$ slope of -1.27 $\pm$ 0.38 (2σ). Both slopes are equivalent, considering the errors of regression (Figure 4.3A and B).

Data from the Serra da Paciência Fm. (Figure 4.3C) are quite distinct and show a $\Delta^{36}S/\Delta^{33}S$ slope of -0.84 $\pm$ 0.09 (2σ). The uncertainty on $\Delta^{36}S/\Delta^{33}S$ slope of these pyrite data is low because of the significant and well correlated spread in $\Delta^{36}S$ and $\Delta^{33}S$. This further reinforces the distinction in the S isotope sources of the different pyrite associations and rock types.

4.5. DISCUSSION

The sedimentary rocks of the Jacobina Basin provide geological context for the main constraints for a reducing atmosphere during the Archean ($pO_2 < 10^{-5}$ PAL), viz. the preservation of MIF-S and redox-sensitive detrital minerals (e.g., Farquhar et al., 2014). However, further implications for the nature of these indicators can be explored because of the conspicuous differences recorded between pyrite from continental and marine environments of basin.

4.5.1. Interpretation of textures: Pyrite morphology/mineralogy implications

4.5.1.1. What is detrital? Allogenic vs. authigenic?

The pyrite textures provide context for the sedimentary environment in the Jacobina Basin. The earliest generation of "porous" pyrite, appears to have formed in low energy environments in a basin during sedimentation and diagenesis, trapping other minerals as the pyrite grew. More "massive" pyrite may represent crystallization during late diagenesis or hydrothermal events. Trace elements data further reinforce this interpretation (Chapter 7, Item 7.1). At any stage, grains were subsequently eroded and released by the increasing energy of streams responsible for the conglomerate deposition (Hofmman et al., 2009; Guy et al., 2014; Agangi et al., 2015).

The type 3 pyrites may be derived from earlier lithified sediments, whereas type 4 pyrites likely formed during the subsequent regional greenschist facies metamorphism.

4.5.2. What about the Serra da Paciência Fm. pyrites? Is there anything distinctive?

Pyrite from the marine samples define a $\Delta^{36}S/\Delta^{33}S$ slope of -0.84 (Figure 4.3C), which is indistinguishable from the Archean array ($\Delta^{36}S/\Delta^{33}S \sim -0.9$; Farquhar et al., 2000). This array has been interpreted as a mix resulting from atmospheric production of SO_2 (with $\Delta^{33}S < 0$) and S_8 (with $\Delta^{33}S > 0$) (Farquhar et al., 2000). While this is most

clear in the $\Delta^{33}S$-$\Delta^{36}S$ relationship, there is also a relationship predicted between $\Delta^{33}S$ and $\delta^{34}S$ with $\Delta^{33}S \sim 0.9 \times \delta^{34}S$ (Ono et al., 2003). For the marine samples, a correlation between $\delta^{34}S$ and $\Delta^{33}S$ is not as distinct or systematic as that for $\Delta^{33}S$ and $\Delta^{36}S$ (Fig. 3C). We note that the S isotopes can be affected by a variety of processes which could induce mass dependent fractionation, which will affect the measured $\delta^{34}S$, but not $\Delta^{33}S$ and $\Delta^{36}S$. The pattern is not systematic in that the analyses with the highest $\Delta^{33}S$ are not associated with the analyses with the highest $\delta^{34}S$.

On the other hand, samples from the continental conglomerates are characterized by no or only small positive $\Delta^{33}S$ anomalies (up to +1.1‰), they have a similar range of $\delta^{34}S$ values, and there is no evident correlation between $\Delta^{33}S$ and $\delta^{34}S$ (Figure 4.3A and B). These similarities indicate that the three groups of detrital pyrite have similar S sources, albeit slightly different from the Archean array sulfur, with their steeper negative $\Delta^{36}S/\Delta^{33}S$ slopes (~ 1.4). Low $\Delta^{33}S$ values and $\Delta^{36}S/\Delta^{33}S \sim 1.5$ are characteristic of the Mesoarchean interval of the MIF-S record and this is thought to be associated with changes in the sources of MIF-S reactions and the atmospheric chemistry (Farquhar et al., 2007). Although the considered age for the deposition of Jacobina Basin (~ 3.3 Ga) is close to the interval of minimum $\Delta^{33}S$ values, changes in the atmospheric composition or in the sources of MIF-S reactions do not explain the steeper slopes for the continental samples. Indeed, pyrites formed in the coeval marine environment have greater fractionation in $\Delta^{33}S$, and follow the atmospheric trend ($\Delta^{36}S/\Delta^{33}S \sim -0.9$) that ruled most of the Archean. Instead, the isotopic composition of the conglomerates suggests that S was mostly derived from MDF-S sources (juvenile and crustal, $\Delta^{33}S = 0$), and in some cases from MIF-S sources (sedimentary S, $\Delta^{33}S > 0$). The lack of correlation between $\Delta^{33}S$ and $\delta^{34}S$ and more negative $\Delta^{36}S/\Delta^{33}S$ slopes are indicative of mixing between these reservoirs (Johnston, 2011; Guy et al., 2014). Furthermore, these data can be considered as a signal from the sources of sediments; which according to Teles et al. (2015) were derived from the Paleoarchean rocks of Gavião Block, including TTG and supracrustal rocks that were submitted to intensive chemical weathering.

This interpretation is directly supported in the pyrites studied here. Pyrites from the marine sediments preserve the greatest variability in $\Delta^{33}S$- $\Delta^{36}S$ and this is attributable to incorporation of S derived from atmospheric fractionations, including both positive $\Delta^{33}S$ (S_8-rich) and negative $\Delta^{33}S$ (SO_2-rich) sources. These sources have evidently been incorporated and remained distinct during sedimentary processes. A key distinction between preservation of S_8 as opposed to SO_2 would be the effective water insolubility

of S_8. Hence, S_8 might be expected to fall out and be deposited in muds where it can be incorporated in to pyrite. In the case of SO_2, this would stay in solution and might only be fixed in the sediments during sulfate precipitation or biological activity.

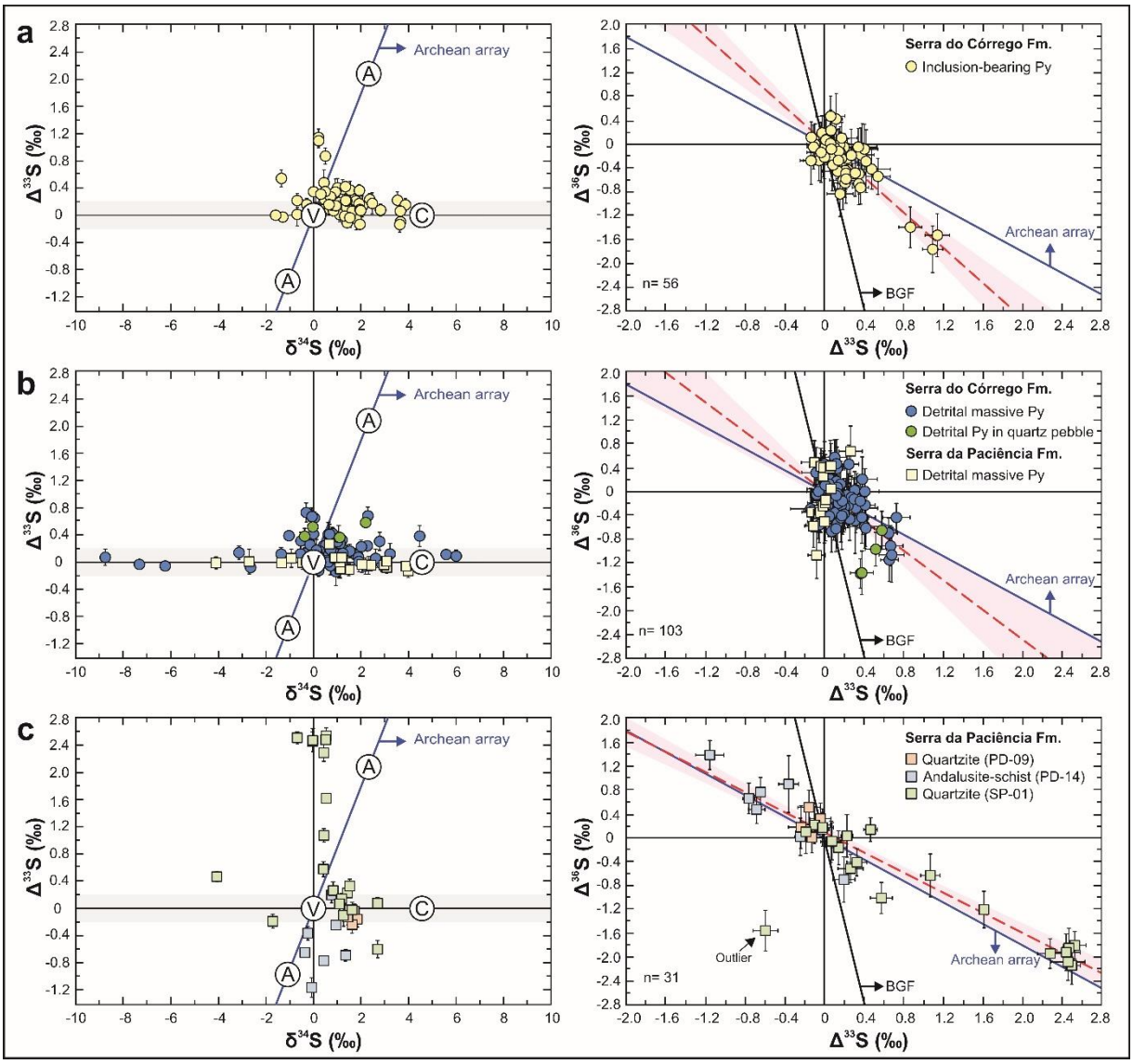

Figure 4.3. Multiple S isotopes plots of pyrite grains analyzed in this study. In the $\Delta^{33}S$ vs. $\delta^{34}S$ plots, the Archean array (blue line), juvenile (V), atmospheric (A) and crustal (C) sulfur sources are indicated (after Guy et al., 2014). In the $\Delta^{36}S$ vs. $\Delta^{33}S$ diagrams, the Archean and the biogeochemical (BGF; Ono et al., 2006) arrays are indicated, as well as the regression lines for the data (red dashed lines) and their respective 95% confidence envelopes (pink shaded areas). In all plots, error bars are 2σ. (a) Serra do Córrego Fm. detrital inclusion-bearing pyrites; (b) Plots for detrital massive and pyrite hosted by quartz pebble from the Serra do Córrego and Serra da Paciência Fms.; and (c) Sedimentary and hydrothermal pyrites data of Serra da Paciência Fm.

On the other hand, the continental rocks appear to be more homogenised and cluster more closely back towards primitive S ($\Delta^{33}S \approx 0$). It would be expected that both S_8 and SO_2 would rain out to the terrestrial surface. However, in the case of terrestrial environments, these components are mixed, recombined, and resulting in the preservation of a rather muted signal of MIF-S.

4.5.3. Implications for Archean gold mineralization

The occurrence of the detrital inclusion-bearing pyrite in alluvial conglomerates of Serra do Córrego Fm. is significant, because this type of pyrite is common in the auriferous reefs of Witwatersrand Basin. It is also enriched in gold compared to the other types of pyrite found in conglomerates (eg. Agangi et al., 2015). Inclusion-bearing pyrite in Witwatersrand is thought to be formed in wet sediments of low-energy environments of the alluvial system (Hofmann et al., 2009; Guy et al., 2014; Agangi et al., 2015). Eventually, this pyrite is eroded from these environments by the increasing energy of the fluvial streams, transported with coarse-grained sediments, and finally deposited as conglomerates. Because this type of pyrite is commonly related to organic matter, it is believed that microorganisms drove the pyrite growth and trapped Au from solution (Horscroft et al., 2011; Frimmel and Henning, 2015; Heinrich, 2015).

However, this process requires high S contents in the atmosphere and river waters; intense chemical weathering on the surface, causing dissolution of Au from source rocks and its chemical transportation; and wide presence of microbial mats at the deposition site, whose localized O_2 production would be responsible for the Au precipitation. These environmental conditions would only be possible during the Archean, after the appearance of the first O_2-producing organisms, which favored the giant and unique Au accumulation of Witwatersrand Basin (Frimmel and Henning, 2015; Heinrich, 2015).

A similar scenario could have occurred in the paleoenvironment of the Jacobina Basin, as evidenced by the inclusion-bearing pyrite described here. It is enriched in Au compared to the detrital massive and hydrothermal overgrowths (Figures 4.2 and 7.8); and its isotopic composition indicates S sourced from rocks with MDF-S and limited MIF-S signatures, which were likely submitted to intensive chemical weathering (Teles et al., 2015). This is also supported by Magee et al. (2016), who presented evidence of localized production of oxygen at the São Francisco Craton, penecontemporaneously to the deposition of Jacobina Basin. However, the common occurrence of organic matter in

the auriferous conglomerates, as in Witwatersrand, is not present in the Jacobina deposit. Few references have been made to the sparse occurrence of carbon "flyspeck" grains in Jacobina reefs (e.g., Horscroft et al., 2011). This may be an explanation for the great difference in Au endowment between the deposits. Nevertheless, the Jacobina Basin deposits may represent an initial stage or even the onset of the major gold accumulation that occurred in the Mesoarchean.

4.6. CONCLUSION

We have identified distinct types of pyrite in samples from the continental and marine settings of Jacobina Basin. The S isotope compositions are largely distinct between these environments. In the alluvial Serra do Córrego Fm., both detrital inclusion-bearing and massive pyrites show only small positive MIF-S anomalies, with a steeper $\Delta^{36}S/\Delta^{33}S$ slope (-1.4) relative to the Archean array.

S isotopic compositions of pyrites from the marine Serra da Paciência Fm. are more variable and show a large range of MIF-S, with a $\Delta^{36}S/\Delta^{33}S$ slope of -0.84, that lie close to the Archean array caused by S photolysis in a low O_2 atmosphere.

These data suggest that MIF-S is preferentially preserved in marine settings as opposed to continental. Such a scenario can be related to the distinct paths for S_8 and SO_2 raining out on to terrestrial and shallow marine environments. On the land mass, S_8 and SO_2 stay in close association and could recombine and requilibrate, largely removing the MIF-S. In marine conditions, S_8 might be expected to fall to the sea floor while SO_2 would go into solution.

The detrital inclusion-bearing pyrites, found in the auriferous conglomerates of Jacobina Basin, record anoxic formation conditions and a distinct mechanism for gold fixation, similar to the recently proposed scenario for the Witwatersrand deposits (Frimmel and Henning, 2015; Heinrich, 2015).

Evidence of O_2 production at the time of sedimentation of Jacobina Basin has been presented by Magee et al., (2016). According to our data, this is not related to a global oxygenation, but to a local phenomenon instead. This is in agreement with the statements of Lalonde and Konhauser (2015), which suggest that benthic communities could produce oxygen locally, without affecting the overall anoxic Archean atmosphere. However, further investigations are needed to provide evidence of biological activity in O_2 production and its implications for gold accumulation in the Jacobina Basin.

4.7. ACKNOWLEDGMENTS

We acknowledge Cid Bonfim, Pablo Borges, Anselmo Rúbio, and Yamana Gold Inc. for their assistance during field work and drill-core samples. GST acknowledges CNPq (grants 163459/2013-4 and 202267/2014-8). TRI acknowledges the support of ARC DP140103393.

4.8. REFERENCES CITED

Agangi, A., Hofmann, A., Rollion-Bard, C., Marin-Carbonne, J., Cavalazzi, B., Large, R., Meffre, S., 2015, Gold accumulation in the Archaean Witwatersrand Basin, South Africa – Evidence from concentrically laminated pyrite: Earth-Science Reviews, v. 140, p. 27-53, doi: 10.1016/j.earscirev.2014.10.009.

Barbosa, J.S.F., Sabaté, P., 2004, Archean and Paleoproterozoic crust of the São Francisco Craton, Bahia, Brazil: geodynamic features: Precambrian Research, v. 133, p. 1-27, doi: 10.1016/j.precamres.2004.03.001.

Farquhar, J., Bao, H., Thiemens, M., 2000, Atmospheric Influence of Earth's Earliest Sulfur Cycle: Science, v. 289, p. 756-758.

Farquhar, J., Peters, M., Johnston, D.T., Strauss, H., Masterson, A., Wiechert, U., Kaufman, A.J., 2007, Isotopic evidence for Mesoarchean anoxia and changing atmospheric sulphur chemistry: Nature, v. 449, p. 706-709, doi: 10.1038/nature06202.

Farquhar, J., Zerkle, A.L., Bekker, A., 2014, Geologic and Geochemical Constraints on Earth's Early Atmosphere, *in* Holland, H., and Turekian, K., eds., Treatise on Geochemistry 2nd Edition: Amsterdam, Elservier, p. 91-129, doi: 10.1016/B978-0-08-095975-7.01304-8.

Frimmel, H.E., Hennigh, Q., 2015, First whiffs of atmospheric oxygen triggered onset of crustal gold cycle: Mineralium Deposita, v. 50, p. 5-23, doi: 10.1007/s00126-014-0574-8.

Guy, B.M., Ono, S., Gutzmer, J., Lin, Y., Beukes, N.J., 2014, Sulfur sources of sedimentary "buckshot" pyrite in the Auriferous Conglomerates of the Mesoarchean Witwatersrand and Ventersdorp Supergroups, Kaapvaal Craton, South Africa: Mineralium Deposita, v. 49, p. 751-775, doi: 10.1007/s00126-014-0518-3.

Heinrich, C.A., 2015, Witwatersrand gold deposits formed by volcanic rain, anoxic rivers and Archaean life: Nature Geoscience, v. 8, p. 206-209, doi: 10.1038/ngeo2344.

Hendrickson, B.R., 1984, Stratigraphic Position, Mineralogy, Depositional Environment, and Gold Distribution of the Main Reef at Morro do Cuscuz and Morro do Vento near Jacobina, Bahia, Brazil [MSc. thesis]: Rapid City, School of Mines and Technology, 157 p.

Hofmann, A., Bekker, A., Rouxel, O., Rumble, D., Master, S., 2009, Multiple sulphur and iron isotope composition of detrital pyrite in Archaean sedimentary rocks: A new tool for provenance analysis: Earth and Planetary Science Letters, v. 286, p. 436-445, doi: 10.1016/j.epsl.2009.07.008.

Horscroft, F.D.M., Mossman, D.J., Reimer, T.O., 2011, Witwatersrand metallogenesis: the case for (modified) syngenesis: SEPM Special Publications, v. 101, p. 75-95.

Ireland, T.R., Schram, N., Holden, P., Lanc, P., Ávila, J., Armstrong, R., Amelin, Y., Latimore, A., Corrigan, D., Clement, S., Foster, J.J., Compston, W., 2014, Charge-mode electrometer measurements of S-isotopic compositions on SHRIMP-SI: International Journal of Mass Spectrometry, v. 359, p. 26-37, doi: 10.1016/j.ijms.2013.12.020.

Johnston, D.T., 2011, Multiple sulfur isotopes and the evolution of Earth's surface sulfur cycle: Earth-Science Reviews, v. 106, p. 161-183, doi: 10.1016/j.earscirev.2011.02.003.

Lalonde, S.V., Konhauser, K.O., 2015, Benthic perspective on Earth's oldest evidence for oxygenic photosynthesis: Proceedings of the National Academy of Sciences, v. 112, p. 995-1000, doi: 10.1073/pnas.1415718112.

Lyons, T.W., Reinhard, C.T., Planavsky, N.J., 2014, The rise of oxygen in Earth's early ocean and atmosphere: Nature, v. 506, p. 307-315, doi: 10.1038/nature13068.

Magee, C.W., Teles, G., Vicenzi, E.P., Taylor, W., Heaney, P., 2016, Uranium irradiation history of carbonado diamond; implications for Paleoarchean oxidation in the São Francisco craton (South America): Geology, v. 44, p. 527-530, doi: 0.1130/G37749.1.

Milesi, J.P., Ledru, P., Marcoux, E., Mougeot, R., Johan, V., Lerouge, C., Sabaté, P., Bailly, L., Respaut, J.P., Skipwith, P., 2002, The Jacobina Paleoproterozoic gold-bearing conglomerates, Bahia, Brazil: a "hydrothermal shear-reservoir" model: Ore Geology Reviews, v. 19, p. 95-136, doi: 10.1016/S0169-1368(01)00038-5.

Ono, S., Eigendrode, J.L, Pavlov, A.A., Kharecha, P., Rumble III, D., Kasting, J.F., Freeman, K.H., 2003, New insights into Archean sulfur cycle from mass-independent

sulfur isotope records from the Hamersley Basin, Australia: Earth and Planetary Science Letters, v. 213, p. 15-30.

Ono, S., Wing, B., Johnston, D., Farquhar, J., Rumble, D., 2006, Mass-dependent fractionation of quadruple stable sulfur isotope system as a new tracer of sulfur biogeochemical cycles: Geochimica et Cosmochimica Acta, v. 70, p. 2238-2252, doi: 10.1016/j.gca.2006.01.022.

Pavlov, A.A., Kasting, J.F., 2002, Mass-independent fractionation of sulfur isotopes in Archean sediments: Strong evidence for an anoxic Archean atmosphere: Astrobiology, v. 2, p. 27–41.

Teles, G., Chemale Jr., F., Oliveira, C.G., 2015, Paleoarchean record of the detrital pyrite-bearing, Jacobina Au–U deposits, Bahia, Brazil: Precambrian Research, v. 258, p. 289-313, doi: 10.1016/j.precamres.2014.11.004.

4.9. PROOF OF SUBMISSION

Submission Confirmation for Contrasting preservation of MIF-S in the Jacobina Basin, São Francisco Craton: implications for atmospheric conditions and formation of Au-(U)-Py deposits. - [EMID:e416504c195d0d3c]

E Journal Geology <em@editorialmanager.com>
seg 02/10/2017 19:14
Para: Guilherme dos Santos Teles (guilhermettell@hotmail.com)

Responder

Dear Mr. Teles ,

Your submission entitled " Contrasting preservation of MIF-S in the Jacobina Basin, São Francisco Craton: implications for atmospheric conditions and formation of Au-(U)-Py deposits. " has been received by GEOLOGY.

You will be able to check on the progress of your paper by logging on to Editorial Manager at http://geology.edmgr.com/ .

Your manuscript will be given a manuscript number once an Editor has been assigned.

Thank you for submitting your work to GEOLOGY.

Kind regards,

Geology Staff

CAPÍTULO 5

Multiple sulfur isotopes and trace elements geochemistry of sulfides from the Paleoarchean (3.3 Ga) Mundo Novo Greenstone Belt, São Francisco Craton, Brazil: clues on S and metal sources in ancient hydrothermal systems.

Guilherme S. Teles[1], Farid Chemale Jr.[1,3], Janaína N. Ávila[2], Trevor R. Ireland[2], and Daniele S. S. P. Teles[4]

[1]Instituto de Geociências, Universidade de Brasília, Brasília-DF 70904-970, Brazil.

[2]Research School of Earth Sciences, The Australian National University, Canberra ACT 2601, Australia.

[3]Programa de Pós-Graduação em Geologia, Universidade do Vale do Rio dos Sinos, São Leopoldo-RS 93022-000, Brazil.

[4]Independent Researcher, Av. Paulo Maia Lopes 79, Barra dos Coqueiros-SE 49140-000, Brazil.

ABSTRACT

The Paleoarchean (3.3 Ga) Mundo Novo Greenstone Belt, São Francisco Craton, Brazil hosts volcanogenic massive sulfide (VMS) deposits that allow the assessment to ancient hydrothermal systems. We investigated two VMS occurrences and associated rocks in this belt: a barren pyrite lens in the north, and the Fazenda Coqueiro Zn-Cu-Pb prospect in the south. Our approach is based on in situ analysis of multiple sulfur isotopes (^{32}S, ^{33}S, ^{34}S and ^{36}S) and trace elements compositional data for a variety of sulfides. S isotopes data show limited $\delta^{34}S$ fractionations that are comparable to the range of values for Archean VMS deposits. On the other hand, large mass-independent fractionation (MIF-S) are noted in the majority of samples, with $\Delta^{33}S$ values of between -1.2 and 2.2‰ and $\Delta^{36}S$ from -2.4 to 2.3‰. Trace elements data vary according to the sulfide types and the relative stratigraphic position of sample in the deposits. The data suggest distinct S sources for the VMS occurrences; the barren lens yields only negative $\Delta^{33}S$ values, that were originated from seawater sulfate; whereas the sulfides from the Zn-Cu-Pb prospect have dominantly positive $\Delta^{33}S$ values, which are indicative for a sedimentary source of S in this deposit. Moreover, multiple S isotopic composition of barren pyrite lens is close

to the Paleoarchean barite deposits, and may indicate mass dependent processing from a global and well-mixed sulfate pool at this time. The VMS from Fazenda Coqueiro diverges from the majortity of Archean deposits, in which the sulfur sources are dominantly magmatic/hydrothermal, with a minor component of seawater sulfate. These factors must have critical issues on the size and metals endownment in the Fazenda Coqueiro deposit.

Key-words: Paleoarchean, Mundo Novo Greenstone Belt, VMS deposits, S isotopes.

5.1. INTRODUCTION

Volcanogenic massive sulfide deposits (VMS) are some of the most important sources for base- (Cu-Zn-Pb) and precious metals (Ag-Au; Hannington, 2014). These deposits are among the oldest known ore deposits on Earth, with some examples dating back to the Paleoarchean (~3.45 Gyr; Huston et al., 2001; Golding et al., 2011). Due to the antiquity and distribution of these deposits through the geologic time, they record important pieces of evidences for the evolution of tectonic processes, atmosphere, hydrosphere, and biosphere (e.g., Huston et al., 2010; Farquhar et al., 2010).

In general, the VMS deposits are stratiform and stratabound accumulations of base-metals formed at or just below the seafloor, by precipitation from upwelling hydrothermal fluids mixing with ambient seawater (Hannington, 2014). These fluids are generated by the interaction of convective circulation of heated seawater and sub-seafloor rocks, driven by a magmatic body that contribute fluids to the hydrothermal cell (Huston et al., 2010). Therefore, the metals could be sourced from the leaching of wall-rocks, or by the direct input from magmatic fluids.

Sulfur isotopes have been used to trace the possible metal sources in these environments, as sulfur composes the sulfide ores, and it is the principal complexing anion that carries metals in the ore forming fluids. In the case of Archean deposits, the limited range of $\delta^{34}S$ (-2 to +2‰) values, compared to younger deposits, is thought to reflect low sulfate concentration in the Archean oceans (Huston et al., 2010); although Paleoarchean VMS deposits contain abundant barite (Huston et al., 2004).

It is believed that the Archean sulfur cycle was largely different from today, and the record of mass-independent fractionation of sulfur isotopes (MIF-S, noted as $\Delta^{33}S$ and $\Delta^{36}S$) in Archean rocks is the best clue for this statement (Farquhar et al., 2000).

Experimental data and atmospheric models (Farquhar et al., 2001; Pavlov and Kasting, 2002) suggest that MIF-S was generated by photochemical reactions of volcanic sulfur species driven by UV radiation in an anoxic atmosphere. In this condition, the production, transference, and preservation of these anomalies occurred by two distinct pathways: a reduced and insoluble component (e.g., S_8) that carries a positive $\Delta^{33}S$ and negative $\Delta^{36}S$ signals; and an oxidized and soluble sulfur species (e.g., SO_4^{2-}) with negative $\Delta^{33}S$ and positive $\Delta^{36}S$ signatures (Farquhar and Wing, 2003). The importance of this framework, and the multiple sulfur isotope analyses of sulfide minerals have been demonstrated in several studies of Archean mineral deposits, especially those applied to VMS deposits, once they allow the identification of the involvement of anomalous S that was cycled through the Archean atmosphere and hydrosphere, and its contribution to the mineralizing system (e.g., Bekker et al., 2009; Golding et al., 2011; Jamieson et al., 2013; Xue et al., 2013; Sharman et al., 2015; Chen et al., 2015; Agangi et al., 2016).

This study presents in situ multiple sulfur isotopes (^{32}S, ^{33}S, ^{34}S and ^{36}S) and trace elements data of sulfides from the 3.3 Ga VMS deposits and associated rocks from the Mundo Novo Greenstone Belt (MNGB), São Francisco Craton, Brazil. This approach provides clues on the sulfur and metals sources, and ultimately the nature of mineralizing fluids. Our data allow comparison to other Archean VMS deposits, regarding to the sources, metal budgets, and deposit sizes. Furthermore, the VMS deposits of MNGB are coeval to several Paleoarchean barite deposits (3.5 to 3.2 Ga) found in Australia, South Africa and India, which may have a global significance to the Paleoarchean oceans and sulfur cycle.

5.2. GEOLOGY OF THE MUNDO NOVO GREENSTONE BELT

The northeastern portion of the São Francisco Craton, Brazil, contains some of the oldest known rocks in the South America. These rocks belong to the Paleoarchean Gavião Block, which is largely consisted by TTG assemblies (tonalite-trondhjemite-granodiorite) and supracrustal sequences, such as the Mundo Novo Greenstone Belt (MNGB; Barbosa and Sabaté, 2004). This greenstone crops out in the eastern margin of Gavião Block (Figure 5.1), in a narrow strip that is tectonically limited to by the Jacobina Basin (Teles et al., 2015) to the west, through the Pindobaçu Fault; and by the high-grade rocks of Mairi and Saúde complexes to the east (Mascarenhas and Silva, 1994; Zincone et al., 2017).

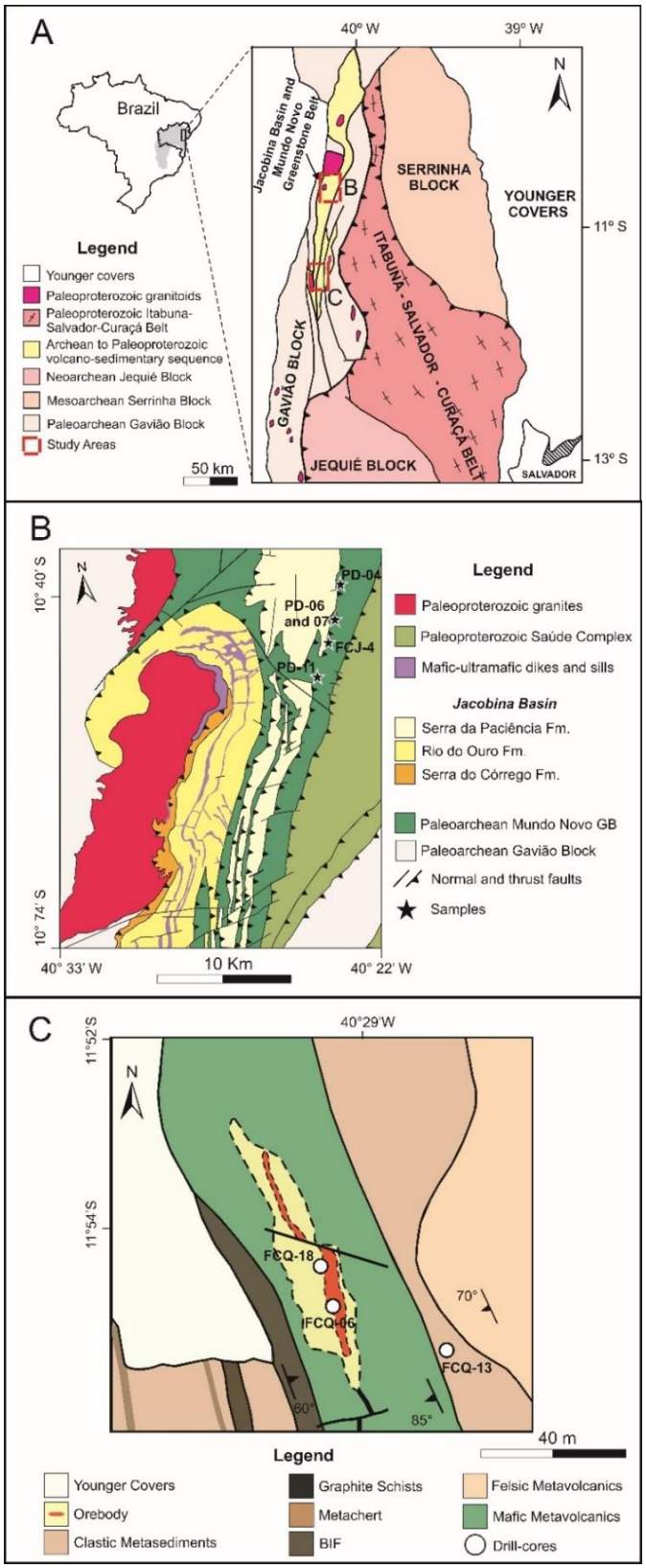

Figure 5.1. (A) Geotectonic setting of the studied areas; (B) Geologic map of the northern portion of the Mundo Novo Greenstone Belt, with respective samples locations (modified from Teles et al., 2015); (C) Simplified geologic map of the Fazenda Coqueiro target, showing locations of the sampled drill cores (modified from Souza et al., 2002).

The Paleoarchean age of the MNGB was firstly determined by Peucat et al. (2002), which obtained a SHRIMP U-Pb zircon age of 3305 ± 9 Ma in a metadacite sample. Recently, Zincone et al. (2016) obtained a similar U-Pb zircon age of 3303 ± 7 Ma for a rhyolite sample by the LA-ICP-MS method. The greenstone rocks are metamorphosed to green-schist facies, preserving primary features, which can be classified into three main groups: (1) mafic metavolcanics – chloritized and tremolitized metabasalts, in some cases with pillow-lavas; (2) intermediary to felsic metavolcanics (andesites, dacites and rhyolites); and (3) metasedimentary chemical and clastic rocks (BIF's, manganesiferous BIF's and metapelites, cherts, carbonaceous-schists, and metapelites). The geochemical data of metavolcanic rocks suggest that basalts have tholeiitic affinity, like seafloor tholeiites formed in extensional back-arc settings; whereas the intermediate and felsic rocks have calc-alkaline affinity, with REE patterns similar to those formed in active continental margins (Mascarenhas et al., 1998; Borges et al., 2004).

Volcanogenic massive sulfides occur in both northern and southern segments of MNGB. The most prominent occurrence is located in the southern portion of belt, at the Fazenda Coqueiro target, which host a Zn-Cu-Pb deposit. This mineralization occurs associated with the metamafic unit of greenstone, that is dominantly composed of metabasalts interleaved with BIF's, cherts, micaceous-schists (locally graphite-bearing), and minor felsic metavolcanics. Syn-volcanic hydrothermal alteration features are found in both mafic and felsic volcanics, being the latter indicative for the existence of an ancient volcanic center (Souza et al., 2002). The main massive sulfide lens totalizes 8 m of thickness and 400 m of extension along the strike (approximately N-S). The grades associated with this interval are 6.2% of Zn, 0.7% of Pb, 498 ppm of Cu, 35 g/t of Ag, and 103 ppb of Au (Souza et al., 2002). At the northern greenstone, massive sulfides lens crops out in association to metabasalts, BIF's and carbonaceous-schists.

5.2.1. Samples

Our samples were collected from outcrops and fresh drill-cores, respectively from the northern and southern areas of the MNGB. Four outcrops were sampled from the northern area, that include pillow basalt (Figure 5.2A), BIF, carbonaceous-schist, and massive pyrite lens (Figure 5.2B). The pillow basalt sample (PD-04) is a greenish, very fine-grained rock, which matrix is indicative of syn-volcanic hydrothermal alteration, dominantly composed by chlorite, quartz, and sericite. Some amygdalas are found in the

matrix, which are commonly filled by quartz, microcrystalline silica, carbonate and sericite. Pyrite grains are typically small (<100 μm), exhibiting subhedral and anhedral habits.

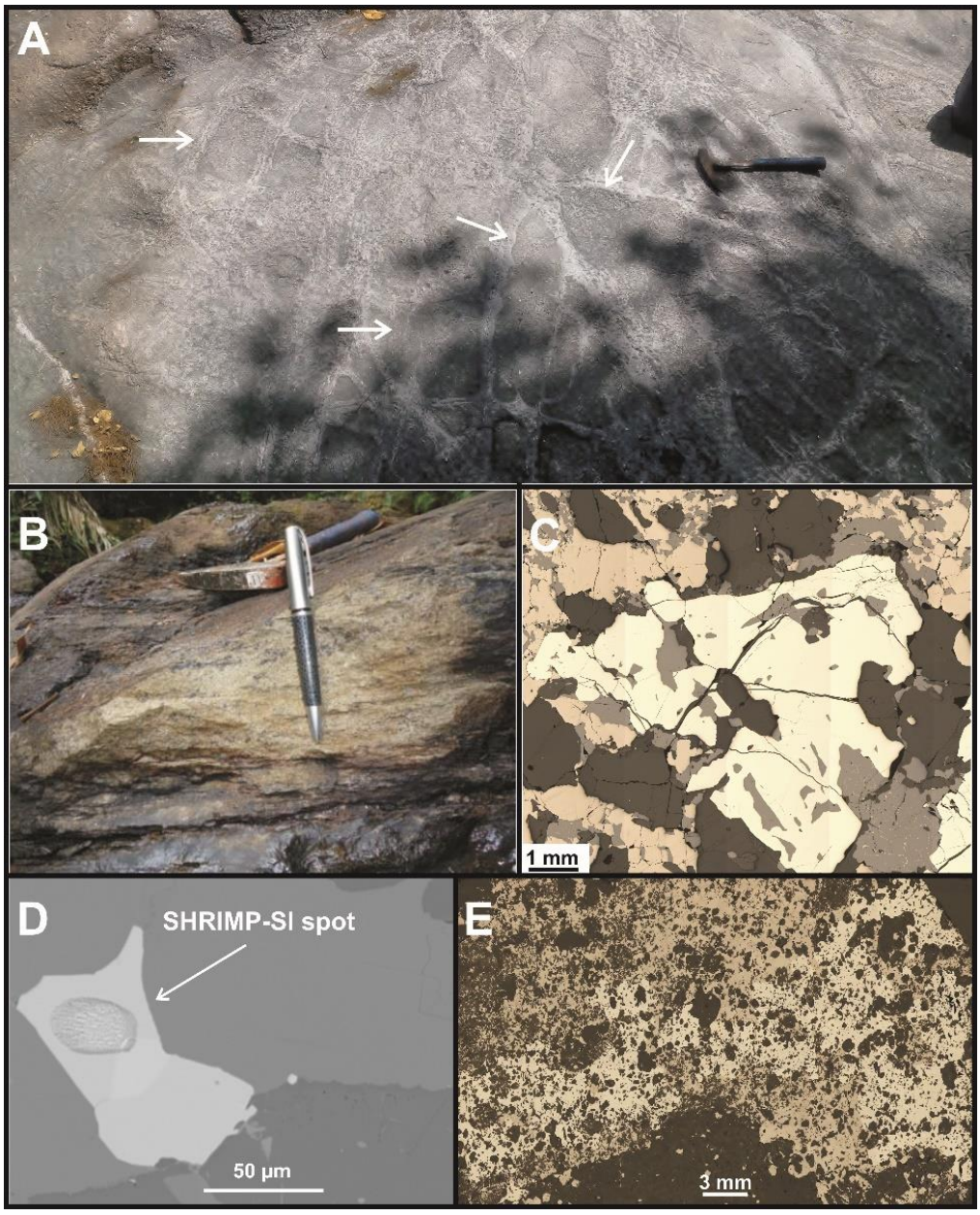

Figure 5.2. (A) Pillow-basalt outcrop (sample PD-04) at the northern Mundo Novo Greenstone Belt (MNGB). White arrows point to the pillow features; (B) Barren massive pyrite lens, correspondent to samples PD-06 and PD-07, at northern MNGB; (C) Reflected-light photomicrography of high-grade zinc massive sulfide ore from the Fazenda Coqueiro target; (D) Fine-grained pyrrhotite grain from tremolite metabasalt sample (FCQ-06.5), showing a SHRIMP-SI spot; (E) Massive sulfide portion of the micaceous-chert sample (FCQ-06.2).

The BIF sample (PD-11) is a typical Algoma-type BIF, with millimetric alternations of magnetite (partially altered to hematite) and microcrystalline silica layers. Similarly to the sample PD-04, pyrite grains from BIF are scarce, small, and with subhedral habits. The carbonaceous-schist (sample FCJ-4) is dominantly composed of quartz and graphite in a fine-grained matrix, with some arenaceous lenses. Pyrite is found as anhedral grains disseminated in the matrix, following the original bedding, but also as euhedral pyrite associated to quartz veins. The samples PD-06 and PD-07 were collected from a massive pyrite lens associated to chloritized basalts. They are respectively from the inner and outer portion of massive sulfide lens. In these samples, anhedral pyrite and calcedony replace the original host basalt, and are indicative of syn-volcanic hydrothermal alteration.

The samples from the Fazenda Coqueiro target were obtained from three drill-cores (FCQ-13, FCQ-06, and FCQ-18; Figures 5.1C and 5.3), which represent the overall stratigraphy of the deposit. A total of 8 samples were studied, of which two represent the deposit footwall: a quartz-mica-schist (sample FCQ-13), in which sulfide mineralization is represented by anhedral chalcopyrite and pyrite along foliation (Figure 5.3); and a micaceous-chert (sample FCQ-06.2) that locally can be made by up to 60% of sulfides, mainly pyrite and pyrrhotite (Figure 5.2E), but also have disseminated sulfides along the matrix, and filling fractures. Stringer mineralization is represented by quartz veins in a silicified tremolitite-metabasalt (sample FCQ-1), that host galena > pyrite >> arsenopyrite.

The main massive sulfide horizon that hosts the highest Zn grades are represented by four samples (Figures 5.2C and 5.3). Two of them were collected from drill-core FCQ-06 (samples FCQ-06.1 and 06.3), which contain 13% Zn; and the remaining were sampled from drill-core FCQ-18 (samples FCQ-18.1 and FCQ-18.2), that have 6.5% of Zn (Figure 5.3). The Fazenda Coqueiro hangingwall is represented by the sample FCQ-06.5 that is a silicified tremolitite with a carbonate and chlorite-rich matrix, where fine-grained pyrrhotite and arsenopyrite occur along foliation.

5.3. METHODS

5.3.1. SHRIMP-SI Multiple Sulfur Isotope Analyses

The in situ 4-sulfur isotope measurements were performed at the Research School of Earth Sciences (RSES), The Australian National University (ANU), Canberra, using

the Sensitive High-Resolution Ion Microprobe – Stable Isotopes (SHRIMP-SI). Pyrite, pyrrhotite, chalcopyrite and galena were analyzed during two sessions in 2015. The precision and accuracy of in situ S isotopes analysis by SHIMP-SI are highly dependent on the use of appropriate sulfide standards, preferably homogeneous matrix-matched sulfides. In this study, our sulfide standards were Ruttan and Balmat pyrites, Anderson pyrrhotite, Trout Lake and Norilsk chalcopyrites, and Balmat galena. These standards have been demonstrated suitable for in situ S isotopes analysis (e.g., Crowe and Vaughan, 1996; Whitehouse et al., 2005; Kozdon et al., 2010; Williford et al., 2011; Whitehouse, 2013). Prior to analysis, these sulfides were cast together with the samples pieces in 25 mm epoxy mounts.

Instrumental configuration and analytical procedures were similar to those described by Ireland et al., (2014). In summary, a 15kV Cs^+ primary beam is focused to sputter an area of ~ 25 μm in diameter on sample surface. Negative secondary ions were accelerated to real ground from the −10kV sample potential and focused by the quadrupole triplet lenses before passing through the source slit and entering the secondary mass analyzer. The low mass, auxiliary, axial and high mass heads detectors equipped with Faraday cups were used for simultaneously detection of $^{32}S^-$, $^{33}S^-$, $^{34}S^-$ and $^{36}S^-$ respectively. The collector slit widths were set at 400 μm for $^{32}S^-$, 150 μm for $^{33}S^-$, 200 μm for $^{34}S^-$ and 300 μm for $^{36}S^-$, which resolve potential interferences of sulfur hydrides on mass 33 and 34.

The count rates varied according to the sulfide species analyzed, and the number of sets for data acquisition (see Table 7.12), which varied between 2 sets of 10 measurements (20s each), 4 sets of 10 measurements, and a single set for galena analysis. Nevertheless, each spot analysis was preceded by 300s of pre-sputtering of sample surface, during which the background was monitored; 100s of automated steering of secondary ions; and 5s of automated centering of the secondary ions in the collector slits. To correct instrumental mass-dependent fractionation and for calculation of isotopic ratios, each session was started by at least three measurements on the appropriate standards, which were repeated after every 10 spots analysis on unknown samples.

The isotopic compositions are reported as per mil (‰) deviations from the V-CDT standard (*Vienna Canyon Diablo Troilite*) using the conventional notation:

$$\delta^{34}S = 1000 \times [(^{34}S/^{32}S)_{sample} / (^{34}S/^{32}S)_{V\text{-}CDT} - 1] \times 1000$$

The mass-independent fractionation (MIF) represents the deviation from the terrestrial mass-dependent fractionation line, which measure is expressed as $\Delta^{33}S$ and $\Delta^{36}S$:

$$\Delta^{33}S = 1000 \times [(1 + \delta^{33}S/1000) - (1 + \delta^{34}S/1000)^{0.515}]$$

$$\Delta^{36}S = 1000 \times [(1 + \delta^{36}S/1000) - (1 + \delta^{34}S/1000)^{1.89}]$$

The internal errors (2σ) are typically better than 0.04‰, 0.1‰, and 0.3‰ for $\delta^{34}S$, $\Delta^{33}S$ and $\Delta^{36}S$, respectively. External reproducibility (2SD), as estimated from replicate measurements on standards, and the associated individual spots are available as Supplementary Material.

5.3.2. LA-ICP-MS trace elements analysis

Laser-Ablation Inductively-Coupled-Plasma Mass-Spectrometry (LA-ICP-MS) was used to measure trace elements concentration in sulfides from the MNGB. The analysis was undertaken at the RSES, ANU, using a Lambda Physik laser-ablation system that operates at a wavelength of 193 nm, which was set with an output energy of 45 mJ, and repetition rate of 5 Hz. The ablated samples were carried by a H-He-Ar mixture to an Agilent Technologies 7700 series quadrupole ICP-MS. The sulfide samples were analyzed with a spot size of 28 µm, and the dwell time was kept to ~1 s for most of elements, but in some cases, it was set to maximize counting statistics of presumably lower concentration elements. Data reduction followed the standards procedures of Longerich et al., (1996), using the software Iolite (Paton et al., 2011)

Sulfides standards as MASS-1 (Wilson et al., 2002) and STDGL-1 (Norman et al., 2003) were used together with NIST-610 to calibrate the trace element contents of unknown samples. The standards were analyzed on the beginning and conclusion of each session, and regularly between 10 spots on unknowns. Stoichiometric proportions of Fe, Zn and Pb were used as internal standards for data reduction of pyrite (Fe), pyrrhotite (Fe), chalcopyrite (Fe), arsenopyrite (Fe), sphalerite (Zn), and galena (Pb).

5.4. RESULTS

Our results for isotopic and trace elements analyses are summarized in the following sessions, and are available as Supplementary Material. These data can be evaluated by the geographic location of samples in the MNGB, as well as by the host rocks and the relative stratigraphic position of samples in the deposits.

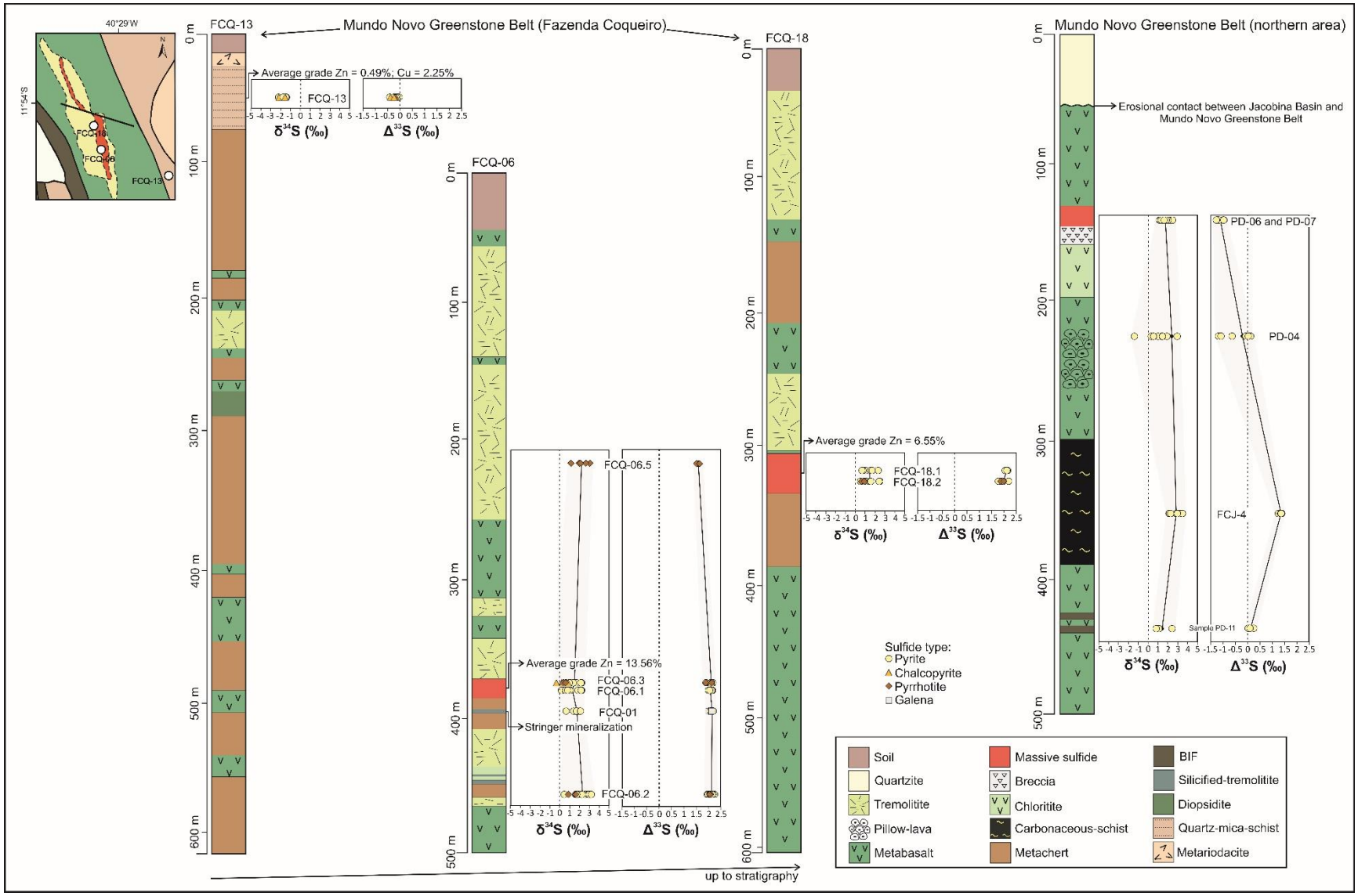

Figure 5.3. Stratigraphy of the sampled drill-cores at the Fazenda Coqueiro location, as well as the simplified stratigraphic column of the northern MNGB area. S isotopes data ($\delta^{34}S$ and $\Delta^{33}S$) are shown in their relative stratigraphic position.

5.4.1. Multiple Sulfur Isotopes Geochemistry

The multiple S isotopic composition of pyrite samples from the northern MNGB vary according to their host rock. However, the limited range of $\delta^{34}S$ values is common for all samples (Figures 5.4A and 7.9). The pillow-basalt pyrites (PD-04) yield mean $\delta^{34}S$ of 1.09 $\pm$ 0.93‰ (n= 9); $\Delta^{33}S$ ranging between -1.2 and 0.35‰, with mean of -0.25 $\pm$ 0.46‰; and $\Delta^{36}S$ varying from -0.23 to 1.3‰ (mean= 0.38 $\pm$ 0.45‰). The BIF sample (PD-11) is characterized by the absence of MIF-S anomalies, with $\Delta^{33}S$ = 0.08 $\pm$ 0.23‰ and $\Delta^{36}S$ = 0.06 $\pm$ 0.49‰ (n= 3), besides slightly positive $\delta^{34}S$ (mean= 1.5 $\pm$ 2.1‰), which together suggest a mantellic source of S in this sample (Figure 5.4).

The carbonaceous-schist sample (FCJ-4) have pyrites with homogeneous isotopic compositions, irrespective to their textural type (euhedral in quartz vein or disseminated in matrix); with $\delta^{34}S$ values slightly more positive compared to the other samples from the northern MNGB (mean= 2.86 $\pm$ 0.37‰; n= 10), positive $\Delta^{33}S$ (mean= 1.35 $\pm$ 0.02‰), and negative $\Delta^{36}S$ (mean= -0.84 $\pm$ 0.24‰). These values indicate a MIF-S source (Figure 5.4), similarly to sedimentary sulfides in Archean black-shales.

The samples PD-06 and PD-07 were collected from the inner and outer portions of a massive pyrite lens, respectively. The multiple S isotopic compositions are similar among them (Figure 5.4), however, sample PD-07 has slightly lighter $\delta^{34}S$ and $\Delta^{33}S$, and higher $\Delta^{36}S$ values ($\delta^{34}S$= 1.66 $\pm$ 0.3‰, $\Delta^{33}S$= -1.22 $\pm$ 0.02‰, and $\Delta^{36}S$= 1.21 $\pm$ 0.3‰) compared to sample PD-06 ($\delta^{34}S$= 2.0 $\pm$ 0.34‰, $\Delta^{33}S$= -0.97 $\pm$ 0.02‰, and $\Delta^{36}S$= 1.09 $\pm$ 0.42‰).

The sulfides from Fazenda Coqueiro target (southern MNGB) are remarkably similar in respect to their multiple S isotopic compositions, regardless of the stratigraphic position of samples in the deposit (Figures 5.3, 5.4, and 7.9). There are only two exceptions among the eight samples from this location, which represent the footwall and hangingwall (samples FCQ-13 and FCQ-06.5, respectively). The sulfides from sample FCQ-13 yield quite homogeneous isotopic compositions (Figure 5.4), with $\delta^{34}S \sim$ -1.6‰, $\Delta^{33}S \sim$ -0.2‰, and $\Delta^{36}S \sim$ 0.3‰; that suggest S derived from a juvenile source ($\Delta^{33}S$= 0‰) with some contribution from the seawater sulfate ($\Delta^{33}S$ < 0‰). The sample FCQ-06.5 yields pyrrhotite grains whose isotopic compositions are relatively homogeneous: $\delta^{34}S$= 2.8 $\pm$ 0.73‰, $\Delta^{33}S$= 1.59 $\pm$ 0.05‰, and $\Delta^{36}S$= -1.12 $\pm$ 0.13‰ (n= 5).

The remaining samples, micaceous-chert (FCQ-06.2), stringer mineralization (FCQ-1), and massive sulfide (FCQ-06.1, FCQ-06.3, FCQ-18.1, and FCQ-18.2) yield

systematically similar MIF-S anomalies irrespective of the analyzed sulfide phase (Figure 5.4 and 7.9). The $\Delta^{33}S$ anomalies are positive (vary between 1.8 and 2.2‰), and cluster around 2.1‰ (Figure 5.4A). The $\Delta^{36}S$ are negative, but more variable, ranging from -2.2 to -0.17‰, with a cluster around -1.3‰ (Figure 5.4B). The $\delta^{34}S$ is limited to a narrow range from -0.35 to 3.2‰, but most of data plot between 0 and 2‰ (Figure 5.4A and 7.9). These values are within the $\delta^{34}S$ ranges of sulfides in Archean VMS deposits (Huston et al., 2010).

On the other hand, galena analysis (sample FCQ-1) yield the largest range in $\delta^{34}S$ values (from 1.62 to 7.06‰), though their $\Delta^{33}S$ and $\Delta^{36}S$ are similar to the other analyzed sulfides (Figure 5.4). This behavior is not related to compositional variability of galena crystal. Instead, it is explained by crystal orientation effects of galena during SIMS sulfur isotopes analysis (e.g., Kozdon et al., 2010). However, the $\Delta^{33}S$ and $\Delta^{36}S$ measurements are not affected by this phenomenon, because it is mass dependent.

5.4.2. Trace Elements Content in Sulfide Minerals

The LA-ICP-MS trace elements compositions of pyrite, chalcopyrite, sphalerite, pyrrhotite, galena, and arsenopyrite are presented in Supplementary Material (Item 7.2). The trace elements data can be evaluated according to the stratigraphic position of samples, host rock, and mainly to the sulfide type.

Pyrite has, in general, low contents for most of analyzed trace elements, except Co, As and Se (Figure 5.5; Table 7.6). Co is particularly enriched in most samples from Fazenda Coqueiro prospect (up to 10000 ppm). Similarly, pyrrhotite yields low contents for most of trace elements, with relatively high concentrations for Ni, As and Se (Figure 7.12; Table 7.9). Arsenopyrite from samples FCQ-01 and FCQ-06.5 has also low trace elements contents, except Co, Ni, Se and Sb (Table 7.11).

Chalcopyrite, sphalerite, and galena host the highest contents for several trace elements. The chalcopyrite is enriched in Ni, As, Se, Ag, Cd, In and Sn (Figure 7.10; Table 7.7), whereas galena has high Se, Ag, Cd, Sb, Te, Tl, and Bi (Figure 7.13; Table 7.10), and sphalerite is enriched in Mn, Se, Cd, In, and Hg (Figure 7.11; Table 7.8). These results agree previous investigations of sulfide minerals in VMS systems (Huston et al., 1995; Cook et al., 2009; George et al., 2015; Wohlgemuth-Ueberwasser et al., 2015).

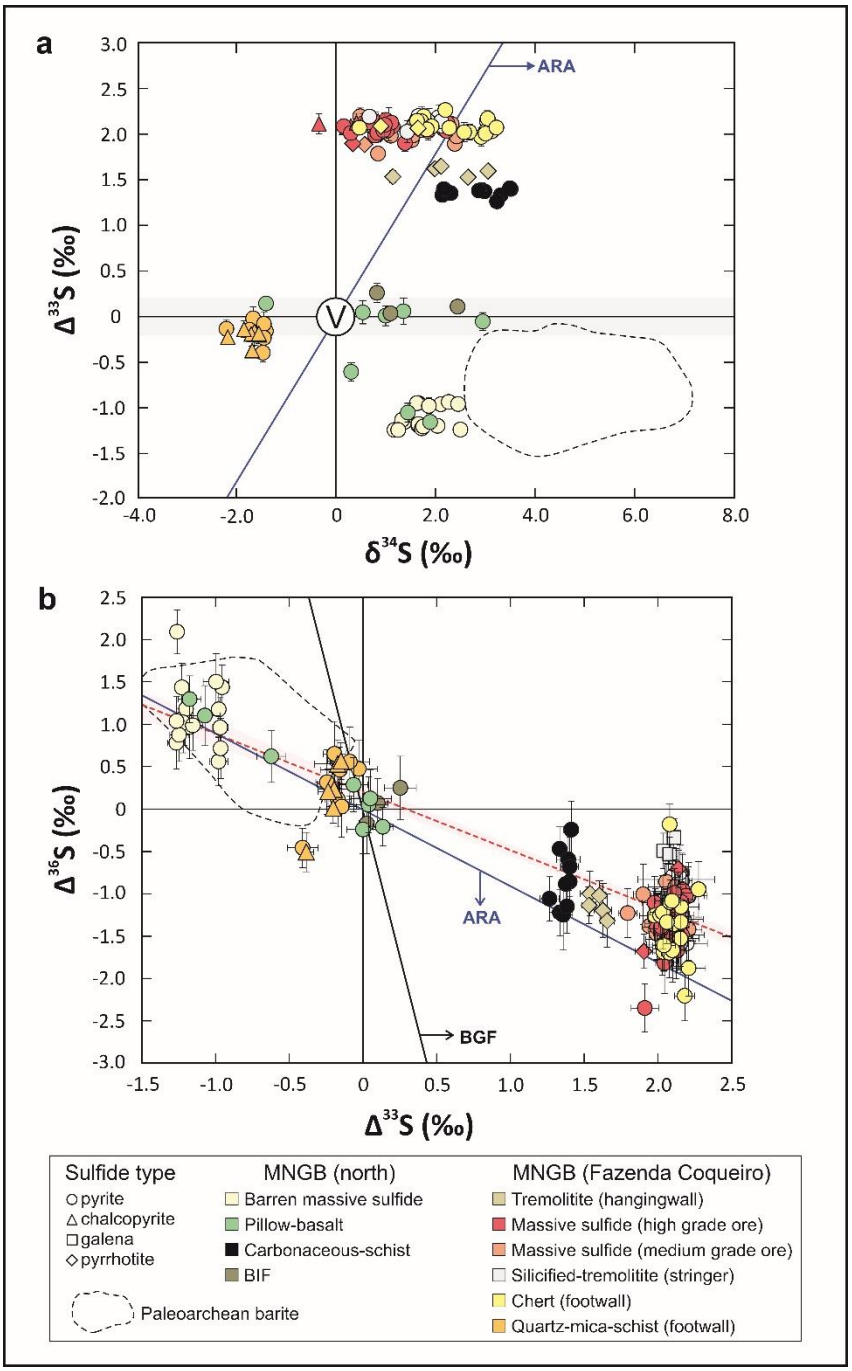

Figure 5.4. Multiple sulfur isotopes plots of the sulfides from the Mundo Novo Greenstone Belt. In the $\Delta^{33}S$ vs. $\delta^{34}S$ plot (a), the blue line indicates the Archean reference array (ARA, Ono et al., 2003), the letter (V) indicates juvenile sulfur, and the grey shaded area is the field that indicates the absence of MIF-S anomalies. In the $\Delta^{36}S$ vs. $\Delta^{33}S$ plot (b), the Archean (ARA, blue) and the predicted biogeochemical (BGF, Ono et al., 2006) arrays are indicated, as well as the regression line for the data (red dashed line) and its respective 95% confidence envelope (pink shaded areas). In both plots, the area bounded by the dashed line indicates the range of the multiple-S isotopic composition of Paleoarchean barite (data from Ueno et al., 2008; Shen et al., 2009; Roerdink et al., 2012; Montinaro et al., 2015; and Müller et al., 2017), and the error bars are 2σ.

In order to constrain the sources and conditions for mineralization of the VMS deposits from MNGB, we used the trace elements content and isotopic composition of pyrite (the most analyzed sulfide in this work) as an attempt to observe some systematic relationships. Despite the absence of covariation between the data plots shown in Figure 5.6, the pyrite can be distinguished in relatively well-defined groups according to geographic location of samples and their host rocks, which have implications for the VMS forming processes (see Discussion section).

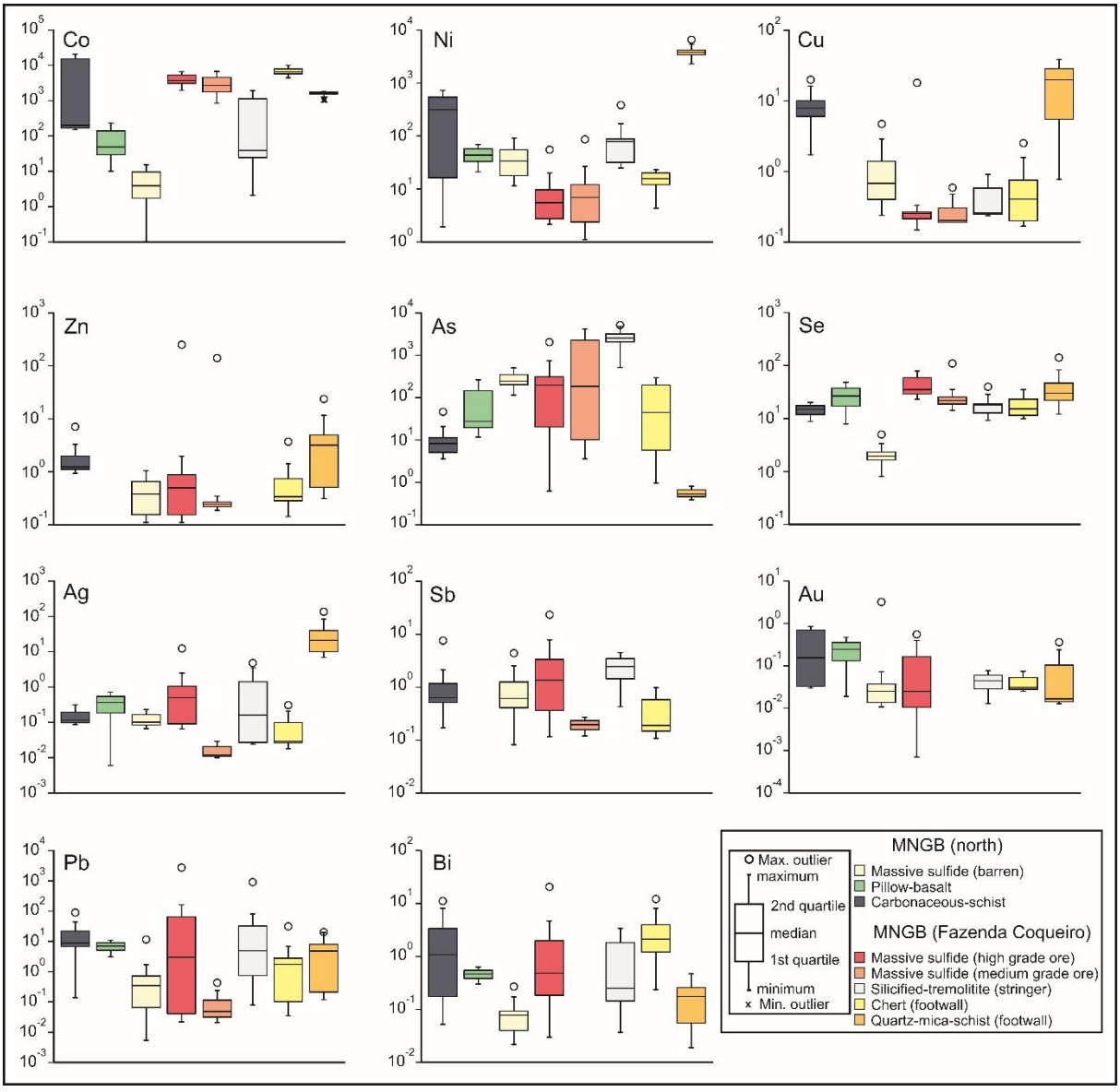

Figure 5.5. Box-whiskers diagrams of selected trace elements concentrations (ppm) for pyrite grains from the MNGB samples.

5.5. DISCUSSION

5.5.1. Sulfur Sources in the 3.3 Ga Mundo Novo Greenstone Belt VMS deposits

The most accepted idea about the mass-independent fractionation of sulfur isotopes (MIF-S) is that it forms during photochemical reactions involving volcanic SO_2 gas in an anoxic atmosphere, which was typical for the Archean Eon (Farquhar et al., 2000; 2001). These reactions produced two main sulfur species that carried the anomalous signatures from atmosphere to the surface: a reduced species (elemental sulfur - S_8) with positive $\Delta^{33}S$ and negative $\Delta^{36}S$, and an oxidized species (sulfate - SO_4^{2-}) with negative $\Delta^{33}S$ and positive $\Delta^{36}S$ signals (Farquhar and Wing, 2003). These S species have distinct geochemical behaviors in the surficial reservoirs, while SO_4^{2-} is soluble in water column; the S_8 is insoluble, and accumulates on the seafloor in pore-water spaces; as indicated by the isotopic composition of syngenetic and diagenetic sulfides in Archean sediments (e.g., Bekker et al., 2009).

In this sense, MIF-S should not be associated to a purely magmatic ore-forming processes, which result in near-zero $\Delta^{33}S$ signatures. Due to the conservative nature of MIF-S, these anomalies cannot be altered by the conventional mass-dependent fractionation processes that affect the $\delta^{34}S$. Thus, it can be used as a valuable indicative for distinct sulfur sources in Archean ore deposits.

From this basis, the multiple sulfur isotopes investigation of sulfides from the Mundo Novo Greenstone Belt was fundamental, because the contribution from distinct S sources would be hidden if the $\delta^{34}S$ data were considered alone, as the $\delta^{34}S$ values in these sulfides would suggest a purely igneous S source, which was previously considered the main source for Archean VMS deposits (see Huston et al., 2010 for review). Instead, our data in both northern and southern segments of belt suggest distinct S sources for the sulfides budget.

At the northern MNGB, the sulfides from BIF sample (PD-11) lack the MIF-S signals, which is compatible with a juvenile (magmatic) sulfur source (Figure 5.4). The carbonaceous schist yielded positive $\Delta^{33}S$ (Figure 5.4) values that if considered with the pyrite textures, agree with a diagenetic origin, in which the S_8 was the main sulfur source. During metamorphism these sulfides were remobilized to quartz veins without significant isotopic modification from the sedimentary pyrite. The pillow-basalt sulfides show isotopic data that are consistent with a magmatic source of sulfur (Figure 5.4). However, some data points in this sample have significant negative $\Delta^{33}S$ anomalies that are

accompanied by positive $\Delta^{36}S$ values. This systematic is also observed in the massive pyrite lens samples, which means that SO_4^{2-} was the main sulfur source for these pyrites. Furthermore, it is a good indication for the involvement and hydrothermal circulation of seawater on ancient seafloor, similarly to that observed in komatiitic lavas in Barberton Greenstone Belt (Montinaro et al., 2015) and pillow basalts in Yilgarn Craton (Chen et al., 2015), and also comparable to modern seawater hydrothermal circulation on seafloor (Hannington et al., 2005).

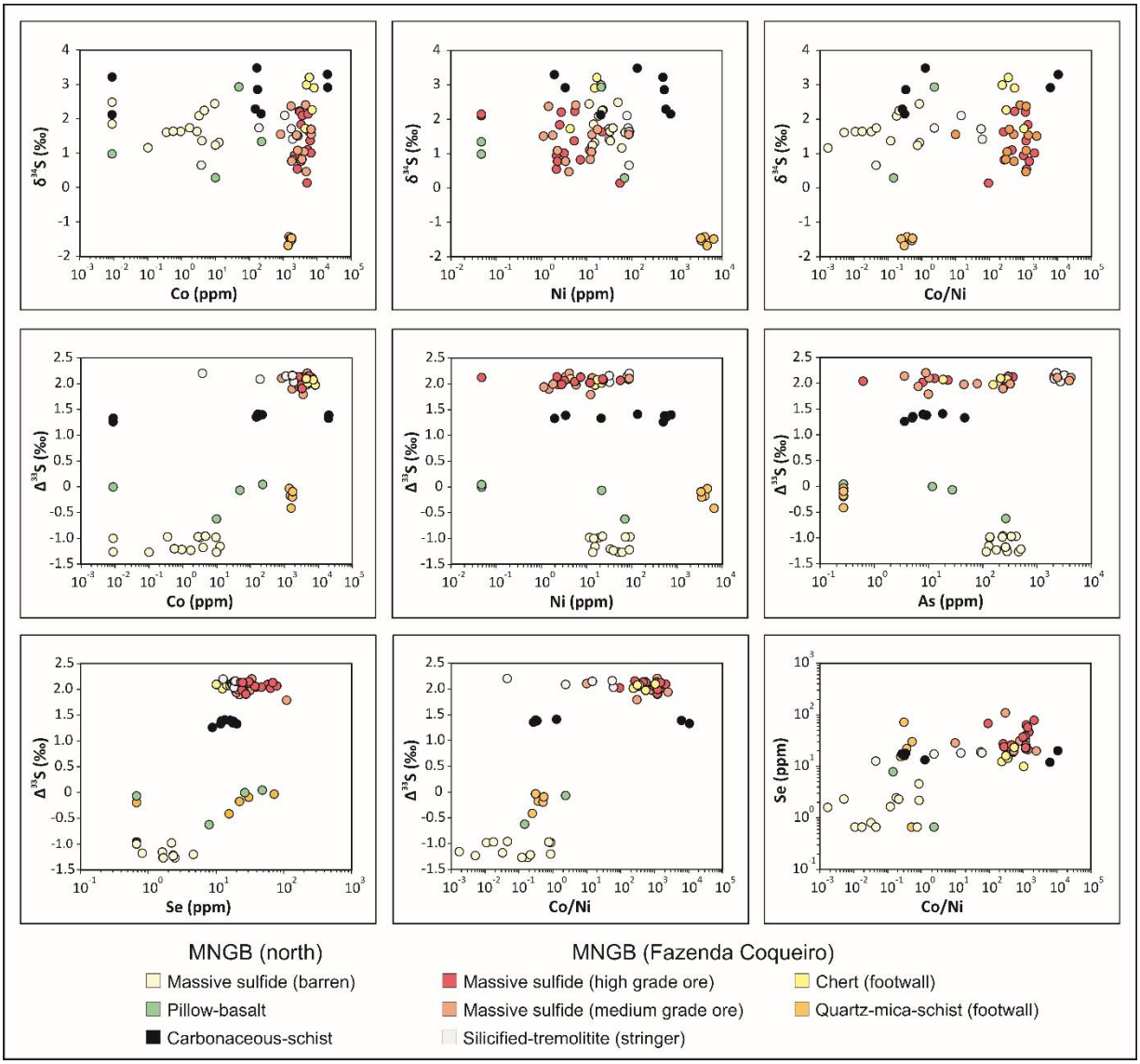

Figure 5.6. Binary plots of selected trace elements and isotopic compositions ($\delta^{34}S$ and $\Delta^{33}S$) for pyrite grains from the MNGB samples. In some plots, there is a clear distinction between pyrite samples, which relates to their respective stratigraphic position (see text for discussion).

At the southern MNGB, Fazenda Coqueiro prospect, most sulfide samples yield systematic anomalous MIF-S signatures, irrespective of their stratigraphic position (footwall, stringer, massive sulfide, and hangingwall), host rock or sulfide type. They show homogeneous positive $\Delta^{33}S$ (~2.1‰), and more variable negative $\Delta^{36}S$ anomalies that plot above the Archean reference array (Figure 5.4b), and may be associated to the larger uncertainties on ^{36}S measurements or a fractionation mechanism that has not been described so far. A tremolite metabasalt sample in the hangingwall, has in turn less pronounced positive $\Delta^{33}S$ (~1.5‰). These signatures suggest that elemental sulfur (S_8) was the main S source for the sulfides. As this sulfur species accumulates on seafloor, mainly in pore water space in sediments, it is likely that the sulfides from the Fazenda Coqueiro prospect were formed by assimilation of sulfur in connate pore waters. Furthermore, the homogeneous compositions of these sulfides may be an indication for the leaching of a local sedimentary source, which may also explain the higher contents of Zn and Pb compared to the widespread mafic-dominated VMS deposits during the Archean (Franklin et al., 2005; Huston et al., 2010). In these respects, the Fazenda Coqueiro prospect resembles the Paleoarchean Sulfur Springs deposits, in the Panorama field, Pilbara Craton (Golding et al., 2011).

The only exception for our data from the Fazenda Coqueiro prospect corresponds to the quartz-mica schist sample in its footwall. This sample yields negative $\delta^{34}S$ (-2‰), and $\Delta^{33}S$ ~0‰ to slightly negative values, which suggest a major magmatic/hydrothermal source of sulfur in this sample, but with some contribution from seawater sulfate. These signatures may indicate mixing between magmatic S from the volcanic substrate and seawater derived fluids, or a direct magmatic input. In both cases, this explain the higher Cu content in this sample, which is in agreement to a magmatic-dominated source (Huston et al., 2011).

5.5.1.1. Temperature constraints

Additional information about the formation and distinction between the VMS deposits in MNGB can be explored by trace elements and S isotopes temperature proxy data.

Sulfide mineral pairs at thermodynamic equilibrium should follow the $\delta^{34}S_{pyrite} > \delta^{34}S_{pyrrhotite} > \delta^{34}S_{sphalerite} > \delta^{34}S_{chalcopyrite} > \delta^{34}S_{galena}$ fractionation order (Seal, 2006), but also have the same $\Delta^{33}S$ within the analytical uncertainties (at 2σ level; Jamieson et al., 2006). The analyzed sulfide pairs from the Fazenda Coqueiro prospect meet these requirements,

thus we attempted to calculate the temperatures for formation of these sulfides (after Jamieson et al., 2006; Sharman et al., 2015). Our calculations provided geological reasonable temperatures (ranging from 250° to 350°C) for the formation of VMS deposits (see Table 7.17). This temperature range is also in accordance to the trace elements content of pyrites (Figure 5.6), which yield elevated Co/Ni ratios and high concentrations of Se, and consistent with higher temperature conditions in VMS systems (Huston et al., 1995; Huston et al., 2011).

An opposite relationship is observed in the massive pyrite lens samples from the northern area of MNGB, despite the absence of isotopic constraints on sulfide pairs. The Co/Ni ratios and Se contents in these samples are much lower compared to the Fazenda Coqueiro sulfides, which together with the negative $\Delta^{33}S$ values are good indicative of colder temperatures for the pyrite precipitation, and in accordance with assimilation of sulfur from cold downwelling seawater.

5.5.2. Comparison to other Archean VMS deposits

The size, sources, and the efficiency of hydrothermal fluids to form VMS deposits have been subject of research for many modern and ancient VMS deposits (e.g., Huston et al., 2001, 2010, 2011; Golding et al., 2011; Jamieson et al., 2013; Sharman et al., 2015; Chen et al., 2015). In the case of the Archean VMS deposits, in the last few years, the adoption of multiple sulfur isotopes approach has clarified our understanding about their formation.

The recent findings of Jamieson et al., (2013), Sharman et al., (2015) and Chen et al., (2015) have demonstrated the important role of sulfur sources and the composition of hydrothermal fluids for the size and metal budget of a VMS, through the study of Neoarchean deposits in Canada and Australia. Modeling between the proportion of S derived from a magmatic/hydrothermal or seawater source, and the respective metal budget in the deposit suggest that those deposits with larger magmatic contributions had more efficiency to accumulate metals on seafloor. This is also a plausible explanation for the giant metal accumulations in Neoarchean VMS systems in Canada (e.g., Kidd Creek; Jamieson et al., 2013).

Accordingly, there is an important implication for the Mundo Novo Greenstone Belt VMS deposits, as our data suggest that a magmatic/hydrothermal source played a minor role for the formation of Zn-Cu-Pb mineralization at the Fazenda Coqueiro

prospect. Instead, a local sedimentary source for sulfur and metals should have acted as limiting factor for the size and metal accumulation in this prospect.

Besides, the quite distinct tectonic regime, differences in the volume of continental land mass, the large plume magmatism in the Neoarchean, and the restricted character of Paleoarchean basins may have been a first order control that severely influenced the large discrepancies on metals endowment between the mid and late Archean VMS deposits.

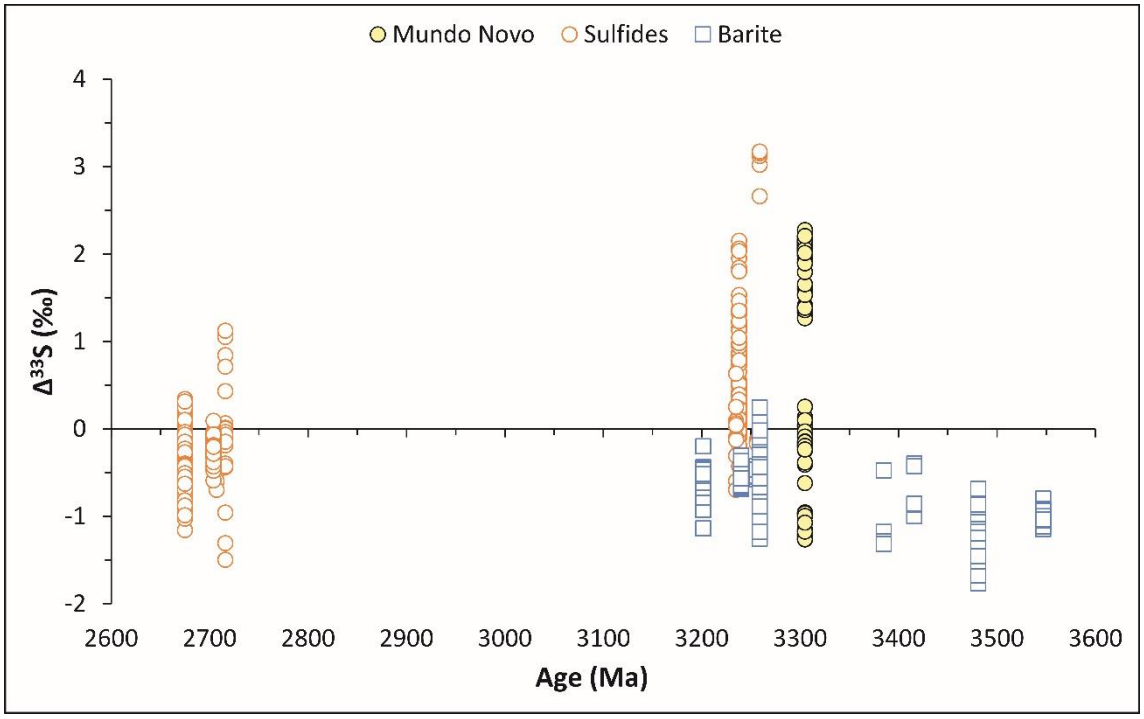

Figure 5.7. Summary of published $\Delta^{33}S$ data for sulfides from Archean VMS deposits, for the Paleoarchean barites, and the Mundo Novo Greenstone Belt VMS deposits. The respective symbols are illustrated in the chart. VMS data are from Bekker et al., (2009), Golding et al., (2011), Jamieson et al., (2013), Chen et al., (2015), Sharman et al., (2015), and Montinaro et al., (2015). Barite data are from Farquhar et al., (2000), Bao et al., (2007), Ueno et al., (2008), Shen et al., (2009), Golding et al., (2011), Roerdink et al., (2012), Montinaro et al., (2015), Muller et al., (2016), and Muller et al., (2017).

5.5.3. Implications for the Paleoarchean Seawater Sulfate Reservoir

The best estimate for the sulfur isotopic composition of Paleoarchean seawater comes from the 3.5 to 3.2 Ga barite deposits (see Figure 5.7 for references) that occur in Western Australia (Pilbara Craton, Warrawoona and Sulfur Springs Group), South Africa

(Kaapvaal Craton, Onverwacht and Fig Tree Group), and India (Dharwar Craton, Sargur Group). The multiple S isotopes data for massive pyrite lens, and pillow basalt from northern MNGB ($\Delta^{33}S$), suggests that seawater sulfate was a major sulfur source for pyrite in these samples, and the close relationship between our data and the compositional ranges of Paleoarchean barites in $\Delta^{33}S$- $\delta^{34}S$ (Figure 5.4a) and $\Delta^{36}S$-$\Delta^{33}S$ (Figure 5.4b) spaces are good indicatives for this observation. Besides that, the lighter values of pyrite $\delta^{34}S$ relative to barite suggest limited mass dependent fractionation processes between pyrite and the seawater sulfate reservoir (Roerdink et al., 2012), during the hydrothermal circulation of seawater on the seafloor. This may also be an indication that the northern portion of MNBG was a restricted basin with a limited SO_4^{2-} supply from a larger oceanic sulfate reservoir (Roerdink et al., 2012). Besides that, the absence of larger negative $\Delta^{33}S$ at Fazenda Coqueiro prospect indicates the predominance of anoxic and deeper water conditions in the southern portion of belt; whereas in the north, shallow waters and sulfate-bearing environments were dominant, in accordance to the stratified model for Paleoarchean oceans (Huston and Logan, 2004).

Further evidence for the existence of a globally linked oceanic sulfate reservoir (e.g., Huston and Logan, 2004; Roerdink et al., 2012) should come from the investigations of barite deposits (Itapura Mine) also found in the Mundo Novo Greenstone Belt. This occurrence has been associated to a hydrothermal-exhalative context (e.g. Mascarenhas et al., 1998; Neumann et al., 2002), similarly to Paleoarchean barite deposits elsewhere.

5.6. CONCLUSION

We investigated the multiple S isotopes and trace elements compositions of sulfides from VMS deposits of the Paleoarchean (3.3 Ga) Mundo Novo Greenstone Belt, in order to constrain the sulfur and metal sources, and also to investigate hydrothermal processes responsible for seafloor ore deposits formation in Archean times.

The $\delta^{34}S$, $\Delta^{33}S$, and $\Delta^{36}S$ compositions of pyrite in pillow basalt and massive pyrite lens of the northern MNGB reveal an important role of seawater sulfate as the main sulfur source in these rocks. Moreover, their compositional similarities to the Paleoarchean (3.5-3.2 Ga) barite deposits in Australia, South Africa and India support a common and globally homogeneous oceanic sulfate reservoir. Further investigations of the barite deposit in the MNGB may reinforces this interpretation.

The sulfide minerals from the VMS deposit at the Fazenda Coqueiro prospect, southern MNGB, have remarkably homogenous isotopic compositions, regardless of the

sulfur species, host rock and stratigraphic position of sample. These sulfides carry positive MIF-S ($\Delta^{33}S$) signatures, that indicate assimilation of elemental sulfur (S_8) during the formation of sulfides, which ultimately suggest a sedimentary source for this deposit. This may be a limiting factor for the size and economic potential of the deposit, because the majority of Archean VMS deposits show evidences for a major role of magmatic/hydrothermal fluids with subordinate seawater sulfate contributions (Figure 5.7). This is particularly evident in the giant Neoarchean VMS deposits of Canada, where it is hypothesized that magmatic sources are responsible for their large metal budgets.

5.7. ACKNOWLEDGEMENTS

G.S. Teles acknowledges CNPq for financial support (grants 163459/2013-4 and 202267/2014-8). Cid Bonfim is acknowledge for his assistance during field work, and the Companhia Baiana de Pesquisa Mineral (CBPM) is thanked for providing drill-cores samples. T.R. Ireland acknowledges the support of ARC DP140103393.

5.8. REFERENCES

Agangi, A., Hofmann, A., Eickmann, B., Marin-Carbonne, J., Reddy, S.M., 2016. An atmospheric source of S in Mesoarchaean structurally-controled gold mineralisation of the Barberton Greenstone Belt. Precambrian Research 285, 10-20.

Bao, H., Rumble III, D., Lowe, D.R., 2007. The five stable isotope compositions of Fig Tree barites: implications on sulfur cycle in ca. 3.2 Ga oceans. Geochimica et Cosmochimica Acta 71, 4868-4879.

Bekker, A., Barley, M.E., Fiorentini, M.L., Rouxel, O.J., Rumble, D., Beresford, S.W., 2009. Atmospheric sulfur in Archaean komatiite hosted nickel deposits. Science 326, 1086-1089.

Borges, V.S.M., Silva, M.G., Leal, A.B.M, Cunha, J.C., 2004. Litogeoquímica e Metalogênese das rochas da Fazenda Coqueiro, Greenstone Belt de Mundo Novo, Bahia. In: Anais do 42° Congresso Brasileiro de Geologia, Araxá, 3 pp.

Chen, M., Campbell, I.H., Xue, Y., Tian, W., Ireland, T.R., Holden, P., Cas, R.A.F., Hayman, P.C., Das, R., 2015. Multiple Sulfur Isotope Analyses Support a Magmatic Model for the Volcanogenic Massive Sulfide Deposits of the Teutonic Bore Volcanic Complex, Yilgarn Craton, Western Australia. Economic Geology 110, 1411-1423.

Cook, N.J., Ciobanu, C.L., Pring, A., Skinner, W., Shimizu, M., Danyushevsky, L., Saini-Eidukat, B., Melcher, F., 2009. Trace and minor elements in sphalerite: a LA-ICPMS study. Geochimica et Cosmochimica Acta 73, 4761-4791.

Crowe, D.E., and Vaughan, G., 1996. Characterization and use of isotopically homogeneous standards for in situ laser microprobe analysis of $^{34}S/^{32}S$ ratios. American Mineralogist 81, 187-193.

Farquhar, J., Bao, H., Thiemens, M., 2000. Atmospheric influence of Earth's earliest súlfur cycle. Science 289, 756-758.

Farquhar, J., Wu, N.P., Canfield, D.E., Oduro, H., 2010. Connections between sulfur cycle evolution, sulfur isotopes, sediments, and base metal sulfide deposits. Economic Geology 105, 509-533.

Farquhar, J., Wing, B.A., 2003. Multiple sulfur isotopes and the evolution of the atmosphere. Earth and Planetary Science Letters 213, 1-13.

Farquhar, J., Savarino, J., Airieau, S., Thiemens, M.H., 2001. Observation of wavelength-sensitive mass-independent sulfur isotope effects during SO_2 photolysis: Implications for the early atmosphere. Journal of Geophysical Research 106, 32829-32839.

George, L., Cook, N.J., Ciobanu, C.L., Wade, B.P., 2015. Trace and minor elements in galena: A reconnaissance LA-ICP-MS study. American Mineralogist 100, 548-569.

Golding, S.D., Duck, L.J., Young, E., Baublys, K.A., Glikson, M., Kamber, B.S., 2011. Earliest seafloor hydrothermal systems on Earth: comparisons with modern analogues. *In*: Golding, S.D., (eds.), Earliest life on Earth:habitats, environments and methods of detection: Dordrecht, Springer, p. 15-49.

Hannington, M.D., de Ronde, C.E.J., Peterson, S., 2005. Sea-floor tectonics and submarine hydrothermal systems. *In*: Hedenquist, J.W., Thompson, J.F.H., Goldfarb, R.J., Richards, J.P., (eds.), 100^{th} Anniversary Volume of Economic Geology, p.111-141.

Hannington, M.D., 2014. Volcanogenic Massive Sulfide Deposits. *In*: Holland, H., Turekian, K., (eds.), Treatise on Geochemistry 2nd Edition: Amsterdam, Elsevier, p. 463-488.

Huston, D. L., Sie, S. H., Suter, G. F., Cooke, D. R. and Both, R. A., 1995 Trace elements in sulfide minerals from eastern Australian volcanic-hosted massive sulfide deposits: Part I. Proton microprobe analyses of pyrite, chalcopyrite, and sphalerite, and Part II. Selenium levels in pyrite: comparison with $\delta^{34}S$ values and implications for the

source of sulfur in volcanogenic hydrothermal systems. Economic Geolology 90, 1167–1196.

Huston, D.L., Brauhart, C.W., Drieberg, S.L., Davidson, G.J., Groves, D.I., 2001. Metal leaching and inorganic sulfate reduction in volcanic-hosted massive sulfide mineral systems: Evidence from the paleo-Archean Panorama district, western Australia. Geology 29 (8), 687-690.

Huston, D.L., Logan, G.A., 2004. Barite, BIFs and bugs: evidence for the evolution of the Earth's early hydrosphere. Earth and Planetary Science Letters 220, 41-55.

Huston, D.L., Pehrsson, S., Eglington, B.M., Zaw, K., 2010. The geology and metallogeny of volcanic-hosted massive sulfide deposits: variations through geologic time and with tectonic setting. Economic Geology 105, 571-591.

Huston, D.L., Relvas, J.M.R.S., Gemmel, J.B., Drieberg, S., 2011. The role of granites in volcanic-hosted massive sulphide ore-forming systems: an assessment of magmatic-hydrothermal contributions. Mineralium Deposita 46, 473-507.

Ireland, T.R., Schram, N., Holden, P., Lanc, P., Ávila, J., Armstrong, R., Amelin, Y., Latimore, A., Corrigan, D., Clement, S., Foster, J.J., Compston, W., 2014. Charge-mode electrometer measurements of S-isotopic compositions on SHRIMP-SI. International Journal of Mass Spectrometry 359, 26-37, doi: 10.1016/j.ijms.2013.12.02.

Jamieson, J.W., Wing, B., Hannington, M.D., Farquhar, J., 2006. Evaluating isotopic equilibrium among sulfide mineral pairs in Archean Ore Deposits: case study from the Kidd Creek VMS Deposit, Ontario, Canada. Economic Geology 101, 1055-1061.

Jamieson, J.W., Wing, B.A., Farquhar, J., Hannington, M.D., 2013. Neoarchaean seawater sulphate concentrations from Sulphur isotopes in massive sulphide ore. Nature Geoscience 6, 61-64, doi: 10.1038/NGEO1647.

Kozdon, R., Kita, N.T., Huberty, J.M., Fournelle, J.H., Johnson, C.A., Valley, J.W., 2010. *In situ* sulfur isotope analysis of sulfide minerals by SIMS: Precision and accuracy, with application to thermometry of ~3.5 Ga Pilbara cherts. Chemical Geology 275, 342-253, doi: 10.1016/j.chemgeo.2010.05.015.

Longerich, H.P., Jackson, S.E., Günther, D., 1996. Laser Ablation Inductively Coupled Plasma Mass Spectrometric Transient Signal Data Acquisition and Analyte Concentration Calculation. Journal of Analytical Atomic Spectrometry 11, 899-904

Mascarenhas, J.F., Silva, E.F.A., 1994. *Greenstone Belt* de Mundo Novo: caracterização e implicações metalogenéticas e geotectônicas no Cráton do São Francisco. Companhia Baiana de Pesquisa Mineral, Salvador. Série Arquivos Abertos 5, 32 pp.

Mascarenhas, J.F., Ledru, P., Souza, S.L., Conceição Filho, V.M., Melo, L.F.A., Lorenzo, C.L., Milesi J.P., 1998. Geologia e recursos minerais do Grupo Jacobina e da parte sul do Greenstone Belt de Mundo Novo. Companhia Baiana de Pesquisa Mineral, Salvador. Série Arquivos Abertos 13, 58 pp.

Montinaro, A., Strauss, H., Mason, P.R.D., Roerdink, D., Münker, C., Schwarz-Schampera, U., Arndt, N.T., Farquhar, J., Beukes, N.J., Gutzmer, J., Peters, M., 2015. Paleoarchean sulfur cycling: Multiple sulfur isotope constraints from the Barberton Greenstone Belt, South Africa. Precambrian Research 267, 311-322.

Muller, É., Philippot, P., Rollion-Bard, C., Cartigny, P., 2016. Multiple sulfur-isotope signatures in Archean sulfates and their implications for the chemistry and dynamics of the early atmosphere. Proceedings of National Academy of Sciences 113 (27), 7432-7437.

Muller, É., Philippot, P., Rollion-Bard, C., Cartigny, P., Assayag, N., Marin-Carbonne, J., Mohan, M.R., Sarma, D.S., 2017. Primary sulfur isotope signatures preserved in high-grade Archean barite deposits of the Sargur Group, Dharwar Craton, India. Precambrian Research 295, 38-47.

Neumann, R., Menezes, R.O.G., Alcover Neto, A., 2002. Caracterização tecnológica da barita de Miguel Calmon, BA. In: Anais do XIX Encontro Nacional de Tratamento de Minérios e Metalurgia Extrativa, Recife, 686-693.

Norman, M., Robinson, P., Clarck, D., 2003. Major and Trace-Element Analysis of Sulfide Ores by Laser-Ablation ICP-MS, Solution ICP-MS, and XRF: New Data on International Reference Materials. The Canadian Mineralogist 41, 293-305.

Paton, C., Hellstrom, J., Paul, B., Woodhead, J., Hergt, J., 2011. Iolite: Freeware for the visualisation and processing of mass spectrometric data. Journal of Analytical Atomic Spectrometry 26, 2508-2518.

Peucat, J.J., Mascarenhas, J.F., Barbosa, J.S.F., Souza, S.L., Marinho, M.M., Fanning, C.M., Leite, C.M.M., 2002. 3.3 Ga SHRIMP U–Pb zircon age of a felsic metavolcanic rock from the Mundo Novo greenstone belt in the São Francisco Craton, Bahia (NE Brazil). Journal of South American Earth Sciences 15, 363-373.

Pavlov, A.A., Kasting, J.F., 2002. Mass-Independent Fractionation of Sulfur Isotopes in Archean Sediments: Strong Evidence for an Anoxic Archean Atmosphere. Astrobiology 2 (1), 27-41.

Roerdink, D.L., Mason, P.R.D., Farquhar, J., Reimer, T., 2012. Multiple sulfur isotopes in Paleoarchean barites indentify an important role for microbial sulfate reduction in the early marine environment. Earth and Planetary Science Letters 331-332, 177-186.

Seal, R.R., 2006. Sulfur isotope geochemistry of sulfide minerals. Reviews in Mineralogy and Geochemistry 61, 633-677.

Sharman, E.R., Taylor, B.E., Minarik, W.G., Dubé, B., Wing, B.A., 2015. Sulfur and trace element data from ore sulphides in the Noranda district (Abitibi, Canada): implications for volcanogenic massive sulfide deposit genesis. Mineralium Deposita 50, 591-606.

Shen, Y., Farquhar, J., Masterson, A., Kaufman, A. J., Buick, R., 2009. Evaluating the role of microbial sulfate reduction in the early Archean using quadruple isotope systematics. Earth and Planetary Science Letters 279, 383-391.

Souza, S.L. et al., 2002, Projeto Greenstone Belt de Mundo Novo: escala 1:100.000, Salvador, CBPM.

Teles, G., Chemale Jr., F., Oliveira, C.G., 2015, Paleoarchean record of the detrital pyrite-bearing, Jacobina Au–U deposits, Bahia, Brazil. Precambrian Research 258, 289-313, doi: 10.1016/j.precamres.2014.11.004.

Ueno, Y., Ono, S., Rumble, D., Maruyama, S., 2008. Quadruple sulfur isotope analysis of ca. 3.5Ga Dresser Formation: New evidence for microbial sulfate reduction in the early Archean. Geochimica et Cosmochimica Acta 72, 5675-5691.

Wohlgemuth-Ueberwasser, C.C., Viljoen, F., Petersen, S., Vorster, C., 2015. Distribution and solubility limits of trace elements in hydrothermal black smoker sulfides: An in-situ LA-ICP-MS study. Geochimica et Cosmochimica Acta 159, 16-41.

Williford, K.H., Van Kranendonk, M.J., Ushikubo, T., Kozdon, R., Valley, J.W., 2011, Constraining atmospheric oxygen and seawater sulfate concentrations during Paleoproterozoic glaciation. In situ sulfur three-isotope microanalysis of pyrite fom the Turee Creek Group, Western Australia. Geochimica et Cosmochimica Acta 75, 5686-5707, doi: 10.1016/j.gca.2011.07.010.

Wilson, S.A., Ridley, W.I., Koenig, A.E., 2002. Development of sulphide calibration standards for the laser ablation inductively-coupled plasma mass spectrometry technique. Journal of Analytical Atomic Spectrometry 17, 406-409.

Whitehouse, M.J., Kamber, B.S., Fedo, C.M., Lepland, A., 2005. Integrated Pb- and S-isotope investigation of sulphide minerals from the early Archaean of southwest Greenland 222, 112-131, doi: 10.1016/j.chemgeo.2005.06.004.

Whitehouse, M.J., 2013, Multiple Sulfur Isotope Determination by SIMS: Evaluation of Reference Sulfides for $\Delta^{33}S$ with Observations and Case Study on the Detemination of $\Delta^{36}S$. Geostandards and Geoanalytical Research 37, 19-33, doi: 10.1111/j.1751-908X.2012.00188.x.

Xue, Y., Campbell, I., Ireland, T.R., Holden, P., Armstrong, R., 2013. No mass-independent sulfur isotope fractionation in auriferous fluids supports a magmatic origin for Archean gold deposits. Geology 41 (7), 791-794.

Zincone, S.A., Oliveira, E.P., Laurent, O., Zhang, H., Zhai, M., 2016. 3.30 Ga high-silica intraplate volcanic-plutonic system of the Gavião Block, São Francisco Craton, Brazil: Evidence of an intracontinental rift following the creation of insulating continental crust. Lithos 266-267, 414-434, doi: 10.1016/j.lithos.2016.10.011.

Zincone, S.A., Barbuena, D., Oliveira, E.P., Baldim, M.R., 2017. Detrital zircon U-Pb ages as evidence for deposition of the Saúde Complex in a Paleoproterozoic foreland basin, northern São Fancisco Craton, Brazil. Journal of South American Earth Sciences, doi: 0.1016/j.jsames.2017.09.009.

CAPÍTULO 6

6.1. CONSIDERAÇÕES FINAIS

As sequências supracrustais do Bloco Gavião, Cráton do São Francisco, especificamente o *Greenstone Belt* Mundo Novo e a Bacia de Jacobina hospedam depósitos do tipo VMS e auríferos, respectivamente, que possibilitam o acesso às condições ambientais vigentes ao final do Paleoarqueano (~3.3 Ga); bem como aos processos associados à formação de depósitos minerais nesse período. Neste estudo, ambos os aspectos foram investigados a partir de análises isotópicas do enxofre e elementos traço em sulfetos. Os dados obtidos permitiram as seguintes observações:

i) Nos conglomerados da Formação Serra do Córrego, Bacia de Jacobina, foram descritos três tipos de pirita detrítica: (1) com inclusões, (2) maciça, e (3) inclusa em seixo de quartzo. O primeiro tipo possui origem sedimentar, e ocorre nos depósitos auríferos de Witwatersrand. Pirita detrítica também ocorre em amostras da seção marinha da bacia, a qual deve ter sido retrabalhado dos ambientes continentais. Pirita singenética (formada em contato com a coluna d'água) e diagenética (formada nos poros dos sedimentos) são comuns, respectivamente para as amostras de metapelito e quartzito da seção marinha.

ii) Os dados isotópicos de S revelam a ausência de fracionamento anômalo (MIF-S) para a maioria das piritas detríticas analisadas nos conglomerados de Jacobina. Entretanto, parte dos dados apresenta anomalias positivas ($\Delta^{33}S>0$). O mesmo comportamento não é obsevado nas amostras marinhas, as quais apresentam anomalias proeminentes, positivas ($\Delta^{33}S$ até 2.5‰) em pirita diagenética em amostra de quartizito, e negativas ($\Delta^{33}S$ até -1.2‰) em pirita singenética em metapelito. Essas discrepâncias sugerem diferentes mecanismos para preservação dessas anomalias nos ambientes terrestres e marinhos.

iii) Apesar da evidência de oxidação no Cráton do São Francisco em 3.3 Ga (Item 7.3), os dados isotópicos obtidos se assemelham à relação que caracteriza o Éon Arqueano ($\Delta^{36}S/\Delta^{33}S\sim1$), a qual representa o sinal atmosférico associado

ao fracionamento anômalo (MIF-S), considerado o melhor indicativo de uma atmosfera deficiente em oxigênio (Capítulo 2).

iv) A pirita detrítica com inclusões possui, em comparação aos outros tipos de pirita estudados, as maiores concentrações de ouro, além de ser enriquecida na maioria dos elementos traço analisados. Essa informação, associada a outros fatores observáveis na Bacia de Jacobina (Capítulo 4), sugerem que acumulação inicial de ouro na bacia tenha sido singenética, de forma semelhante ao modelo recentemente proposto para Witwatersrand (Capítulo 2).

v) Dados dos múltiplos isótopos de enxofre revelam fontes distintas associadas à formação das mineralizações VMS, entre as porções norte e sul (Fazenda Coqueiro) do *Greenstone Belt* Mundo Novo. No segmento norte, os sulfetos associados à amostra de xisto carbonoso apresentam $\Delta^{33}S = 1.4‰$, compatível com uma origem sedimentar, pela assimilação de S_8; a amostra de *BIF* possui composição isotópica que sugere origem mantélica ($\Delta^{33}S = 0‰$); o *pillow*-basalto possui pirita com S de origem mantélica, mas também de origem atmosférica, derivada do SO_4^{2-} ($\Delta^{33}S < 0‰$); a lente de pirita maciça amostrada apresenta somente $\Delta^{33}S < 0‰$, o que evidencia a assimilação de sulfato oceânico nas células hidrotermais. Na porção sul do *greenstone* (Fazenda Coqueiro), as composições isotópicas do enxofre são semelhantes para a maioria das amostras, independentemente do tipo de rocha, do sulfeto analisado, ou da posição estratigráfica relativa da amostra no depósito (*footwall*, *stringer*, sulfeto maciço e *hangingwall*). Essas amostras apresentam MIF-S, com valores do $\Delta^{33}S$ até 2.1‰, indicativos de enxofre elementar como principal fonte dos sulfetos, provavelmente derivado da água conata presente em uma fonte sedimentar. A única exceção corresponde a uma amostra no *footwall* do depósito (quartzo-mica xisto) em que a assinatura do enxofre sugere fonte mantélica, mas com possível mistura com um componente de sulfato oceânico.

vi) Os elementos traço analisados nos sulfetos dos VMS de Mundo Novo variam de acordo com o tipo de sulfeto analisado, bem como em função da posição da amostra nos depósitos. De maneira geral, pirita e pirrotita são empobrecidas na maioria dos elementos, mas apresentam enriquecimento em Co, As e Se, e

Ni, As e Se, respectivamente; calcopirita é enriquecida em Ni, Se, Ag e In; a arsenopirita é empobrecida na maioria dos elementos, com exceção de Co, Ni, Se e Sb; enquanto que esfalerita e galena são os sulfetos que possuem enriquecimento da maior quantidade de elementos traço, sendo a galena rica em Se, Ag, Cd, Sb, Te, Tl e Bi, e a esfalerita rica em Mn, Se, Cd, In, e Hg.

vii) A composição isotópica dos sulfetos maciços e da porção norte do *Greenstone Belt* Mundo Novo se assemelha com aquela das baritas de depósitos paleoarqueanos, o que pode indicar um reservatório global homogêneo de sulfato oceânico. Em relação ao depósito da Fazenda Coqueiro, este se diferencia da maioria dos depósitos VMS arqueanos, cuja composição isotópica sugere maior proporção de S derivado do manto ($\Delta^{33}S = 0‰$) e subordinadamente de sulfato marinho ($\Delta^{33}S < 0‰$); o que seria um fator fundamental para a formação de depósitos gigantes no Neoarqueano.

Por fim, algumas questões levantadas nesta tese carecem de maior esclarecimento, e podem ser objeto de estudos futuros:

a) Seriam a produção de O_2 em 3.3 Ga no Cráton do São Francisco, e consequentemente, a acumulação singenética do ouro em Jacobina mediadas por micro-organismos? Até o momento, existem poucos relatos de matéria-orgânica associada aos conglomerados auríferos de Jacobina. Em Witwatersrand, os conglomerados com os maiores teores de ouro possuem forte associação com matéria-orgânica, cujos organismos precursores seriam fotossintetizantes (Capítulo 2). Essa diferença poderia explicar a discrepância entre o volume de Au acumulado em Witwatersrand e em Jacobina, ou mesmo refletir condições ambientais menos favoráveis para proliferação/preservação de micro-organismos no Paleoarqueano.
b) As assinaturas isotópicas do S refletem a existência de sulfato oceânico na bacia Mundo Novo, exemplificado pelos valores negativos do $\Delta^{33}S$ na lente de pirita maciça e nas *pillow-lavas* no norte do *greentone*. Esses valores são similares às assinaturas observadas nos depósitos de barita paleoarqueanos na África do Sul, Austrália, e Índia. No *Greenstone Belt* Mundo Novo existe um depósito de barita (Mina de Itapura), cujo contexto geológico sugere formação em sistema hidrotermal oceânico (Rúbio, comunicação pessoal), com possíveis similaridades aos outros depósitos paleoarqueanos ao redor do

globo. É importante, portanto, avaliar a composição dos múltiplos isótopos de enxofre da barita de Mundo Novo, a qual pode confirmar a origem atmosférica do enxofre, bem como a existência de um reservatório homogêneo de sulfato fotolítico nos oceanos do Paleoarqueano.

A Figura 6.1 apresenta a variação do $\Delta^{33}S$ ao longo do tempo geológico, com incremento dos dados *in-situ* (SHRIMP-SI) obtidos ao longo deste estudo para a Bacia de Jacobina e *Greenstone Belt* Mundo Novo.

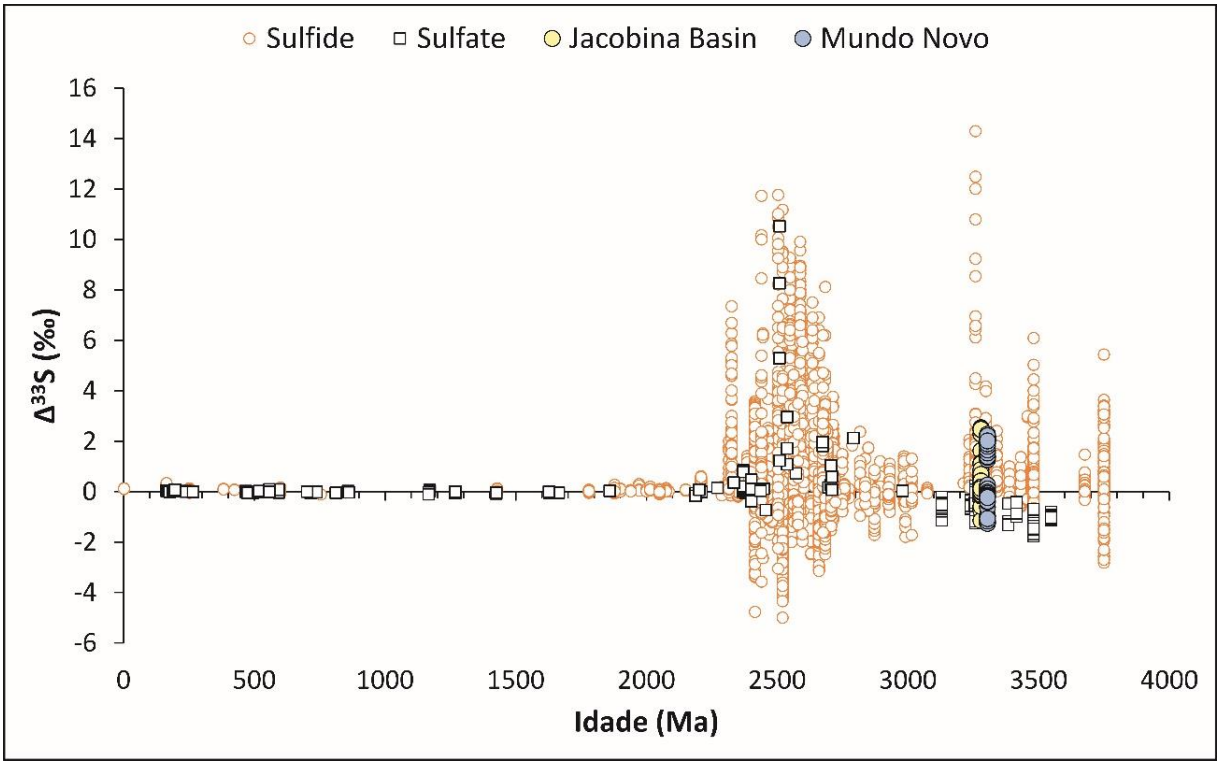

Figura 6.1. Registro do $\Delta^{33}S$ de sulfetos e sulfatos ao longo do tempo geológico (extraído de http://www.cet.edu.au/research-projects/special-projects/gssid-global-sedimentary-sulfurisotope-database), além dos dados obtidos para a Bacia de Jacobina e *Greenstone Belt* Mundo Novo.

CAPÍTULO 7

APÊNDICES

7.1. MATERIAL SUPLEMENTAR DO CAPÍTULO 4

7.1.1. Geotectonic Setting

The current configuration of the NE portion of São Francisco Craton basement (Figure 7.1) was established during the Transamazonian-Eburnean Cycle (2.1 – 1.9 Ga; Ledru et al., 1997; Barbosa and Sabaté, 2004). During this tectonic event, the four major crustal segments of craton (Gavião, Jequié, Serrinha and Itabuna-Salvador-Curaçá) were juxtaposed, generating a large mountain belt in the region (Barbosa and Sabaté, 2004). The Jacobina-Contendas-Mirante Lineament (Figure 7.1) is an important expression of this orogeny, and represents the suture zone formed by the collision between the Gavião, Jequié, and Itabuna-Salvador-Curaçá blocks (Cruz et al., 2016). Because of the proximity and apparent relationship between the Jacobina Basin and the lineament, some authors (eg. Mougeot, 1996; Ledru et al., 1997; Milesi et al., 2002) suggested that Jacobina is a foreland basin formed due to the collapse of the Transamazonian-Eburnean orogen. However, some authors (Mascarenhas et al., 1992; Pearson et al., 2005; Teles et al., 2015) suggest that Jacobina is a rift basin, based on it sedimentological-stratigraphic pattern, as well as the detrital zircon U-Pb age spectra of sediments, which lack the age peaks related to Transamazonian-Eburnean Cycle (2.1 to 1.9 Ga).

7.1.2. The Jacobina Basin units

The Jacobina Basin is exposed in a range of NNE-SSW trending hills in an area more than 200 km long by 8–10 km wide. Its basement consists of Paleoarchean rocks of the Gavião Block (3.6 to 3.3 Ga), as TTG (tonalite-trondhjemite-granodiorite) suites, and supracrustal rock associations such as the 3.3 Ga Mundo Novo Greenstone Belt (Peucat et al., 2002).

The siliciclastic rocks of basin are metamorphosed to lower greenschist facies and preserve primary features such as bedding and sedimentary structures. The Jacobina Basin is divided into three units, the Serra do Córrego, Rio do Ouro, and Serra da

Paciência formations (Figure 7.2); which show an overall finning-upward pattern (Figure 4.1), indicative of deposition in a rift setting; and comprise an estimated thickness of 7 km (Mascarenhas et al., 1992; Pearson et al., 2005; Teles et al., 2015).

The Serra do Córrego Fm., the basal unit of Jacobina Basin (Figures 4.1 and 7.2), is exposed along the western edge of basin, with thicknesses ranging between 500 and 1000 m (Pearson et al., 2005). This unit consists of two levels of conglomerate members, which host the main Au-(U) and pyrite mineralization. A thick sequence of quartzites separates these two conglomeratic levels. The conglomerates may vary in terms of their clast rounding, packing, textural maturity, gold concentration, presence of sulfides, and the degree of late oxidation (Pearson et al., 2005; Teles et al., 2015). However, they are essentially oligomictic, with quartz and less common chert pebbles embedded in a quartz and generally fuchsite-rich sandy matrix, where pyrite and gold are found.

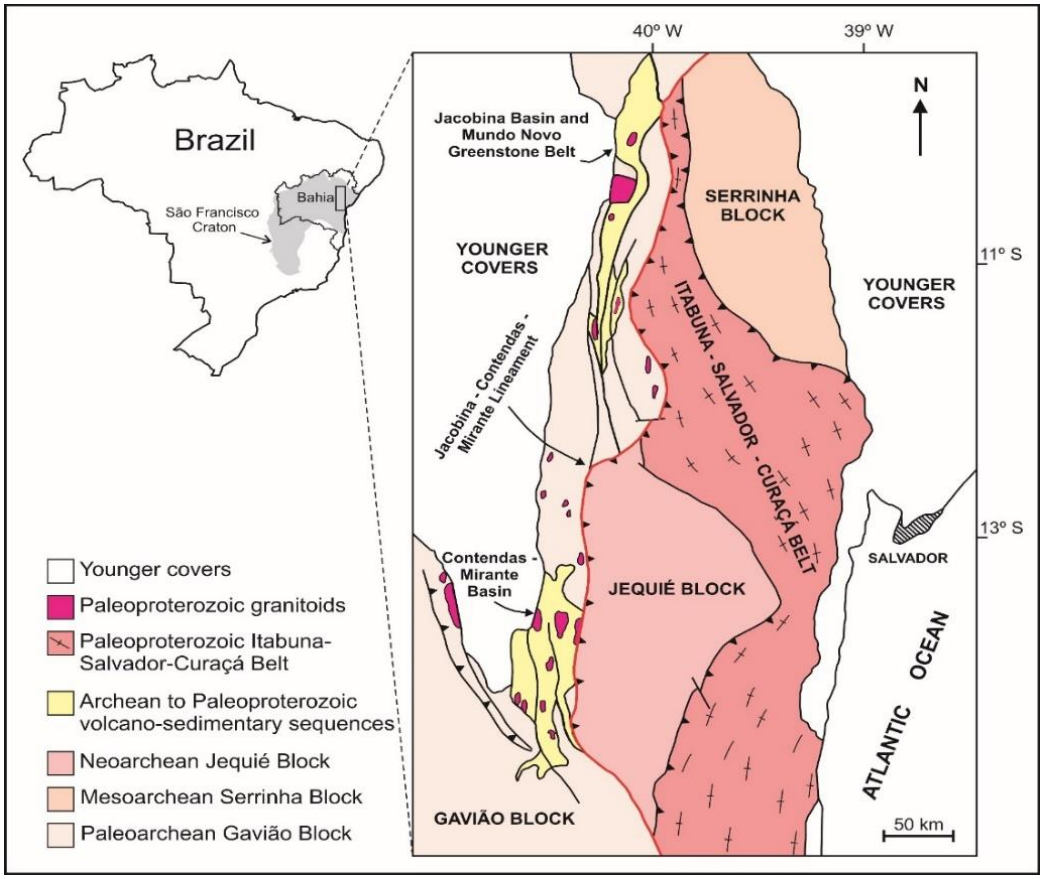

Figure 7.1. Geotectonic setting of the NE portion of São Francisco Craton in Bahia State, Brazil. The Jacobina Basin is located at the eastern margin of the Paleoarchean Gavião Block.

Quartzites of the Serra do Córrego Fm. can be white, greenish, or reddish, depending on the amount of fuchsite or the degree of oxidation, but they commonly resemble the composition of conglomerate matrix, except for the gold grades and presence of pyrite. The deposition of this unit is associated with an alluvial system, in which alluvial fans graded into intertwined fluvial channels (Hendrickson, 1984; Mascarenhas et al., 1992; Pearson et al., 2005; Teles et al., 2015).

The Rio do Ouro Fm. crops out in the central part of the Jacobina ridge (Figure 7.2), and is dominated by high-purity, fine-to-medium grained quartzites. Discontinuous conglomerate beds are present along the base of unit (Figure 4.1, Chapter 4), marking the gradational contact with the Serra do Córrego Fm. (Pearson et al., 2005). It also contains lenses of carbonaceous metapelites (Mascarenhas et al., 1992). Its deposition occurred by an extensive transgression in the Jacobina Basin, representing the transition from a continental sedimentation to a shallow-marine system dominated by tidal processes (Mascarenhas et al., 1992).

The Serra da Paciência Fm. is exposed along the eastern margin of the Jacobina ridge (Figure 7.2) and may represent deeper portions of the tidal-dominated platform (Figure 4.1, Chapter 4; Mascarenhas et al., 1992). It consists of packages of fine-to-coarse grained quartzites, conglomeratic quartzites, and subordinated conglomerate lenses that can be interpreted as distal pulses of the fluvial channels from the Serra do Córrego Fm. (Figure 7.2). Deeper-water facies, likely deposited below the influence of storm-waves, are represented by quartzite beds interbedded with andalusite and graphite-bearing schists (metapelites).

Intrusive dikes and sills of metamorphosed and hydrothermally altered mafic-ultramafic rocks represent an important magmatic event of unknown age in the Jacobina ridge region. The ultramafic rocks are N-S oriented (Figure 4.1, Chapter 4) and are classified as metaperidotite and metapyroxenites with komatiitic affinity (Teixeira et al., 2001; Santos, 2011). The mafic rocks represent more evolved melts (metagabbro and metadiorites) that fill an *en echelon* system with E-W orientation (Figure 7.2). Both mafic and ultramafic intrusive rocks commonly assimilate the country metasediments.

Figure 7.2. Geologic map of Jacobina Basin. The black stars indicate the location of sampled outcrops and drill-cores. The latter coincide to the gold mines site.

7.1.3. Samples

Our samples encompass the continental and marine intervals of Jacobina Basin, the Serra do Córrego and Serra da Paciência formations, respectively.

The Serra do Córrego samples were collected from outcrops and drill cores, where quartz-pebble conglomerates that host the Au-(U) and pyrite mineralization are mined. The three-sampled drill-cores cross-cut the lower and upper conglomerate levels of formation (Figure 4.1, Chapter 4; and Figure 7.2). Samples previously studied by Teles et al., (2015) were also used. Examples of detrital pyrite found in these samples are illustrated in Figure 7.3.

Samples of Serra da Paciência Fm. were collected at four different localities (Figure 7.2), representing conglomerate, metapelite and quartzite outcrops that correspond to the upper portion of Jacobina Basin (Figure 4.1, Chapter 4). One pyrite-rich conglomerate sample (FCJ-3), similar to the conglomerate samples from Serra do Córrego Fm., has massive detrital pyrites in a heavy-mineral lag (Figure 7.3A). Pyrite grains from deeper-water facies, as quartzite (SP-01) intercalated with andalusite-schists (PD-14) are shown in Figure 7.4.

The sample SP-01 revealed pyrite grains with inclusion-bearing cores, as well as rounded massive grains that are similar to those of Serra do Córrego samples (Figure 7.4), which are likely of detrital origin. Some of these grains have overgrowths that carry strong positive MIF-S anomalies (see Table 7.3). Considerable MIF-S signals were also detected in euhedral grains, which together with the overgrown pyrites are interpreted as diagenetic.

Pyrite grains from sample PD-14 are small, anhedral to subeuhedral (Figure 7.4), and carry only negative $\Delta^{33}S$ (see Table 7.3). These grains are likely syngenetic, formed in contact with the water column.

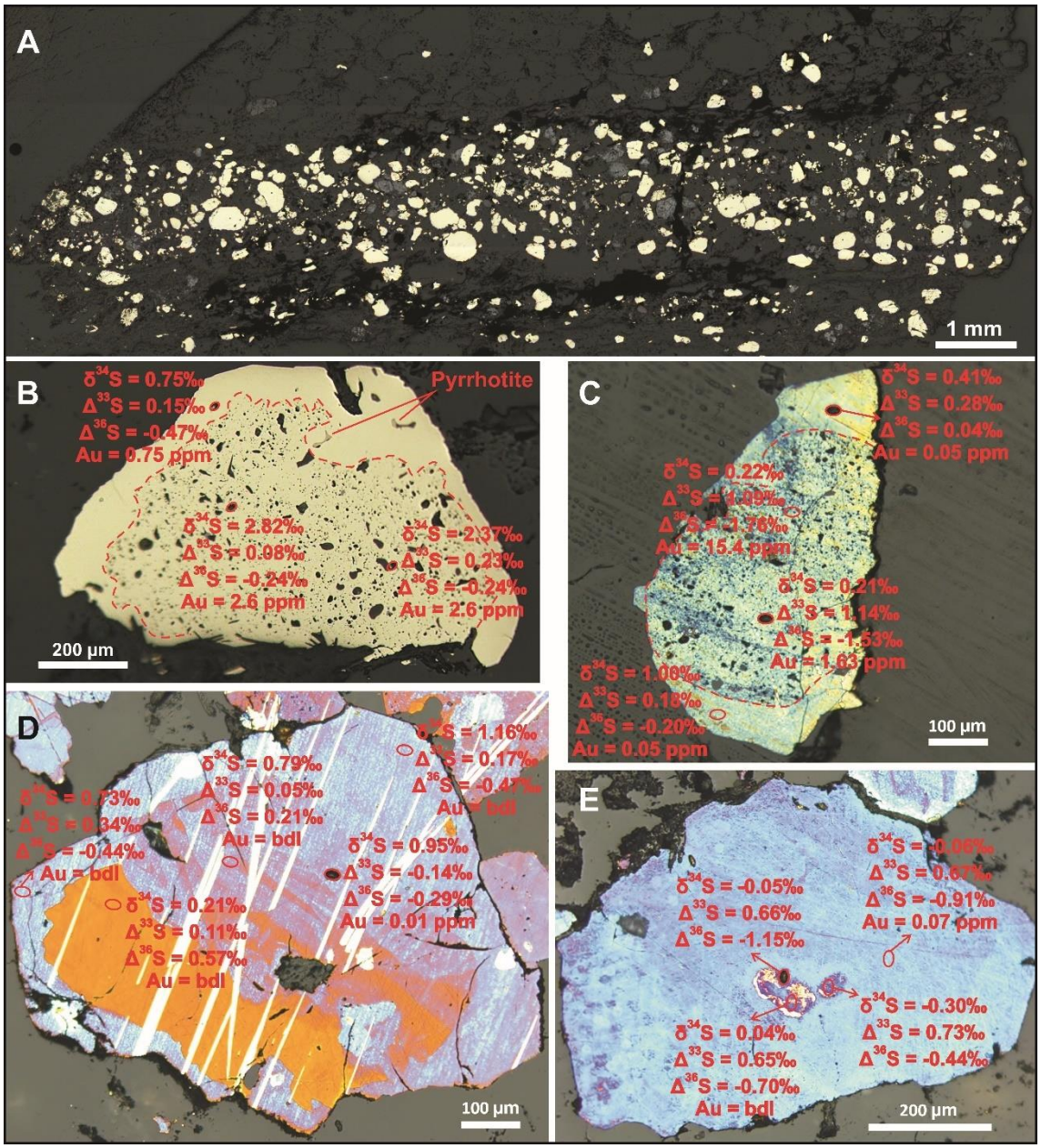

Figure 7.3. (A) Heavy minerals lag at the base of the conglomerate sample from Serra da Paciência Fm. (FCJ-3). Detrital pyrite is associated with chromite and zircon grains; (B to E) Examples of inclusion-bearing (B and C) and massive (D and E) detrital pyrites from samples of Serra do Córrego Fm. SHRIMP-SI spots and multiple sulfur isotopic compositions, and respective gold content are indicated in each grain. Grains shown in C to E were etched with NaOCl.

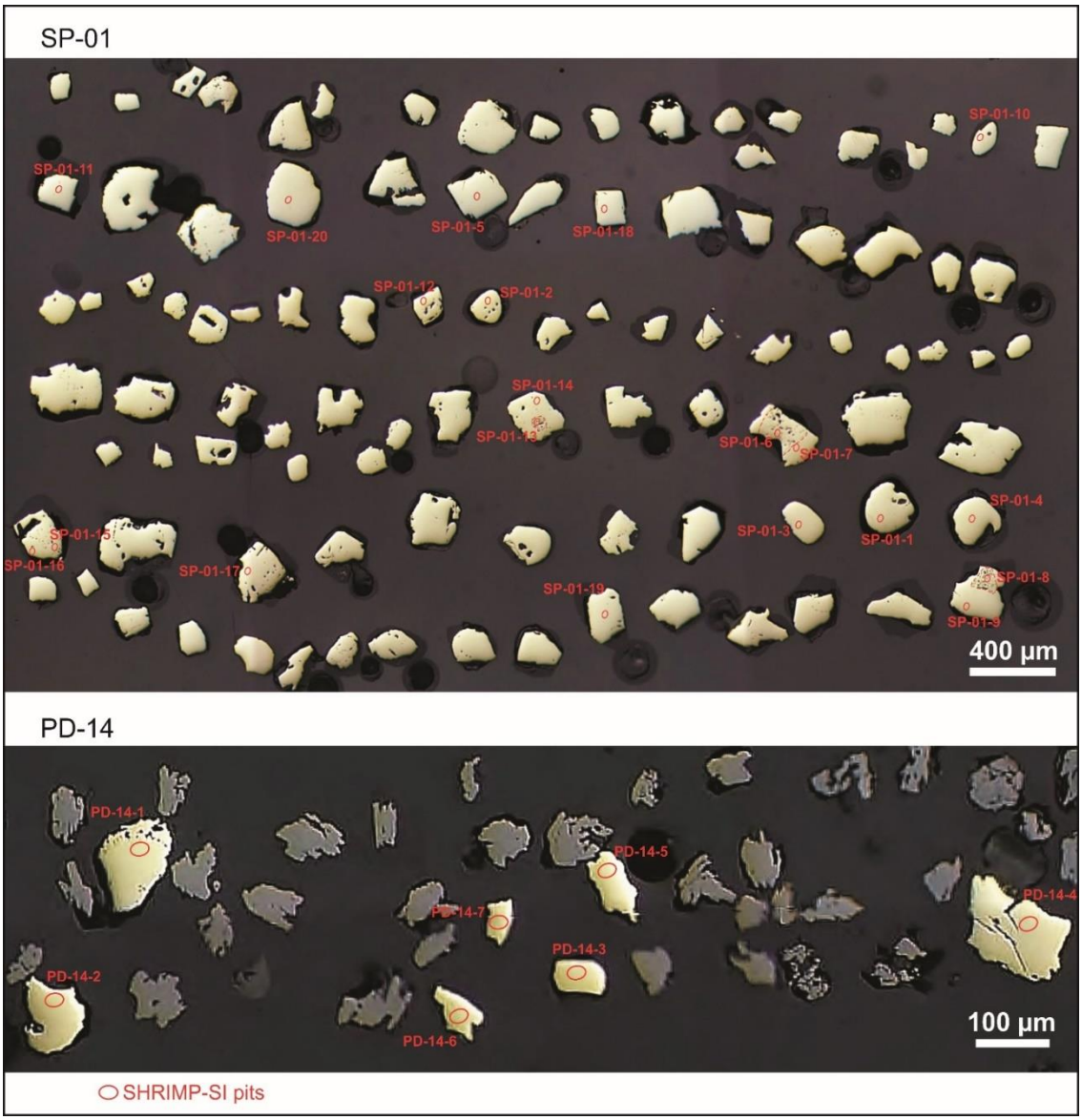

Figure 7.4. Pyrite grains from samples SP-01 and PD-14. Note that sample SP-01 has grains with inclusion-bearing cores (dashed red lines) and rounded massive grains, both similar to those pyrites found in Serra do Córrego Fm. SHRIMP-SI spots are indicated, and correspondent isotopic compositions are displayed in a spreadsheet accompanying this supplementary material.

7.1.4. Methodology - SHRIMP-SI Multiple Sulfur Isotope Analyses

After detailed observations under the optical microscope and Scanning Electron Microscope (SEM), appropriate samples were chosen for multiple sulfur isotope analyses. Pyrite grains from samples PD-09, PD-14, and SP-01 were handpicked after using of heavy liquids, and then were casted in 25 mm epoxy mounts together with Ruttan and Balmat pyrite grains. The same procedure was done for the selected Serra do Córrego and

FCJ-3 (Serra da Paciência) samples, however, rock pieces were used because these samples have greater amount of pyrite.

After drying of epoxy resin, the mounts were trimmed to a thickness of 6mm and polished, with initial stages conducted by hand sanding to remove coarse surface and expose the grains. The subsequent steps were done by automated diamond pasting polishing pads, during 10 minutes on 3µm, and 5 minutes on 1µm. After, photographic mosaics of mounts were produced under a reflected light microscope to easily identify the grains of interest during the SHRIMP-SI analysis. Finally, the mounts were cleaned and coated with 50 nm of gold to ensure surface conductivity.

The SHRIMP-SI 4-sulfur isotope measurements were performed in two sessions (March and July - 2015). A Cs^+ primary beam with a total primary ion impact energy of 15 keV was focused to sputter an area of ~ 25 µm in diameter. Negative secondary ions were accelerated to real ground from the −10kV sample potential and focused by the quadrupole triplet lenses before passing through the source slit and entering the secondary mass analyzer. The low mass, auxiliary, axial, and high mass heads detectors equipped with Faraday cups were used for simultaneously detection of $^{32}S^-$, $^{33}S^-$, $^{34}S^-$, and $^{36}S^-$, respectively. The collector slit widths were set at 400 µm for $^{32}S^-$, 150 µm for $^{33}S^-$, 200 µm for $^{34}S^-$ and 300 µm for $^{36}S^-$, which well resolved potential interferences of sulfur hydrides on mass 33 and 34.

$^{32}S^-$ signals were collected on 10^{11} Ω resistor (50V range), $^{33}S^-$ and $^{34}S^-$ on 10^{11} Ω resistor (5V range) and the $^{36}S^-$ signals by charge mode on a 22 pF capacitor (Ireland et al., 2014). Count rates on $^{32}S^-$ were ~ 1360 MHz, ~ 10 MHz on $^{33}S^-$, ~ 60 MHz on $^{34}S^-$, and ~ 0.2 MHz on $^{36}S^-$. Each analysis took about 15 min and consisted of 300 s of pre-sputtering, ~ 100 s of automated steering of secondary ions, ~ 5 s of automated centering of the secondary ions in the collector slits with magnet control, and 400 s of data collection, which consisted of 2 set of 10 measurements, 20 s each. Background was monitored during 300 s of pre-sputtering of each individual spot measured.

Each analytical session was started with three spots on Ruttan pyrite and two on Balmat pyrite. For the following analyses, two spots on Ruttan and one on Balmat were performed after every ten unknowns to correct instrumental mass-dependent fractionation. Ruttan pyrite have published values for $\delta^{34}S$ of 1.2 $\pm$ 0.1‰ (2σ; Crowe and Vaughan, 1996) and assumed $\Delta^{33}S = 0$ and $\Delta^{36}S = 0$ (Williford et al., 2011; Withehouse, 2013). Balmat pyrite has $\delta^{34}S$ composition of 15.1 ± 0.2‰ (2σ; and Vaughan, 1996) and $\Delta^{33}S = 0$ and $\Delta^{36}S = 0$ (Williford et al., 2011; Withehouse, 2013). Ruttan pyrite was used

as primary standard for calculation of isotopic ratios and as a monitor of instrumental stability, because it has been demonstrated that Balmat pyrite is not very homogeneous (Figure 7.5).

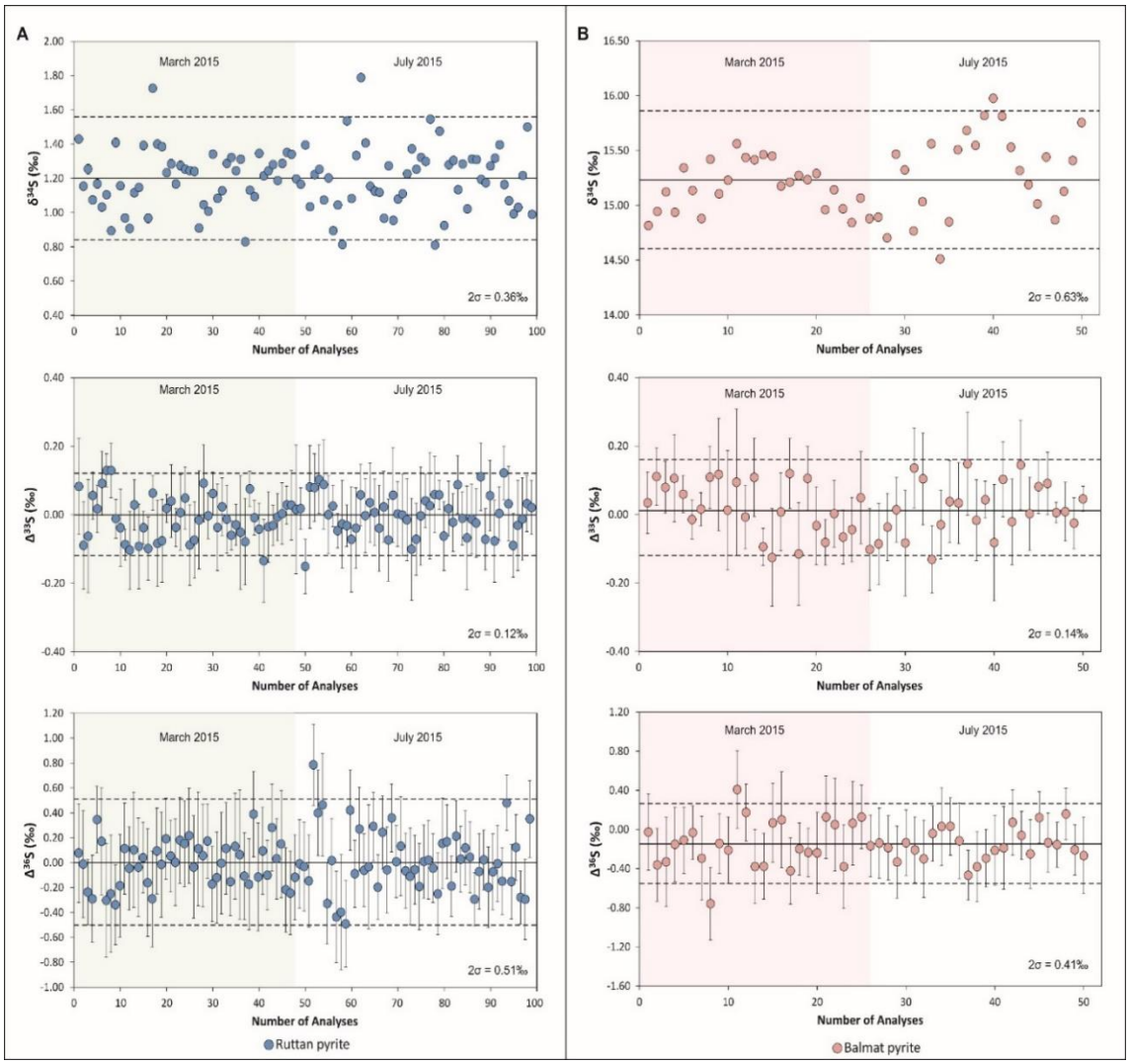

Figure 7.5. $\delta^{34}S$, $\Delta^{33}S$ and $\Delta^{36}S$ compositions of pyrite standards used in this study. (A) Ruttan pyrite spots; (B) Balmat pyrite spots. The black solid line is the weighted mean of the analyses and the dotted black line is the 2σ standard deviation of the mean.

Isotopic compositions are represented by standard delta notation with respect to V-CDT (*Vienna Canyon Diablo Troilite*) scale:

$$\delta^{3x}S = \left[\frac{\left({}^{3x}S/{}^{32}S\right)_{sample} - \left({}^{3x}S/{}^{32}S\right)_{standard}}{\left({}^{3x}S/{}^{32}S\right)_{standard}}\right] \times 1000,$$

where x represents the ^{33}S, ^{34}S, and ^{36}S isotopes. The anomalous mass-independent fractionation of ^{33}S and ^{36}S isotopes (MIF-S) are represented as:

$$\Delta^{33}S = \delta^{33}S - 1000 \times \left[\left(1 + \frac{\delta^{34}S}{1000}\right)^{0.515} - 1\right]$$

$$\Delta^{36}S = \delta^{36}S - 1000 \times \left[\left(1 + \frac{\delta^{34}S}{1000}\right)^{1.91} - 1\right]$$

The average external reproducibility of analyses, as estimated from replicate measurements of the standards was generally better than 0.36‰, 0.12‰, and 0.51‰ (2SD) for $\delta^{34}S$, $\Delta^{33}S$, and $\Delta^{36}S$, respectively. Average uncertainties (2σ) on the $\delta^{34}S$, $\Delta^{33}S$, and $\Delta^{36}S$ values of unknown samples were 0.02‰, 0.10‰, and 0.35‰, respectively.

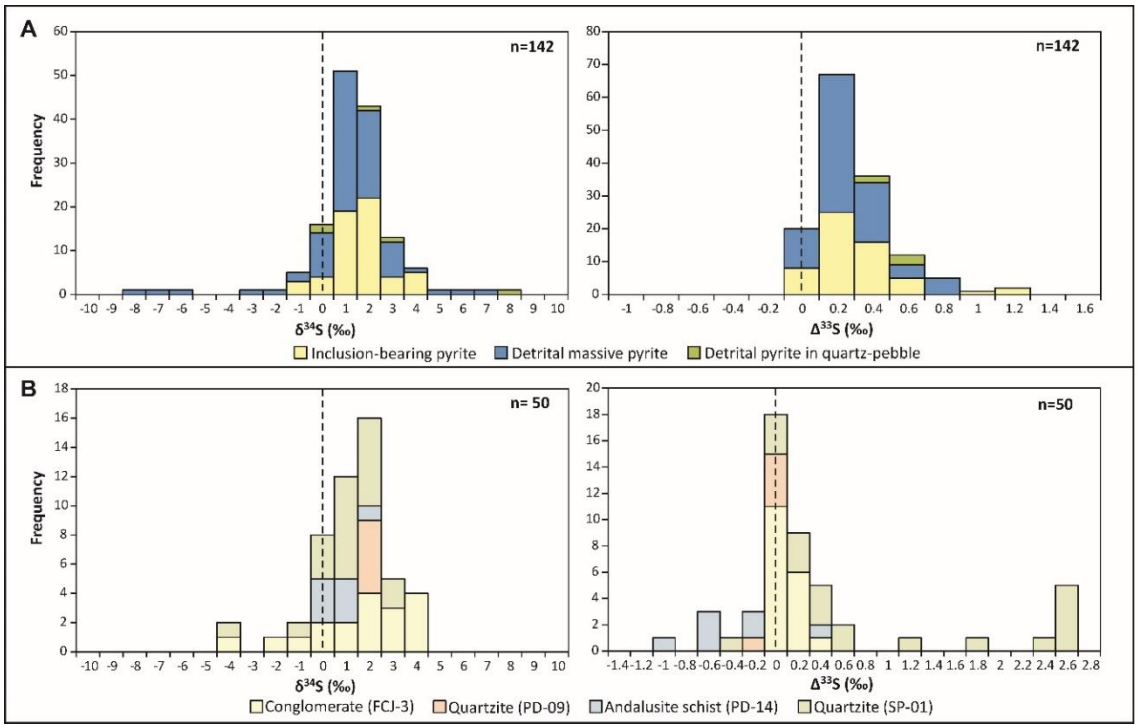

Figure 7.6. Distribution of $\delta^{34}S$ and $\Delta^{33}S$ values of pyrites analyzed in this study; (A) Serra do Córrego Fm. detrital pyrites histograms (B) Histograms for the Serra da Paciência Fm. data.

7.1.5. Pyrite Trace Elements

Trace elements analysis were performed with LA-ICP-MS technique in the groups of pyrite described in samples from the continental and marine settings of Jacobina Basin, in order to provide a complementary tool to evaluate their origins. The detailed analytical

procedures are described in Teles (this volume). In summary, the LA-ICP-MS analysis were carried out at the Research School of Earth Sciences (RSES), ANU, using a 193nm Lambda Physik laser ablation system coupled to an Agilent 7700 series quadrupole ICP-MS. The samples and standards were analyzed with the spot sizes of 28µm, with exception to the sample PD-14, which was analyzed with 13µm spots. Sulfide standards MASS-1 (Wilson et al., 2002) and STDGL-1 (Norman et al., 2003) were used together with NIST-610 to calibrate the trace element contents of samples. Stoichiometric Fe was used as internal standard, and data reduction followed the procedures of Longerich et al. (1996), using the software Iolite (Paton et al., 2011).

The summary of LA-ICP-MS data is shown in Table 7.1 (the complete dataset is available in Table 7.4). Among all the investigated pyrites, the detrital inclusion-bearing type from the Serra do Córrego Fm. conglomerates has the highest contents of trace elements, including gold. In comparison to the detrital inclusion-bearing, the massive detrital pyrites are impoverished in trace elements, except for their higher concentrations of Co and As. For the pyrite grains in marine samples, the concentrations are below the detection limit (bdl) for the most of trace elements. Boxplots of selected elements are shown in Figure 7.7. We note that data of marine samples should be evaluated with caution, due to the small number of analysis.

Compositional fields for the pyrites analyzed in this study can be delineated in binary plots of selected trace elements (Figure 7.8), despite the overlap of part of data. The detrital inclusion-bearing pyrites of Serra do Córrego Fm. have the highest concentrations for most of trace elements, which comprise a relatively narrow compositional range, and show a perceptible positive correlation between some trace elements (eg., Au-Ag and Pb-Bi). Massive detrital pyrite has the largest compositional range among the pyrite groups, which should be indicative of varied source rocks. On the other hand, pyrite grains from the marine samples show the smallest variation in trace elements contents, clustering in the smallest field compared to the other groups of pyrite.

Table 7.1. Summary of element concentrations (ppm) and Co/Ni ratios for the pyrites samples of Jacobina Basin described in this study.

Detrital Inclusion-Bearing Pyrite(n=49)															
	^{55}Mn	**^{59}Co**	**^{60}Ni**	**^{65}Cu**	**^{66}Zn**	**^{75}As**	**^{77}Se**	**^{107}Ag**	**^{121}Sb**	**^{125}Te**	**^{197}Au**	**^{202}Hg**	**^{205}Tl**	**^{208}Pb**	**^{209}Bi**	**Co/Ni**
Range	bdl-171	bdl-6290	bdl-2000	bdl-64	bdl-600	70.2-13850	bdl-132.7	bdl-29	0.3-152	0.6-66.7	bdl-26	bdl-0.5	bdl-26	bdl-4100	bdl-210	0.1-15.9
Avg.	14.1	709.4	458.9	9.7	19.3	1363.7	38.9	1.2	12.6	13.9	1.7	0.18	1.5	178.3	27.2	2.1
SD	29.3	966	440.7	13.7	89.5	2655.8	33	4.3	23.4	13.2	4.2	0.09	5	592.1	32.5	2.9
Detrital Massive Pyrite (n=130)																
	^{55}Mn	**^{59}Co**	**^{60}Ni**	**^{65}Cu**	**^{66}Zn**	**^{75}As**	**^{77}Se**	**^{107}Ag**	**^{121}Sb**	**^{125}Te**	**^{197}Au**	**^{202}Hg**	**^{205}Tl**	**^{208}Pb**	**^{209}Bi**	**Co/Ni**
Range	bdl-50.2	bdl-8430	bdl-4600	bdl-209	bdl-100.6	bdl-9130	bdl-762	bdl-4.3	bdl-597	bdl-310	bdl-28	bdl-0.4	bdl-30.1	bdl-710	bdl-600	0.02-85.6
Avg.	2.8	788.6	331.6	6.5	4	960	32	0.4	18.7	9.4	0.67	0.15	3.7	30.7	10.9	6.1
SD	6.6	1046.2	584	22.7	14.4	1354.6	72.4	0.8	71	39.7	3	0.08	6.9	89.1	58.6	13.3
Pyrite from marine samples																
PD-09 (n=3)	**^{55}Mn**	**^{59}Co**	**^{60}Ni**	**^{65}Cu**	**^{66}Zn**	**^{75}As**	**^{77}Se**	**^{107}Ag**	**^{121}Sb**	**^{125}Te**	**^{197}Au**	**^{202}Hg**	**^{205}Tl**	**^{208}Pb**	**^{209}Bi**	**Co/Ni**
Range	bdl	252.3-541	176-547	bdl	bdl	1129- 4050	15.1-24.3	bdl	bdl	bdl	bdl	bdl	bdl	bdl-0.4	bdl-0.12	0.8-1.4
Avg.	-	423.1	407.7	-	-	2435.3	20.9	-	-	-	-	-	-	0.21	-	1.1
SD	-	151.4	201.9	-	-	1484.7	5	-	-	-	-	-	-	0.3	-	0.3
PD-14 (n=4)*	**^{55}Mn**	**^{59}Co**	**^{60}Ni**	**^{65}Cu**	**^{66}Zn**	**^{75}As**	**^{77}Se**	**^{107}Ag**	**^{121}Sb**	**^{125}Te**	**^{197}Au**	**^{202}Hg**	**^{205}Tl**	**^{208}Pb**	**^{209}Bi**	**Co/Ni**
Range	bdl-4.9	1-13700	41.5-730	bdl-3	bdl-0.5	85-541	bdl-40.1	bdl	bdl-1.8	bdl	bdl	bdl	bdl-0.07	bdl-12.7	bdl-0.3	0.03-72.1
Avg.	-	3458.4	250.8	-	-	273	19.1	-	-	-	-	-	0.04	7.3	-	18.2
SD	-	6827.9	327	-	-	192.6	18.2	-	-	-	-	-	0.05	7.5	-	35.9
SP-01 (n=7)	**^{55}Mn**	**^{59}Co**	**^{60}Ni**	**^{65}Cu**	**^{66}Zn**	**^{75}As**	**^{77}Se**	**^{107}Ag**	**^{121}Sb**	**^{125}Te**	**^{197}Au**	**^{202}Hg**	**^{205}Tl**	**^{208}Pb**	**^{209}Bi**	**Co/Ni**
Range	bdl-65	74-2270	161-1040	4-36	bdl-3.9	153-2430	8-55.9	0.2-3.1	4.3-16	bdl-21.2	bdl-0.7	bdl-1	bdl-0.08	22.3-86	1.9-26.2	0.2-4
Avg.	26	948.1	436	13	2.2	996.8	24.1	0.7	7.8	6.9	0.26	0.9	0.06	45.5	8.5	2.5
SD	20.8	798.1	321.3	13.1	1.5	876.6	18.5	1	4.8	9.5	0.24	0.09	0.03	22.1	9	1.5

*Laser spots for sample PD-14 were reduced to 13µm due to the small size of pyrite grains in this sample. Bdl: below detection limit.

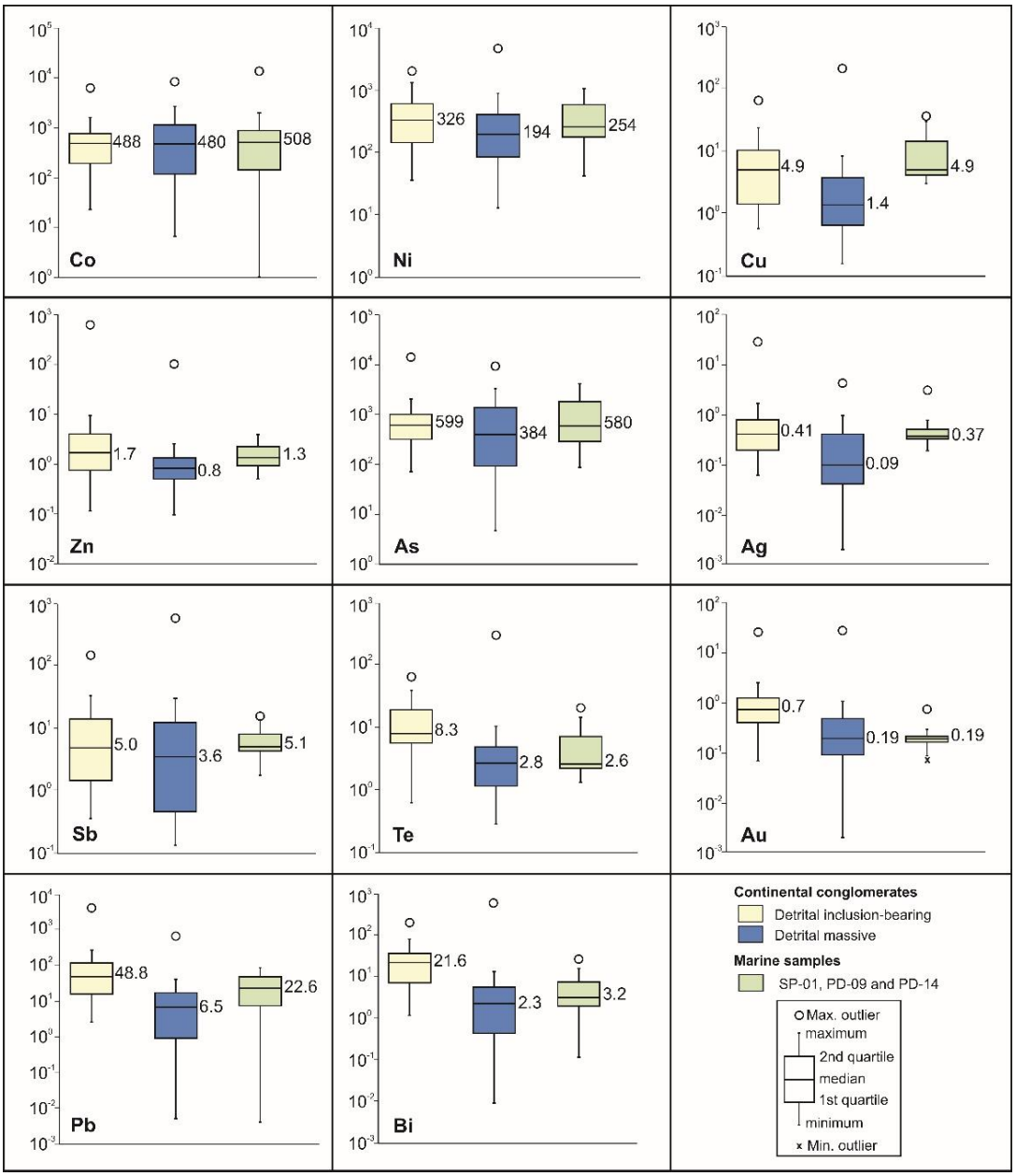

Figure 7.7. Boxplots for selected trace elements (in ppm) analyzed in pyrites from the continental and marine settings of Jacobina Basin. The marine samples (PD-09, PD-14 and SP-01) are plotted together, and they yield data below the detection limit for the most of spot analysis (see Table 7.4).

The Co/Ni ratio in pyrites has been considered a good indicator for their environment formation (Bralia et al., 1979; Guy et al., 2010), and recently as trace for the provenance of detrital grains (eg. Hofmann et al., 2009; Koglin et al., 2010). These studies have demonstrated that Co/Ni ratios <1 with low standard deviations are commonly associated to pyrites of sedimentary origin, whereas higher Co/Ni ratios (>>1) and standard deviations are suggestive of pyrites formed by hydrothermal process. Moreover,

the Co/Ni ratios in sedimentary pyrite is dependent on the granulometry and composition of the host sediments. In this sense, Guy et al., (2010) have reported 0.1<Co/Ni<1 ratios for sedimentary pyrites from carbonaceous shales in Witwatersrand Basin, whereas in the coarser-grained rocks (sandstones and diamictites) the Co/Ni ratios are between 1 and 2.

The Co/Ni ratios in pyrites of marine samples from the Jacobina Basin vary according to their host lithologies. The sample PD-09 has homogeneous Co/Ni ratios (~ 1) and low standard deviation (Table 7.1), which together with high concentrations of As are indicative of hydrothermal origin of their pyrite grains. The sample metapelite sample (PD-14) yields Co/Ni ratios characteristic of syngenetic pyrite formed in shales in associations with organic matter (0.1<Co/Ni<1; Guy et al., 2010), disregarding one data outlier with Co/Ni = 72 (see Table 7.4). The pyrites from quartzite sample SP-01 has, in average, higher Co/Ni ratios relative to the other marine samples (Table 7.1), that are compatible with sedimentary pyrite formed in sandstones (Guy et al., 2010).

The detrital massive pyrites from continental conglomerates yield the highest average Co/Ni ratio, and standard deviation among the samples (Table 7.1), which together with variable trace elements content, is suggestive of hydrothermal sources for these grains (Koglin et al., 2010). However, a sedimentary origin for some of these grains cannot be ruled out, because of some low Co/Ni data points, and the occurrence of MIF-S signatures in some grains.

The Co/Ni ratios of detrital inclusion-bearing pyrites from Serra do Córrego Fm. samples vary between 0.1 and 15.9, with average value of 2, and a standard deviation of 2.9 (Table 7.1). Despite some higher Co/Ni values, most of the data plot around or below Co/Ni<1 (Figure 7.8), which is compatible for a sedimentary origin for these grains (Guy et al., 2010; Koglin et al., 2010). In fact, these grains show textural and isotopic evidence (positive MIF-S) for a sedimentary/diagenetic origin. Furthermore, these pyrites are comparable to those found in other conglomerate-hosted gold deposits, which have elevated trace elements content, including gold (eg. Koglin et al., 2010; Ulrich et al., 2011; Agangi et al., 2013; and Large et al., 2013). For instance, at Witwatersrand Basin, these inclusion-bearing pyrites have been linked to diagenesis of black shales in suboxic to anoxic environments, in conditions favorable to the incorporation of several trace elements (including Au) in pyrite lattice (see Agangi et al., 2013; Large et al., 2013).

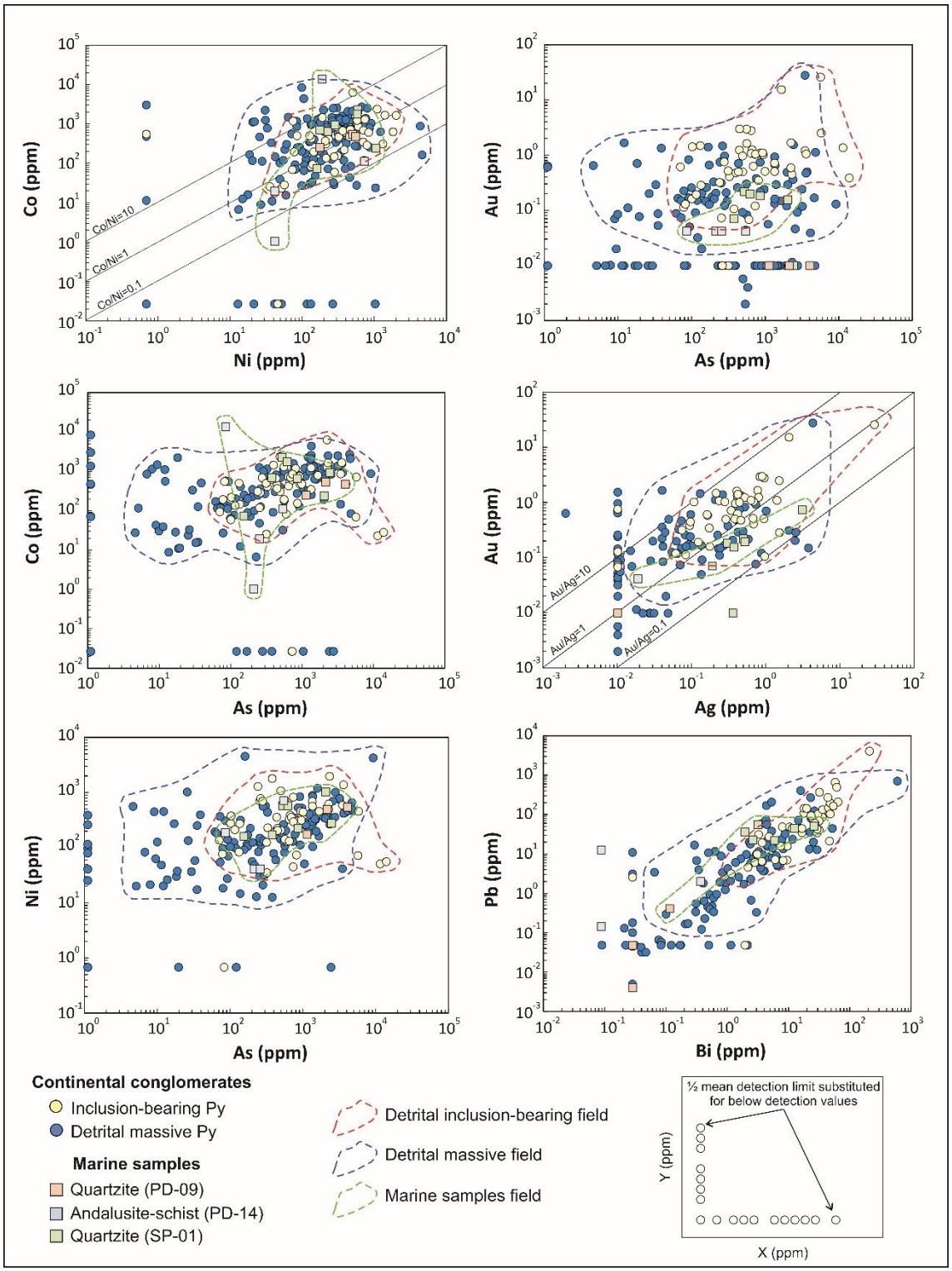

Figure 7.8. Binary scatter plots of selected trace elements, displaying the compositional fields of the continental conglomerates (inclusion-bearing and detrital massive pyrites), and pyrites from marine samples of the Jacobina Basin. Data below the detection limit of the technique were replaced by the half of mean detection limit.

7.1.6. References

Agangi, A., Hofmann, A., Wohlgemuth-Ueberwasser, C.C., 2013, Pyrite Zoning as a Record of Mineralization in the Ventersdorp Contact Reef, Witwatersrand Basin, South Africa: Economic Geology, v. 108, p. 1243-1272.

Barbosa, J.S.F., Sabaté, P., 2004, Archean and Paleoproterozoic crust of the São Francisco Craton, Bahia, Brazil: geodynamic features: Precambrian Research, v. 133, p. 1-27, doi: 10.1016/j.precamres.2004.03.001.

Bralia, A., Sabatini, G., Troja, F., 1979, A Revaluation of the Co/Ni Ratio in Pyrite as Geochemical Tool in Ore Genesis Problems: Evidences from Southern Tuscany Pyritic Deposits: Mineralium Deposita, v. 14, p. 353-374.

Crowe, D.E., and Vaughan, G., 1996, Characterization and use of isotopically homogeneous standards for in situ laser microprobe analysis of $^{34}S/^{32}S$ ratios: American Mineralogist, v. 81, p. 187-193.

Cruz, S.C.P., Barbosa, J.S.F., Pinto, M.S., Peucat, J.J, Paquette, J.L., Souza, J.S., Martins, V.S., Chemale Jr., F., Carneiro, M.A., 2016, The Siderian-Orosirian magmatism in the Gavião Paleoplate, Brazil: U-Pb geochronology, geochemistry and tectonic implications: Journal of South American Earth Sciences, v. 69, p. 43-79, doi: 10.1016/j.jsames.2016.02.007.

Ellen Santos, D., 2011, Geologia e Geoquímica dos Corpos Máficos e Ultramáficos da Porção Sul da Serra de Jacobina, Cinturão de Ouro, Bahia [Monography]: São Cristóvão, Universidade Federal de Sergipe, 91 p.

Guy, B.M., Beukes, N.J., Gutzmer, J., 2010, Paleoenvironmental Controls on the Texture and Chemical Composition of Pyrite from Non-Conglomeratic Sedimentary Rocks of the Mesoarchean Witwatersrand Supergroup, South Africa: South African Journal of Geology, v. 113 (2), p. 195-228, doi: 10.2113/gssajg.113.2.195.

Hendrickson, B.R., 1984, Stratigraphic Position, Mineralogy, Depositional Environment, and Gold Distribution of the Main Reef at Morro do Cuscuz and Morro do Vento near Jacobina, Bahia, Brazil [MSc. thesis]: Rapid City, School of Mines and Technology, 157 p.

Hofmann, A., Bekker, A., Rouxel, O., Rumble, D., Master, S., 2009, Multiple sulphur and iron isotope composition of detrital pyrite in Archaean sedimentary rocks: A new tool for provenance analysis: Earth and Planetary Science Letters, v. 286, p. 436-445, doi: 10.1016/j.epsl.2009.07.008.

Ireland, T.R., Schram, N., Holden, P., Lanc, P., Ávila, J., Armstrong, R., Amelin, Y., Latimore, A., Corrigan, D., Clement, S., Foster, J.J., Compston, W., 2014, Charge-mode electrometer measurements of S-isotopic compositions on SHRIMP-SI: International Journal of Mass Spectrometry, v. 359, p. 26-37.

Koglin, N., Frimmel, H.E., Minter, W.E.L., Brätz, H., 2010, Trace-element characteristics of different pyrite types in Mesoarchaean to Paleoproterozoic placer deposits: Mineralium Deposita, v. 45, p. 259-280, doi: 10.1007/s00126-009-0272-0.

Large, R.R., Meffre, S., Burnett, R., Guy, B., Bull, S., Gilbert, S., Goemann, K., Danyushevsky, L., 2013, Evidence for an Intrabasinal Source and Multiple Concentration Processes in the Formation of the Carbon Leader Reef, Witwatersrand Supergroup, South Africa: Economic Geology, v.108, p. 1215-1241.

Ledru, P., Milési, J.P., Johan, V., Sabaté, P., Maluski, H., 1997, Foreland basins and gold-bearing conglomerates: a new model for the Jacobina Basin (São Francisco province, Brasil): Precambriam Research, v. 86, p. 155-176.

Longerich, H.P., Jackson, S.E., Günther, D., 1996, Laser Ablation Inductively Coupled Plasma Mass Spectrometric Transient Signal Data Acquisition and Analyte Concentration Calculation: Journal of Analytical Atomic Spectrometry, v. 11, p. 899-904.

Mascarenhas, J.F., Filho, V.M.C., Griffon, J.C, 1992, Contribuição à Geologia do Grupo Jacobina na Região Jacobina/Pindobaçu: 37° Congresso Brasileiro de Geologia, São Paulo, SP, Boletim de Resumos Expandidos, v. 2, p. 141-142.

Milesi, J.P., Ledru, P., Marcoux, E., Mougeot, R., Johan, V., Lerouge, C., Sabaté, P., Bailly,L., Respaut, J.P., Skipwith, P., 2002, The Jacobina Paleoproterozoic gold-bearing conglomerates, Bahia, Brazil: a "hydrothermal shear-reservoir" model: Ore Geology Reviews, v. 19, p. 95-136, doi: 10.1016/S0169-1368(01)00038-5.

Mougeot, R., 1996, Etude de la limite Archéen-Protérozoïque et des minéralisa-tions Au ± U associées. Exemples de la région de Jacobina, Etat de Bahia, Brésilet de Carajás État de Pará, Brésil [Ph.D. thesis]: Montpellier, Université of Montpellier II, 301 p.

Norman, M., Robinson, P., Clarck, D., 2003, Major and Trace-Element Analysis of Sulfide Ores by Laser-Ablation ICP-MS, Solution ICP-MS, and XRF: New Data on International Reference Materials: The Canadian Mineralogist, v. 41, p. 293-305.

Paton, C., Hellstrom, J., Paul, B., Woodhead, J., Hergt, J., 2011, Iolite: Freeware for the visualisation and processing of mass spectrometric data: Journal of Analytical Atomic Spectrometry, v. 26, p. 2508-2518.

Pearson, W., Macêdo, P.M., Rúbio, A., Lorenzo, C.L., Karpeta, P., 2005, Geology and gold mineralization of the Jacobina Mine and Bahia Gold Belt, Bahia, Brazil and comparison to Tarkwa and Witwatersrand, *in* Proceedings, Geological Society of Nevada Symposium, Reno, May 2005, Volume 1: Window to the World, p. 757–786.

Peucat, J.J., Mascarenhas, J.F., Barbosa, J.S.F., Souza, S.L., Marinho, M.M., Fanning, C.M., Leite, C.M.M., 2002, 3.3 Ga SHRIMP U–Pb zircon age of a felsic metavolcanic rock from the Mundo Novo greenstone belt in the São Francisco Craton, Bahia (NE Brazil): Journal of South America Earth Sciences, v. 15, p. 363–373, doi: 10.1016/S0895-9811(02)00044-5.

Teixeira, J.B.G., Souza, J.A.B., Silva, M.G., Leite, C.M.M., Barbosa, J.S.F., Coelho, C.E.S., Abram, M.B., Filho, V.M.C., Iyer, S.S.S., 2001, Gold mineralization in the Serra de Jacobina region, Bahia Brazil: tectonic framework metallogenesis: Mineralium Deposita, v. 36, p. 332-344.

Teles, G., Chemale Jr., F., Oliveira, C.G., 2015, Paleoarchean record of the detrital pyrite-bearing, Jacobina Au–U deposits, Bahia, Brazil: Precambrian Research, v. 258, p. 289-313, doi: 10.1016/j.precamres.2014.11.004.

Ulrich, T., Long, D.G.F., Kamber, B.S., Whitehouse, M.J., 2011, In Situ Trace Element and Sulfur Isotope Analysis of Pyrite in a Paleoproterozoic Gold Placer Deposit, Pardo and Clement Townships, Ontario, Canada: Economic Geology, v. 106, p. 667-686.

Williford, K.H., Van Kranendonk, M.J., Ushikubo, T., Kozdon, R., Valley, J.W., 2011, Constraining atmospheric oxygen and seawater sulfate concentrations during Paleoproterozoic glaciation: In situ sulfur three-isotope microanalysis of pyrite fom the Turee Creek Group, Western Australia: Geochimica et Cosmochimica Acta, v. 75, p. 5686-5707, doi: 10.1016/j.gca.2011.07.010.

Whitehouse, M.J., 2013, Multiple Sulfur Isotope Determination by SIMS: Evaluation of Reference Sulfides for $\Delta^{33}S$ with Observations and Case Study on the Detemination of $\Delta^{36}S$: Geostandards and Geoanalytical Research, v. 37, p. 19-33, doi: 10.1111/j.1751-908X.2012.00188.x.

Table 7.2. SHRIMP-SI analysis for the pyrite standards (Ruttan and Balmat) used for the isotopic determinations of samples from Jacobina Basin.

Spot title	Date	Time	$\delta^{33}S$ (‰)	2σ	$\delta^{34}S$ (‰)	2σ	$\delta^{36}S$ (‰)	2σ	$\Delta^{33}S$ (‰)	2σ	$\Delta^{36}S$ (‰)	2σ	^{32}S cps (median)	^{33}S cps (median)	^{34}S cps (median)	^{36}S cps (median)
RUTTAN_1-1.1	19/03/15	9:28:24	0.82	0.15	1.43	0.02	2.80	0.39	0.08	0.14	0.08	0.40	1.30E+09	1.02E+07	5.68E+07	2.04E+05
RUTTAN_1-1.2		9:43:15	0.50	0.11	1.15	0.02	2.18	0.40	-0.09	0.13	-0.01	0.43	1.29E+09	1.01E+07	5.64E+07	2.02E+05
RUTTAN_1-1.3		9:58:00	0.58	0.16	1.25	0.03	2.15	0.25	-0.06	0.16	-0.24	0.26	1.28E+09	1.00E+07	5.61E+07	2.01E+05
RUTTAN_1-1.4		10:20:46	0.61	0.07	1.07	0.03	1.75	0.33	0.06	0.07	-0.29	0.35	1.27E+09	9.93E+06	5.55E+07	1.99E+05
BALMAT_1-1.1		10:41:26	7.64	0.09	14.82	0.03	28.31	0.37	0.03	0.09	-0.03	0.39	1.36E+09	1.07E+07	6.04E+07	2.19E+05
RUTTAN_1-1.5		15:08:47	0.62	0.06	1.17	0.03	2.57	0.27	0.02	0.07	0.35	0.27	1.29E+09	1.01E+07	5.65E+07	2.03E+05
BALMAT_1-1.2		15:27:52	7.78	0.08	14.94	0.02	28.22	0.34	0.11	0.08	-0.36	0.37	1.40E+09	1.11E+07	6.22E+07	2.26E+05
RUTTAN_5-1.1		23:30:49	0.63	0.10	1.05	0.02	2.05	0.40	0.09	0.11	0.06	0.41	1.29E+09	1.01E+07	5.65E+07	2.02E+05
RUTTAN_5-1.2		23:44:45	0.52	0.07	1.01	0.02	2.09	0.29	0.00	0.07	0.17	0.30	1.28E+09	1.00E+07	5.59E+07	2.00E+05
RUTTAN_5-1.3		23:58:42	0.75	0.07	1.34	0.02	2.38	0.28	0.06	0.06	-0.17	0.30	1.29E+09	1.01E+07	5.64E+07	2.02E+05
BALMAT_5-1.1	20/03/15	0:12:40	7.79	0.11	15.18	0.02	29.13	0.46	0.01	0.11	0.10	0.49	1.36E+09	1.07E+07	6.03E+07	2.19E+05
BALMAT_5-1.2		0:26:37	7.92	0.10	15.21	0.02	28.68	0.30	0.12	0.10	-0.42	0.34	1.34E+09	1.06E+07	5.97E+07	2.17E+05
RUTTAN_5-1.4		3:00:56	0.52	0.13	1.08	0.02	1.94	0.39	-0.04	0.13	-0.12	0.37	1.29E+09	1.01E+07	5.64E+07	2.02E+05
RUTTAN_5-1.5		3:14:52	0.60	0.08	1.13	0.02	2.14	0.40	0.02	0.08	0.00	0.41	1.27E+09	9.99E+06	5.58E+07	2.00E+05
BALMAT_5-1.3		3:28:54	7.72	0.14	15.27	0.02	29.02	0.26	-0.12	0.15	-0.20	0.27	1.32E+09	1.04E+07	5.87E+07	2.13E+05
RUTTAN_5-1.6		6:02:53	0.65	0.10	1.29	0.02	2.56	0.35	-0.01	0.10	0.11	0.37	1.29E+09	1.01E+07	5.66E+07	2.03E+05
RUTTAN_5-1.7		6:16:49	0.62	0.04	1.32	0.02	2.36	0.26	-0.06	0.04	-0.15	0.27	1.29E+09	1.01E+07	5.64E+07	2.02E+05
BALMAT_5-1.4		6:30:50	7.92	0.10	15.23	0.02	28.91	0.25	0.11	0.09	-0.24	0.25	1.33E+09	1.05E+07	5.91E+07	2.15E+05
RUTTAN_5-1.8		9:19:29	0.61	0.05	1.24	0.02	2.50	0.43	-0.03	0.06	0.13	0.42	1.28E+09	1.01E+07	5.63E+07	2.02E+05
RUTTAN_5-1.9		9:33:28	0.62	0.17	1.31	0.02	2.56	0.53	-0.05	0.17	0.06	0.52	1.31E+09	1.02E+07	5.72E+07	2.05E+05
BALMAT_5-1.5		9:47:29	7.81	0.11	15.29	0.02	29.01	0.40	-0.03	0.11	-0.24	0.41	1.33E+09	1.05E+07	5.93E+07	2.15E+05
RUTTAN_2-1.1		14:02:47	0.62	0.10	1.03	0.02	2.13	0.42	0.09	0.09	0.17	0.43	1.32E+09	1.04E+07	5.81E+07	2.08E+05
RUTTAN_2-1.2		14:16:43	0.70	0.05	1.10	0.02	1.80	0.47	0.13	0.05	-0.30	0.46	1.32E+09	1.04E+07	5.79E+07	2.08E+05
RUTTAN_2-1.3		14:30:43	0.59	0.08	0.89	0.02	1.45	0.44	0.13	0.08	-0.25	0.47	1.34E+09	1.05E+07	5.89E+07	2.11E+05
BALMAT_2-1.1		14:44:41	7.84	0.07	15.12	0.02	28.60	0.43	0.08	0.08	-0.33	0.46	1.25E+09	9.89E+06	5.57E+07	2.02E+05
BALMAT_2-1.2		14:58:39	7.77	0.11	14.94	0.02	28.42	0.37	0.11	0.13	-0.15	0.38	1.23E+09	9.71E+06	5.46E+07	1.98E+05
RUTTAN_2-1.4		17:46:58	0.71	0.06	1.41	0.03	2.34	0.30	-0.01	0.06	-0.34	0.32	1.35E+09	1.06E+07	5.91E+07	2.12E+05
BALMAT_2-1.3		18:14:53	7.93	0.05	15.34	0.03	29.24	0.33	0.06	0.05	-0.11	0.34	1.26E+09	9.95E+06	5.60E+07	2.03E+05
RUTTAN_2-1.6		20:49:53	0.56	0.11	1.16	0.02	2.01	0.43	-0.04	0.11	-0.18	0.41	1.33E+09	1.04E+07	5.84E+07	2.09E+05
RUTTAN_2-1.7		21:04:08	0.41	0.04	0.97	0.03	1.95	0.34	-0.09	0.05	0.11	0.37	1.27E+09	9.96E+06	5.57E+07	2.00E+05
BALMAT_2-1.4		21:18:31	7.75	0.05	15.13	0.02	28.92	0.28	-0.01	0.06	-0.03	0.27	1.30E+09	1.03E+07	5.78E+07	2.10E+05
RUTTAN_2-1.8		23:54:50	0.36	0.11	0.91	0.02	1.68	0.33	-0.10	0.11	-0.05	0.33	1.27E+09	9.98E+06	5.58E+07	2.00E+05
BALMAT_2-1.5	21/03/15	0:23:12	7.65	0.05	14.88	0.02	28.17	0.41	0.02	0.05	-0.29	0.43	1.27E+09	1.00E+07	5.65E+07	2.05E+05
RUTTAN_2-1.10		2:59:00	0.60	0.07	1.12	0.02	2.22	0.41	0.03	0.07	0.10	0.46	1.34E+09	1.05E+07	5.87E+07	2.11E+05
RUTTAN_2-1.11		3:12:56	0.50	0.12	1.15	0.02	2.14	0.42	-0.09	0.12	-0.04	0.40	1.35E+09	1.06E+07	5.91E+07	2.12E+05
BALMAT_2-1.6		3:27:19	8.02	0.08	15.42	0.03	28.74	0.35	0.11	0.09	-0.76	0.37	1.27E+09	1.00E+07	5.64E+07	2.05E+05
RUTTAN_2-1.12		6:01:38	0.68	0.05	1.39	0.03	2.69	0.28	-0.04	0.05	0.04	0.28	1.31E+09	1.03E+07	5.73E+07	2.06E+05
RUTTAN_2-1.13		6:15:35	0.40	0.09	0.97	0.03	1.68	0.43	-0.10	0.09	-0.16	0.43	1.28E+09	1.01E+07	5.62E+07	2.01E+05
BALMAT_2-1.7		6:29:36	7.87	0.16	15.10	0.02	28.75	0.31	0.12	0.16	-0.14	0.31	1.27E+09	1.00E+07	5.64E+07	2.05E+05

RUTTAN_2-1.14		8:50:16	0.95	0.05	1.73	0.02	2.99	0.39	0.06	0.05	-0.29	0.38	1.36E+09	1.07E+07	5.98E+07	2.14E+05
RUTTAN_2-1.15		9:04:16	0.64	0.11	1.40	0.02	2.76	0.34	-0.08	0.13	0.09	0.35	1.34E+09	1.05E+07	5.89E+07	2.12E+05
BALMAT_2-1.8		9:18:18	7.83	0.16	15.23	0.02	28.92	0.32	0.01	0.17	-0.21	0.34	1.27E+09	1.01E+07	5.65E+07	2.05E+05
RUTTAN_4-1.1		9:32:40	0.64	0.13	1.39	0.02	2.62	0.40	-0.08	0.12	-0.01	0.42	1.36E+09	1.07E+07	5.97E+07	2.14E+05
RUTTAN_4-1.2		9:46:37	0.65	0.04	1.23	0.02	2.54	0.32	0.02	0.04	0.19	0.33	1.33E+09	1.05E+07	5.85E+07	2.10E+05
RUTTAN_4-1.3		10:00:36	0.70	0.09	1.28	0.03	2.50	0.28	0.04	0.11	0.05	0.29	1.34E+09	1.05E+07	5.90E+07	2.11E+05
BALMAT_4-1.1		10:14:36	8.08	0.19	15.56	0.02	30.18	0.37	0.09	0.21	0.41	0.40	1.29E+09	1.02E+07	5.76E+07	2.09E+05
BALMAT_4-1.2		10:28:36	7.91	0.09	15.44	0.02	29.71	0.28	-0.01	0.09	0.17	0.29	1.29E+09	1.02E+07	5.76E+07	2.09E+05
RUTTAN_4-1.4		13:03:13	0.56	0.05	1.17	0.02	2.22	0.33	-0.04	0.06	0.00	0.35	1.34E+09	1.05E+07	5.88E+07	2.11E+05
RUTTAN_4-1.5		13:17:12	0.66	0.10	1.27	0.03	2.60	0.34	0.01	0.11	0.18	0.35	1.32E+09	1.04E+07	5.80E+07	2.08E+05
BALMAT_4-1.3		13:31:12	8.02	0.11	15.42	0.02	29.11	0.33	0.11	0.11	-0.38	0.38	1.31E+09	1.04E+07	5.84E+07	2.12E+05
RUTTAN_4-1.7		16:06:47	0.69	0.09	1.25	0.02	2.54	0.39	0.05	0.09	0.15	0.34	1.33E+09	1.04E+07	5.83E+07	2.09E+05
RUTTAN_4-1.8		18:43:17	0.55	0.11	1.24	0.02	2.58	0.40	-0.09	0.12	0.22	0.38	1.32E+09	1.04E+07	5.80E+07	2.08E+05
RUTTAN_4-1.9		18:57:31	0.56	0.09	1.24	0.02	2.32	0.36	-0.07	0.11	-0.04	0.41	1.35E+09	1.06E+07	5.93E+07	2.12E+05
BALMAT_4-1.5		19:11:31	7.84	0.05	15.46	0.02	29.20	0.33	-0.09	0.05	-0.38	0.34	1.32E+09	1.04E+07	5.88E+07	2.14E+05
RUTTAN_4-1.11		21:47:02	0.45	0.14	0.91	0.02	1.84	0.42	-0.02	0.14	0.11	0.46	1.30E+09	1.02E+07	5.70E+07	2.05E+05
BALMAT_4-1.6		22:01:02	7.80	0.13	15.45	0.02	29.62	0.39	-0.13	0.14	0.07	0.40	1.32E+09	1.04E+07	5.88E+07	2.14E+05
RUTTAN_6-1.1		0:11:00	0.35	0.11	0.83	0.02	1.47	0.34	-0.08	0.13	-0.11	0.35	1.30E+09	1.02E+07	5.72E+07	2.05E+05
RUTTAN_6-1.2		0:27:05	0.66	0.05	1.13	0.02	1.98	0.34	0.08	0.05	-0.17	0.36	1.32E+09	1.04E+07	5.81E+07	2.09E+05
RUTTAN_6-1.3		0:41:02	0.55	0.05	1.09	0.02	2.47	0.33	-0.01	0.05	0.39	0.34	1.33E+09	1.04E+07	5.82E+07	2.09E+05
BALMAT_6-1.1		0:55:02	7.59	0.07	14.96	0.03	28.74	0.38	-0.08	0.07	0.13	0.42	1.23E+09	9.73E+06	5.48E+07	1.99E+05
BALMAT_6-1.2		1:08:59	7.77	0.09	15.14	0.03	29.01	0.44	0.00	0.10	0.05	0.47	1.24E+09	9.84E+06	5.54E+07	2.01E+05
RUTTAN_6-1.4		3:39:17	0.65	0.07	1.35	0.02	2.44	0.42	-0.04	0.08	-0.12	0.43	1.33E+09	1.04E+07	5.82E+07	2.09E+05
RUTTAN_6-1.5		3:53:14	0.49	0.13	1.21	0.02	2.40	0.34	-0.13	0.12	0.09	0.35	1.33E+09	1.04E+07	5.83E+07	2.09E+05
BALMAT_6-1.3		4:07:12	7.61	0.08	14.97	0.02	28.25	0.41	-0.07	0.08	-0.38	0.43	1.28E+09	1.01E+07	5.68E+07	2.06E+05
RUTTAN_6-1.6		6:55:06	0.60	0.09	1.24	0.02	2.26	0.27	-0.04	0.10	-0.10	0.28	1.33E+09	1.04E+07	5.83E+07	2.09E+05
RUTTAN_6-1.7	22/03/15	7:09:05	0.63	0.06	1.28	0.02	2.72	0.33	-0.03	0.06	0.28	0.35	1.33E+09	1.04E+07	5.81E+07	2.09E+05
BALMAT_6-1.4		7:23:03	7.57	0.08	14.84	0.03	28.45	0.40	-0.04	0.09	0.06	0.43	1.26E+09	9.93E+06	5.59E+07	2.03E+05
RUTTAN_8-1.1		7:37:23	0.60	0.07	1.19	0.02	2.29	0.30	-0.01	0.07	0.03	0.32	1.33E+09	1.04E+07	5.82E+07	2.09E+05
RUTTAN_8-1.2		7:51:20	0.67	0.08	1.29	0.02	2.60	0.42	0.00	0.09	0.15	0.43	1.30E+09	1.02E+07	5.72E+07	2.05E+05
RUTTAN_8-1.3		8:05:16	0.72	0.05	1.35	0.02	2.35	0.30	0.03	0.06	-0.22	0.34	1.31E+09	1.03E+07	5.76E+07	2.07E+05
BALMAT_8-1.1		8:19:15	7.78	0.12	15.07	0.03	28.95	0.29	0.05	0.13	0.13	0.32	1.23E+09	9.69E+06	5.46E+07	1.98E+05
BALMAT_8-1.2		8:33:11	7.53	0.11	14.88	0.03	28.29	0.32	-0.10	0.12	-0.17	0.32	1.20E+09	9.48E+06	5.33E+07	1.94E+05
RUTTAN_8-1.4		10:14:09	0.72	0.09	1.34	0.03	2.30	0.34	0.03	0.10	-0.24	0.33	1.32E+09	1.04E+07	5.80E+07	2.08E+05
RUTTAN_8-1.5		10:28:09	0.63	0.17	1.20	0.02	2.16	0.34	0.02	0.19	-0.12	0.34	1.31E+09	1.03E+07	5.75E+07	2.06E+05
BALMAT_8-1.3		10:42:08	7.56	0.11	14.89	0.03	28.35	0.34	-0.09	0.12	-0.14	0.36	1.21E+09	9.55E+06	5.38E+07	1.95E+05
RUTTAN-1.2		10:28:27	0.66	0.06	1.17	0.02	2.35	0.35	0.02	0.06	-0.01	0.36	1.31E+09	1.03E+07	5.74E+07	2.07E+05
RUTTAN-1.3		10:43:40	0.58	0.07	1.40	0.03	2.63	0.35	-0.15	0.08	-0.03	0.36	1.32E+09	1.04E+07	5.80E+07	2.09E+05
BALMAT-1.1		10:58:43	7.54	0.09	14.70	0.03	28.03	0.31	-0.04	0.10	-0.19	0.33	1.26E+09	9.96E+06	5.59E+07	2.03E+05
BALMAT-1.2	20/07/15	11:13:45	7.95	0.09	15.47	0.03	29.25	0.35	0.01	0.09	-0.33	0.37	1.26E+09	1.00E+07	5.62E+07	2.04E+05
RUTTAN-1.4		12:54:37	0.64	0.12	1.03	0.03	1.90	0.36	0.08	0.12	-0.15	0.37	1.33E+09	1.05E+07	5.84E+07	2.10E+05
BALMAT-1.3		13:10:48	7.77	0.14	15.32	0.03	29.14	0.31	-0.08	0.15	-0.14	0.34	1.26E+09	9.96E+06	5.59E+07	2.03E+05
RUTTAN-1.5		15:05:42	0.72	0.10	1.22	0.02	3.15	0.32	0.08	0.10	0.79	0.32	1.35E+09	1.06E+07	5.90E+07	2.12E+05

RUTTAN-1.6		15:20:50	0.77	0.10	1.25	0.03	2.83	0.34	0.10	0.10	0.40	0.34	1.37E+09	1.08E+07	6.03E+07	2.17E+05
BALMAT-1.4		15:35:59	7.70	0.11	14.77	0.03	27.95	0.32	0.14	0.12	-0.21	0.34	1.27E+09	1.00E+07	5.63E+07	2.05E+05
RUTTAN-1.7		15:56:27	0.63	0.12	1.07	0.03	2.43	0.39	0.09	0.13	0.46	0.41	1.37E+09	1.08E+07	6.01E+07	2.16E+05
RUTTAN-1.8		16:17:29	0.59	0.11	1.20	0.02	1.85	0.33	0.00	0.11	-0.33	0.33	1.42E+09	1.12E+07	6.22E+07	2.23E+05
RUTTAN-1.9		18:39:49	0.46	0.06	0.89	0.03	1.59	0.33	0.03	0.06	0.02	0.34	1.36E+09	1.07E+07	5.94E+07	2.14E+05
RUTTAN-1.11		21:30:37	0.46	0.05	1.04	0.03	1.42	0.35	-0.05	0.05	-0.44	0.37	1.36E+09	1.07E+07	5.97E+07	2.14E+05
RUTTAN-1.10		21:52:56	0.39	0.13	0.81	0.03	1.12	0.45	-0.03	0.13	-0.40	0.46	1.33E+09	1.05E+07	5.84E+07	2.10E+05
BALMAT-1.5		22:08:20	7.79	0.14	15.03	0.02	28.34	0.38	0.10	0.13	-0.30	0.39	1.27E+09	1.00E+07	5.63E+07	2.05E+05
RUTTAN-2.3		0:26:10	0.77	0.06	1.54	0.03	2.46	0.33	-0.03	0.06	-0.49	0.35	1.46E+09	1.15E+07	6.39E+07	2.30E+05
RUTTAN-2.4		0:41:13	0.49	0.14	1.08	0.03	2.47	0.32	-0.07	0.15	0.42	0.32	1.46E+09	1.15E+07	6.39E+07	2.30E+05
BALMAT-1.7	21/07/15	0:56:16	7.87	0.09	15.56	0.03	29.77	0.27	-0.13	0.10	-0.04	0.28	1.38E+09	1.09E+07	6.13E+07	2.23E+05
RUTTAN-2.4		9:06:34	0.65	0.12	1.33	0.02	2.45	0.26	-0.04	0.12	-0.09	0.27	1.59E+09	1.25E+07	6.98E+07	2.51E+05
RUTTAN-2.5		12:12:48	1.01	0.09	1.79	0.03	3.78	0.33	0.06	0.09	0.27	0.34	1.63E+09	1.28E+07	7.13E+07	2.57E+05
RUTTAN-1.1		13:47:04	0.66	0.10	1.41	0.02	2.39	0.29	0.00	0.11	-0.06	0.29	1.45E+09	1.14E+07	6.37E+07	2.29E+05
RUTTAN-1.2		14:02:35	0.60	0.11	1.15	0.02	2.06	0.49	0.04	0.11	-0.03	0.50	1.42E+09	1.12E+07	6.22E+07	2.24E+05
BALMAT-1.1		14:18:07	7.51	0.09	14.51	0.03	28.12	0.37	-0.03	0.10	0.03	0.40	1.39E+09	1.10E+07	6.20E+07	2.25E+05
RUTTAN-1.3		16:26:06	0.66	0.09	1.13	0.02	2.72	0.27	0.01	0.10	0.29	0.27	1.46E+09	1.15E+07	6.39E+07	2.30E+05
RUTTAN-1.4		16:41:41	0.53	0.12	1.12	0.02	1.89	0.25	-0.04	0.12	-0.20	0.26	1.43E+09	1.12E+07	6.27E+07	2.25E+05
BALMAT-1.2	23/07/15	16:57:20	7.68	0.12	14.85	0.03	28.50	0.29	0.04	0.12	0.03	0.29	1.43E+09	1.13E+07	6.34E+07	2.31E+05
RUTTAN-1.1		19:46:55	0.47	0.09	0.97	0.02	1.97	0.29	0.02	0.10	0.24	0.29	1.38E+09	1.09E+07	6.06E+07	2.18E+05
RUTTAN-1.2		20:02:41	0.55	0.12	1.27	0.02	2.34	0.33	-0.07	0.12	-0.06	0.34	1.33E+09	1.04E+07	5.82E+07	2.09E+05
BALMAT-1.1		20:18:13	8.00	0.12	15.51	0.03	29.69	0.38	0.03	0.12	-0.12	0.39	1.45E+09	1.15E+07	6.47E+07	2.36E+05
RUTTAN-1.3		23:09:37	0.56	0.14	0.95	0.03	2.28	0.27	0.06	0.14	0.36	0.27	1.34E+09	1.05E+07	5.87E+07	2.11E+05
RUTTAN-1.4		23:25:08	0.54	0.09	1.08	0.03	2.06	0.29	0.00	0.09	0.01	0.29	1.35E+09	1.06E+07	5.91E+07	2.13E+05
BALMAT-1.2		23:40:55	8.17	0.14	15.68	0.03	29.54	0.24	0.15	0.15	-0.47	0.26	1.49E+09	1.18E+07	6.61E+07	2.41E+05
RUTTAN-1.5		2:32:13	0.53	0.12	1.11	0.03	2.18	0.40	0.00	0.12	0.13	0.40	1.34E+09	1.05E+07	5.87E+07	2.11E+05
RUTTAN-1.6		2:47:44	0.56	0.11	1.23	0.03	2.15	0.30	-0.01	0.12	-0.07	0.30	1.33E+09	1.05E+07	5.84E+07	2.10E+05
BALMAT-1.3		3:03:17	7.90	0.11	15.55	0.02	29.24	0.34	-0.02	0.12	-0.38	0.36	1.43E+09	1.14E+07	6.38E+07	2.32E+05
RUTTAN-1.7		5:54:46	0.60	0.14	1.37	0.03	2.56	0.38	-0.10	0.15	-0.11	0.39	1.31E+09	1.03E+07	5.73E+07	2.06E+05
RUTTAN-1.8		6:10:17	0.55	0.10	1.25	0.02	2.32	0.26	-0.07	0.11	-0.06	0.28	1.31E+09	1.03E+07	5.76E+07	2.07E+05
BALMAT-1.4		6:26:04	8.16	0.05	15.82	0.02	30.08	0.28	0.04	0.05	-0.29	0.29	1.46E+09	1.16E+07	6.49E+07	2.36E+05
RUTTAN-1.9		9:17:16	0.70	0.13	1.32	0.02	2.49	0.33	0.00	0.14	-0.19	0.35	1.33E+09	1.05E+07	5.83E+07	2.10E+05
RUTTAN-1.10		9:32:47	0.67	0.08	1.30	0.03	2.41	0.30	0.04	0.08	0.01	0.29	1.32E+09	1.04E+07	5.81E+07	2.09E+05
BALMAT-1.5	24/07/15	9:48:19	8.05	0.16	15.98	0.03	30.20	0.34	-0.08	0.17	-0.21	0.36	1.47E+09	1.17E+07	6.55E+07	2.38E+05
RUTTAN-1.11		12:39:21	0.85	0.15	1.55	0.03	3.13	0.31	0.03	0.16	0.02	0.32	1.36E+09	1.07E+07	5.97E+07	2.14E+05
RUTTAN-1.12		12:54:52	0.42	*0.11*	0.81	0.02	1.38	0.27	0.06	0.11	-0.04	0.28	1.35E+09	1.06E+07	5.92E+07	2.13E+05
BALMAT-1.6		13:10:25	8.20	0.10	15.81	0.02	30.09	0.41	0.10	0.11	-0.19	0.42	1.43E+09	1.13E+07	6.36E+07	2.32E+05
RUTTAN-2.1		15:15:06	0.82	0.04	1.48	0.03	2.64	0.33	0.06	0.04	-0.25	0.33	1.41E+09	1.11E+07	6.19E+07	2.22E+05
BALMAT-1.7		15:30:39	7.93	0.12	15.53	0.02	29.83	0.32	-0.02	0.12	0.07	0.33	1.43E+09	1.13E+07	6.35E+07	2.32E+05
RUTTAN-2.4		18:43:21	0.37	0.10	0.92	0.02	1.77	0.34	-0.06	0.10	0.15	0.36	1.47E+09	1.15E+07	6.43E+07	2.31E+05
BALMAT-2.1		18:58:53	7.99	0.13	15.32	0.02	29.23	0.24	0.14	0.13	-0.06	0.25	1.44E+09	1.14E+07	6.39E+07	2.33E+05
RUTTAN-3.1		21:35:00	0.68	0.08	1.28	0.03	2.63	0.28	0.02	0.08	0.17	0.30	1.54E+09	1.21E+07	6.74E+07	2.42E+05
RUTTAN-3.2		21:50:31	0.67	0.07	1.30	0.03	2.37	0.24	-0.02	0.09	-0.19	0.24	1.50E+09	1.18E+07	6.59E+07	2.37E+05

RUTTAN-3.3		0:25:56	0.71	0.08	1.13	0.02	2.54	0.28	0.09	0.08	0.21	0.29	1.53E+09	1.20E+07	6.71E+07	2.41E+05
RUTTAN-3.4		0:41:27	0.64	0.07	1.28	0.02	2.45	0.27	-0.01	0.08	0.03	0.27	1.51E+09	1.19E+07	6.61E+07	2.38E+05
BALMAT-2.2		0:56:59	7.75	0.10	15.19	0.02	28.64	0.33	0.00	0.11	-0.25	0.35	1.45E+09	1.15E+07	6.46E+07	2.35E+05
RUTTAN-1.1		1:13:18	0.48	0.15	1.02	0.03	2.15	0.29	-0.07	0.15	0.12	0.30	1.49E+09	1.17E+07	6.54E+07	2.35E+05
RUTTAN-2.1		3:18:37	0.68	0.10	1.31	0.02	2.61	0.27	-0.01	0.10	0.04	0.29	1.50E+09	1.18E+07	6.57E+07	2.36E+05
RUTTAN-2.2		3:34:08	0.63	0.10	1.31	0.02	2.14	0.21	-0.02	0.10	-0.29	0.21	1.52E+09	1.19E+07	6.65E+07	2.39E+05
BALMAT-1.1		3:50:04	7.82	0.08	15.01	0.03	29.01	0.27	0.08	0.08	0.12	0.26	1.52E+09	1.20E+07	6.75E+07	2.46E+05
RUTTAN-2.3		5:58:47	0.71	0.09	1.19	0.03	2.16	0.29	0.11	0.10	-0.07	0.30	1.53E+09	1.20E+07	6.70E+07	2.41E+05
RUTTAN-2.4		6:14:33	0.50	0.09	1.17	0.02	2.16	0.24	-0.07	0.09	0.02	0.24	1.54E+09	1.21E+07	6.77E+07	2.43E+05
BALMAT-1.2		6:30:06	8.00	0.08	15.44	0.02	29.36	0.29	0.09	0.09	-0.14	0.30	1.51E+09	1.19E+07	6.71E+07	2.44E+05
RUTTAN-2.5		8:51:30	0.65	0.10	1.27	0.03	2.01	0.31	0.06	0.10	-0.20	0.32	1.52E+09	1.20E+07	6.68E+07	2.40E+05
RUTTAN-1.1	25/07/15	12:00:17	0.57	0.12	1.32	0.02	2.35	0.31	-0.08	0.12	-0.07	0.30	1.53E+09	1.20E+07	6.69E+07	2.40E+05
RUTTAN-1.2		12:15:48	0.73	0.07	1.40	0.02	2.73	0.31	0.00	0.08	-0.01	0.31	1.50E+09	1.18E+07	6.57E+07	2.36E+05
BALMAT-1.1		12:31:22	7.61	0.03	14.87	0.02	28.22	0.22	0.01	0.03	-0.16	0.23	1.41E+09	1.12E+07	6.26E+07	2.27E+05
RUTTAN-1.3		15:22:33	0.69	0.07	1.16	0.02	1.98	0.29	0.12	0.08	-0.15	0.27	1.48E+09	1.16E+07	6.47E+07	2.32E+05
RUTTAN-1.4		15:38:05	0.62	0.10	1.07	0.03	2.70	0.22	0.03	0.11	0.48	0.22	1.45E+09	1.14E+07	6.37E+07	2.29E+05
BALMAT-1.2		15:53:38	7.77	0.08	15.13	0.02	29.15	0.25	0.01	0.09	0.16	0.26	1.38E+09	1.10E+07	6.14E+07	2.23E+05
RUTTAN-2.1		18:45:00	0.41	0.08	0.99	0.03	1.75	0.30	-0.09	0.09	-0.15	0.30	1.42E+09	1.12E+07	6.22E+07	2.23E+05
RUTTAN-2.2		19:00:32	0.51	0.13	1.03	0.02	2.17	0.26	-0.03	0.13	0.12	0.26	1.45E+09	1.14E+07	6.37E+07	2.29E+05
BALMAT-1.3		19:16:05	7.85	0.07	15.41	0.02	29.22	0.24	-0.03	0.07	-0.21	0.26	1.40E+09	1.11E+07	6.24E+07	2.27E+05
RUTTAN-2.3		22:08:41	0.60	0.12	1.22	0.02	2.02	0.20	-0.01	0.12	-0.28	0.21	1.48E+09	1.16E+07	6.47E+07	2.32E+05
RUTTAN-2.4		22:24:12	0.80	0.08	1.50	0.02	2.58	0.31	0.03	0.08	-0.29	0.32	1.49E+09	1.17E+07	6.54E+07	2.35E+05
RUTTAN-2.5		23:57:42	0.54	0.07	0.99	0.02	2.29	0.29	0.02	0.08	0.35	0.31	1.51E+09	1.19E+07	6.62E+07	2.38E+05
BALMAT-1.4	26/07/15	0:13:15	8.14	0.03	15.76	0.03	29.98	0.37	0.05	0.04	-0.27	0.39	1.47E+09	1.16E+07	6.53E+07	2.38E+05

Table 7.3. SHRIMP-SI sulfur isotopic data for the pyrite samples from Jacobina Basin.

Serra do Córrego Formation																
Sample	**Rock Type**	**Outcrop/DC (m)**	**Pyrite Type**	**Spot**	**Date**	**Time**	**$\delta^{34}S$ (‰)**	**2σ**	**$\Delta^{33}S$ (‰)**	**2σ**	**$\Delta^{36}S$ (‰)**	**2σ**	**^{32}S cps (median)**	**^{33}S cps (median)**	**^{34}S cps (median)**	**^{36}S cps (median)**
CANIF-37 (1.1)	Cgl	DC1 (228.1 - 228.2)	1	3.1	20/03/15	18:57:40	3.53	0.02	0.22	0.12	-0.32	0.30	1.29E+09	1.01E+07	5.66E+07	2.03E+05
				5.1		19:39:37	0.10	0.02	0.12	0.16	-0.05	0.29	1.31E+09	1.03E+07	5.73E+07	2.05E+05
				6.1		19:53:38	0.72	0.02	0.20	0.16	-0.05	0.23	1.35E+09	1.06E+07	5.90E+07	2.12E+05
				7.1		20:21:35	1.11	0.02	0.01	0.10	-0.04	0.28	1.29E+09	1.01E+07	5.66E+07	2.03E+05
				11.1		22:01:11	1.80	0.03	-0.05	0.16	-0.27	0.34	1.25E+09	9.78E+06	5.47E+07	1.96E+05
				13.1		22:29:23	1.09	0.02	0.19	0.13	-0.60	0.49	1.37E+09	1.07E+07	6.00E+07	2.15E+05
			2	1.1	20/03/15	18:29:10	0.95	0.02	-0.14	0.20	-0.29	0.34	1.25E+09	9.83E+06	5.50E+07	1.97E+05
				4.1		19:25:37	1.14	0.02	0.03	0.14	0.06	0.34	1.31E+09	1.03E+07	5.74E+07	2.06E+05
				8.1		20:35:35	-1.03	0.02	0.39	0.06	-0.44	0.28	1.34E+09	1.05E+07	5.89E+07	2.11E+05
				9.1		21:32:34	0.63	0.02	0.41	0.17	-0.59	0.36	1.37E+09	1.08E+07	6.01E+07	2.15E+05
				10.1		21:46:34	1.00	0.03	0.08	0.15	-0.04	0.32	1.33E+09	1.04E+07	5.82E+07	2.09E+05
				12.1		22:15:26	-0.53	0.02	0.31	0.13	-0.49	0.55	1.24E+09	9.69E+06	5.41E+07	1.93E+05
				1.1-2	25/07/15	1:45:02	0.21	0.03	0.11	0.12	0.57	0.29	1.47E+09	1.16E+07	6.44E+07	2.31E+05

				1.1-3		2:00:33	0.79	0.03	0.05	0.08	0.21	0.36	1.45E+09	1.14E+07	6.37E+07	2.29E+05
CANIF-37 (1.2)	Cgl	DC1 (228.1 - 228.2)	1	3.1	20/03/15	1:36:32	1.22	0.02	0.38	0.14	-0.06	0.41	1.32E+09	1.03E+07	5.77E+07	2.07E+05
				5.1		2:18:31	1.55	0.02	0.37	0.13	-0.18	0.45	1.33E+09	1.04E+07	5.82E+07	2.09E+05
			2	1.1		0:40:39	2.87	0.03	-0.02	0.11	0.02	0.33	1.31E+09	1.03E+07	5.76E+07	2.07E+05
				2.1	20/03/15	1:08:33	1.04	0.03	0.13	0.11	-0.49	0.47	1.34E+09	1.05E+07	5.87E+07	2.11E+05
				2.2		1:22:30	1.06	0.02	0.32	0.22	-0.28	0.41	1.33E+09	1.04E+07	5.84E+07	2.09E+05
CANIF-37 (2.2)	Cgl	DC1 (229.6 - 229.8)	1	1.1	21/03/15	2:30:36	0.44	0.03	0.48	0.19	-0.42	0.33	1.24E+09	9.69E+06	5.42E+07	1.94E+05
				9.1		5:19:38	1.01	0.02	0.41	0.13	-0.08	0.42	1.35E+09	1.06E+07	5.93E+07	2.13E+05
				10.1		5:33:35	1.39	0.02	0.12	0.06	0.42	0.43	1.30E+09	1.02E+07	5.68E+07	2.04E+05
				17.1		7:53:56	3.66	0.03	-0.09	0.08	0.00	0.34	1.26E+09	9.92E+06	5.55E+07	2.00E+05
				10.2	25/07/15	7:32:38	-1.30	0.03	-0.02	0.05	0.19	0.29	1.43E+09	1.13E+07	6.28E+07	2.25E+05
				10.3		7:48:33	1.76	0.03	0.08	0.07	-0.08	0.30	1.53E+09	1.21E+07	6.72E+07	2.42E+05
			2	4.1	21/03/15	3:55:20	1.79	0.02	0.10	0.10	-0.02	0.32	1.35E+09	1.06E+07	5.92E+07	2.13E+05
				5.1		4:09:43	0.89	0.02	0.24	0.11	-0.15	0.35	1.22E+09	9.59E+06	5.36E+07	1.92E+05
				5.2		4:23:42	0.84	0.03	0.20	0.12	-0.14	0.35	1.23E+09	9.68E+06	5.41E+07	1.94E+05
				6.1		4:37:42	2.26	0.03	0.24	0.06	-0.14	0.43	1.40E+09	1.10E+07	6.15E+07	2.21E+05
				11.1		5:47:35	5.59	0.03	0.11	0.06	0.14	0.39	1.29E+09	1.01E+07	5.67E+07	2.04E+05
				12.1		6:43:38	0.87	0.02	0.19	0.05	-0.28	0.45	1.35E+09	1.06E+07	5.92E+07	2.12E+05
				15.1		7:26:01	0.43	0.02	0.24	0.07	-0.24	0.38	1.26E+09	9.85E+06	5.51E+07	1.97E+05
				16.1		7:39:58	-6.24	0.02	-0.05	0.05	-0.30	0.39	1.27E+09	9.91E+06	5.52E+07	1.97E+05
				9.2	25/07/15	6:45:42	1.20	0.03	0.33	0.04	0.02	0.27	1.54E+09	1.21E+07	6.74E+07	2.42E+05
				9.3		7:01:13	1.34	0.03	0.18	0.06	-0.20	0.29	1.52E+09	1.20E+07	6.66E+07	2.39E+05
				9.4		7:16:44	1.19	0.02	0.20	0.04	-0.26	0.35	1.53E+09	1.21E+07	6.72E+07	2.41E+05
				11.2		8:19:36	1.23	0.02	0.13	0.12	-0.54	0.36	1.47E+09	1.16E+07	6.46E+07	2.32E+05
				22.1		5:26:56	0.70	0.03	0.03	0.11	0.05	0.26	1.53E+09	1.20E+07	6.70E+07	2.41E+05
CANIF-37 (3)	Cgl	DC1 (237.6 - 237.8)	1	1.2	19/03/15	12:17:35	0.21	0.02	1.14	0.12	-1.53	0.36	1.46E+09	1.14E+07	6.38E+07	2.28E+05
				3.1		13:02:00	0.41	0.03	0.08	0.10	-0.32	0.46	1.31E+09	1.03E+07	5.73E+07	2.05E+05
				3.3		13:34:37	-0.09	0.03	0.02	0.08	0.08	0.32	1.33E+09	1.05E+07	5.84E+07	2.09E+05
				4.1		13:49:40	0.47	0.02	0.24	0.11	-0.43	0.25	1.33E+09	1.04E+07	5.82E+07	2.08E+05
				1.4	23/07/15	14:50:18	0.22	0.02	1.09	0.10	-1.76	0.39	1.48E+09	1.17E+07	6.49E+07	2.33E+05
				8.1	25/07/15	15:06:57	1.78	0.02	0.21	0.09	-0.44	0.36	1.56E+09	1.23E+07	6.84E+07	2.45E+05
				8.4		16:09:13	1.40	0.02	0.21	0.11	-0.65	0.24	1.52E+09	1.19E+07	6.64E+07	2.39E+05
				9.1		16:25:08	-0.69	0.03	0.02	0.17	0.07	0.34	1.50E+09	1.18E+07	6.56E+07	2.35E+05
				10.1		16:56:13	2.37	0.02	0.23	0.08	-0.24	0.33	1.44E+09	1.13E+07	6.31E+07	2.27E+05
				10.2		17:11:45	2.82	0.02	0.08	0.09	-0.24	0.27	1.51E+09	1.19E+07	6.62E+07	2.38E+05
				12.1		17:42:49	0.68	0.02	0.09	0.08	-0.06	0.33	1.48E+09	1.17E+07	6.49E+07	2.33E+05
				13.1		18:13:54	3.87	0.03	0.16	0.09	0.00	0.21	1.20E+09	9.42E+06	5.26E+07	1.89E+05
				13.2		18:29:26	2.06	0.03	0.14	0.15	-0.45	0.29	1.47E+09	1.16E+07	6.47E+07	2.32E+05
				14.1		19:47:15	1.42	0.02	-0.11	0.07	-0.05	0.37	1.55E+09	1.22E+07	6.78E+07	2.44E+05
				17.1		20:18:23	1.95	0.02	-0.13	0.05	0.12	0.26	1.58E+09	1.24E+07	6.93E+07	2.49E+05
			2	2.1	19/03/15	12:32:25	-0.37	0.02	0.13	0.08	0.38	0.36	1.31E+09	1.03E+07	5.73E+07	2.05E+05
				2.2		12:47:11	-0.55	0.02	0.12	0.14	-0.04	0.31	1.32E+09	1.04E+07	5.78E+07	2.07E+05
				6.1		14:34:19	-0.05	0.02	0.66	0.09	-1.15	0.36	1.30E+09	1.02E+07	5.68E+07	2.03E+05
				6.2	23/07/15	15:06:23	-0.30	0.02	0.73	0.14	-0.44	0.24	1.40E+09	1.11E+07	6.15E+07	2.21E+05

				6.3		15:22:16	0.04	0.02	0.65	0.09	-0.70	0.25	1.40E+09	1.10E+07	6.12E+07	2.19E+05
				6.4		15:37:55	-0.06	0.02	0.67	0.13	-0.91	0.34	1.37E+09	1.08E+07	6.02E+07	2.16E+05
			3	11.1	25/07/15	12:46:55	1.10	0.02	0.37	0.05	-1.38	0.25	1.65E+09	1.30E+07	7.22E+07	2.59E+05
				11.2		13:02:27	-0.03	0.02	0.52	0.11	-0.97	0.28	1.54E+09	1.21E+07	6.75E+07	2.42E+05
				11.3		13:17:59	-0.37	0.02	0.38	0.12	-1.37	0.37	1.60E+09	1.26E+07	7.01E+07	2.51E+05
				11.5		13:49:18	2.19	0.02	0.58	0.03	-0.65	0.32	1.91E+09	1.51E+07	8.39E+07	3.02E+05
CANIF-37 (4)	Cgl	DC1 (251.5 - 251.8)	1	1	25/07/15	22:39:46	1.35	0.02	0.22	0.09	-0.49	0.27	1.51E+09	1.19E+07	6.62E+07	2.38E+05
				2		22:55:18	0.81	0.02	0.10	0.06	-0.06	0.23	1.46E+09	1.15E+07	6.41E+07	2.30E+05
				4		23:26:21	0.50	0.03	0.87	0.12	-1.39	0.34	1.50E+09	1.18E+07	6.56E+07	2.35E+05
				5		23:41:53	0.84	0.02	0.07	0.06	0.23	0.34	1.57E+09	1.24E+07	6.89E+07	2.47E+05
			2	3	25/07/15	23:10:50	-2.65	0.02	-0.08	0.06	-0.06	0.24	1.45E+09	1.14E+07	6.35E+07	2.27E+05
JB-04	Cgl	João Belo mine	1	1.1	21/03/15	19:25:32	0.00	0.02	0.35	0.06	-0.66	0.35	1.33E+09	1.04E+07	5.83E+07	2.09E+05
				7.1		21:03:23	1.63	0.02	0.06	0.15	0.47	0.34	1.31E+09	1.03E+07	5.76E+07	2.07E+05
			2	3.1	21/03/15	20:07:23	-8.76	0.03	0.07	0.12	0.00	0.45	1.26E+09	9.86E+06	5.49E+07	1.95E+05
				5.1		20:35:22	2.32	0.03	-0.04	0.13	0.04	0.30	1.31E+09	1.03E+07	5.76E+07	2.07E+05
				6.1		20:49:23	-7.33	0.02	-0.03	0.06	0.25	0.39	1.30E+09	1.01E+07	5.65E+07	2.01E+05
				8.1		21:17:20	2.01	0.02	0.23	0.10	-0.06	0.49	1.23E+09	9.69E+06	5.42E+07	1.95E+05
				9.1		21:31:42	4.47	0.02	0.38	0.15	0.20	0.37	1.24E+09	9.76E+06	5.46E+07	1.97E+05
JBA-08	Cgl	João Belo mine	1	1.1	22/03/15	8:47:12	0.92	0.02	0.34	0.19	-0.04	0.31	1.29E+09	1.01E+07	5.64E+07	2.02E+05
				2.1		9:01:11	-1.35	0.03	0.54	0.12	-0.54	0.30	1.28E+09	1.00E+07	5.60E+07	2.00E+05
MRF-04	Cgl	Morro do Cuscuz mine	1	1.1	22/03/15	9:15:14	-0.28	0.02	0.16	0.09	-0.14	0.43	1.23E+09	9.66E+06	5.39E+07	1.93E+05
			2	5.1	22/03/15	9:57:49	0.77	0.02	0.38	0.14	-0.44	0.43	1.27E+09	9.97E+06	5.57E+07	2.00E+05
				6.1		11:05:33	0.00	0.02	0.41	0.10	-0.23	0.46	1.28E+09	1.00E+07	5.61E+07	2.01E+05
MS-1	Cgl	Canavieiras mine	1	1.1	20/03/15	3:42:56	1.31	0.02	-0.01	0.07	-0.16	0.39	1.29E+09	1.01E+07	5.67E+07	2.04E+05
				2.1		4:10:54	1.92	0.02	0.17	0.13	-0.24	0.32	1.35E+09	1.06E+07	5.91E+07	2.12E+05
				5.1		4:52:52	0.72	0.03	0.27	0.05	-0.19	0.44	1.34E+09	1.05E+07	5.89E+07	2.11E+05
			2	3.1	20/03/15	4:24:52	0.82	0.02	0.15	0.09	-0.06	0.44	1.29E+09	1.01E+07	5.66E+07	2.03E+05
				7.1		5:34:51	0.65	0.02	0.13	0.12	-0.03	0.27	1.28E+09	1.00E+07	5.61E+07	2.01E+05
				8.1		5:48:52	2.79	0.02	0.31	0.13	0.02	0.31	1.32E+09	1.03E+07	5.78E+07	2.08E+05
MS-2	Cgl	Canavieiras mine	2	1.1	20/03/15	6:45:13	1.07	0.02	-0.08	0.15	0.31	0.42	1.32E+09	1.03E+07	5.77E+07	2.07E+05
				2.1		6:59:11	1.89	0.03	0.07	0.05	-0.67	0.35	1.26E+09	9.85E+06	5.51E+07	1.98E+05
				3.1		7:13:11	2.61	0.02	0.06	0.14	-0.16	0.28	1.29E+09	1.01E+07	5.65E+07	2.03E+05
				4.1		7:27:25	1.21	0.02	0.04	0.15	-0.26	0.23	1.28E+09	1.01E+07	5.62E+07	2.02E+05
				5.1		7:41:23	1.16	0.02	0.06	0.13	0.38	0.48	1.35E+09	1.06E+07	5.93E+07	2.13E+05
				6.1		7:55:20	1.05	0.02	0.09	0.06	-0.36	0.46	1.28E+09	1.00E+07	5.61E+07	2.01E+05
				6.2		8:09:17	0.88	0.02	0.12	0.16	-0.35	0.31	1.31E+09	1.03E+07	5.73E+07	2.05E+05
				7.1		8:23:32	1.12	0.02	0.28	0.15	-0.10	0.36	1.35E+09	1.06E+07	5.90E+07	2.12E+05
				8.1		8:37:30	1.05	0.02	0.12	0.09	0.17	0.39	1.32E+09	1.03E+07	5.78E+07	2.07E+05
				9.1		8:51:27	0.95	0.02	0.12	0.10	-0.63	0.39	1.27E+09	9.93E+06	5.55E+07	1.99E+05
				10.1		9:05:26	2.18	0.02	-0.06	0.12	0.00	0.28	1.34E+09	1.05E+07	5.88E+07	2.11E+05
MS-3	Cgl	Canavieiras mine	1	1.1	22/03/15	4:21:15	1.95	0.02	0.09	0.20	-0.35	0.35	1.30E+09	1.02E+07	5.72E+07	2.05E+05
				2.1		4:35:15	0.49	0.03	0.35	0.06	-0.50	0.34	1.30E+09	1.02E+07	5.69E+07	2.04E+05
				5.1		5:45:08	-1.59	0.02	0.00	0.07	-0.22	0.36	1.27E+09	9.93E+06	5.54E+07	1.98E+05
				6.1		5:59:10	3.63	0.02	-0.13	0.11	-0.27	0.40	1.32E+09	1.04E+07	5.83E+07	2.09E+05

				6.3		6:27:03	3.65	0.03	0.06	0.10	0.01	0.33	1.34E+09	1.05E+07	5.89E+07	2.12E+05
			2	3.1		5:03:12	1.01	0.02	0.30	0.06	-0.13	0.36	1.31E+09	1.03E+07	5.73E+07	2.06E+05
				4.1	22/03/15	5:31:07	0.55	0.02	0.17	0.18	-0.23	0.36	1.30E+09	1.02E+07	5.70E+07	2.04E+05
				7.1		6:41:04	-0.15	0.03	0.26	0.10	-0.46	0.36	1.20E+09	9.42E+06	5.26E+07	1.89E+05
MVTEX-09 (6.2)	Cgl	DC2 (459.5 to 459.8)	1	3.1		15:54:36	2.47	0.02	0.18	0.15	0.10	0.26	1.31E+09	1.03E+07	5.75E+07	2.07E+05
				6.1	20/03/15	16:36:55	-0.69	0.03	0.22	0.10	-0.58	0.41	1.28E+09	1.00E+07	5.59E+07	2.00E+05
				7.1		16:50:54	0.81	0.02	0.15	0.12	-0.12	0.38	1.36E+09	1.06E+07	5.94E+07	2.13E+05
				6.2	25/07/15	3:02:38	1.98	0.02	0.07	0.10	-0.08	0.34	1.43E+09	1.13E+07	6.30E+07	2.26E+05
			2	1.1		15:12:41	1.04	0.02	0.36	0.05	-0.16	0.38	1.23E+09	9.65E+06	5.39E+07	1.93E+05
				2.1		15:40:38	0.81	0.03	0.42	0.09	-0.62	0.31	1.35E+09	1.06E+07	5.93E+07	2.13E+05
				4.1		16:08:33	1.91	0.02	0.01	0.15	-0.37	0.46	1.27E+09	9.98E+06	5.58E+07	2.00E+05
				5.1	20/03/15	16:22:57	2.29	0.02	0.68	0.13	-1.07	0.46	1.35E+09	1.06E+07	5.93E+07	2.13E+05
				8.1		17:04:51	3.23	0.02	0.12	0.15	0.46	0.40	1.34E+09	1.06E+07	5.91E+07	2.13E+05
				9.1		17:18:55	-3.13	0.02	0.14	0.10	-0.20	0.42	1.32E+09	1.03E+07	5.76E+07	2.06E+05
				10.1		17:32:55	0.68	0.03	0.20	0.10	-0.38	0.30	1.31E+09	1.03E+07	5.75E+07	2.06E+05
				6.3		2:31:36	6.01	0.03	0.09	0.09	-0.01	0.33	1.46E+09	1.15E+07	6.45E+07	2.33E+05
				6.4	25/07/15	2:47:07	0.52	0.03	0.25	0.10	0.45	0.32	1.50E+09	1.18E+07	6.59E+07	2.37E+05
				11.1		4:06:02	-0.29	0.02	0.01	0.12	-0.16	0.34	1.47E+09	1.16E+07	6.44E+07	2.31E+05
MVTEX-09 (8.1)	Cgl	DC2 (518.2 to 518.6)	1	1.1		1:25:00	1.34	0.02	0.42	0.04	-0.29	0.53	1.73E+09	1.36E+07	7.61E+07	2.73E+05
				2.1		1:47:21	1.93	0.02	0.37	0.08	-0.73	0.28	1.43E+09	1.12E+07	6.27E+07	2.25E+05
				5.1	22/03/15	2:29:17	0.31	0.03	0.31	0.07	-0.48	0.39	1.36E+09	1.06E+07	5.95E+07	2.13E+05
				7.1		2:57:18	0.94	0.02	0.14	0.10	-0.27	0.39	1.36E+09	1.07E+07	5.97E+07	2.14E+05
				8.1		3:11:18	0.65	0.03	0.16	0.13	-0.83	0.38	1.35E+09	1.06E+07	5.90E+07	2.11E+05
			2	3.1		2:01:18	0.40	0.03	0.00	0.09	-0.35	0.26	1.23E+09	9.63E+06	5.38E+07	1.93E+05
				4.1	22/03/15	2:15:15	0.71	0.02	-0.05	0.13	-0.56	0.30	1.29E+09	1.01E+07	5.66E+07	2.03E+05
				6.1		2:43:18	0.24	0.03	0.17	0.08	-0.44	0.41	1.30E+09	1.02E+07	5.70E+07	2.04E+05
				9.1		3:25:15	0.22	0.02	-0.12	0.09	-0.33	0.34	1.30E+09	1.02E+07	5.71E+07	2.04E+05
MVTEX-09 (8.2)	Cgl	DC2 (518.2 to 518.6)	2	1.1		16:22:50	0.68	0.02	0.41	0.14	0.00	0.38	1.28E+09	1.01E+07	5.62E+07	2.02E+05
				3.1		16:50:50	1.53	0.02	0.17	0.10	0.12	0.38	1.34E+09	1.05E+07	5.88E+07	2.11E+05
				4.1	21/03/15	17:04:48	0.63	0.02	0.00	0.10	0.46	0.38	1.29E+09	1.01E+07	5.67E+07	2.04E+05
				4.2		17:18:45	0.16	0.03	0.13	0.12	0.07	0.30	1.34E+09	1.05E+07	5.88E+07	2.11E+05
				6.1		17:46:44	0.72	0.02	0.18	0.11	-0.16	0.27	1.28E+09	1.00E+07	5.61E+07	2.01E+05
				8.1		18:15:17	0.90	0.03	0.05	0.09	-0.42	0.34	1.24E+09	9.73E+06	5.44E+07	1.95E+05
MVTEX-01 (18.1)	Cgl	DC3 (387.3 to 387.6)	1	1.1	21/03/15	13:45:14	1.53	0.02	-0.03	0.14	-0.14	0.50	1.26E+09	9.88E+06	5.53E+07	1.98E+05
			2	1.2		13:59:11	1.24	0.03	0.13	0.11	-0.04	0.35	1.28E+09	1.00E+07	5.61E+07	2.01E+05
				2.1		14:13:08	1.20	0.02	-0.03	0.08	-0.29	0.40	1.24E+09	9.71E+06	5.43E+07	1.95E+05
				3.1		14:27:05	0.21	0.02	0.05	0.09	-0.11	0.37	1.33E+09	1.04E+07	5.82E+07	2.09E+05
				3.2	21/03/15	14:41:02	0.18	0.02	0.05	0.05	0.12	0.33	1.35E+09	1.06E+07	5.93E+07	2.12E+05
				4.1		14:55:01	-0.04	0.03	0.01	0.12	0.10	0.52	1.31E+09	1.03E+07	5.74E+07	2.06E+05
				7.1		15:37:04	0.13	0.02	0.18	0.16	-0.41	0.57	1.25E+09	9.84E+06	5.50E+07	1.97E+05
				8.1		15:51:05	-1.36	0.03	0.12	0.10	-0.07	0.40	1.21E+09	9.47E+06	5.29E+07	1.89E+05
Serra da Paciência Formation																

Sample	Rock Type	Outcrop/DC (m)	Pyrite Type	Spot	Date	Time	$\delta^{34}S$ (‰)	2σ	$\Delta^{33}S$ (‰)	2σ	$\Delta^{36}S$ (‰)	2σ	^{32}S cps (median)	^{33}S cps (median)	^{34}S cps (median)	^{36}S cps (median)
FCJ-3	Cgl	Outcrop	2	1.1	20/07/15	11:35:44	2.04	0.03	-0.03	0.11	0.42	0.30	1.43E+09	1.13E+07	6.28E+07	2.26E+05
				1.2		11:50:48	-0.93	0.03	0.06	0.13	0.39	0.29	1.44E+09	1.13E+07	6.29E+07	2.26E+05
				1.3		12:06:07	0.67	0.03	0.27	0.12	0.67	0.42	1.37E+09	1.08E+07	5.99E+07	2.15E+05
				1.4		12:21:31	-2.70	0.03	0.01	0.18	-0.19	0.32	1.33E+09	1.05E+07	5.83E+07	2.09E+05
				1.5		12:36:35	3.08	0.03	0.01	0.13	-0.14	0.43	1.29E+09	1.02E+07	5.67E+07	2.04E+05
				1.6		13:49:50	1.20	0.03	0.07	0.12	0.43	0.37	1.28E+09	1.01E+07	5.61E+07	2.02E+05
				1.7		14:05:01	-0.46	0.03	-0.01	0.10	0.40	0.28	1.36E+09	1.07E+07	5.94E+07	2.13E+05
				1.8		14:20:06	1.13	0.03	-0.10	0.13	0.49	0.36	1.27E+09	9.96E+06	5.55E+07	2.00E+05
				1.10		14:35:15	-4.10	0.03	-0.01	0.09	0.25	0.43	1.35E+09	1.06E+07	5.88E+07	2.10E+05
				1.11		14:50:25	0.89	0.02	0.07	0.08	0.04	0.37	1.34E+09	1.05E+07	5.85E+07	2.10E+05
				1.12		18:54:55	1.13	0.03	0.00	0.17	-0.51	0.36	1.41E+09	1.11E+07	6.20E+07	2.23E+05
				1.13		19:10:03	-1.34	0.03	-0.01	0.04	-0.25	0.36	1.33E+09	1.04E+07	5.80E+07	2.08E+05
				1.14		19:41:37	2.42	0.03	-0.04	0.08	-0.32	0.37	1.27E+09	1.00E+07	5.58E+07	2.01E+05
				1.15		20:14:15	2.97	0.03	-0.04	0.06	-0.35	0.31	1.41E+09	1.11E+07	6.18E+07	2.22E+05
				1.16		20:29:44	3.90	0.03	-0.06	0.05	-0.38	0.42	1.35E+09	1.06E+07	5.93E+07	2.14E+05
				1.17		20:44:53	1.49	0.02	-0.11	0.09	-0.58	0.35	1.27E+09	1.00E+07	5.58E+07	2.01E+05
				1.18		21:00:02	3.09	0.03	-0.08	0.09	-1.07	0.39	1.26E+09	9.91E+06	5.53E+07	1.99E+05
				1.19		21:15:12	3.99	0.02	-0.13	0.10	-0.35	0.25	1.32E+09	1.04E+07	5.80E+07	2.09E+05
PD-09	Qtz	Outcrop	4	1	23/07/15	22:38:30	1.71	0.02	-0.04	0.11	0.31	0.26	1.48E+09	1.17E+07	6.51E+07	2.34E+05
				2		22:54:02	1.52	0.03	-0.01	0.07	0.14	0.28	1.49E+09	1.17E+07	6.52E+07	2.34E+05
				3		23:56:30	1.85	0.02	-0.15	0.11	0.50	0.29	1.49E+09	1.17E+07	6.54E+07	2.35E+05
				4	24/07/15	0:12:02	1.63	0.02	-0.23	0.13	0.17	0.36	1.45E+09	1.14E+07	6.38E+07	2.30E+05
				5		0:27:34	1.44	0.02	-0.12	0.11	0.00	0.26	1.48E+09	1.17E+07	6.50E+07	2.34E+05
PD-14	Ads	Outcrop	6	1	24/07/15	2:16:39	1.35	0.02	-0.68	0.08	0.47	0.23	1.36E+09	1.07E+07	5.95E+07	2.14E+05
				2		3:18:50	-0.36	0.02	-0.64	0.05	0.76	0.24	1.43E+09	1.12E+07	6.27E+07	2.25E+05
			6.1	3	24/07/15	3:34:22	0.76	0.02	0.20	0.11	-0.70	0.38	1.27E+09	1.00E+07	5.58E+07	2.01E+05
				4		3:49:54	0.94	0.03	-0.24	0.06	0.01	0.31	1.39E+09	1.10E+07	6.11E+07	2.20E+05
			6	5	24/07/15	4:05:26	-0.24	0.02	-0.36	0.10	0.89	0.48	1.32E+09	1.04E+07	5.78E+07	2.08E+05
				6		19:15:05	0.44	0.02	-0.76	0.06	0.65	0.26	1.53E+09	1.21E+07	6.72E+07	2.42E+05
				7		19:30:36	-0.07	0.02	-1.15	0.14	1.38	0.24	1.51E+09	1.19E+07	6.61E+07	2.37E+05
SP-01	Qtz	Outcrop	2	1	24/07/15	4:21:14	2.70	0.02	-0.59	0.13	-1.56	0.34	1.47E+09	1.16E+07	6.47E+07	2.33E+05
				2		4:36:46	1.27	0.02	-0.10	0.16	0.21	0.31	1.40E+09	1.10E+07	6.13E+07	2.20E+05
				3		4:52:19	0.83	0.02	0.27	0.13	-0.52	0.24	1.41E+09	1.11E+07	6.17E+07	2.21E+05
				4		5:07:51	-1.71	0.02	-0.18	0.10	0.09	0.36	1.41E+09	1.10E+07	6.15E+07	2.21E+05
			4.1	5	24/07/15	5:23:23	0.53	0.03	2.53	0.11	-1.81	0.23	1.38E+09	1.09E+07	6.05E+07	2.17E+05
			1	6	24/07/15	5:38:55	1.43	0.02	0.23	0.06	0.03	0.36	1.45E+09	1.14E+07	6.37E+07	2.29E+05
			2	7	24/07/15	6:41:40	1.20	0.03	0.15	0.08	-0.17	0.28	1.37E+09	1.08E+07	6.02E+07	2.16E+05
			1	8	24/07/15	6:57:11	1.10	0.02	0.07	0.10	-0.07	0.34	1.68E+09	1.32E+07	7.37E+07	2.64E+05
			5	9	24/07/15	7:12:43	0.52	0.02	2.47	0.06	-1.85	0.33	1.40E+09	1.10E+07	6.13E+07	2.20E+05
			2	10	24/07/15	20:48:21	2.70	0.02	0.08	0.08	-0.06	0.31	1.44E+09	1.13E+07	6.32E+07	2.27E+05
			4.1	11	24/07/15	21:03:54	0.44	0.02	2.28	0.13	-1.94	0.25	1.50E+09	1.18E+07	6.57E+07	2.35E+05
			5	12	24/07/15	21:19:26	-0.03	0.02	2.45	0.14	-1.92	0.31	1.51E+09	1.19E+07	6.62E+07	2.37E+05

1	13	24/07/15	22:06:06	-4.07	0.02	0.47	0.07	0.13	0.20	1.66E+09	1.30E+07	7.23E+07	2.58E+05
5	14	24/07/15	22:21:37	-0.68	0.02	2.50	0.09	-2.14	0.32	1.44E+09	1.13E+07	6.30E+07	2.26E+05
1	15	24/07/15	22:37:09	1.53	0.02	0.33	0.10	-0.41	0.23	1.50E+09	1.18E+07	6.57E+07	2.36E+05
5	16	24/07/15	22:52:40	0.53	0.03	1.62	0.04	-1.21	0.31	1.48E+09	1.17E+07	6.49E+07	2.33E+05
	17		23:08:12	0.42	0.02	0.58	0.11	-1.01	0.26	1.50E+09	1.18E+07	6.59E+07	2.36E+05
4.1	18	24/07/15	23:23:44	-0.03	0.02	2.46	0.17	-2.08	0.31	1.49E+09	1.17E+07	6.51E+07	2.33E+05
	19		23:39:16	0.44	0.02	1.08	0.10	-0.64	0.36	1.53E+09	1.20E+07	6.70E+07	2.40E+05
2	20	24/07/15	23:54:48	1.62	0.03	-0.01	0.11	0.17	0.31	1.51E+09	1.18E+07	6.61E+07	2.37E+05

Abbreviations: Cgl (conglomerate); Qtz (quartzite); Ads (andalusite-schist). Pyrite types: (1) detrital inclusion-bearing; (2) detrital massive; (3) detrital in quartz-pebble; (4) euhedral-hydrothermal; (4.1) euhedral-diagenetic; (5) euhedral overgrowth-diagenetic; (6) anhedral-syngenetic; and (6.1) subhedral-syngenetic.

Table 7.4. LA-ICP-MS trace elements data (in ppm) for pyrite samples from Jacobina Basin. The correspondent SHRIMP-SI spots are indicated.

Serra do Córrego Formation																									
Sample	**Pyrite Type**	**Spot**	**^{49}Ti**	**^{51}V**	**^{53}Cr**	**^{55}Mn**	**^{59}Co**	**^{60}Ni**	**^{65}Cu**	**^{66}Zn**	**^{75}As**	**^{77}Se**	**^{95}Mo**	**^{107}Ag**	**^{118}Sn**	**^{121}Sb**	**^{125}Te**	**^{181}Ta**	**^{195}Pt**	**^{197}Au**	**^{202}Hg**	**^{205}Tl**	**^{208}Pb**	**^{209}Bi**	**Co/Ni**	**SHRIMP-SI spot**
CANIF-37 (1.1)	1	2	1210	4.3	84	1.3	348	699	3.1	1.1	1335	9.9	bdl	0.3	bdl	1.8	10.9	0.6	bdl	0.7	0.2	0	34.8	16.6	0.5	3.1
		5	24	0.5	bdl	bdl	119	720	bdl	0.6	253	76.5	0	bdl	bdl	0.4	34.9	bdl	bdl	0.1	0.1	bdl	6.1	2.8	0.2	6.1
		7	40.7	1.8	8.5	80	155	310	41.2	1.8	860	39.2	bdl	1.4	0.3	152	24.4	0	0	1.1	0.3	0.1	663	57.9	0.5	5.1
	2	1.2	6.8	bdl	bdl	bdl	8430	98.4	0.4	bdl	bdl	8.3	bdl	bdl	bdl	bdl	bdl	bdl	bdl	bdl	0.2	bdl	bdl	bdl	85.7	1.1-2
		1.3	7.5	bdl	bdl	bdl	1112	20.6	0.4	0.1	12	5.1	bdl	bdl	bdl	bdl	bdl	bdl	bdl	bdl	bdl	bdl	bdl	0.2	54	1.1-3
		1.4	9	bdl	bdl	0.6	1144	21.7	0.5	0.4	7.9	5.7	bdl	bdl	0.4	bdl	bdl	bdl	bdl	0	bdl	bdl	0	0	52.7	1.1
		4	24.2	3.2	169	3.4	1178	465	37	1.3	1398	21.7	0.2	0.4	bdl	0.2	bdl	bdl	bdl	0.3	0.2	0.1	38	5.3	2.5	4.1
		9	19.4	0.6	23.8	10.5	126	113	5.1	3.2	263	1.6	1.5	0.1	bdl	5.4	13.5	bdl	bdl	1.5	0.1	0.9	13.3	22	1.1	8.1
		10	18.1	0.1	bdl	1.5	16.1	17.6	0.9	0.7	34.8	2.7	bdl	bdl	bdl	0.3	bdl	bdl	bdl	0.1	0.2	0.2	2.3	2.4	0.9	9.1
		11	19.2	0.1	bdl	bdl	1042	900	0.9	0.6	1340	13.2	bdl	0	bdl	0.5	bdl	bdl	bdl	0.1	0.1	bdl	9.8	2.1	1.2	10.1
		12	19.8	0	bdl	0.5	72.3	227.6	2.1	1.6	188	4.4	0.1	0.1	bdl	4.5	3.4	bdl	bdl	0.2	0.1	5.4	17.3	6.7	0.3	12.1
		13	23.7	0	bdl	bdl	12.5	14.9	0.4	0.8	136.4	bdl	bdl	bdl	bdl	bdl	bdl	bdl	bdl	0	0.1	bdl	0.2	0.2	0.8	14.1
CANIF-37 (1.2)	1	5	810	1.2	8.8	0.9	82	132.7	0.6	0.7	599	48.2	bdl	bdl	0.3	0.4	10.1	0.3	bdl	0.1	0.1	bdl	6.4	3.8	0.6	3.1
		9	420	1.2	17.7	0.7	866	597	4.8	bdl	3470	90.9	0.1	0.4	bdl	3.4	46.5	0.2	bdl	1.2	bdl	0	82	33.7	1.5	5.1
	2	1.2-1	13.3	0	bdl	bdl	755	249	0.4	0.2	1106	14.3	bdl	bdl	bdl	6.6	0.7	bdl	bdl	bdl	0.1	0.2	2.6	1.5	3	2.1
		2	14.6	1.1	6.6	7	172	198	1.8	0.6	61.5	8.3	bdl	0	bdl	0.3	1.1	bdl	bdl	0.1	0.2	bdl	3.7	4.1	0.9	1.1
CANIF-37 (2.2)	1	1.1	10.3	0.3	1.6	71	59.3	280	4.3	2.3	100.6	5.7	bdl	0.2	bdl	1.3	2.1	bdl	bdl	0.2	0.2	bdl	49	7.9	0.2	9.1
		2.1	7.4	0.2	11.2	0.8	69	73	48	9.6	5650	19.4	bdl	29	bdl	6.2	19.7	0	0	26	0.2	bdl	4100	210	0.9	10.1
		2.2	bdl	bdl	bdl	bdl	23.2	51.5	bdl	bdl	11400	1.4	bdl	0.4	bdl	3.1	9.2	bdl	bdl	1.4	0.1	bdl	75	25	0.5	10.2
		2.3	9.2	0	0.4	bdl	28.3	56.6	0.8	0.1	13850	bdl	bdl	0.1	bdl	0.7	0.6	0	0	0.4	0.1	bdl	3.2	1.2	0.5	10.3
		16	28.1	0.2	5.2	bdl	25.5	35.6	1.2	0.7	317	57.4	bdl	bdl	bdl	0.5	24.2	bdl	bdl	bdl	0.1	bdl	2.6	bdl	0.7	1.1
	2	1.2	bdl	0.1	2.9	bdl	164	4600	3.9	0.5	159	6.5	bdl	0.1	0.5	0.6	1	0	bdl	0.3	0.2	bdl	23	4.6	0	9.3
		1.3	180	1.1	115	1.2	932	433	6.2	1.6	3700	16.8	0.1	0	bdl	0.3	bdl	0.1	bdl	0.5	0.2	bdl	11	bdl	2.2	9.2
		1.4	7.9	0	bdl	0.5	1527	351	3.7	0.5	2380	21.1	bdl	0	bdl	0.2	bdl	bdl	bdl	0.4	0.2	bdl	6.8	0.3	4.4	9.4
		3.1	33	0.5	33	0.8	800	278	3.3	3.7	850	3.8	bdl	bdl	bdl	bdl	bdl	0.0	bdl	0.7	0.2	bdl	9	3.2	2.9	11.1
		3.2	17.7	1.1	66	0.7	1527	424	3.2	1.3	3590	23.1	bdl	0.1	bdl	0.2	0.9	bdl	bdl	0.5	0.2	bdl	3.4	0.8	3.6	11.2
		3	1220	1.8	40	0.7	2710	670	3	1.2	4640	21	0.2	0.1	0.3	1	bdl	6.8	bdl	0.2	0.2	0	7.7	2.7	4	22.1
		4	25.8	0.1	bdl	0.4	2260	197	bdl	bdl	1220	21.2	bdl	bdl	bdl	0.3	bdl	bdl	bdl	bdl	0.1	bdl	4	0.3	11.5	16.1
		5	22.6	bdl	0.3	bdl	1396	288	2.5	2.4	1359	19.8	bdl	bdl	bdl	bdl	bdl	bdl	bdl	0.7	0.1	bdl	11.7	0.6	4.8	15.1

		7	24.3	0.4	23.8	1.1	1590	353	17.1	1.7	755	20.4	0	0.3	bdl	0.1	bdl	bdl	bdl	0.4	0.1	bdl	6	2.4	4.5	12.1
		9	23.9	0.1	bdl	bdl	1270	364	0.7	0.6	2720	20.4	bdl	bdl	bdl	bdl	bdl	bdl	bdl	0.1	0.2	bdl	0.1	0	3.5	
		12	24.1	bdl	bdl	bdl	1385	327	bdl	bdl	1468	23.7	bdl	bdl	bdl	bdl	bdl	bdl	bdl	bdl	0.2	bdl	bdl	bdl	4.2	5.1
		13	24.5	0	bdl	bdl	bdl	bdl	0.8	1.2	bdl	24.3	bdl	0	bdl	bdl	bdl	bdl	bdl	0.6	0.1	bdl	0.1	0.1	-	
		14	200	0.2	7.4	bdl	1387	760	0.8	0.8	3190	24.3	bdl	bdl	0.2	0.2	bdl	0.8	0.0	0.1	0.1	bdl	1.7	1.9	1.8	4.1
		15	19.7	0.3	11.1	0.6	bdl	116	14.6	1.3	168	bdl	0.1	0.3	0.3	3.6	22.3	0	0.1	1.4	0.1	10.9	12.8	29.2	-	
		17	21.7	0.1	bdl	bdl	1454	257	0.5	0.7	1309	20.9	bdl	bdl	bdl	bdl	bdl	bdl	bdl	bdl	0.1	bdl	bdl	0	5.7	
		1.1	28	0.4	2.7	6.7	194	143.8	7.4	1.1	559	86.5	bdl	0.4	bdl	7.6	19.5	0	bdl	1.6	0.1	bdl	110	17.9	1.3	1.2
		1.2	26	13.2	121	29.6	1308	629	12.1	15.8	2240	63.1	0.1	0.8	0.5	16	16	0	bdl	1.7	0.1	0	370	32.1	2.1	
		1.3	79	1.9	24.6	22.4	794	465	10.7	12.9	1660	80.8	bdl	2.1	bdl	23.2	33.4	0	bdl	15.4	bdl	0.1	493	61.3	1.7	1.4
		3.1	18	2.3	23.5	bdl	bdl	45.6	64	2.5	728	133	0.4	0.1	bdl	1.1	6.3	bdl	bdl	1	0.3	bdl	bdl	2	-	3.3
	1	3.2	750	2.9	17.5	1.1	1650	2000	bdl	0.5	2298	73.1	bdl	0.1	0.7	1	4.9	0.1	bdl	0.5	0.2	bdl	4.6	2.2	0.8	3.1
		3.3	1110	3.8	10.9	6.9	6290	502	1.6	0.3	2230	76.8	bdl	0.2	bdl	1.7	2.1	0	bdl	0.6	0.2	bdl	27.5	4.8	12.5	
		3.1-1	5400	12.3	88	7.9	611	392	6.3	3.6	662	34.2	bdl	0.8	bdl	9.6	31.6	4.9	0.5	1.3	0.4	0.1	109	43.6	1.6	8.1
		3.1-4	390	12.2	83	4	459	229	12.2	3	444	22.8	bdl	0.5	bdl	7.5	25.2	0.2	bdl	1.2	0.1	0.1	86	35.9	2	8.4
		3.1-10c	10.4	3.5	4.2	37.2	501	84.6	23	4	131	20.2	bdl	0.2	bdl	5.3	4.2	bdl	bdl	1.5	bdl	bdl	44.3	16.6	5.9	14.1
CANIF-37 (3)		3.1-13	15.3	0.7	7.7	8.2	307	211	6	9	492	21.7	bdl	0.4	bdl	5	4.9	0	bdl	0.5	0.3	0.6	104	30.4	1.5	9.1
		2.1	30	4.9	134	0.7	1278	164.6	2.9	4.4	1634	53.8	0.4	0.1	0.7	4.1	2.6	bdl	bdl	0.1	0.2	0.1	15.7	4.5	7.8	2.2
		2.2	7	0	bdl	0.6	1248	30.9	5	0.8	252	73.4	0.8	2	0.5	5	3.6	bdl	bdl	0.3	0.2	16.8	170.5	4.4	40.4	2.1
		2.3	7	0	bdl	0.4	779	32.8	3.2	0.8	295	51.1	1	0.4	0.6	2.5	1.6	bdl	bdl	0.2	0.1	3.4	59.2	3.7	23.8	
		2.4	7.6	0	bdl	0.6	1167	83.3	6.8	0.7	553	58.4	1.1	0.5	0.5	3.4	2.6	bdl	bdl	0.3	0.1	1.4	72.9	4.3	14	
	2	6.1	7.6	bdl	bdl	0.4	28.7	276	16.2	0.6	16.9	2.6	bdl	0	bdl	0.4	bdl	bdl	bdl	bdl	0.2	0.7	8.9	0.8	0.1	6.2
		6.2	7.9	bdl	bdl	bdl	43.3	456	1	0.5	9.0	4.3	0	0	bdl	0.1	bdl	bdl	bdl	0.1	0.1	0.5	16.8	0.3	0.1	6.3
		9.1	9	bdl	bdl	bdl	479	471	bdl	0.1	4100	20.3	bdl	bdl	bdl	bdl	bdl	bdl	bdl	0.0	0.3	bdl	0	0	1	
		3.1-7	17.6	bdl	bdl	bdl	bdl	bdl	bdl	0.5	2410	29.9	bdl	bdl	bdl	bdl	6.7	bdl	bdl	1.6	bdl	bdl	0.1	bdl	-	
		3.1-16	75	4.4	57	2.3	661	350	48	0.9	1980	12.9	bdl	0.4	bdl	56.9	13.7	0	bdl	0.5	bdl	0.4	44.3	52	1.9	
		4-2	36.4	2.9	7.3	17.9	427	134	32.7	bdl	645	3.2	bdl	0.2	bdl	15	66.7	bdl	bdl	1.1	0.5	26	134	36	3.2	5
	1	4-4	16.6	bdl	2.1	1.6	288	789	1.1	1.3	260	bdl	0	bdl	bdl	1.1	7	bdl	0	bdl	0.3	0.9	6.2	3.7	0.4	4
CANIF-37 (4)		4-5	800	10.2	8.4	1	690	706	37	0.5	276	8.4	bdl	bdl	0.3	0.9	9.6	0.2	bdl	0.8	0.1	bdl	6.5	3.7	1	2
		4-1	23.1	bdl	bdl	bdl	92	79.5	0.4	0.7	392	35.3	bdl	bdl	bdl	bdl	2.7	bdl	bdl	bdl	0.2	bdl	0.3	0.1	1.2	
	2	4-3	24.4	0.5	bdl	bdl	576	313	bdl	bdl	85.5	118	bdl	bdl	bdl	bdl	bdl	0	bdl	bdl	0.3	bdl	bdl	bdl	1.8	3
		4-6	16	0	bdl	0.6	77.4	126.8	1.7	0.9	111.9	1.2	0.1	0	bdl	24.2	bdl	bdl	bdl	0.1	0.2	2.1	15.0	1.2	0.6	
CANIF-37 (4.2)	2	4.2-4	34.6	0.1	bdl	bdl	552	71.4	1.2	1.1	93.5	21.1	bdl	0.1	bdl	0.6	bdl	bdl	bdl	0.1	0.1	0.5	4.3	1	7.7	
		4.2-6	40.3	0.1	bdl	0.3	510	529	1.0	1.5	964	19.7	bdl	bdl	bdl	0.3	3.4	bdl	bdl	0.2	0	bdl	0.5	0.6	1	
		5_4	15.7	bdl	bdl	bdl	3030	bdl	bdl	bdl	bdl	bdl	bdl	bdl	bdl	bdl	bdl	bdl	bdl	bdl	bdl	bdl	bdl	bdl	-	
		5_5	20.1	0.1	bdl	0.3	127	255	0.3	0.2	34.9	56	bdl	bdl	bdl	bdl	0.5	bdl	bdl	0.1	bdl	bdl	0.3	0.3	0.5	
CANIF-37 (5)	2	5_6	13.1	0.4	18.4	2.3	2230	30.5	2.7	1.1	18.1	38.6	0	bdl	bdl	bdl	2.5	bdl	bdl	0.7	bdl	bdl	0.1	0.1	73.1	
		5_7	14.3	0	bdl	bdl	129.9	113.6	0.2	0.1	911	10.6	bdl	bdl	bdl	bdl	bdl	bdl	bdl	bdl	bdl	bdl	0	bdl	1.1	
		5_8	11.9	bdl	0.3	bdl	344	292	5.3	bdl	1060	7.8	0	bdl	bdl	4.4	1.9	bdl	bdl	bdl	bdl	2.4	bdl	2.1	1.2	
		6.1_2	10.8	0	bdl	1.8	27.4	98.4	2.1	0.7	78.2	1.6	bdl	0	bdl	95.8	3.1	bdl	bdl	0.2	0.1	1.6	8.3	4.7	0.3	
CANIF-37 (6)	2	6.1_3	11.7	0	bdl	1.6	179	110	0.6	0.3	560	4.7	bdl	bdl	0.2	0.6	0.4	bdl	bdl	0.1	0.1	3.5	1.8	0.9	1.6	
		6.1_6	15.4	0.6	1.5	2.3	1000	417	3.7	1	1950	29.2	bdl	0.1	0.3	1.4	1.2	bdl	bdl	0.1	bdl	0.3	16.5	4.5	2.4	
CANIF-37 (7)	2	7.1_2	13.6	bdl	bdl	bdl	147	42.1	26	bdl	3460	3.7	bdl	4.3	bdl	15.9	310	bdl	bdl	28	bdl	bdl	710	600	3.5	
		7.1_3	14	0.03	bdl	bdl	882	4320	0.4	bdl	9130	12.1	bdl	bdl	bdl	bdl	19.2	bdl	bdl	0.1	bdl	bdl	0.5	0.5	0.2	
	1	1	1720	8.1	218	2.5	1670	1400	5	2.3	3580	40.6	bdl	0.7	bdl	25.8	17.8	1.1	bdl	1.1	bdl	0.1	104	48	1.2	
JBA-04		3C	2600	11.9	648	2.7	751	467	7.3	2.7	920	45.6	bdl	0.6	0.9	15.5	15.4	1.4	bdl	1.1	bdl	0.1	69.2	31.7	1.6	
	2	2	21.1	0.2	6.8	bdl	113	27.8	6.7	0.5	90.7	28.6	bdl	0.5	bdl	10.9	4.2	bdl	bdl	0.8	0.1	9.6	23.6	11.7	4.1	

		5	18.4	bdl	bdl	1.8	bdl	131.7	0.2	0.3	720	23.7	bdl	bdl	bdl	bdl	bdl	0	bdl	bdl	bdl	bdl	bdl	bdl	-	
JBA-08	1	2	24	1.4	53.8	bdl	2380	1092	6.2	0.6	491	48.2	bdl	0.4	bdl	9.3	7.2	bdl	bdl	1	0.1	0.1	48.5	10.4	2.2	2.1
		3	17.3	1.1	27.7	0.6	94.1	138.6	1	0.8	70.2	5	bdl	0.2	0.4	17.3	1.6	bdl	bdl	0.6	0.1	1.8	19.3	3.7	0.7	1.1
		3C	34.8	6.1	197	6.1	736	331	6.9	3.7	640	bdl	bdl	1	0.9	50.9	8.3	0	bdl	2.8	bdl	0.8	150	44.7	2.2	
	2	8	9	0	bdl	1.8	33.3	136.5	0.7	0.3	26.4	1.8	bdl	0	bdl	15.2	bdl	bdl	bdl	0.2	0.1	0.1	10.8	0.5	0.2	
		1	29.3	0.1	bdl	2.1	bdl	21.3	bdl	0.8	279	762	0.6	bdl	bdl	35	bdl	0	bdl	1	bdl	bdl	1	0.7	-	
JBA-06	1	4	2120	11.4	453	14.2	720	465	6.4	18.3	5740	28.4	0.1	1.5	1.3	46.6	21.3	0.6	bdl	2.5	bdl	0.6	273	43.9	1.5	
		5	84	1.9	40	2.3	500	127	2.6	3.1	313	12.9	0	0.7	bdl	11.5	6.8	0	bdl	0.5	bdl	0.1	144	19.8	3.9	
	2	1	430	0.9	18.8	bdl	820	215	7.5	0.5	433	34.9	bdl	1	bdl	3.8	7.9	0.1	bdl	0.7	bdl	bdl	17.8	2.4	3.8	
		3	34.9	3.4	154	4.4	249	85.2	3.44	bdl	242	7.2	bdl	0.4	0.7	31.7	7	0	bdl	0.8	bdl	0.8	92.7	24.9	2.9	
JBA-05	1	1	26	0.2	25.3	5.4	369	209	10.9	1.5	446	9.3	0	0.9	bdl	32	8	0	bdl	3	bdl	0.5	60.1	27.2	1.8	
		3C	840	8.1	1180	9.2	476	450	20.9	26.8	991	24.8	0	0.9	1.1	36.1	22.3	0.1	bdl	0.5	bdl	0.3	165	53.9	1.1	
	2	4	bdl	bdl	bdl	bdl	322	409	bdl	bdl	1210	10.7	0	bdl	bdl	bdl	5.6	0	0	bdl	bdl	bdl	3.1	bdl	0.8	
JBA-03	1	3	48	0.2	12.2	bdl	629	1817	1.3	0.6	375	52.9	0	1	bdl	2.6	3	0	0	0.1	bdl	0	145	18	0.3	
		4	18.7	0.5	31	2.4	553	bdl	1.6	bdl	82	7	bdl	bdl	0.8	1.8	5.8	0	bdl	0.1	bdl	bdl	9.9	3.1	-	
		5C	340	4.2	305	5.1	1450	190	10.4	1.2	398	91.2	bdl	0.5	bdl	15.6	6.3	0	0	0.5	bdl	bdl	40.9	31.7	7.6	
		6C	226	18.6	325	5.8	670	363	7.0	1	432	12.4	0.1	0.3	0.5	14.5	6.3	0.1	0	0.5	bdl	bdl	43.2	29.4	1.8	
	2	1	bdl	bdl	3.5	bdl	410	320	1.9	bdl	137	20.1	bdl	0.1	0.7	1.2	1.6	bdl	0	0.2	0.2	bdl	10	3	1.3	
		3	11.8	1.9	209	1.4	349	126	2.1	1	202	4	bdl	0.1	bdl	56.5	0.9	bdl	bdl	0.2	0.2	1	11.5	3.3	2.8	
		5	11.6	bdl	bdl	bdl	bdl	12.8	0.8	bdl	377	27.7	bdl	bdl	bdl	1.3	2.2	bdl	bdl	bdl	0.1	bdl	7.5	1.7	-	
		6	13.5	0.03	bdl	bdl	6.7	13.1	0.3	bdl	227	19.8	bdl	bdl	bdl	0.3	0.6	bdl	bdl	bdl	0.1	bdl	1.8	0.4	0.5	
		9	bdl	bdl	bdl	1.0	360	129	0.8	bdl	260	28.6	bdl	0	bdl	0.8	bdl	bdl	bdl	bdl	0.1	bdl	2.1	1.1	2.8	
		11	14	0.6	39	bdl	204	172.7	4.8	0.3	173	1.7	bdl	0.1	0.4	5.7	1.1	0	bdl	0.1	0.1	0.4	9.7	3.8	1.2	
		1	110	0.8	4.8	bdl	65.1	105.2	3.3	bdl	99.3	31.4	bdl	0.2	bdl	6.1	1.8	0	0	0.3	bdl	bdl	32.3	8.8	0.6	
		5C	340	4.2	305	5.1	1450	190	10.4	1.2	398	91.2	bdl	0.5	bdl	15.6	6.3	0	0	0.5	bdl	bdl	40.9	31.7	7.6	
		7	18.9	bdl	bdl	bdl	48.3	151.6	1.5	0.6	253	bdl	bdl	0	bdl	68.7	bdl	0	0	bdl	bdl	0.3	3.7	3.9	0.3	
JB-04	1	9	15.1	0.3	8.6	1.1	1184	74.7	1.3	1.7	808	42.5	bdl	0.2	bdl	4.3	14	bdl	bdl	0.3	bdl	bdl	34.4	29.4	15.9	7.1
	2	2C	23.4	bdl	bdl	bdl	32.4	270	bdl	bdl	535	65.2	bdl	bdl	bdl	bdl	4	0	bdl	0	bdl	bdl	0.9	0.5	0.1	
		3	121	3.3	19.8	1.2	84.3	471	0.6	0.7	4820	23.1	bdl	0.2	bdl	5.7	3.1	0	bdl	1.1	bdl	bdl	23.7	7.8	0.2	5.1
		7	11.1	0	bdl	bdl	467	25.7	bdl	bdl	bdl	9.2	bdl	bdl	0.4	bdl	bdl	bdl	bdl	bdl	bdl	bdl	bdl	bdl	18.2	6.1
		10	12.4	bdl	bdl	1.6	271	581	bdl	1.6	303	23.2	bdl	0.2	0.9	2.8	6	0	bdl	0.1	0.3	bdl	8	5.5	0.5	8.1
		11	5200	11.2	32.1	1.9	2560	302	1.3	0.5	1340	14.7	bdl	0.7	0.9	10.6	4.8	0.1	bdl	0.9	bdl	bdl	46.1	14.5	8.5	9.1
		12	112	1.5	58	1.2	406	145	1.2	0.9	490	7	0.0	0.1	bdl	3.7	3.9	0	bdl	0.1	bdl	bdl	5	6.6	2.8	
MRF-04	1	5	7.3	0	0.2	12.7	147.1	277	3.3	0.8	134	14.4	bdl	1.5	bdl	6.7	11.1	bdl	bdl	0.3	0.1	6	15.9	9.6	0.5	1.1
		7	9.4	bdl	0.2	0.6	135.4	214.4	1.3	0.2	115.2	6.4	bdl	0.1	0.5	3.2	7.3	bdl	bdl	0.2	0.1	2.5	7.2	6.1	0.6	
		16	19	4.9	97	1.1	610	835	1.2	0.8	729	22.7	bdl	0.1	0.5	1.5	4.5	bdl	bdl	0.1	0.2	bdl	15.8	7.5	0.7	
	2	10	28.2	0.1	7	0.8	2510	800	1.6	0.3	3150	43.7	bdl	0.1	0.4	1.3	2.7	bdl	bdl	0.2	0.1	bdl	56	4.4	3.1	5.1
		12	bdl	bdl	bdl	bdl	2490	269	bdl	bdl	2311	31.6	bdl	0	bdl	bdl	bdl	bdl	bdl	0	0.2	bdl	3.4	0.1	9.3	
		14	10.8	bdl	0.6	bdl	bdl	bdl	0.3	bdl	120.5	97.7	bdl	bdl	bdl	bdl	4.1	bdl	bdl	0	0.1	bdl	0.1	0.4	-	6.1
MS-1	1	6	19.5	3.55	188	5.5	465	321	4.8	3.0	940	12.5	bdl	0.4	bdl	12.5	7.7	bdl	bdl	1	0.2	1.12	85	24	1.4	2.1
	2	2	14.2	0	bdl	bdl	8.9	26.7	1	0.3	13.6	44.7	bdl	0.2	bdl	7.7	0.5	bdl	bdl	0.1	bdl	0.1	1.9	0.8	0.3	
		8	15.5	0.1	2.9	bdl	844	710	0.2	bdl	2550	38.2	bdl	bdl	bdl	0.2	0.7	bdl	bdl	0	0.3	bdl	1.2	0.9	1.2	3.1
MS-3	1	4	24.1	13.1	7.5	5	194	77.2	1.1	0.8	77.8	119	bdl	0.1	bdl	1	1.3	bdl	bdl	0.1	bdl	bdl	7	9.4	2.51	2.1
		6	240	1.4	29.5	0.6	310	1310	1.3	0.4	239	12.9	bdl	0.1	bdl	1.1	1.2	0.2	bdl	0.3	0.1	bdl	6.8	8.2	0.2	
		16	82	9.5	106	15.7	221	381	4.6	1.2	102.1	4.6	0	0.4	bdl	5.1	6.4	bdl	bdl	1.4	0.1	0.1	21.3	46.7	0.6	6.1
	2	1	16.6	0.0	bdl	bdl	30.5	128.3	0.4	0.2	9.9	1.1	0	0	bdl	0.4	0.3	bdl	bdl	0.1	0	7.2	20.1	2.3	0.2	3.1

		2	21.4	0.1	bdl	bdl	956	132.6	0.2	0.6	544	33.5	bdl	bdl	bdl	bdl	bdl	bdl	bdl	0	0.1	bdl	0.2	0.2	7.2	
		9	14.7	0.1	bdl	0.5	90.5	107.4	3.2	0.6	173	bdl	0.1	0.4	bdl	12.6	11.5	bdl	bdl	0.7	0	13.2	20.1	25.6	0.8	
		12	17.3	bdl	bdl	bdl	bdl	1027	0.2	0.2	2750	35.5	bdl	bdl	bdl	bdl	bdl	bdl	bdl	bdl	0.1	bdl	bdl	bdl	-	
		13	17.6	0.1	bdl	0.3	697	191.9	0.2	0.2	497	23.4	bdl	bdl	bdl	bdl	bdl	bdl	bdl	0.0	0.1	bdl	bdl	bdl	3.6	
	1	2	50	2.1	111	41	409	232	7	85	325	21.6	0	0.7	bdl	4.7	7.4	bdl	bdl	0.4	0.1	bdl	198	48	1.8	3.1
		8	503	5.8	96	7.2	1300	735	9.6	18.3	555	54.8	bdl	0.8	bdl	12.7	22.3	0.2	0	3.0	0.2	0.1	210	64.4	1.8	7.1
		1	18.5	0	bdl	1.8	116	184	1.4	1.6	65	4.7	bdl	0.1	bdl	47.8	bdl	bdl	bdl	0.2	0.2	5.9	8.4	6.3	0.6	2.1
MVTEX-09 (6.2)		3	25.7	bdl	bdl	bdl	131	143	2.9	bdl	91.6	3.2	0	0.3	bdl	3.9	bdl	bdl	bdl	0.2	0.1	bdl	13.5	8.2	0.9	10.1
	2	4	1410	3	4.8	3.3	225	57.3	2.1	0.9	199	18.5	bdl	0.1	bdl	0.4	3.5	0.1	bdl	0.3	0.2	bdl	5.9	6.7	3.9	4.1
		6	335	1.6	230	4.3	276	540	11.4	69	850	19.4	0.2	0.6	bdl	21.7	3.8	0.2	bdl	0.2	0.2	0.1	271	23	0.5	5.1
		7	21.6	bdl	bdl	0.4	100.7	49.1	5.9	1.4	213	9.7	0.2	2.5	bdl	21	bdl	bdl	bdl	0.2	0.2	0.1	209	5.3	2.1	8.1
		6	650	3.7	119	13.9	706	362	2.2	4.8	686	36.5	0	0.4	0.2	13.6	13.2	0.3	bdl	0.6	0	0.1	94	23.4	2	2.1
	1	9	31.7	3.7	1480	171	850	299	0.9	600	733	12.9	bdl	0.3	bdl	1.5	3.4	0	bdl	1	bdl	bdl	31.3	3.3	2.8	5.1
		14	112	1.5	147	4.6	1230	575	4.1	19.5	1340	79	0.1	0.4	0.3	4.8	37.2	0	0	0.5	bdl	0.1	44.5	11.5	2.1	7.1
		1	32.7	bdl	bdl	bdl	11	38.1	bdl	bdl	18.6	5.8	bdl	bdl	bdl	bdl	bdl	bdl	bdl	bdl	bdl	bdl	bdl	0.1	0.3	
MVTEX-09 (8.1)		2	33	0.1	bdl	bdl	1155	370	0.6	0.3	1877	15.8	bdl	bdl	bdl	bdl	bdl	bdl	bdl	bdl	0	bdl	0.0	0	3.1	4.1
		3	25.2	bdl	bdl	bdl	bdl	264.3	1.5	bdl	bdl	2.5	0.3	0.1	bdl	32.5	2.9	bdl	0	0.6	0.1	1.4	14.1	5.5	-	6.1
	2	4	24.2	0.1	1.9	0.8	15.5	59.3	0.9	0.48	32.5	3.1	bdl	0	bdl	26.7	2.2	bdl	bdl	0.3	bdl	0.2	7	3.1	0.3	3.1
		5	29.3	0.1	0.5	bdl	256	858	0.9	0.3	1350	29.9	0	0	bdl	1.4	2.31	bdl	bdl	0.2	bdl	bdl	6.3	3.5	0.3	
		10	25.8	bdl	bdl	bdl	166.3	18.7	bdl	bdl	79.3	60.9	bdl	bdl	bdl	bdl	bdl	bdl	bdl	bdl	bdl	bdl	bdl	0.1	8.9	9.1
		15	18.1	0.2	113	5.2	1197	263	0.2	58	1090	14.6	0	0	bdl	0.4	0.6	bdl	bdl	0.1	bdl	bdl	0.8	0.6	4.6	
		3	62	4.1	16.9	8.3	253	92.8	1	0.8	154	64.8	bdl	bdl	bdl	1.8	bdl	bdl	bdl	0.1	bdl	bdl	9.1	6.28	2.7	8.1
		4	10.4	bdl	bdl	1	972	207	0.6	bdl	576	26.5	bdl	bdl	bdl	bdl	bdl	0	bdl	0	0.4	bdl	bdl	bdl	4.7	6.1
MVTEX-09 (8.2)		5	10.4	0.1	bdl	bdl	630	1215	bdl	bdl	1570	25.4	bdl	bdl	bdl	bdl	bdl	0	bdl	bdl	bdl	bdl	0.4	0.5	0.5	
	2	8	10.6	0.1	bdl	bdl	72.4	395	1.4	4.4	bdl	97	bdl	bdl	0.4	bdl	bdl	0	bdl	bdl	bdl	bdl	0.2	bdl	0.2	3.1
		9	14.8	bdl	bdl	bdl	990	431	0.8	bdl	1270	22.1	bdl	bdl	bdl	bdl	bdl	0	bdl	bdl	bdl	bdl	bdl	0.2	2.3	1.1
		11	13.7	bdl	bdl	1.2	23.8	1037	bdl	bdl	25.5	bdl	bdl	bdl	bdl	bdl	3.9	0	bdl	bdl	bdl	bdl	0.2	0.4	0	4.1
		1	9.8	bdl	bdl	1	1150	445	bdl	bdl	323	20.7	bdl	bdl	bdl	bdl	bdl	0	bdl	bdl	0.3	bdl	bdl	bdl	2.6	2.1
		2	13	bdl	bdl	bdl	bdl	41.3	bdl	bdl	bdl	bdl	bdl	bdl	bdl	bdl	bdl	0	bdl	bdl	bdl	bdl	bdl	1.2	-	
MVTEX-01 (18.1)	2	3	10.4	bdl	2.6	1.5	200	98.9	68	100	119	8.2	bdl	3.8	bdl	0.8	2	0	bdl	0.2	bdl	0.5	35.9	22.5	2	
		4	7.9	0.1	2.3	3.3	120	54.9	bdl	2.8	72	10.8	bdl	0.1	bdl	597	1.1	0	bdl	0.1	0.3	0.3	5.5	7.3	2.2	4.1
		7C	10.1	0.1	17.5	12.6	118.9	376	1.6	3	71.9	bdl	bdl	0.2	bdl	6.2	2.3	0	bdl	0.2	bdl	26.7	124	26.5	0.3	3.1
		2	31	0.2	1.5	bdl	4390	105	bdl	bdl	1350	39.6	bdl	bdl	bdl	bdl	bdl	0	bdl	bdl	0.3	bdl	0.6	0.4	41.8	
MVT-06	2	3	15.9	bdl	bdl	bdl	2110	498	0.8	bdl	4720	107	bdl	bdl	bdl	bdl	bdl	0	bdl	bdl	bdl	bdl	0.3	0.6	4.2	
		5	12.4	bdl	bdl	bdl	1278	402	bdl	bdl	2067	53.1	bdl	0	bdl	1.8	bdl	0	bdl	bdl	bdl	bdl	5.3	6.5	3.2	
MVT-05	2	1	15.1	bdl	bdl	bdl	1300	335	bdl	bdl	1451	40.2	0	bdl	bdl	bdl	bdl	0	bdl	bdl	bdl	bdl	bdl	bdl	3.9	
		2	14.7	bdl	bdl	bdl	bdl	51.6	bdl	bdl	1037	34.7	bdl	bdl	bdl	bdl	bdl	bdl	bdl	bdl	bdl	bdl	bdl	bdl	-	
MVT-04	2	1	14.1	bdl	0.4	bdl	1006	134.9	bdl	bdl	287	163	bdl	bdl	bdl	bdl	11.6	0	bdl	bdl	0.1	bdl	bdl	0	7.5	
		5	13.4	0	bdl	bdl	797	855	bdl	bdl	895	102	bdl	bdl	bdl	bdl	bdl	0	bdl	bdl	bdl	bdl	bdl	bdl	0.9	
		2	13.6	bdl	bdl	bdl	480	bdl	0.7	bdl	bdl	22	bdl	bdl	bdl	bdl	bdl	0	0	bdl	bdl	bdl	bdl	bdl	-	
MVT-01	2	4	17.4	bdl	bdl	1.1	640	202	bdl	bdl	1502	42.5	bdl	bdl	bdl	bdl	bdl	0	bdl	bdl	bdl	bdl	bdl	bdl	3.2	
		5	12.1	0.1	bdl	bdl	1087	177.9	bdl	bdl	771	30.4	bdl	bdl	bdl	bdl	bdl	bdl	bdl	bdl	bdl	bdl	0	bdl	6.1	
		1	11.8	bdl	bdl	bdl	334	37.2	0.5	bdl	29.2	7.9	bdl	bdl	bdl	bdl	0.8	0	bdl	bdl	bdl	bdl	bdl	bdl	9	
MVT-08	2	4	9.7	bdl	bdl	1.3	39.5	49.2	1.2	bdl	11.3	bdl	bdl	0	bdl	bdl	bdl	0	bdl	bdl	bdl	bdl	0.6	0.3	0.8	
		5	15.6	bdl	bdl	bdl	117	20.4	1.3	bdl	5.1	8.9	bdl	bdl	bdl	bdl	bdl	0	bdl	bdl	0.3	bdl	0.3	3	5.7	

Serra da Paciência Formation

Sample	Pyrite Type	Spot	^{49}Ti	^{51}V	^{53}Cr	^{55}Mn	^{59}Co	^{60}Ni	^{65}Cu	^{66}Zn	^{75}As	^{77}Se	^{95}Mo	^{107}Ag	^{118}Sn	^{121}Sb	^{125}Te	^{181}Ta	^{195}Pt	^{197}Au	^{202}Hg	^{205}Tl	^{208}Pb	^{209}Bi	Co/Ni	SHRIMP-SI spot
FCJ-3	2	1	600	30	40	50.2	670	571	18.8	11.7	279	2	bdl	0.9	1.9	15.4	15.4	0.9	bdl	0.1	0.1	0.4	72	14.5	1.2	1.1
		2	bdl	bdl	bdl	bdl	509	401	5.2	17.6	38.7	23.1	bdl	0.5	bdl	bdl	bdl	bdl	bdl	1.3	0.1	30.1	bdl	bdl	1.3	
		3	30.2	0.1	bdl	0.3	1479	63.7	3.6	1.1	9.4	13.5	bdl	0	bdl	bdl	bdl	bdl	bdl	0	0.1	bdl	4.4	3.5	23.2	
		4	24.4	0.1	1.9	bdl	563	460	4.5	3.2	12.1	10.3	0.6	0	bdl	0.14	2.9	bdl	bdl	1.7	0.1	bdl	0.7	2.5	1.2	1.6
		6	28.3	bdl	bdl	bdl	70.8	80.7	bdl	1	bdl	21.5	bdl	bdl	bdl	bdl	bdl	bdl	bdl	bdl	bdl	bdl	bdl	bdl	0.9	1.18
		7	27.4	0.1	bdl	bdl	27.8	567	4.6	0.8	4.6	16.7	bdl	bdl	bdl	bdl	bdl	bdl	bdl	0.7	0.4	bdl	bdl	0	0	
		8	27.1	0	bdl	bdl	11.4	bdl	1.2	bdl	19.4	bdl	bdl	0.7	bdl	4.6	bdl	bdl	bdl	0.1	0.2	bdl	80	23.4	-	
		9	28.4	0.4	12.1	bdl	305	60.8	0.6	1.1	419	3.6	bdl	bdl	bdl	0.78	bdl	bdl	bdl	0.3	0.1	bdl	6.1	1.4	5	1.13
		10	25.8	0.1	bdl	1.1	195	347	209	1.8	2020	8.7	0.14	2.5	0.3	45.5	12.8	bdl	bdl	0.3	0.1	0.1	408	15.8	0.6	1.12
		11	26.2	bdl	bdl	bdl	1370	117	bdl	1.1	bdl	1.2	bdl	bdl	bdl	bdl	bdl	bdl	bdl	bdl	0.1	bdl	bdl	bdl	11.7	
		13	23.9	0.1	bdl	bdl	854	84	bdl	bdl	6.7	7.6	bdl	bdl	bdl	bdl	bdl	bdl	bdl	bdl	0.1	bdl	bdl	0	10.2	1.17
PD-09	4	1	9.8	bdl	bdl	bdl	541	500	bdl	bdl	2127	24.3	bdl	bdl	bdl	bdl	bdl	0	bdl	bdl	bdl	bdl	0.4	0.1	1.1	4
		2	8.3	bdl	bdl	bdl	252.3	176.1	bdl	bdl	1129	15.1	bdl	bdl	bdl	bdl	bdl	0	bdl	bdl	bdl	bdl	0	bdl	1.4	3
		3	11.3	bdl	bdl	bdl	476	547	bdl	bdl	4050	23.4	bdl	bdl	bdl	bdl	bdl	0	bdl	bdl	bdl	bdl	bdl	bdl	0.9	2
PD-14	6.1	1	8.4	bdl	bdl	bdl	1	41.5	bdl	bdl	211	bdl	0	bdl	bdl	bdl	bdl	0	bdl	bdl	bdl	0	bdl	bdl	0	4
		2	9.3	bdl	bdl	bdl	13700	190	bdl	0.5	85	40.1	0	bdl	bdl	bdl	bdl	bdl	bdl	bdl	bdl	bdl	2	0.4	72.1	3
	6	4	7.5	bdl	bdl	bdl	113	730	3	bdl	541	7.3	bdl	bdl	bdl	1.8	bdl	bdl	bdl	bdl	bdl	0.1	12.7	bdl	0.2	1
		5	bdl	bdl	bdl	4.9	19.6	41.8	bdl	bdl	255	10.1	bdl	bdl	bdl	bdl	bdl	0	bdl	bdl	bdl	bdl	bdl	bdl	0.5	2
SP-01	5	1	24.8	1	2.1	15.3	700	175	3.8	bdl	375	16.7	bdl	0.2	bdl	4.5	bdl	0	bdl	0.1	bdl	0	36	2	4	9
	1	2C	73	2.8	35.7	24.9	620	251	10.6	2.1	929	57.6	bdl	0.4	bdl	8.5	32	0	bdl	0.1	bdl	bdl	28.1	7.4	2.5	6
	2	2R	341	7.6	145	65	653	226	9.9	3.9	849	43.9	bdl	0.3	bdl	13.5	21.2	0.1	bdl	0.2	0.9	0.1	44.8	12.5	2.9	7
	5	3	460	1.3	bdl	26.6	2270	587	5.5	1.7	521	8.4	bdl	0.5	bdl	4.8	2.7	0.1	bdl	0.2	0.8	bdl	50.9	26.2	3.9	14
	4.1	4	19.2	0.3	3.4	bdl	941	283	4.2	bdl	2430	13.4	bdl	0.4	bdl	6.5	1.4	0	bdl	bdl	bdl	bdl	56	3.2	3.3	
		4.1	9	bdl	11	26	1760	580	36	bdl	620	55.9	bdl	0.5	bdl	5.5	bdl	0	bdl	0.2	1	bdl	22.6	2.6	3	5
		5	240	0.5	2.6	5	239	1040	4.3	bdl	2030	21.3	1.33	0.4	bdl	4.3	2.6	0.2	bdl	0.2	bdl	bdl	22.3	5.9	0.2	11
	1	6	bdl	1.8	50	59	394	368	35.7	2.6	374	5.8	bdl	0.8	1.9	18.6	4.4	bdl	bdl	0.2	0.7	bdl	62	10.5	1.1	15
	4.1	7	26.2	0.8	7.7	16.3	74	161	27.2	1.1	153	9	bdl	3.1	bdl	16	bdl	0	bdl	0.7	bdl	bdl	86	7.4	0.5	17

Pyrite types: (1) detrital inclusion-bearing; (2) detrital massive; (3) detrital in quartz-pebble; (4) euhedral-hydrothermal; (4.1) euhedral-diagenetic; (5) euhedral overgrowth-diagenetic; (6) anhedral-syngenetic; and (6.1) subhedral-syngenetic. bdl is below detection limit.

Table 7.5. Information on sample locations from the Jacobina Basin.

Sample	Location	Latitude	Longitude	Note
CANIF-37 (1.1)	Canavieiras Mine	11° 14' 57.1" S	40° 30' 21.8" W	DC1*
CANIF-37 (1.2)				
CANIF-37 (2.2)				
CANIF-37 (3)				
CANIF-37 (4)				
CANIF-37 (4.2)				
CANIF-37 (5)				
CANIF-37 (6)				
CANIF-37 (7)				
JBA-04	João Belo Mine	-	-	-
JBA-08				
JBA-06				
JBA-05				
JBA-03				
JB-04	João Belo Mine open pit	-	-	-
MRF-04	Morro dos Cuscuz Mine	-	-	-
MS-1	Canavieiras Mine	-	-	-
MS-2				
MS-3				
MVTEX-09 (6.2)	Morro do Vento Mine	11° 15' 36.2" S	40° 30' 43.8" W	DC2*
MVTEX-09 (8.1)				
MVTEX-09 (8.2)				
MVTEX-01 (18.1)	Morro do Vento Mine	11° 16' 32.1" S	40° 30' 37.6" W	DC3*
MVT-06	Morro do Vento Mine	-	-	-
MVT-05				
MVT-04				
MVT-01				
MVT-08				
FCJ-3	Pindobaçu Region	10° 41' 49.3" S	40° 22' 27.8" W	-
PD-09	Pindobaçu Region	10° 41' 26.2" S	40° 22 ' 09.5" W	-
PD-14	Pindobaçu Region	10° 47' 49.8" S	40° 24' 14.8" W	-
SP-01	Close to the Jacobina entrance	11° 12' 28.8" S	40° 28' 28.4" W	-

7.2. MATERIAL SUPLEMENTAR DO CAPÍTULO 5

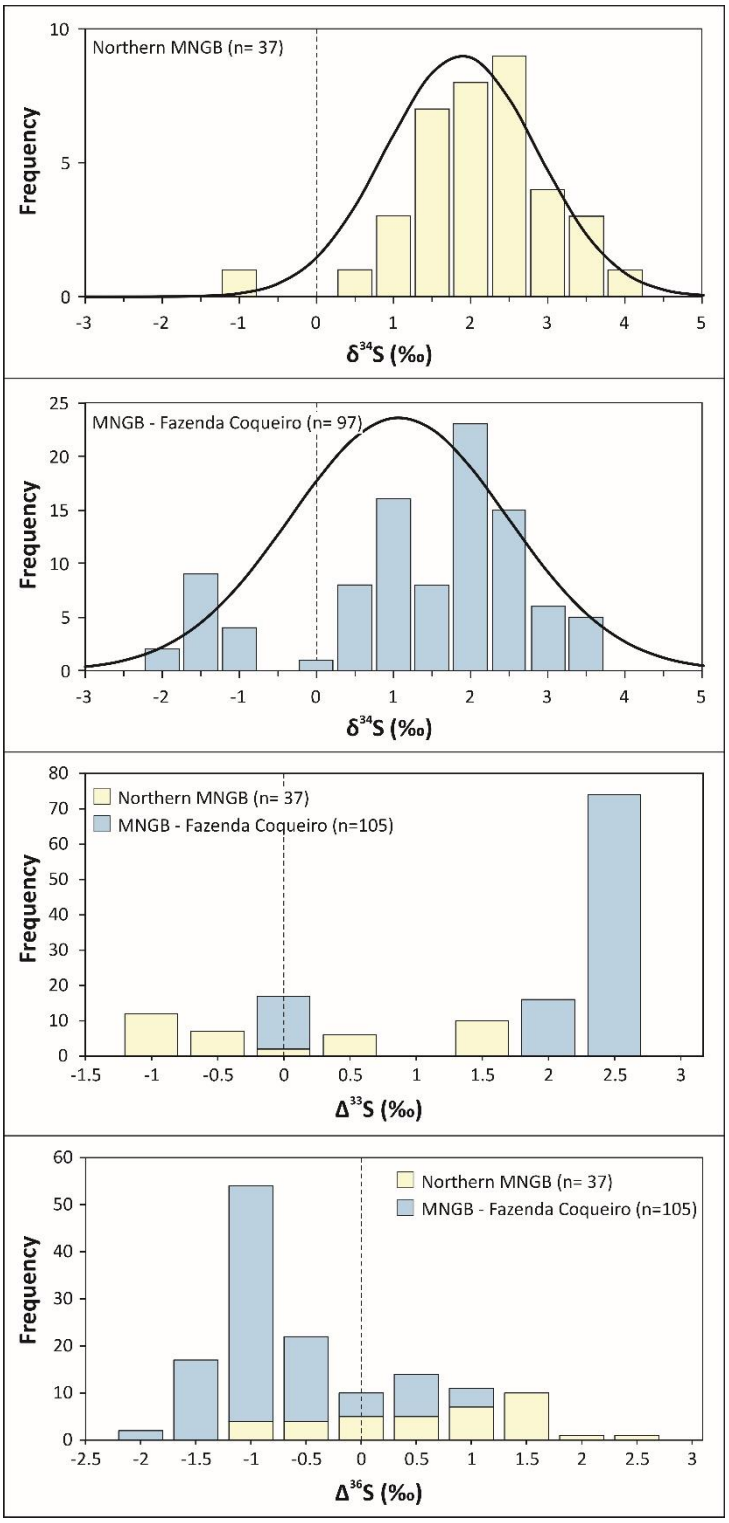

Figure 7.9. $\delta^{34}S$, $\Delta^{33}S$ and $\Delta^{36}S$ histograms of samples from Mundo Novo Greenstone Belt.

Table 7.6. Summary of selected pyrite trace elements data for samples from Mundo Novo Greenstone Belt.

Sample	^{55}Mn	^{59}Co	^{60}Ni	^{65}Cu	^{66}Zn	^{75}As	^{77}Se	^{121}Sb	^{197}Au	^{202}Hg	^{208}Pb	^{209}Bi	Co/Ni
FCJ-4 (n=8)													
Range	bdl-114	bdl-20600	1.9-723	1.7-20	0.9-7	3.6-46	8.8-20	bdl-7.5	0.03-0.8	0.06-0.1	0.14-90	bdl-11	0.26-10466
Avg.	29.2	6919	308	8.5	2.1	12.9	14.7	1.7	0.3	0.08	22.4	2.9	2764
SD	56.5	10443	297.6	5.4	2.07	14.1	3.8	2.6	0.3	0.02	31.1	4.3	4496
PD-04* (n=4)													
Range	bdl-2.3	bdl-230	bdl- 69	-	-	bdl-264	bdl-48	bdl-5.3	bdl-0.47	-	bdl-11	bdl-0.6	0.14-2.3
Avg.	2.1	96.3	45	-	-	101	27.4	-	0.24	-	7	0.4	1.2
SD	0.2	117.3	33.8	-	-	141.3	20	-	0.3	-	5.6	0.2	1.5
PD-06 (n=11)													
Range	bdl-1.5	bdl-15	11.4-91.4	bdl-4.7	bdl-0.5	134- 408	bdl-2.4	bdl-1.4	bdl-3.2	bdl-0.2	bdl-2.7	bdl-0.2	0.005-0.8
Avg.	1.3	6.5	41	1.9	0.3	267.2	2.4	0.7	0.8	0.2	1	0.13	0.24
SD	0.2	5.2	29.8	2.1	0.2	92.5	1.3	0.5	1.6	0.04	1.2	0.13	0.25
PD-07 (n=8)													
Range	bdl-0.5	bdl-12.7	13.5-87.2	bdl-1.4	bdl-1	115-502	0.8-4.6	bdl-4.4	bdl-2.8	0.07-0.2	bdl-11.6	bdl-0.08	0.002-0.85
Avg.	-	4.3	41.2	0.80	0.55	273.6	2.2	2.3	0.57	0.14	2.1	0.06	0.25
SD	-	5	24.3	0.4	0.4	141.8	1.12	2.8	1.2	0.05	4.6	0.03	0.37
FCQ-06.3 (n=10)													
Range	bdl-3.3	2960-6300	bdl-35	bdl-0.9	bdl-1.6	bdl-880	bdl-70	bdl-23.4	bdl-0.04	bdl-0.7	bdl-2760	bdl-20.6	180-1556
Avg.	1.06	4653.	12.6	0.37	0.6	308.9	45.4	4.3	0.02	0.4	418.2	4	642.5
SD	1.1	1239.2	10.8	0.3	0.5	319.4	14.7	8.5	0.02	0.19	959.5	7.6	477.1
FCQ-06.1 (n=11)													
Range	bdl-16	1962-6600	bdl-55	bdl-18	0.1-250	0.6-2037	23-78.7	bdl-3.8	bdl-0.5	bdl-0.4	bdl-69	bdl-0.5	92-2075
Avg.	5.55	3619.2	9.35	-	125.1	320	40.7	-	-	0.3	13.8	-	993.6
SD	8.97	1468.7	17.2	-	176.7	586.8	22.6	-	-	0.13	30.8	-	642.5
FCQ-18.1 (n=10)													
Range	bdl-1.06	841-6700	2.3-86	bdl-0.6	bdl-140	3.6-4190	14.3-28.6	bdl-0.27	-	bdl-0.2	bdl-0.4	bdl-0.03	9.7-894
Avg.	0.96	3257.5	17.4	-	15.7	1558.5	19.2	0.2	-	0.12	0.13	-	371.8
SD	0.15	2168.5	24.5	-	46.6	1670	4.04	0.1	-	0.07	0.17	-	246
FCQ-18.2 (n=7)													
Range	-	1710-4750	1.1-12	bdl-0.21	bdl-0.2	6.43-318	20-109.5	-	-	bdl-0.1	bdl-0.22	-	297.7-2432.4
Avg.	-	3205	4	0.2	0.2	100.2	37.5	-	-	0.1	0.1	-	1204.8
SD	-	1128	3.9	0.01	0.02	125.4	32.1	-	-	0.01	0.11	-	649.4
FCQ-1 (n=9)													
Range	bdl-0.36	2.1-1910	25-383	bdl-0.9	bdl-0.2	513-5150	9.2-39.6	bdl-4.5	bdl-0.08	bdl-0.4	bdl-910	bdl-3.4	0.04-60.2
Avg.	0.34	561.1	107	0.4	-	2625.4	18.8	2.4	0.04	0.2	137.3	1.2	14.8
SD	0.04	797.7	117.9	0.4	-	1558	8.9	2.9	0.04	0.1	341	1.9	24.8
FCQ-06.2 (n=10)													
Range	bdl-14.2	4460-9980	4.3-23	bdl-2.5	bdl-3.7	0.96-294	10-35	bdl-1	bdl-0.07	bdl-0.17	bdl-31.4	bdl-12.1	232.5-1038
Avg.	5.8	6732	14.8	0.7	1	104.6	18.4	0.4	0.04	0.15	4.8	3.3	543.6
SD	5.5	1689.5	6.1	0.8	1.2	119.6	8.7	0.5	0.03	0.03	10	3.8	275.5
FCQ-13 (n=10)													
Range	bdl-0.2	1072-1786	2298-6540	0.7-38.4	bdl-23.7	bdl-0.81	bdl-141	-	0.01-0.36	0.03-0.6	bdl-20.3	0.02-0.4	0.24-0.5
Avg.	0.2	1591.2	3931.7	17.8	6.5	0.6	44.9	-	0.1	0.3	5.9	0.2	0.4
SD	0.03	223.9	1111.2	13.4	8.7	0.21	40.4	-	0.17	0.2	6.8	0.15	0.1

Table 7.7. Summary of selected chalcopyrite trace elements data for samples from Fazenda Coqueiro Deposit.

Sample	^{55}Mn	^{59}Co	^{60}Ni	^{66}Zn	^{71}Ga	^{74}Ge	^{75}As	^{77}Se	^{107}Ag	^{111}Cd	^{115}In	^{118}Sn	^{121}Sb	^{202}Hg	^{205}Tl	^{208}Pb
FCQ-06.3 (n=4)																
Range	2.2-4.8	0.4-1.9	7.6-11.2	473-616	bdl-0.3	bdl-0.9	19.2-25.5	58.4-87	57.3-81.4	2.4-4.2	28.8-36.6	22.4-32.7	2.41-15.9	1.46-2.06	bdl-0.8	2.1-220
Avg.	3.1	0.9	9	0.37	0.3	0.8	22.9	70.8	57.3	3.4	33.2	28.1	10.3	1.7	0.55	57.6
SD	1.2	0.7	1.5	63	0.04	0.1	3	13.4	61	0.7	3.3	4.5	6.4	0.3	0.21	108.2
FCQ-06.1 (n=2)																
Range	2-2.4	0.4-0.46	4.7-5.9	511-637	0.7-1.4	1.2-1.3	46.9-56.1	103-105	51.8-57.2	1.4-3.2	19-19.6	2-5.8	0.3-1.7	0.7-1.5	bdl-1	0.3-0.7
Avg.	2.2	0.4	5.3	574	1.06	1.3	51.5	104.3	54.5	2.3	19.3	3.9	1.07	1.11	-	0.5
SD	0.3	0.03	0.8	89	0.4	0.08	6.5	1.3	3.8	1.3	0.4	2.7	1	0.6	-	0.3
FCQ-18.1 (n=3)																
Range	6.5-170	0.5-2	5.9-7.3	427-39000	1.9-2.6	-	13.2-15.1	49-59.2	75.6-85.9	1.8-129	14.1-16.9	137.7-154	9.1-21.8	2.4-15.4	0.1-0.2	3.8-12.4
Avg.	62.2	1.02	6.8	13382	2.1	-	14.4	52.5	79.1	44.8	15	146.3	14.9	7.2	0.2	7.6
SD	93.3	0.8	0.8	22186	0.4	-	1	5.8	5.8	72.9	1.6	8.2	6.4	7.1	0.1	4.3
FCQ-18.2 (n=3)																
Range	bdl-440	0.3-8.1	5.1-17.3	531-131000	0.8-1.2	1-1..3	32.3-45.2	67.8-99	49.5-69.3	1.7-420	22-31.1	3.1-4.7	2.5-24.1	0.3-27.8	0.08-2.1	23-380
Avg.	222.1	2.9	9.4	44040	1.1	1.2	39.8	80.8	61.3	141.4	25.2	3.7	11.6	9.8	1.01	168.6
SD	308.1	4.4	6.8	75309.5	0.2	0.1	6.7	16.2	10.4	241.2	5.07	0.8	11.2	15.6	1.03	187.4
FCQ-13 (n=6)																
Range	bdl-0.63	6.1-11	bdl-0.6	547-1140	0.2-0.64	bdl-0.9	14-19.3	37-44.7	bdl-5.5	16-29	21.4-34	2.8-4.4	-	0.6-0.8	bdl-0.05	0.65-1.5
Avg.	0.56	7.9	0.4	781.8	0.43	-	17.3	40.3	2.3	21.1	26.3	3.9	-	0.7	-	1.1
SD	0.1	2.1	0.2	235.9	0.17	-	2.4	3	2.1	4.6	4.9	0.6	-	0.09	-	0.3

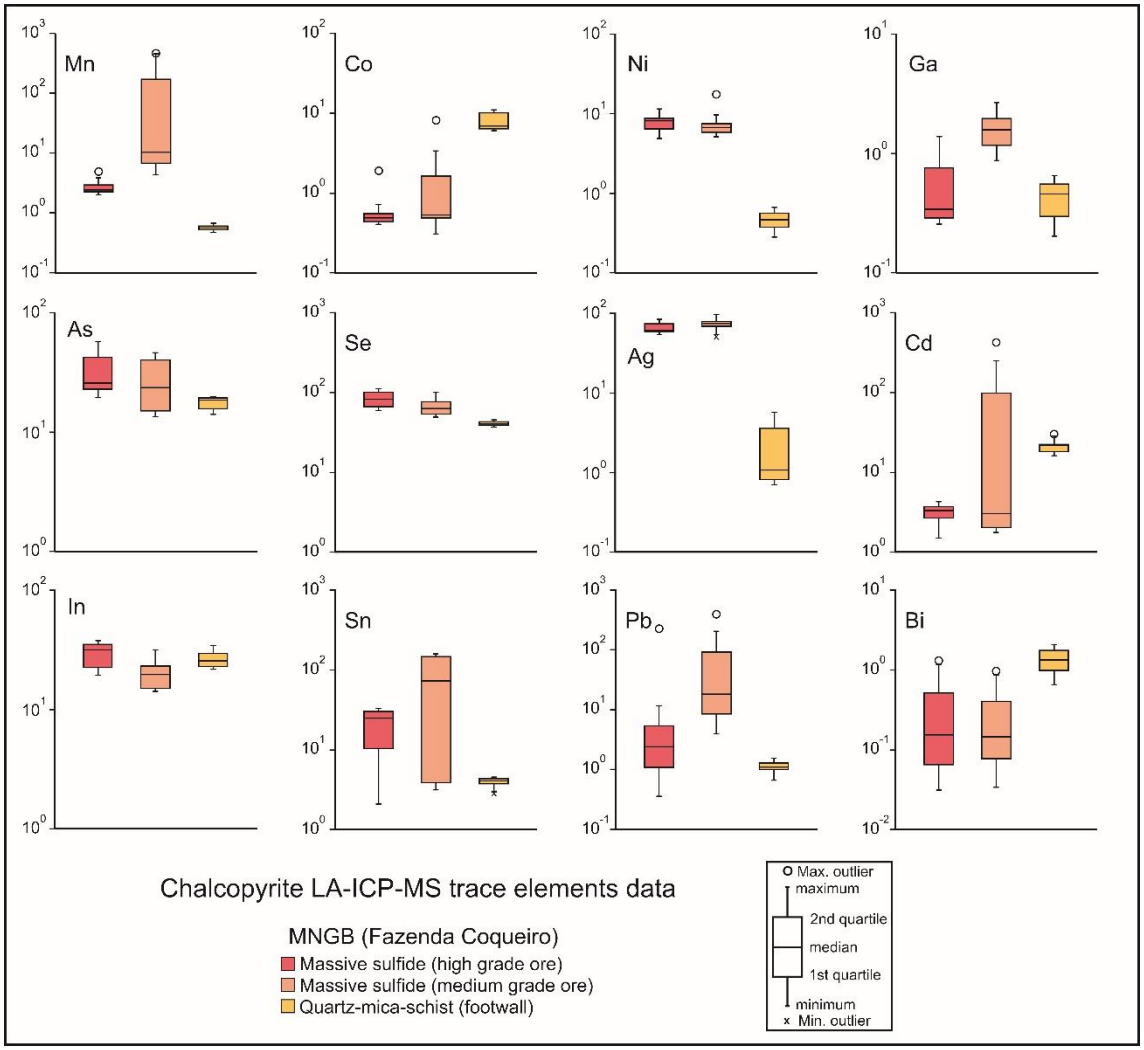

Figure 7.10. Box-whiskers plots for selected trace elements in chalcopyrites from samples of Fazenda Coqueiro Deposit.

Table 7.8. Summary of selected sphalerite trace elements data for samples from Fazenda Coqueiro Deposit.

Sample	^{55}Mn	^{57}Fe	^{59}Co	^{60}Ni	^{65}Cu	^{71}Ga	^{74}Ge	^{75}As	^{77}Se	^{107}Ag	^{111}Cd	^{115}In	^{118}Sn	^{121}Sb	^{197}Au	^{202}Hg	^{205}Tl	^{208}Pb
FCQ-06.3 (n=9)																		
Range	1364-1615	41910-50200	9.3-24.5	bdl-0.9	91-5100	0.2-0.6	0.5-0.7	8.3-18	55.5-76.3	2.5-13.4	1879-2250	77.6-88	0.2-0.9	1.7-9.9	0.04-0.4	99.2-120	bdl-0.1	1.2-27
Avg.	1461	46745.5	19.1	0.5	2133	0.4	0.6	12.3	69.2	7.3	2010.2	83.8	0.47	5.5	0.17	110.1	0.08	7.8
SD	76.7	2552.1	4.6	0.2	1765.8	0.12	0.06	3.1	6.3	3.7	100.8	3.8	0.25	2.8	0.11	6.4	0.03	8.3
FCQ-06.1 (n=2)																		
Range	2213-2473	51140-56400	9.4-128	bdl-0.1	28.6-438	0.4-0.5	0.5-0.7	2.9-18	61.2-71.6	0.6-1.9	1719-1851	50-53.6	bdl-0.3	bdl-1.4	bdl-0.2	57.6-76	bdl-0.1	0.1-1
Avg.	2365.4	52806.2	29.6	-	108.3	0.5	0.6	11.3	66.4	1.3	1780.2	51.6	0.3	0.6	0.12	70.8	0.04	0.5
SD	84.4	1772.3	39.9	-	149.3	0.02	0.08	4.6	3.5	0.6	47.5	1.2	0.05	0.5	0.06	5.5	0.04	0.3
FCQ-18.1 (n=11)																		
Range	2376-3118	53200-61110	4.1-26.7	bdl-0.2	20.5-2590	1.2-2.1	0.2-0.4	7.4-15	31.3-40.6	1-10.5	1588-1797	36.2-40	0.2-2.5	0.3-13.3	bdl-0.8	41.4-52.7	bdl-0.2	0.3-48
Avg.	2762	56867.2	16.3	0.2	824.8	1.8	0.3	11.4	36.6	4.5	1721.4	37.5	0.8	4.5	0.3	49	0.1	7.7
SD	218.5	3110	7.3	0.05	972.3	0.2	0.08	2.7	2.9	3.7	65.9	1	0.7	4.8	0.3	2.8	0.08	13.9
FCQ-18.2 (n=8)																		
Range	2184-2485	50400-53400	2.8-20	bdl-0.1	28.5-960	0.4-0.5	0.4-0.7	7.5-19.2	44.1-64	1-8.5	1612-1836	51.2-61.4	bdl-1.4	0.3-8.8	bdl-0.1	53-61.5	bdl-0.5	0.3-13.7
Avg.	2351	52022.5	13	-	246.4	0.5	0.6	13.9	55.7	3.2	1746.6	54.1	0.4	3	0.1	58.6	0.2	2.6
SD	97	1099.9	7.4	-	334.1	0.04	0.1	3.8	6.4	2.7	69.4	3.1	0.5	3.1	0.03	2.6	0.2	4.5
FCQ-13 (n=2)																		
Range	151.3-157.3	43190-43900	463-465	0.3-1.3	92-2020	0.1-0.2	0.2-0.3	21-23	25.4-29.6	0.9-4.6	8329-8459	83.6-85.3	0.2-0.9	-	0.02-0.06	24.8-32.5	-	0.3-5.6
Avg.	154.3	43545	464.1	0.8	1056	0.1	0.3	21.9	27.5	2.7	8394	84.4	0.5	-	0.04	28.6	-	3
SD	4.2	502	1.2	0.7	1363.3	0.07	0.07	1.4	2.9	2.6	91.9	1.2	0.5	-	0.03	5.4	-	3.8

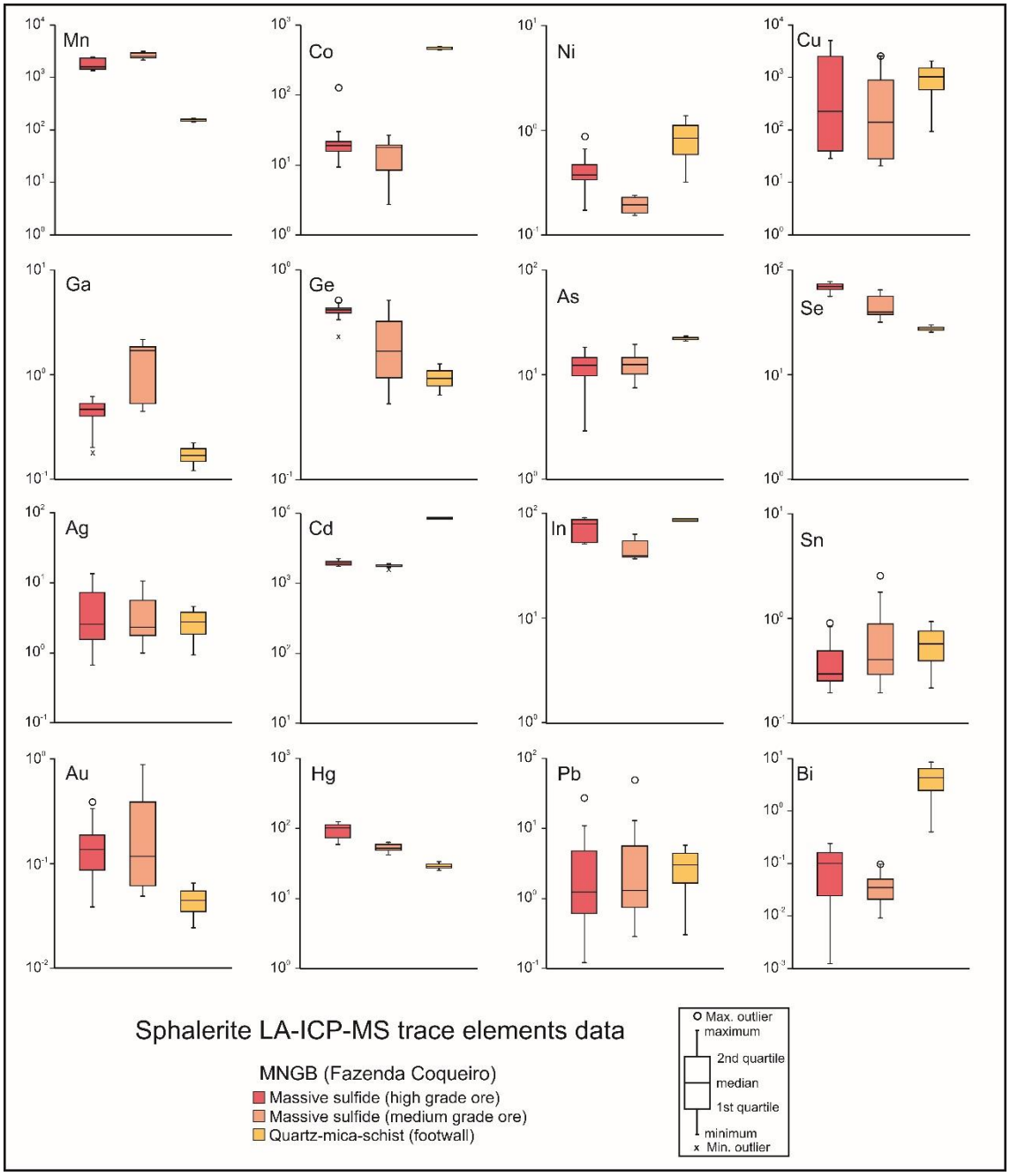

Figure 7.11. Box-whiskers plots for selected trace elements in sphalerite from samples of Fazenda Coqueiro Deposit.

Table 7.9. Summary of selected pyrrhotite trace elements data for samples from Fazenda Coqueiro Deposit.

Sample	^{55}Mn	^{59}Co	^{60}Ni	^{65}Cu	^{66}Zn	^{74}Ge	^{75}As	^{77}Se	^{107}Ag	^{121}Sb	^{202}Hg	^{208}Pb	^{209}Bi
FCQ-06.3 (n=9)													
Range	bdl-9.6	59-73.1	253.2-464	bdl-2.2	bdl-2.4	bdl-1.1	244-386	54.5-76.5	0.05-2.8	bdl-290	0.4-1.5	bdl-12.8	bdl-2
Avg.	3.5	69.5	330.6	-	1.5	0.9	312	66.4	1.1	42.4	0.7	5.4	0.8
SD	2.9	4.5	78.5	-	1	0.1	46.7	8.3	1	109.1	0.4	4	0.7
FCQ-06.1 (n=6)													
Range	2-8.4	46.3-52	361-387	bdl-0.7	bdl-0.4	0.6-1.2	179-232	79.1-93	0.08-0.6	bdl-0.6	bdl-0.4	0.3-2.9	bdl-0.1
Avg.	4.4	49.1	376	0.5	0.3	0.9	208.6	85.7	0.2	0.4	0.3	1.2	0.06
SD	2.5	2	11.5	0.1	0.06	0.2	21.20	5.6	0.2	0.2	0.06	1	0.05
FCQ-18.1 (n=6)													
Range	1.5-6	45-53.6	264-339	bdl-0.6	bdl-0.3	bdl-0.9	336-418	38.6-48.4	0.1-1.3	bdl-0.7	bdl-0.9	bdl-3.8	bdl-0.2
Avg.	4.2	47.1	303.3	-	-	-	355.3	45.1	0.5	-	0.5	1.3	0.1
SD	1.7	3.2	33.2	-	-	-	31	3.6	0.4	-	0.3	1.4	0.08
FCQ-18.2 (n=6)													
Range	bdl-7.2	49-117.3	292-396	bdl-29	bdl-0.5	bdl-1.3	214-270	70-100.6	bdl-2.3	bdl-0.3	bdl-0.2	bdl-1.8	bdl-0.2
Avg.	3.2	62.2	360.1	6.3	0.4	1	239.8	77.4	0.8	-	-	1	0.13
SD	2.9	27	39.1	12.6	0.1	0.3	20.2	11.8	0.9	-	-	0.7	0.06
FCQ-13 (n=10)													
Range	bdl-10.6	0.9-175.2	193.5-1340	bdl-2	bdl-0.6	bdl-0.7	384-593	23.3-51.4	bdl-2.2	-	bdl-0.2	bdl-9.8	bdl-10.8
Avg.	3.9	23.5	940	0.8	0.5	-	485.2	33.7	0.5	-	0.1	2.6	2.3
SD	4.4	53.3	339.8	0.6	0.08	-	65.6	9.5	0.6	-	0.04	2.9	3.3

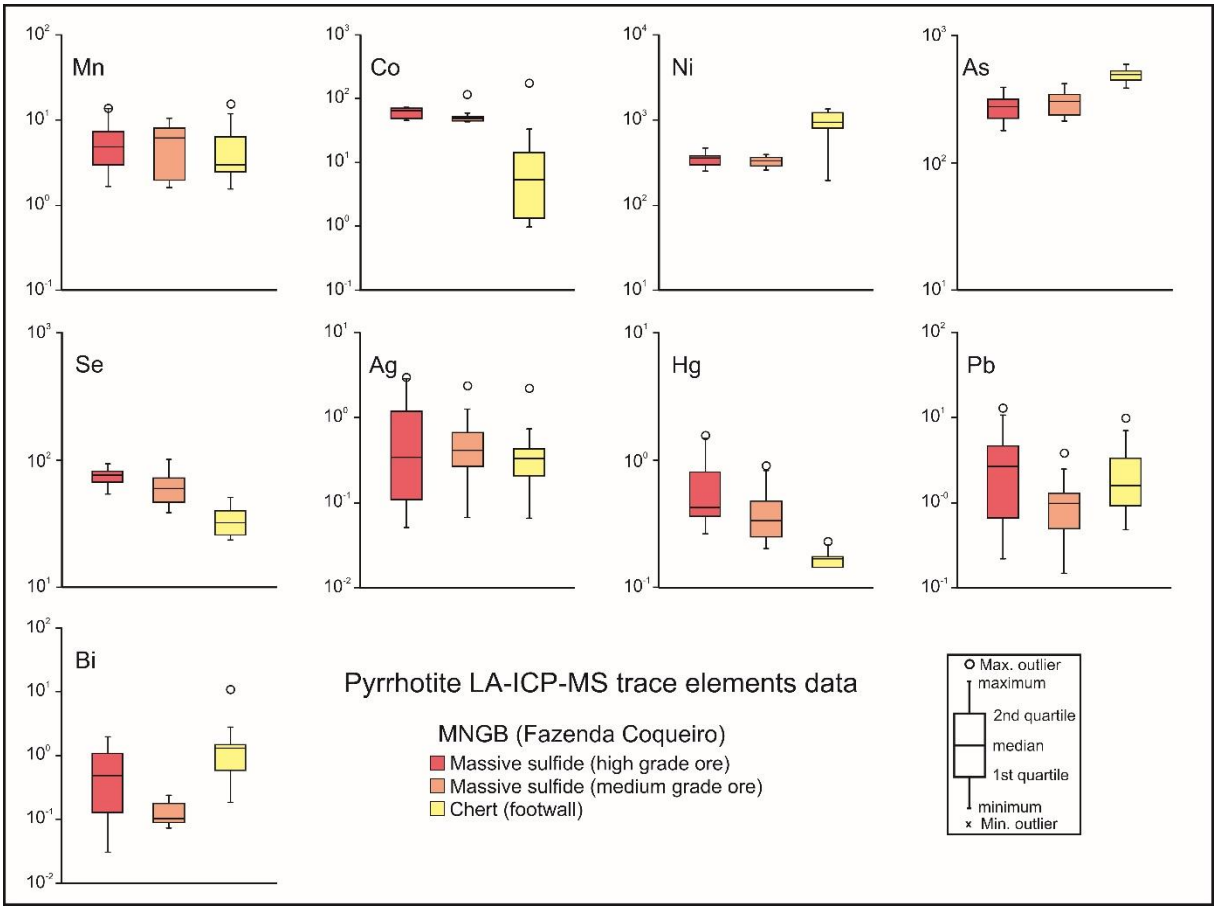

Figure 7.12. Box-whiskers plots for selected trace elements in pyrrhotite from samples of Fazenda Coqueiro Deposit.

Table 7.10. Summary of selected galena trace elements data for samples from Fazenda Coqueiro Deposit.

Sample	^{55}Mn	^{65}Cu	^{74}Ge	^{75}As	^{77}Se	^{107}Ag	^{111}Cd	^{115}In	^{118}Sn	^{121}Sb	^{125}Te	^{137}Ba	^{202}Hg	^{205}Tl	^{209}Bi
FCQ-1 (n=10)															
Range	1.2-5	1.7-87	9.7-10.2	36.7-80.1	1167-1210	2668-4510	148.7-326	0.1-1.2	5-70	1704-7000	24.1-158	0.08-0.4	0.12-0.4	93.7-117.4	2119-2438
Avg.	2	11.9	9.9	55.9	1187.6	3066.7	186.3	0.3	18.9	2442.6	72.3	0.15	0.23	102.3	2277.6
SD	1.3	26.4	0.1	13.8	14.5	548	53	0.3	18.8	1609.9	39.1	0.1	0.1	9.1	99.3

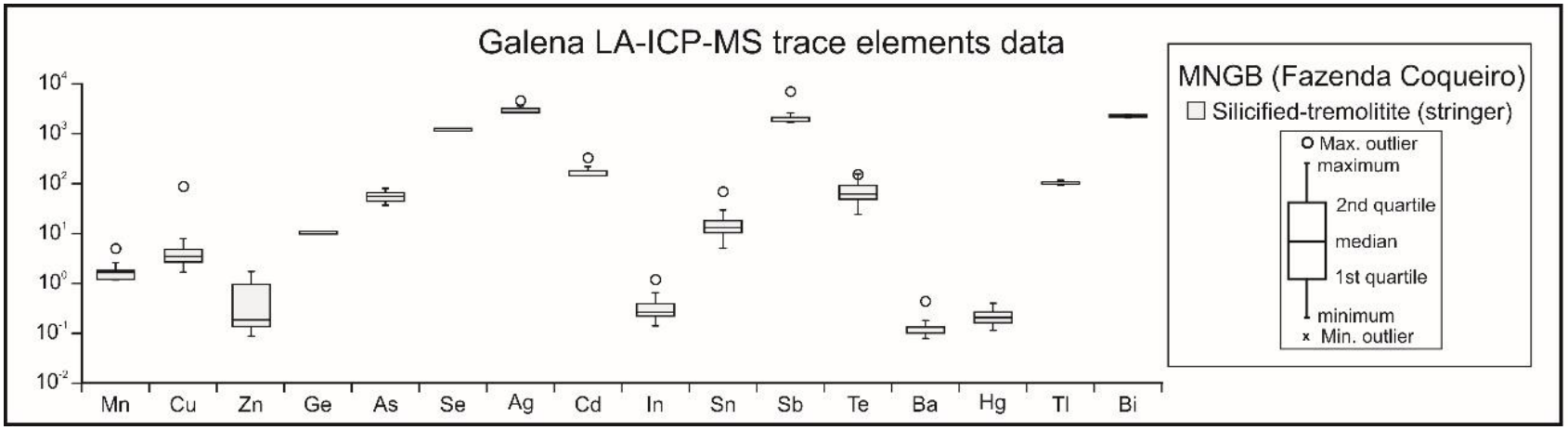

Figure 7.13.Box-whiskers plots for selected trace elements in galena from the stringer ore of Fazenda Coqueiro Deposit.

Table 7.11. Summary of selected arsenopyrite trace elements data for samples from Fazenda Coqueiro Deposit.

Sample	^{55}Mn	^{59}Co	^{60}Ni	^{66}Zn	^{74}Ge	^{77}Se	^{95}Mo	^{107}Ag	^{115}In	^{121}Sb	^{125}Te	^{197}Au	^{202}Hg	^{208}Pb	^{209}Bi
FCQ-06.5 (n=8)															
Range	bdl-66	1121-2480	1440-4220	bdl-9.6	0.7-1.3	57.8-99.2	bdl-1.6	bdl-0.3	0.2-0.3	438-893	9.1-17.2	0.06-0.4	1.7-2.8	bdl-10.2	0.02-0.3
Avg.	20.5	1792.1	2248.6	2.4	1	75.85	0.3	0.08	0.2	644.1	12.7	0.16	2.2	2	0.1
SD	31.1	449	948.4	4.1	0.25	15.35	0.6	0.1	0.03	160.8	3.1	0.12	0.4	4	0.1
FCQ-1 (n=2)															
Range	bdl-0.3	19.8-274	142.4-169.2	-	0.7-0.8	42.9-47.9	0.01-0.001	0.2-1.8	0.25-0.27	26.5-38.8	8-9.8	bdl-0.07	1.5-2.5	bdl-38	0.06-0.08
Avg.	-	146.9	155.8	-	0.78	45.4	0.01	1	0.26	32.6	8.9	-	2	-	0.07
SD	-	179.75	18.9	-	0.02	3.5	0.01	1.1	0.01	8.7	1.2	-	0.7	-	0.01

Table 7.12. SHRIMP-SI S-isotopic values for the sulfides standards used to the sulfide analysis of samples from the Mundo Novo Greenstone Belt.

Ruttan pyrite (Session 1)

Title	Date	Time	Sets	Scans	$\delta^{33}S$ (‰)	2σ	$\delta^{34}S$ (‰)	2σ	$\delta^{36}S$ (‰)	2σ	$\Delta^{33}S$ (‰)	2σ	$\Delta^{36}S$ (‰)	2σ	^{32}S cps (median)	^{33}S cps (median)	^{34}S cps (median)	^{36}S cps (median)
RUTTAN-1.1	22/07/15	10:44:25	2	10	0.34	0.07	0.74	0.02	1.39	0.34	0.03	0.08	0.15	0.33	1.43E+09	1.12E+07	6.25E+07	2.25E+05
RUTTAN-1.2	22/07/15	12:53:43	2	10	0.41	0.09	0.88	0.02	1.49	0.31	-0.01	0.09	-0.18	0.31	1.39E+09	1.09E+07	6.10E+07	2.19E+05
RUTTAN-2.1	22/07/15	13:57:21	2	10	0.49	0.11	1.03	0.02	2.54	0.39	-0.11	0.11	0.19	0.40	1.52E+09	1.20E+07	6.69E+07	2.41E+05
RUTTAN-2.2.	22/07/15	16:33:43	2	10	1.18	0.08	2.23	0.03	4.02	0.39	0.09	0.08	-0.16	0.40	1.51E+09	1.19E+07	6.63E+07	2.39E+05
RUTTAN-1.1	21/07/15	13:34:23	2	10	0.83	0.13	1.54	0.02	3.18	0.26	-0.02	0.13	0.05	0.26	1.48E+09	1.17E+07	6.51E+07	2.34E+05
RUTTAN-1.2	21/07/15	13:49:25	2	10	0.81	0.07	1.50	0.02	2.97	0.44	0.06	0.07	0.20	0.45	1.43E+09	1.12E+07	6.27E+07	2.26E+05
RUTTAN-1.3	21/07/15	14:56:56	2	10	0.54	0.16	1.13	0.03	2.11	0.29	-0.05	0.17	-0.09	0.30	1.42E+09	1.12E+07	6.24E+07	2.24E+05
RUTTAN-1.4	21/07/15	18:17:35	2	10	0.77	0.11	1.59	0.03	2.83	0.24	-0.05	0.12	-0.21	0.25	1.43E+09	1.13E+07	6.29E+07	2.26E+05
RUTTAN-1.5	21/07/15	18:35:08	2	10	0.95	0.12	1.81	0.03	3.37	0.45	0.03	0.13	-0.07	0.44	1.42E+09	1.12E+07	6.24E+07	2.24E+05
RUTTAN-1.2	22/07/15	0:33:25	2	10	0.59	0.09	1.07	0.03	2.12	0.36	0.02	0.09	0.01	0.37	1.39E+09	1.09E+07	6.09E+07	2.19E+05
RUTTAN-1.3	22/07/15	0:48:35	2	10	0.68	0.13	1.09	0.02	2.31	0.34	0.07	0.14	0.04	0.34	1.42E+09	1.12E+07	6.22E+07	2.24E+05
RUTTAN-1.4	22/07/15	3:48:34	2	10	0.54	0.07	0.97	0.03	2.21	0.33	0.00	0.07	0.23	0.34	1.41E+09	1.11E+07	6.18E+07	2.22E+05
RUTTAN-1.5	22/07/15	4:03:29	2	10	0.46	0.07	0.93	0.02	1.66	0.25	0.01	0.08	-0.01	0.26	1.40E+09	1.10E+07	6.15E+07	2.21E+05
RUTTAN-2.1	22/07/15	6:03:14	2	10	0.37	0.11	0.88	0.03	1.70	0.35	-0.12	0.11	-0.12	0.34	1.42E+09	1.12E+07	6.22E+07	2.23E+05
RUTTAN-2.2	22/07/15	6:18:08	2	10	0.42	0.10	1.03	0.02	1.64	0.29	-0.04	0.11	-0.08	0.30	1.40E+09	1.10E+07	6.13E+07	2.20E+05
RUTTAN-2.3	22/07/15	8:35:17	2	10	0.52	0.10	0.87	0.03	1.61	0.30	0.10	0.11	0.04	0.31	1.47E+09	1.16E+07	6.46E+07	2.32E+05
RUTTAN-1.1	22/07/15	20:13:19	2	10	0.60	0.10	1.06	0.02	2.15	0.30	0.01	0.11	-0.06	0.31	1.41E+09	1.11E+07	6.19E+07	2.23E+05
RUTTAN-1.2	22/07/15	20:28:50	2	10	0.63	0.08	1.13	0.02	2.44	0.23	-0.01	0.09	0.06	0.23	1.39E+09	1.10E+07	6.12E+07	2.20E+05
RUTTAN-2.1	22/07/15	23:05:53	2	10	0.64	0.07	1.12	0.03	2.22	0.25	0.05	0.08	0.04	0.26	1.36E+09	1.07E+07	5.98E+07	2.15E+05
RUTTAN-2.2	22/07/15	23:21:38	2	10	0.65	0.13	1.53	0.02	2.58	0.26	-0.03	0.13	0.10	0.27	1.40E+09	1.10E+07	6.16E+07	2.21E+05
RUTTAN-2.3	23/07/15	1:59:55	2	10	0.64	0.09	1.18	0.02	2.09	0.24	0.02	0.09	-0.20	0.24	1.39E+09	1.09E+07	6.10E+07	2.20E+05
RUTTAN-2.4	23/07/15	2:15:26	2	10	0.54	0.11	1.14	0.03	2.17	0.30	-0.03	0.11	0.07	0.30	1.39E+09	1.09E+07	6.10E+07	2.19E+05

Ruttan pyrite (Session 2)

Title	Date	Time	Sets	Scans	$\delta^{33}S$ (‰)	2σ	$\delta^{34}S$ (‰)	2σ	$\delta^{36}S$ (‰)	2σ	$\Delta^{33}S$ (‰)	2σ	$\Delta^{36}S$ (‰)	2σ	^{32}S cps (median)	^{33}S cps (median)	^{34}S cps (median)	^{36}S cps (median)
RUTTAN-1.1	16/11/15	10:48:41	4	10	0.68	0.06	1.22	0.03	2.50	0.36	0.03	0.05	0.09	0.37	2.59E+09	2.04E+07	1.15E+08	4.69E+05
RUTTAN-1.2	16/11/15	11:10:12	4	10	0.72	0.08	1.41	0.02	2.73	0.30	-0.02	0.08	-0.01	0.30	2.60E+09	2.05E+07	1.15E+08	4.71E+05
RUTTAN-2.1	16/11/15	16:21:05	4	10	0.47	0.08	0.95	0.03	1.83	0.30	-0.02	0.07	0.01	0.30	2.53E+09	2.00E+07	1.13E+08	4.60E+05
RUTTAN-2.2	16/11/15	16:42:37	4	10	0.60	0.06	1.17	0.02	2.09	0.31	0.01	0.06	-0.10	0.31	2.57E+09	2.02E+07	1.14E+08	4.65E+05
RUTTAN_1.1	16/11/15	20:00:10	4	10	0.45	0.08	1.13	0.02	1.80	0.28	-0.09	0.07	-0.18	0.27	2.60E+09	2.05E+07	1.16E+08	4.70E+05
RUTTAN_1.2	16/11/15	20:21:55	4	10	0.44	0.06	0.98	0.03	1.55	0.35	-0.08	0.06	-0.35	0.35	2.63E+09	2.07E+07	1.17E+08	4.75E+05
RUTTAN_2.1	17/11/15	0:41:12	4	10	0.51	0.08	0.73	0.03	2.26	0.30	-0.02	0.07	0.32	0.28	2.75E+09	2.16E+07	1.22E+08	4.98E+05
RUTTAN_2.2	17/11/15	1:02:44	4	10	0.79	0.06	1.62	0.02	3.13	0.27	0.01	0.06	0.24	0.27	2.74E+09	2.15E+07	1.22E+08	4.95E+05
RUTTAN-1.1	17/11/15	1:46:37	4	10	0.70	0.05	1.51	0.02	3.02	0.31	-0.06	0.05	0.21	0.30	2.76E+09	2.17E+07	1.23E+08	5.00E+05
RUTTAN-1.2	17/11/15	2:08:33	4	10	0.62	0.09	1.17	0.03	2.32	0.28	0.01	0.08	0.07	0.29	2.75E+09	2.16E+07	1.22E+08	4.97E+05
RUTTAN-1.3	17/11/15	5:24:22	4	10	0.74	0.10	1.22	0.03	2.15	0.28	0.12	0.09	-0.16	0.29	2.63E+09	2.07E+07	1.17E+08	4.76E+05
RUTTAN-1.4	17/11/15	5:46:06	4	10	0.66	0.05	1.15	0.02	1.85	0.34	0.12	0.05	-0.15	0.33	2.60E+09	2.05E+07	1.15E+08	4.70E+05
RUTTAN-1.5	17/11/15	11:47:29	4	10	1.28	0.06	2.60	0.02	3.72	0.32	-0.02	0.05	-1.00	0.31	2.62E+09	2.06E+07	1.16E+08	4.74E+05
RUTTAN-1.6	17/11/15	13:20:05	4	10	1.28	0.08	2.52	0.02	4.16	0.25	-0.05	0.08	-0.71	0.25	2.62E+09	2.06E+07	1.16E+08	4.75E+05
RUTTAN-1.1n	17/11/15	18:01:43	4	10	0.56	0.09	0.99	0.02	2.05	0.28	0.04	0.10	0.12	0.28	2.66E+09	2.09E+07	1.18E+08	4.81E+05

RUTTAN-3.1	17/11/15	18:51:51	4	10	0.67	0.07	1.39	0.02	2.53	0.31	-0.04	0.07	-0.12	0.31	2.74E+09	2.16E+07	1.22E+08	4.96E+05
Ruttan-1.2	17/11/15	21:47:05	4	10	0.86	0.06	1.82	0.02	3.09	0.31	-0.03	0.06	-0.19	0.30	2.58E+09	2.03E+07	1.15E+08	4.67E+05
Ruttan-2.1	18/11/15	1:02:13	4	10	0.50	0.07	0.99	0.02	2.02	0.35	-0.02	0.07	0.13	0.33	2.50E+09	1.97E+07	1.11E+08	4.52E+05
Ruttan-2.3	18/11/15	3:12:28	4	10	0.47	0.07	1.00	0.02	1.93	0.30	-0.04	0.06	0.04	0.30	2.64E+09	2.07E+07	1.17E+08	4.76E+05
RUTTAN-1.1	18/11/15	3:34:51	4	10	0.75	0.10	1.53	0.03	3.01	0.29	-0.02	0.08	0.21	0.29	2.68E+09	2.11E+07	1.19E+08	4.84E+05
RUTTAN-1.2	18/11/15	3:56:36	4	10	0.68	0.06	1.19	0.02	2.65	0.26	0.01	0.05	0.21	0.25	2.64E+09	2.07E+07	1.17E+08	4.77E+05
RUTTAN-1.3	18/11/15	7:32:31	4	10	0.48	0.08	0.92	0.02	1.55	0.29	0.01	0.07	-0.19	0.30	2.48E+09	1.95E+07	1.10E+08	4.48E+05
RUTTAN-1.4	18/11/15	7:54:02	4	10	0.58	0.07	0.99	0.02	1.59	0.32	0.09	0.06	-0.21	0.32	2.50E+09	1.96E+07	1.11E+08	4.50E+05

Balmat pyrite (Session 1)

Title	Date	Time	Sets	Scans	$\delta^{33}S$ (‰)	2σ	$\delta^{34}S$ (‰)	2σ	$\delta^{36}S$ (‰)	2σ	$\Delta^{33}S$ (‰)	2σ	$\Delta^{36}S$ (‰)	2σ	^{32}S cps (median)	^{33}S cps (median)	^{34}S cps (median)	^{36}S cps (median)
BALMAT-1.1	22/07/15	11:10:47	2	10	7.50	0.09	14.55	0.03	28.32	0.31	0.07	0.11	0.51	0.32	1.35E+09	1.07E+07	6.02E+07	2.19E+05
BALMAT-1.2	22/07/15	13:20:16	2	10	7.96	0.11	15.57	0.03	29.99	0.27	0.05	0.12	0.36	0.28	1.57E+09	1.24E+07	6.97E+07	2.54E+05
BALMAT-1.1	21/07/15	15:13:56	2	10	7.92	0.09	15.36	0.02	29.61	0.38	0.00	0.09	0.05	0.39	1.49E+09	1.18E+07	6.65E+07	2.42E+05
BALMAT-1.2	21/07/15	18:50:04	2	10	8.08	0.09	15.68	0.02	30.19	0.27	0.03	0.10	0.17	0.29	1.48E+09	1.17E+07	6.58E+07	2.40E+05
BALMAT-1.1	22/07/15	1:03:30	2	10	7.97	0.13	15.23	0.03	29.02	0.39	0.10	0.13	-0.33	0.41	1.45E+09	1.15E+07	6.45E+07	2.35E+05
BALMAT-1.2	22/07/15	4:18:25	2	10	7.83	0.11	15.18	0.02	28.80	0.30	0.05	0.11	-0.23	0.32	1.45E+09	1.15E+07	6.45E+07	2.35E+05
BALMAT-1.3	22/07/15	6:33:04	2	10	7.59	0.10	14.87	0.03	28.32	0.24	-0.06	0.10	-0.21	0.25	1.42E+09	1.12E+07	6.31E+07	2.29E+05
BALMAT-1.1	22/07/15	20:44:22	2	10	7.72	0.10	15.02	0.02	28.23	0.38	0.05	0.11	-0.36	0.39	1.36E+09	1.08E+07	6.04E+07	2.20E+05
BALMAT-1.2	22/07/15	23:37:26	2	10	7.90	0.15	15.44	0.02	29.56	0.46	-0.07	0.15	-0.18	0.46	1.37E+09	1.09E+07	6.11E+07	2.22E+05
BALMAT-1.3	23/07/15	2:30:58	2	10	7.82	0.05	15.03	0.03	28.63	0.30	0.09	0.05	-0.20	0.31	1.33E+09	1.06E+07	5.94E+07	2.16E+05

Balmat pyrite (Session 2)

Title	Date	Time	Sets	Scans	$\delta^{33}S$ (‰)	2σ	$\delta^{34}S$ (‰)	2σ	$\delta^{36}S$ (‰)	2σ	$\Delta^{33}S$ (‰)	2σ	$\Delta^{36}S$ (‰)	2σ	^{32}S cps (median)	^{33}S cps (median)	^{34}S cps (median)	^{36}S cps (median)
BALMAT-1.1	16/11/15	11:31:45	4	10	7.95	0.04	15.57	0.03	30.02	0.29	-0.03	0.04	0.24	0.29	2.57E+09	2.04E+07	1.16E+08	4.78E+05
BALMAT-1.2	16/11/15	17:04:08	4	10	7.96	0.06	15.36	0.03	29.33	0.31	0.09	0.06	-0.02	0.32	2.56E+09	2.03E+07	1.15E+08	4.77E+05
BALMAT_1.1	16/11/15	20:43:41	4	10	7.83	0.04	15.33	0.02	29.06	0.37	-0.04	0.04	-0.28	0.39	2.52E+09	2.00E+07	1.13E+08	4.67E+05
BALMAT_1.2	17/11/15	1:24:15	4	10	7.77	0.08	15.40	0.02	29.70	0.27	-0.13	0.07	0.25	0.27	2.62E+09	2.08E+07	1.18E+08	4.87E+05
BALMAT-1.2	17/11/15	6:07:50	4	10	7.76	0.05	15.01	0.02	28.79	0.33	0.07	0.04	0.15	0.33	2.74E+09	2.17E+07	1.23E+08	5.08E+05
BALMAT-1.1n	17/11/15	15:10:14	4	10	7.67	0.07	14.87	0.02	29.05	0.28	0.03	0.07	0.53	0.27	2.57E+09	2.04E+07	1.16E+08	4.77E+05
BALMAT-1.2n	17/11/15	17:18:38	4	10	7.65	0.07	14.81	0.02	28.43	0.33	0.02	0.07	-0.02	0.33	2.53E+09	2.01E+07	1.14E+08	4.70E+05
BALMAT-1.3n	17/11/15	17:40:10	4	10	7.62	0.07	14.89	0.02	28.42	0.25	0.04	0.07	0.14	0.27	2.52E+09	1.99E+07	1.13E+08	4.68E+05
BALMAT-1.1.1n	17/11/15	19:34:17	4	10	7.79	0.05	15.16	0.02	28.81	0.30	0.00	0.05	-0.20	0.29	2.52E+09	2.00E+07	1.14E+08	4.68E+05
BALMAT-1.1.1	17/11/15	19:56:35	4	10	7.52	0.08	14.68	0.02	28.10	0.24	0.04	0.07	0.24	0.25	2.66E+09	2.10E+07	1.20E+08	4.93E+05
Balmat-1.1	17/11/15	22:08:37	4	10	7.78	0.07	14.93	0.03	28.37	0.28	0.09	0.07	-0.27	0.28	2.49E+09	1.97E+07	1.12E+08	4.61E+05
Balmat-1.2	18/11/15	1:23:45	4	10	7.41	0.05	14.56	0.02	27.64	0.24	-0.03	0.05	-0.08	0.24	2.62E+09	2.08E+07	1.18E+08	4.86E+05
BALMAT-1.1	18/11/15	4:18:21	4	10	7.62	0.07	14.73	0.03	28.17	0.29	0.05	0.07	-0.04	0.28	2.48E+09	1.96E+07	1.11E+08	4.59E+05
BALMAT-1.2	18/11/15	8:15:47	4	10	7.48	0.07	14.73	0.03	27.79	0.30	-0.05	0.06	-0.28	0.30	2.45E+09	1.94E+07	1.10E+08	4.54E+05

Norilsk chalcopyrite (Session 1)

Title	Date	Time	Sets	Scans	$\delta^{33}S$ (‰)	2σ	$\delta^{34}S$ (‰)	2σ	$\delta^{36}S$ (‰)	2σ	$\Delta^{33}S$ (‰)	2σ	$\Delta^{36}S$ (‰)	2σ	^{32}S cps (median)	^{33}S cps (median)	^{34}S cps (median)	^{36}S cps (median)
NORILSK-CPY-1.1	23/07/15	2:46:30	2	10	4.06	0.14	8.04	0.02	15.42	0.35	-0.12	0.16	0.03	0.35	2.13E+09	1.68E+07	9.41E+07	3.40E+05
NORILSK-CPY-2.1	23/07/15	3:02:01	2	10	4.15	0.08	7.90	0.02	15.28	0.23	0.05	0.10	0.20	0.24	2.04E+09	1.61E+07	9.00E+07	3.26E+05
NORILSK-CPY-1.2	23/07/15	5:22:31	2	10	3.85	0.05	7.39	0.02	14.09	0.25	0.03	0.05	0.04	0.25	2.17E+09	1.71E+07	9.56E+07	3.45E+05
NORILSK-CPY-3.1	23/07/15	5:38:03	2	10	4.31	0.07	8.39	0.02	15.80	0.21	-0.03	0.07	-0.19	0.21	2.14E+09	1.69E+07	9.44E+07	3.41E+05

NORILSK-CPY-2.2	23/07/15	7:58:26	2	10	4.26	0.09	8.11	0.02	15.50	0.31	0.05	0.08	0.01	0.31	2.06E+09	1.63E+07	9.12E+07	3.30E+05
NORILSK-CPY-3.2	23/07/15	8:13:57	2	10	4.21	0.07	8.11	0.02	15.36	0.17	0.01	0.07	-0.11	0.18	2.13E+09	1.68E+07	9.40E+07	3.40E+05
Trout Lake chalcopyrite (Session 1)																		
Title	**Date**	**Time**	**Sets**	**Scans**	**$\delta^{33}S$ (‰)**	**2σ**	**$\delta^{34}S$ (‰)**	**2σ**	**$\delta^{36}S$ (‰)**	**2σ**	**$\Delta^{33}S$ (‰)**	**2σ**	**$\Delta^{36}S$ (‰)**	**2σ**	**^{32}S cps (median)**	**^{33}S cps (median)**	**^{34}S cps (median)**	**^{36}S cps (median)**
TL-CPY-1.1	23/07/15	3:17:34	2	10	-0.07	0.07	-0.34	0.02	0.11	0.25	0.05	0.07	0.68	0.24	2.08E+09	1.64E+07	9.11E+07	3.27E+05
TL-CPY-2.1	23/07/15	3:33:05	2	10	-0.18	0.08	-0.47	0.02	-0.61	0.25	0.06	0.08	0.39	0.24	2.22E+09	1.75E+07	9.73E+07	3.49E+05
TL-CPY-1.2	23/07/15	5:53:35	2	10	-0.05	0.10	-0.20	0.02	0.11	0.19	0.02	0.10	0.47	0.19	2.03E+09	1.60E+07	8.92E+07	3.20E+05
TL-CPY-3.1	23/07/15	6:09:06	2	10	0.10	0.08	0.38	0.02	0.24	0.29	-0.08	0.08	-0.33	0.29	1.98E+09	1.56E+07	8.67E+07	3.12E+05
TL-CPY-2.2	23/07/15	8:29:30	2	10	-0.20	0.08	-0.42	0.02	-0.91	0.27	0.00	0.08	-0.06	0.26	2.18E+09	1.72E+07	9.56E+07	3.43E+05
TL-CPY-3.2	23/07/15	8:45:01	2	10	-0.08	0.13	-0.12	0.02	-0.09	0.24	0.01	0.13	0.35	0.25	2.17E+09	1.71E+07	9.53E+07	3.42E+05
Balmat galena (Session 1)																		
Title	**Date**	**Time**	**Sets**	**Scans**	**$\delta^{33}S$ (‰)**	**2σ**	**$\delta^{34}S$ (‰)**	**2σ**	**$\delta^{36}S$ (‰)**	**2σ**	**$\Delta^{33}S$ (‰)**	**2σ**	**$\Delta^{36}S$ (‰)**	**2σ**	**^{32}S cps (median)**	**^{33}S cps (median)**	**^{34}S cps (median)**	**^{36}S cps (median)**
BALMAT_Ga-1.1	23/07/15	9:45:08	1	10	7.78	0.02	15.06	0.02	28.34	0.24	-0.04	0.03	-0.15	0.25	2.55E+09	2.00E+07	1.11E+08	3.94E+05
BALMAT_Ga-1.2	23/07/15	10:02:03	1	10	8.14	0.04	15.75	0.02	29.37	0.31	-0.02	0.04	-0.40	0.36	2.65E+09	2.07E+07	1.15E+08	4.09E+05
BALMAT_Ga-1.3	23/07/15	10:11:45	1	10	7.66	0.03	14.68	0.02	27.31	0.30	-0.04	0.03	-0.70	0.31	2.38E+09	1.86E+07	1.03E+08	3.67E+05
BALMAT_Ga-2.1	23/07/15	11:09:23	1	10	8.94	0.03	17.23	0.02	32.70	0.47	0.00	0.03	0.03	0.47	2.59E+09	2.03E+07	1.13E+08	4.02E+05
BALMAT_Ga-2.2	23/07/15	11:19:05	1	10	9.26	0.05	17.76	0.02	34.41	0.23	0.05	0.05	0.68	0.24	2.59E+09	2.03E+07	1.13E+08	4.02E+05
BALMAT_Ga-2.3	23/07/15	12:08:01	1	10	9.36	0.03	18.02	0.02	34.62	0.14	0.07	0.03	0.58	0.17	2.50E+09	1.96E+07	1.09E+08	3.89E+05
BALMAT_Ga-2.4	23/07/15	12:17:43	1	10	9.00	0.05	17.40	0.02	32.95	0.36	-0.02	0.04	-0.05	0.38	2.56E+09	2.01E+07	1.11E+08	3.97E+05
Anderson Pyrrhotite (Session 2)																		
Title	**Date**	**Time**	**Sets**	**Scans**	**$\delta^{33}S$ (‰)**	**2σ**	**$\delta^{34}S$ (‰)**	**2σ**	**$\delta^{36}S$ (‰)**	**2σ**	**$\Delta^{33}S$ (‰)**	**2σ**	**$\Delta^{36}S$ (‰)**	**2σ**	**^{32}S cps (median)**	**^{33}S cps (median)**	**^{34}S cps (median)**	**^{36}S cps (median)**
ANDERSON_Po-2.1	17/11/15	10:39:13	4	10	0.54	0.05	1.25	0.02	2.50	0.29	-0.07	0.04	0.30	0.28	3.73E+09	2.93E+07	1.66E+08	6.74E+05
ANDERSON_Po-2.2	17/11/15	12:57:26	4	10	0.80	0.07	1.48	0.02	3.13	0.28	0.00	0.07	0.25	0.27	3.65E+09	2.87E+07	1.62E+08	6.59E+05
ANDERSON_Po-3.1	17/11/15	14:04:46	4	10	0.62	0.06	1.38	0.02	1.92	0.34	-0.10	0.05	-0.67	0.32	2.97E+09	2.33E+07	1.32E+08	5.35E+05
ANDERSON_Po-1	18/11/15	1:45:31	4	10	0.74	0.04	1.41	0.02	2.81	0.25	0.02	0.04	0.16	0.24	2.85E+09	2.24E+07	1.26E+08	5.13E+05
ANDERSON_Po-2	18/11/15	2:50:41	4	10	0.70	0.04	1.39	0.02	2.45	0.30	-0.02	0.04	-0.19	0.28	2.79E+09	2.19E+07	1.23E+08	5.01E+05

Table 7.13. SHRIMP-SI multiple sulfur isotopic compositions of sulfide samples from the northern Mundo Novo Greenstone Belt.

Northern Mundo Novo Greenstone Belt														
Sample	**Rock type**	**Sulfide type**	**Spot title**	**Date**	**Time**	**$\delta^{34}S$ (‰)**	**2σ**	**$\Delta^{33}S$ (‰)**	**2σ**	**$\Delta^{36}S$ (‰)**	**2σ**	**^{32}S cps (median)**	**^{33}S cps (median)**	**^{34}S cps (median)**	**^{36}S cps (median)**
PD-06	Massive sulfide hosted metabasalt.	Py	PD-06_1	18/11/15	4:39:55	2.10	0.03	-0.98	0.06	0.57	0.29	2.48E+09	1.95E+07	1.10E+08	4.50E+05
			PD-06_2	18/11/15	5:01:28	1.64	0.03	-0.97	0.04	0.73	0.36	2.37E+09	1.86E+07	1.05E+08	4.29E+05
			PD-06_4	18/11/15	5:44:32	2.26	0.02	-0.96	0.04	1.45	0.26	2.68E+09	2.11E+07	1.19E+08	4.86E+05
			PD-06_6	18/11/15	6:06:05	2.45	0.03	-0.98	0.05	1.19	0.32	2.65E+09	2.08E+07	1.18E+08	4.80E+05
			PD-06_9	18/11/15	6:49:10	1.62	0.03	-0.97	0.05	0.98	0.36	2.56E+09	2.02E+07	1.14E+08	4.64E+05
			PD-06_10	18/11/15	7:10:43	1.86	0.03	-1.00	0.09	1.52	0.34	2.61E+09	2.05E+07	1.16E+08	4.73E+05
PD-07	Semi-massive sulfide hosted by metabasalt	Py	PD-07_1	16/11/15	21:05:13	2.49	0.02	-1.26	0.04	2.11	0.26	3.12E+09	2.46E+07	1.39E+08	5.68E+05
			PD-07_2	16/11/15	21:26:45	1.17	0.02	-1.27	0.06	0.79	0.31	2.53E+09	1.99E+07	1.13E+08	4.58E+05

			PD-07_3	16/11/15	21:48:17	1.37	0.02	-1.18	0.05	0.98	0.38	2.53E+09	1.99E+07	1.13E+08	4.58E+05
			PD-07_4	16/11/15	22:09:49	1.65	0.02	-1.21	0.02	1.10	0.34	2.56E+09	2.01E+07	1.14E+08	4.64E+05
			PD-07_5	16/11/15	22:31:33	1.65	0.03	-1.20	0.05	1.19	0.31	2.68E+09	2.11E+07	1.19E+08	4.86E+05
			PD-07_6	16/11/15	22:53:05	2.03	0.02	-1.22	0.06	1.03	0.36	2.69E+09	2.11E+07	1.20E+08	4.87E+05
			PD-07_7	16/11/15	23:14:37	1.72	0.03	-1.25	0.06	0.89	0.31	2.47E+09	1.94E+07	1.10E+08	4.46E+05
			PD-07_8	16/11/15	23:36:23	1.75	0.02	-1.23	0.04	1.45	0.28	2.66E+09	2.09E+07	1.18E+08	4.82E+05
			PD-07_9	16/11/15	23:57:54	1.32	0.03	-1.15	0.07	1.00	0.29	2.60E+09	2.04E+07	1.15E+08	4.70E+05
			PD-07_10	17/11/15	0:19:27	1.24	0.02	-1.27	0.04	1.05	0.29	2.60E+09	2.05E+07	1.16E+08	4.71E+05
PD-04	Pillowed metabasalt	Py	PD_04-1	24/07/15	0:43:10	1.35	0.02	0.05	0.14	0.14	0.34	1.39E+09	1.09E+07	6.10E+07	2.20E+05
			PD_04-2	24/07/15	0:58:41	0.99	0.03	0.00	0.11	-0.23	0.29	1.41E+09	1.11E+07	6.19E+07	2.22E+05
			PD_04-3	24/07/15	1:14:13	2.94	0.02	-0.07	0.10	0.30	0.32	1.39E+09	1.10E+07	6.12E+07	2.20E+05
			~~PD_04-4~~	~~24/07/15~~	~~1:29:45~~	~~1.65~~	~~0.03~~	~~0.35~~	~~0.07~~	~~0.71~~	~~0.32~~	~~1.15E+09~~	~~9.04E+06~~	~~5.04E+07~~	~~1.81E+05~~
			PD_04-5	24/07/15	1:45:17	0.30	0.02	-0.62	0.10	0.63	0.31	1.39E+09	1.10E+07	6.11E+07	2.20E+05
			~~PD-04-6~~	~~24/07/15~~	~~2:01:04~~	~~14.68~~	~~0.02~~	~~0.20~~	~~0.14~~	~~-0.48~~	~~0.36~~	~~1.31E+09~~	~~1.04E+07~~	~~5.83E+07~~	~~2.12E+05~~
			PD-04-7	24/07/15	19:46:11	-1.41	0.03	0.13	0.07	-0.20	0.23	1.55E+09	1.22E+07	6.77E+07	2.43E+05
			PD-04-8	24/07/15	20:01:42	1.89	0.02	-1.18	0.08	1.31	0.28	1.52E+09	1.20E+07	6.69E+07	2.41E+05
			PD-04-9	24/07/15	20:17:13	1.44	0.02	-1.07	0.10	1.12	0.36	1.45E+09	1.14E+07	6.36E+07	2.29E+05
			PD-04-10	24/07/15	20:32:44	0.53	0.02	0.04	0.13	0.06	0.33	1.48E+09	1.16E+07	6.48E+07	2.33E+05
FCJ-4	Carbonaceous-schist	Py	FCJ-4_1	16/11/15	11:53:18	3.30	0.03	1.33	0.02	-0.46	0.26	2.66E+09	2.10E+07	1.19E+08	4.84E+05
			FCJ-4_2	16/11/15	12:19:34	2.13	0.03	1.33	0.07	-1.21	0.27	2.34E+09	1.85E+07	1.04E+08	4.24E+05
			FCJ-4_3	16/11/15	12:41:06	2.92	0.03	1.39	0.08	-0.58	0.37	2.66E+09	2.10E+07	1.18E+08	4.83E+05
			FCJ-4_4	16/11/15	13:06:48	3.23	0.03	1.26	0.07	-1.05	0.26	2.50E+09	1.98E+07	1.11E+08	4.55E+05
			FCJ-4_5	16/11/15	15:36:04	3.51	0.04	1.40	0.04	-0.85	0.32	2.60E+09	2.05E+07	1.16E+08	4.72E+05
			FCJ-4_6	16/11/15	13:45:08	3.49	0.04	1.41	0.05	-0.23	0.34	2.63E+09	2.07E+07	1.17E+08	4.78E+05
			FCJ-4_7	16/11/15	14:06:42	2.98	0.04	1.37	0.04	-0.88	0.36	2.47E+09	1.95E+07	1.10E+08	4.48E+05
			FCJ-4_8	16/11/15	15:57:36	2.30	0.04	1.35	0.06	-1.24	0.42	2.28E+09	1.80E+07	1.01E+08	4.13E+05
			FCJ-4_9	16/11/15	14:39:28	2.16	0.03	1.40	0.06	-0.67	0.35	2.55E+09	2.01E+07	1.13E+08	4.63E+05
			FCJ-4_10	16/11/15	15:01:10	2.86	0.03	1.38	0.04	-1.14	0.31	2.49E+09	1.96E+07	1.11E+08	4.52E+05
PD-11	BIF	Py	PD_11-1	23/07/15	20:49:20	1.09	0.02	0.02	0.05	-0.16	0.35	1.47E+09	1.16E+07	6.45E+07	2.32E+05
			PD_11-2	23/07/15	21:04:51	0.81	0.03	0.25	0.11	0.26	0.37	1.49E+09	1.17E+07	6.52E+07	2.34E+05
			PD_11-3	23/07/15	21:20:23	2.43	0.02	0.10	0.07	0.08	0.29	1.41E+09	1.11E+07	6.17E+07	2.22E+05

Abbreviations: Py (pyrite).

Table 7.14. SHRIMP-SI multiple sulfur isotopic compositions of sulfide samples from the southern Mundo Novo Greenstone Belt (Fazenda Coqueiro Deposit).

Southern Mundo Novo Greenstone Belt (Fazenda Coqueiro Deposit)															
Sample	**Drill Core (m)**	**Rock type**	**Sulfide type**	**Spot title**	**Date**	**Time**	**$\delta^{34}S$ (‰)**	**2σ**	**$\Delta^{33}S$ (‰)**	**2σ**	**$\Delta^{36}S$ (‰)**	**2σ**	**^{32}S cps (median)**	**^{33}S cps (median)**	**^{34}S cps (median)**	**^{36}S cps (median)**
FCQ-06.5	FCQ-06 (221.1-222.3)	Silicified tremolite-metabasalt	Po	FCQ-06.5_Po-1	17/11/15	10:16:49	1.13	0.02	1.54	0.07	-0.99	0.26	3.58E+09	2.81E+07	1.58E+08	6.44E+05
				FCQ-06.5_Po-2	17/11/15	11:02:01	3.05	0.02	1.60	0.04	-1.01	0.17	3.77E+09	2.97E+07	1.68E+08	6.83E+05
				FCQ-06.5_Po-3	17/11/15	11:25:02	1.98	0.02	1.62	0.06	-1.19	0.32	3.35E+09	2.64E+07	1.49E+08	6.06E+05
				FCQ-06.5_Po-5	17/11/15	12:13:06	2.65	0.02	1.53	0.05	-1.13	0.21	3.81E+09	3.00E+07	1.69E+08	6.90E+05
				FCQ-06.5_Po-6	17/11/15	12:35:23	2.10	0.02	1.65	0.05	-1.31	0.32	3.56E+09	2.81E+07	1.58E+08	6.43E+05

FCQ-06.3	FCQ-06 (380.1-380.2)	Massive sulfide	Po	FCQ-06.3_Po-1	17/11/15	9:10:56	0.33	0.02	1.90	0.06	-1.67	0.20	3.07E+09	2.42E+07	1.36E+08	5.52E+05
				FCQ-06.3_Po-2	17/11/15	8:31:27	0.59	0.02	2.14	0.05	-0.69	0.21	4.10E+09	3.23E+07	1.82E+08	7.38E+05
			Py	FCQ-06.3-1	22/07/15	23:53:00	2.23	0.02	2.13	0.06	-1.66	0.27	1.44E+09	1.14E+07	6.32E+07	2.27E+05
				FCQ-06.3-2	23/07/15	0:08:55	0.63	0.03	2.14	0.11	-1.25	0.33	1.40E+09	1.10E+07	6.13E+07	2.20E+05
				FCQ-06.3-3	23/07/15	0:24:28	1.64	0.03	2.15	0.09	-1.09	0.24	1.43E+09	1.13E+07	6.28E+07	2.26E+05
				FCQ-06.3-4	23/07/15	9:20:41	1.71	0.03	2.19	0.12	-1.01	0.28	1.43E+09	1.13E+07	6.27E+07	2.25E+05
				FCQ-06.3-5	23/07/15	0:56:11	1.11	0.02	2.13	0.04	-1.48	0.33	1.46E+09	1.15E+07	6.40E+07	2.30E+05
				FCQ-06.3-6	23/07/15	1:12:37	1.38	0.02	1.91	0.09	-2.34	0.28	1.37E+09	1.08E+07	6.01E+07	2.16E+05
				FCQ-06.3-7	23/07/15	1:28:44	0.97	0.03	2.11	0.13	-0.98	0.29	1.45E+09	1.15E+07	6.39E+07	2.29E+05
				FCQ-06.3-8	23/07/15	1:44:20	2.15	0.03	2.12	0.05	-1.54	0.45	1.41E+09	1.11E+07	6.19E+07	2.22E+05
			Cpy	FCQ-06.3_CPY-1.1	23/07/15	6:40:40	0.40	0.02	2.13	0.10	-1.05	0.32	2.23E+09	1.76E+07	9.78E+07	3.51E+05
				FCQ-06.3_CPY-2.1	23/07/15	6:56:13	0.20	0.02	2.08	0.08	-1.32	0.23	2.03E+09	1.60E+07	8.88E+07	3.19E+05
				FCQ-06.3_CPY-3.1	23/07/15	7:11:45	0.29	0.02	2.10	0.06	-1.32	0.24	2.05E+09	1.62E+07	9.00E+07	3.23E+05
				FCQ-06.3_CPY-4.1	23/07/15	7:27:19	0.84	0.02	2.15	0.07	-1.30	0.32	2.14E+09	1.69E+07	9.38E+07	3.37E+05
				FCQ-06.3_CPY-5.1	23/07/15	7:42:52	-0.35	0.02	2.12	0.11	-1.33	0.20	2.16E+09	1.70E+07	9.45E+07	3.39E+05
FCQ-06.1	FCQ-06 (381.55-381.7)	Massive sulfide	Py	FCQ-06.1_1	22/07/15	3:18:38	0.94	0.02	2.05	0.06	-1.29	0.33	1.45E+09	1.15E+07	6.37E+07	2.29E+05
				FCQ-06.1_2	22/07/15	3:03:41	1.02	0.03	2.09	0.05	-1.60	0.19	1.38E+09	1.09E+07	6.07E+07	2.18E+05
				FCQ-06.1_3	22/07/15	2:18:19	1.13	0.02	2.02	0.04	-1.38	0.30	1.44E+09	1.13E+07	6.30E+07	2.26E+05
				FCQ-06.1_4	22/07/15	2:03:23	0.29	0.03	2.09	0.05	-1.31	0.34	1.39E+09	1.10E+07	6.10E+07	2.19E+05
				FCQ-06.1_5	22/07/15	1:18:28	0.15	0.02	2.02	0.09	-1.41	0.36	1.43E+09	1.13E+07	6.26E+07	2.24E+05
				FCQ-06.1_6	21/07/15	22:33:46	0.82	0.03	2.04	0.06	-1.81	0.36	1.38E+09	1.09E+07	6.05E+07	2.17E+05
				FCQ-06.1_7	21/07/15	22:18:51	2.21	0.03	2.14	0.05	-1.16	0.25	1.41E+09	1.11E+07	6.17E+07	2.22E+05
				FCQ-06.1_8	21/07/15	22:03:56	1.86	0.02	2.16	0.15	-1.48	0.41	1.36E+09	1.07E+07	5.95E+07	2.14E+05
				FCQ-06.1_9	21/07/15	23:33:35	2.11	0.02	2.06	0.08	-1.10	0.31	1.50E+09	1.18E+07	6.58E+07	2.36E+05
				FCQ-06.1_10	21/07/15	23:48:31	2.22	0.02	2.16	0.07	-0.95	0.42	1.46E+09	1.15E+07	6.39E+07	2.30E+05
				FCQ-06.1_11	22/07/15	1:33:26	1.00	0.03	2.04	0.08	-1.20	0.26	1.46E+09	1.15E+07	6.39E+07	2.29E+05
				FCQ-06.1_12	22/07/15	0:03:29	1.84	0.03	2.07	0.10	-1.45	0.37	1.39E+09	1.10E+07	6.11E+07	2.20E+05
				FCQ-06.1_13	21/07/15	23:18:36	2.15	0.02	2.13	0.11	-1.50	0.35	1.44E+09	1.13E+07	6.31E+07	2.26E+05
				FCQ-06.1_14	21/07/15	23:03:39	0.55	0.03	1.99	0.10	-1.39	0.38	1.36E+09	1.08E+07	5.98E+07	2.15E+05
				FCQ-06.1_15	21/07/15	22:48:43	0.78	0.03	2.12	0.08	-1.17	0.37	1.36E+09	1.07E+07	5.96E+07	2.14E+05
FCQ-1	FCQ-06 (388.37-389.68)	Quartz vein in silicified Tremolite -metabasalt	Py	FCQ_1-1	22/07/15	11:26:51	1.75	0.03	2.09	0.12	-1.23	0.33	1.43E+09	1.12E+07	6.26E+07	2.25E+05
				FCQ_1-2	22/07/15	11:51:04	1.65	0.03	2.21	0.13	-1.02	0.39	1.37E+09	1.08E+07	6.02E+07	2.16E+05
				FCQ_1-3	22/07/15	12:06:49	1.62	0.02	2.17	0.13	-1.29	0.35	1.34E+09	1.06E+07	5.88E+07	2.11E+05
				FCQ_1-4	22/07/15	12:22:13	2.11	0.02	2.15	0.05	-1.57	0.35	1.47E+09	1.16E+07	6.44E+07	2.31E+05
				FCQ_1-5	22/07/15	12:38:14	1.42	0.02	2.03	0.12	-1.53	0.27	1.41E+09	1.11E+07	6.18E+07	2.22E+05
				FCQ_1-6	22/07/15	13:35:47	0.66	0.02	2.20	0.07	-1.02	0.35	1.38E+09	1.09E+07	6.07E+07	2.18E+05
				FCQ_1-7	22/07/15	14:16:28	1.85	0.03	2.15	0.06	-0.74	0.33	1.48E+09	1.17E+07	6.49E+07	2.33E+05
				FCQ_1-8	22/07/15	14:32:28	2.05	0.03	2.19	0.14	-1.58	0.31	1.41E+09	1.11E+07	6.20E+07	2.23E+05
				FCQ_1-9	22/07/15	14:47:56	1.72	0.02	2.16	0.07	-0.84	0.33	1.49E+09	1.17E+07	6.54E+07	2.35E+05
				FCQ_1-10	22/07/15	15:03:26	2.13	0.03	2.10	0.06	-0.79	0.34	1.46E+09	1.15E+07	6.42E+07	2.31E+05
			Gn	FCQ_1_Ga-1	23/07/15	10:29:54	2.07	0.02	2.08	0.03	-0.53	0.20	2.55E+09	1.99E+07	1.09E+08	3.84E+05
				FCQ_1_Ga-2	23/07/15	10:40:02	2.73	0.02	2.09	0.04	-0.72	0.32	2.48E+09	1.93E+07	1.06E+08	3.73E+05
				FCQ_1_Ga-3	23/07/15	10:49:47	5.02	0.02	2.07	0.04	-0.93	0.33	2.34E+09	1.83E+07	1.01E+08	3.54E+05
				FCQ_1_Ga-4	23/07/15	10:59:36	1.62	0.02	2.07	0.04	-1.07	0.44	2.51E+09	1.96E+07	1.08E+08	3.77E+05

				FCQ_1_Ga-5	23/07/15	11:28:53	3.97	0.02	2.12	0.26	-0.82	0.37	2.49E+09	1.95E+07	1.07E+08	3.76E+05
				FCQ_1_Ga-6	23/07/15	11:38:41	7.06	0.03	2.11	0.03	-0.32	0.22	2.23E+09	1.74E+07	9.60E+07	3.39E+05
				FCQ_1_Ga-7	23/07/15	11:48:26	2.51	0.02	2.07	0.04	-0.94	0.19	2.42E+09	1.88E+07	1.04E+08	3.64E+05
				FCQ_1_Ga-8	23/07/15	11:58:12	3.55	0.02	2.04	0.04	-0.48	0.21	2.55E+09	1.99E+07	1.10E+08	3.85E+05
FCQ-06.2	FCQ-06 (457.42-457.92)	Micaceous chert	Py	FCQ-06.2_1	22/07/15	0:18:26	3.03	0.03	2.15	0.11	-1.33	0.33	1.45E+09	1.14E+07	6.35E+07	2.28E+05
				FCQ-06.2_2	22/07/15	1:48:23	1.62	0.03	2.15	0.12	-1.14	0.27	1.38E+09	1.09E+07	6.05E+07	2.17E+05
				FCQ-06.2_3	22/07/15	2:48:43	2.67	0.02	2.03	0.09	-1.21	0.44	1.53E+09	1.20E+07	6.70E+07	2.41E+05
				FCQ-06.2_4	22/07/15	2:33:32	1.82	0.03	2.06	0.04	-1.33	0.25	1.50E+09	1.19E+07	6.60E+07	2.37E+05
				FCQ-06.2_5	22/07/15	5:48:01	2.57	0.02	2.03	0.11	-1.60	0.36	1.49E+09	1.18E+07	6.55E+07	2.35E+05
				FCQ-06.2_6	22/07/15	5:33:04	3.00	0.03	2.04	0.10	-1.68	0.22	1.43E+09	1.13E+07	6.30E+07	2.26E+05
				FCQ-06.2_7	22/07/15	5:03:13	3.12	0.02	2.04	0.08	-1.60	0.31	1.46E+09	1.15E+07	6.40E+07	2.30E+05
				FCQ-06.2_8	22/07/15	5:18:09	1.92	0.03	2.09	0.11	-1.07	0.36	1.46E+09	1.15E+07	6.42E+07	2.31E+05
				FCQ-06.2_9	22/07/15	4:33:22	1.70	0.02	2.15	0.13	-1.52	0.33	1.37E+09	1.08E+07	6.01E+07	2.16E+05
				FCQ-06.2_10	22/07/15	4:48:17	2.19	0.02	2.27	0.05	-0.94	0.33	1.35E+09	1.07E+07	5.94E+07	2.14E+05
				FCQ-06.2_11	22/07/15	3:33:36	1.75	0.03	2.21	0.11	-1.87	0.33	1.37E+09	1.08E+07	6.01E+07	2.15E+05
				FCQ-06.2_12	22/07/15	8:50:31	1.85	0.02	2.11	0.10	-1.35	0.32	1.30E+09	1.03E+07	5.71E+07	2.05E+05
				FCQ-06.2-1	17/11/15	18:23:17	2.91	0.02	1.98	0.10	-1.25	0.28	2.84E+09	2.25E+07	1.27E+08	5.15E+05
				FCQ-06.2-3	17/11/15	22:30:21	3.04	0.02	2.18	0.07	-2.20	0.30	2.21E+09	1.74E+07	9.83E+07	3.99E+05
				FCQ-06.2-4	17/11/15	22:52:10	0.46	0.02	2.08	0.05	-0.17	0.24	3.64E+09	2.86E+07	1.61E+08	6.56E+05
				FCQ-06.2-5	17/11/15	23:13:43	3.00	0.02	2.01	0.08	-1.24	0.28	2.59E+09	2.04E+07	1.15E+08	4.69E+05
				FCQ-06.2-7	17/11/15	23:35:31	3.21	0.02	2.08	0.07	-1.09	0.27	2.62E+09	2.07E+07	1.17E+08	4.75E+05
				FCQ-06.2-8	17/11/15	23:57:06	2.27	0.02	2.08	0.05	-1.69	0.29	2.58E+09	2.04E+07	1.15E+08	4.67E+05
				FCQ-06.2-10	18/11/15	0:40:36	1.73	0.02	2.10	0.08	-1.66	0.37	2.45E+09	1.93E+07	1.09E+08	4.43E+05
			Po	FCQ-06.2_Po-2	18/11/15	2:29:07	0.89	0.02	2.09	0.05	-0.73	0.28	3.08E+09	2.42E+07	1.36E+08	5.53E+05
				FCQ-06.2_Po-3	18/11/15	2:07:20	1.64	0.02	2.07	0.04	-0.71	0.29	3.23E+09	2.54E+07	1.43E+08	5.82E+05
FCQ-18.1	FCQ-18 (316.6-316.7)	Massive sulfide	Py	FCQ_18-1	21/07/15	15:31:05	1.05	0.02	2.12	0.18	-0.91	0.32	1.39E+09	1.10E+07	6.10E+07	2.19E+05
				FCQ_18-2	21/07/15	15:47:05	0.78	0.03	2.14	0.11	-1.55	0.34	1.38E+09	1.09E+07	6.03E+07	2.16E+05
				FCQ_18-3	21/07/15	16:04:50	1.56	0.03	2.11	0.10	-1.05	0.26	1.37E+09	1.08E+07	6.00E+07	2.16E+05
				FCQ_18-4	21/07/15	16:19:48	2.32	0.02	2.12	0.04	-1.02	0.30	1.42E+09	1.12E+07	6.21E+07	2.23E+05
				FCQ_18-5	21/07/15	16:36:03	1.56	0.02	2.11	0.10	-1.26	0.28	1.42E+09	1.12E+07	6.23E+07	2.24E+05
				FCQ_18-6	21/07/15	17:01:31	0.69	0.02	2.16	0.02	-1.09	0.23	2.11E+09	1.66E+07	9.25E+07	3.32E+05
				FCQ_18-7	21/07/15	17:16:27	1.71	0.03	2.05	0.06	-0.85	0.22	1.41E+09	1.11E+07	6.17E+07	2.22E+05
FCQ-18.2	FCQ-18 (333.35-333.6)	Massive sulfide	Py	FCQ-18.2_1	17/11/15	2:52:35	2.42	0.03	1.98	0.04	-1.29	0.36	2.69E+09	2.12E+07	1.20E+08	4.87E+05
				FCQ-18.2_2	17/11/15	3:14:20	2.38	0.03	1.90	0.07	-1.00	0.36	2.69E+09	2.12E+07	1.20E+08	4.86E+05
				FCQ-18.2_3	17/11/15	3:36:04	1.09	0.03	1.99	0.03	-1.46	0.32	2.75E+09	2.16E+07	1.22E+08	4.96E+05
				FCQ-18.2_4	17/11/15	3:57:36	1.51	0.03	1.94	0.04	-1.37	0.25	2.78E+09	2.19E+07	1.23E+08	5.02E+05
				FCQ-18.2_5	17/11/15	4:19:08	0.84	0.05	1.79	0.06	-1.22	0.29	2.67E+09	2.11E+07	1.19E+08	4.82E+05
				FCQ-18.2_6	17/11/15	4:40:40	1.54	0.05	1.99	0.08	-1.35	0.35	2.67E+09	2.10E+07	1.18E+08	4.82E+05
				FCQ-18.2_7	17/11/15	5:02:23	0.48	0.03	2.21	0.09	-1.41	0.37	2.45E+09	1.93E+07	1.09E+08	4.43E+05
			Po	FCQ-18.2_Po-1	17/11/15	9:32:30	0.57	0.02	1.89	0.04	-1.45	0.22	3.14E+09	2.47E+07	1.39E+08	5.66E+05
				FCQ-18.2_Po-2	17/11/15	9:54:05	0.88	0.02	2.01	0.05	-1.27	0.20	3.67E+09	2.89E+07	1.63E+08	6.61E+05
FCQ-13	FCQ-13 (51.58-51.62)	Biotite-quartz-schist	Py	FCQ-13_Py-1	22/07/15	21:00:33	-1.42	0.02	-0.17	0.09	0.13	0.33	1.37E+09	1.08E+07	6.02E+07	2.16E+05
				FCQ-13_Py-2	22/07/15	21:16:22	-1.48	0.02	-0.41	0.10	-0.45	0.23	1.29E+09	1.02E+07	5.67E+07	2.03E+05
				FCQ-13_Py-3	22/07/15	21:32:11	-1.52	0.03	-0.20	0.08	0.66	0.38	1.33E+09	1.05E+07	5.84E+07	2.10E+05

	FCQ-13_Py-4	22/07/15	21:47:44	-1.68	0.02	-0.03	0.13	0.49	0.34	1.39E+09	1.09E+07	6.08E+07	2.19E+05
	FCQ-13_Py-5	22/07/15	22:03:16	-1.46	0.02	-0.09	0.13	0.57	0.41	1.37E+09	1.07E+07	5.99E+07	2.15E+05
	FCQ-13_Py-6	22/07/15	22:19:13	-2.21	0.03	-0.15	0.10	0.04	0.36	1.29E+09	1.02E+07	5.66E+07	2.03E+05
	FCQ-13_Py-7	22/07/15	22:34:45	-1.74	0.03	-0.16	0.13	0.47	0.27	1.33E+09	1.05E+07	5.83E+07	2.09E+05
	FCQ-13_Py-8	22/07/15	22:50:17	-1.46	0.02	-0.25	0.08	0.33	0.38	1.33E+09	1.04E+07	5.81E+07	2.08E+05
	FCQ-13_CPY-1.1	23/07/15	3:48:39	-1.65	0.02	-0.17	0.16	0.54	0.29	2.01E+09	1.58E+07	8.79E+07	3.15E+05
	FCQ-13_CPY-2.1	23/07/15	4:04:28	-1.70	0.02	-0.39	0.05	-0.50	0.23	2.10E+09	1.65E+07	9.18E+07	3.29E+05
	FCQ-13_CPY-3.1	23/07/15	4:20:17	-1.55	0.02	-0.21	0.10	0.31	0.25	2.04E+09	1.60E+07	8.93E+07	3.21E+05
Cpy	FCQ-13_CPY-4.1	23/07/15	4:35:51	-1.71	0.02	-0.20	0.02	0.02	0.18	2.15E+09	1.69E+07	9.42E+07	3.38E+05
	FCQ-13_CPY-5.1	23/07/15	4:51:23	-1.86	0.02	-0.15	0.09	0.58	0.22	2.04E+09	1.60E+07	8.93E+07	3.20E+05
	FCQ-13_CPY-6.1	23/07/15	5:06:57	-1.56	0.02	-0.20	0.11	0.25	0.28	2.26E+09	1.77E+07	9.87E+07	3.54E+05
	FCQ-13_CPY-7.1	23/07/15	6:24:40	-2.18	0.02	-0.24	0.07	0.22	0.27	2.13E+09	1.68E+07	9.33E+07	3.34E+05

Abbreviations: Py (pyrite), Po (pyrrhotite), Cpy (chalcopyrite), Gn (galena), and Sph (sphalerite).

Table 7.15. LA-ICP-MS trace elements data (in ppm) of sulfide samples from the northern Mundo Novo Greenstone Belt, with the corresponding SHRIMP-SI spots.

Northern Mundo Novo Greenstone Belt																											
Sample	**Sulfide type**	**Spot title**	**^{49}Ti**	**^{51}V**	**^{53}Cr**	**^{55}Mn**	**^{57}Fe**	**^{59}Co**	**^{60}Ni**	**^{65}Cu**	**^{66}Zn**	**^{71}Ga**	**^{74}Ge**	**^{75}As**	**^{77}Se**	**^{95}Mo**	**^{107}Ag**	**^{111}Cd**	**^{115}In**	**^{118}Sn**	**^{121}Sb**	**^{125}Te**	**^{195}Pt**	**^{197}Au**	**^{202}Hg**	**^{205}Tl**	**^{208}Pb**	**^{209}Bi**	**SHRIMP-SI spot**
PD-06	Py	PD-06 1	7.6	0.03	bdl	bdl	-	15.3	32.9	0.24	bdl	nd	nd	245	1.82	bdl	bdl	bdl	nd	bdl	0.08	bdl	bdl	0.01	0.18	bdl	0.17	bdl	
		PD-06 2	9	bdl	bdl	bdl	-	7.4	36.1	bdl	bdl	nd	nd	240	1.92	bdl	bdl	bdl	nd	bdl	0.67	bdl	bdl	bdl	0.21	bdl	0.42	bdl	
		PD-06 3	7.3	bdl	bdl	bdl	-	15.2	91.4	0.29	0.23	nd	nd	378	1.97	bdl	bdl	bdl	nd	0.41	bdl	bdl	bdl	bdl	0.14	bdl	bdl	bdl	
		PD-06 4	8.5	0.08	bdl	bdl	-	2.89	17.2	4.42	0.16	nd	nd	240	1.54	bdl	bdl	bdl	nd	bdl	bdl	bdl	bdl	0.04	0.21	bdl	0.02	0.02	
		PD-06 5	8.6	4.6	0.38	bdl	-	3.88	47.8	4.7	0.53	nd	nd	363	5	bdl	0.23	bdl	nd	bdl	bdl	bdl	bdl	0.03	0.21	bdl	2.7	0.27	
		PD-06_1	11.8	bdl	bdl	bdl	-	3.29	18.4	bdl	bdl	bdl	bdl	228	bdl	bdl	bdl	bdl	bdl	bdl	bdl	bdl	bdl	bdl	bdl	bdl	bdl	bdl	PD-06_1
		PD-06_2	16	bdl	bdl	bdl	-	2.86	89.1	bdl	bdl	0.01	bdl	408	bdl	bdl	bdl	bdl	bdl	bdl	bdl	bdl	bdl	bdl	bdl	bdl	bdl	bdl	PD-06_2
		PD-06_3	12.7	bdl	bdl	bdl	-	4.7	22.1	0.47	bdl	bdl	bdl	235	bdl	bdl	bdl	bdl	bdl	bdl	0.56	bdl	bdl	bdl	bdl	bdl	0.68	bdl	PD-06_4
		PD-06_4	12	bdl	bdl	1.18	-	9.6	11.4	bdl	bdl	bdl	bdl	134.6	2.2	bdl	bdl	bdl	bdl	bdl	bdl	bdl	bdl	bdl	bdl	bdl	0.22	bdl	PD-06_6
		PD-06_6	15.6	1.86	bdl	bdl	-	0.36	70.7	1.34	bdl	bdl	bdl	334	bdl	bdl	0.10	bdl	bdl	bdl	1.46	bdl	bdl	3.2	bdl	bdl	2.74	0.09	PD-06_9
		PD-06_7	13	bdl	bdl	1.54	-	bdl	14.2	bdl	bdl	bdl	bdl	133.9	bdl	bdl	bdl	bdl	bdl	bdl	bdl	bdl	bdl	bdl	0.27	bdl	bdl	bdl	PD-06_10
PD-07	Py	PD-07 1	bdl	bdl	bdl	bdl	-	bdl	49.5	bdl	bdl	nd	nd	280	1.64	bdl	bdl	bdl	nd	bdl	bdl	bdl	bdl	bdl	0.16	bdl	bdl	bdl	PD-07_1
		PD-07 2	8.3	0.10	0.12	bdl	-	0.10	60.1	0.59	0.15	nd	nd	455	2.46	bdl	bdl	bdl	nd	bdl	bdl	bdl	bdl	2.79	0.16	bdl	0.01	bdl	PD-07_2
		PD-07 3	8.6	bdl	bdl	bdl	-	4.01	33.5	bdl	0.11	nd	nd	261	0.81	bdl	bdl	bdl	nd	bdl	bdl	bdl	bdl	bdl	0.16	bdl	bdl	bdl	PD-07_3
		PD-07 4	8.9	0.04	bdl	bdl	-	0.94	87.2	0.33	bdl	nd	nd	502	2.32	bdl	0.07	bdl	nd	bdl	4.38	bdl	bdl	0.03	0.18	bdl	11.6	0.04	PD-07_4
		PD-07 5	8.5	0.03	bdl	0.52	-	0.57	32.8	0.68	bdl	nd	nd	270	4.6	bdl	bdl	bdl	nd	bdl	bdl	bdl	bdl	0.01	0.19	bdl	0.36	0.08	PD-07_5
		PD07-1	27.2	0.08	bdl	bdl	-	1.73	38.4	1.45	1.05	bdl	bdl	178	2.33	bdl	bdl	0.28	bdl	bdl	bdl	bdl	bdl	0.02	0.07	bdl	0.05	bdl	PD-07_8
		PD07-2	24.9	0.06	bdl	bdl	-	12.7	15	0.97	0.87	bdl	bdl	128	1.61	bdl	bdl	bdl	bdl	bdl	0.36	bdl	bdl	0.01	0.09	bdl	0.72	bdl	PD-07_9
		PD07-3	28.4	0.06	bdl	bdl	-	10	13.5	bdl	0.58	bdl	bdl	115	1.66	bdl	bdl	bdl	bdl	bdl	bdl	bdl	bdl	bdl	0.10	bdl	0.07	bdl	PD-07_10
PD-04*	Py	PD-04_1	bdl	bdl	bdl	2.3	-	bdl	bdl	bdl	bdl	bdl	bdl	11.7	26.5	0	0.72	bdl	bdl	bdl	bdl	bdl	bdl	0.02	bdl	bdl	3.1	0.63	PD_04-2
		PD-04_2	bdl	bdl	bdl	2	-	49.1	21.1	bdl	bdl	bdl	bdl	27.4	bdl	1.53	0.01	bdl	bdl	bdl	5.3	bdl	bdl	0.47	bdl	bdl	11	0.3	PD_04-3
		PD-04_3	18	bdl	bdl	bdl	-	230	bdl	bdl	bdl	bdl	1.63	bdl	48	0	bdl	bdl	bdl	bdl	bdl	bdl	bdl	0.04	bdl	bdl	0	bdl	bdl	PD_04-1
		PD-04_6	6	bdl	bdl	bdl	-	10	69	bdl	bdl	bdl	bdl	264	7.9	bdl	bdl	bdl	bdl	bdl	bdl	bdl	bdl	0.02	bdl	bdl	bdl	bdl	PD_04-5
FCJ-4	Py	FCJ4-1	34.3	0.10	bdl	bdl	-	20200	1.93	1.72	1.15	bdl	0.16	5	20.1	bdl	0.11	bdl	bdl	bdl	bdl	bdl	bdl	0.03	0.06	bdl	0.14	0.05	FCJ-4_1
		FCJ4-2	34.9	0.17	bdl	1.13	-	bdl	20.6	9.02	0.93	bdl	bdl	46.2	11.7	bdl	0.12	bdl	0.03	0.22	7.56	20.2	bdl	0.24	0.07	0.05	48.5	11.1	FCJ-4_2
		FCJ4-3	29.4	0.07	bdl	bdl	-	20600	3.37	3.85	1.01	bdl	0.12	8.6	12	bdl	0.09	bdl	0.03	bdl	1.12	bdl	bdl	0.03	0.06	bdl	8.9	bdl	FCJ-4_3

	FCJ4-4	27	0.10	bdl	bdl	-	bdl	490	9.9	1.22	bdl	bdl	3.6	8.8	1.58	bdl	bdl	bdl	bdl	0.58	bdl	0.04	0.65	0.07	0.40	8.7	bdl	FCJ-4_4
	FCJ4-6	bdl	1.3	bdl	114	-	166	132	19.9	7.1	0.45	0.18	18.1	13.4	bdl	0.31	bdl	bdl	bdl	1.21	5.5	bdl	0.07	0.06	0.64	89.8	3.9	FCJ-4_6
	FCJ4-8	27.5	bdl	bdl	bdl	-	150	567	6.9	1.86	bdl	0.16	5.1	17.5	0.23	bdl	bdl	0.04	bdl	0.45	bdl	bdl	0.84	0.11	2.1	2.12	0.09	FCJ-4_8
	FCJ4-9	138	7.3	4.9	0.33	-	223	723	6.7	1.25	1.32	0.39	7.9	16.2	0.86	0.09	bdl	0.04	bdl	0.17	bdl	bdl	0.03	0.10	1.61	12.9	1.73	FCJ-4_9
	FCJ4-10	155	14.4	1.71	1.57	-	175	526	10.5	2.35	1.99	0.86	9.1	17.9	0.52	0.22	bdl	bdl	0.54	0.64	bdl	0.03	0.83	0.11	1.89	8.3	0.44	FCJ-4_10

Abbreviations: Py (pyrite).

Table 7.16. LA-ICP-MS trace elements data (in ppm) of sulfide samples from southern Mundo Novo Greenstone Belt (Fazenda Coqueiro Deposit), with the corresponding SHRIMP-SI spots.

Southern Mundo Novo Greenstone Belt (Fazenda Coqueiro Deposit)																												
Sample	**Sulfide type**	**Spot title**	**^{49}Ti**	**^{51}V**	**^{53}Cr**	**^{55}Mn**	**^{57}Fe**	**^{59}Co**	**^{60}Ni**	**^{65}Cu**	**^{66}Zn**	**^{71}Ga**	**^{74}Ge**	**^{75}As**	**^{77}Se**	**^{95}Mo**	**^{107}Ag**	**^{111}Cd**	**^{115}In**	**^{118}Sn**	**^{121}Sb**	**^{125}Te**	**^{195}Pt**	**^{197}Au**	**^{202}Hg**	**^{205}Tl**	**^{208}Pb**	**^{209}Bi**	**SHRIMP-SI spot**
FCQ-06.5	Aspy	Aspy1	3.81	bdl	bdl	0.34	-	1408	1440	bdl	bdl	bdl	0.87	465000	58.7	bdl	0.03	bdl	0.23	bdl	536	12.2	bdl	0.12	1.88	bdl	bdl	0.09	
		Aspy2	4.18	bdl	bdl	bdl	-	1121	1540	bdl	0.22	bdl	0.84	506000	73.2	0.01	bdl	bdl	0.3	bdl	677	11	bdl	0.06	2.31	bdl	bdl	0.02	
		Aspy3	3.87	bdl	bdl	bdl	-	2210	2350	bdl	0.14	bdl	1.22	477000	91.8	0.31	bdl	bdl	0.30	bdl	820	16.2	bdl	0.10	2.08	bdl	0.05	0.08	
		Aspy4	3.47	bdl	bdl	bdl	-	1748	1710	bdl	bdl	bdl	1.25	386000	64.7	0.01	0.03	bdl	0.23	bdl	477	10.6	0.02	0.06	1.79	bdl	0.22	0.12	
		Aspy5	5.5	0.26	bdl	0.64	-	1820	1739	bdl	0.21	bdl	0.71	343000	57.8	0.05	bdl	bdl	0.24	bdl	438	9.14	bdl	0.12	1.76	bdl	0.18	0.05	
		Aspy6	18.8	0.05	bdl	bdl	-	2060	4220	bdl	bdl	bdl	0.97	382000	75.6	0.10	0.04	bdl	0.28	bdl	893	15.5	bdl	0.44	2.2	bdl	0.40	0.12	
		Aspy7	50	21	11.9	66	-	1490	1960	0.25	9.6	1.66	1.31	394000	85.8	0.43	0.28	bdl	0.28	bdl	607	9.8	bdl	0.18	2.84	bdl	10.2	0.32	
		Aspy8	12.5	5.2	2.1	15.2	-	2480	3030	bdl	1.8	0.107	1.35	397000	99.2	1.64	0.04	bdl	0.27	bdl	705	17.2	bdl	0.18	2.72	bdl	1.12	0.06	
FCQ-06.3	Py	Py1	15.1	0.06	bdl	0.53	-	6300	35	0.26	0.16	bdl	0.26	2.08	32	bdl	0.07	bdl	bdl	bdl	0.5	bdl	bdl	bdl	0.48	bdl	13	0.23	
		Py2	16.6	bdl	bdl	bdl	-	2960	5.48	0.15	bdl	bdl	0.26	482	39.1	bdl	0.07	bdl	bdl	bdl	bdl	bdl	0.29	0.01	0.69	bdl	2.9	bdl	1
		Py3	14.4	0.03	bdl	bdl	-	3820	9.6	bdl	bdl	bdl	0.247	bdl	36.8	bdl	bdl	bdl	bdl	bdl	0.12	bdl	bdl	bdl	0.38	bdl	bdl	0.03	
		Py4	14.5	0.06	bdl	0.39	-	5750	22.4	0.25	bdl	0.03	0.5	50	57.3	2	1.12	bdl	bdl	bdl	3.2	bdl	bdl	0.04	0.43	0.09	470	6.3	3
		Py5	14.6	0.04	bdl	0.4	-	3710	bdl	bdl	0.124	bdl	bdl	201	bdl	bdl	bdl	bdl	bdl	bdl	bdl	bdl	0.13	0.00	bdl	bdl	bdl	bdl	
		Py6	15.2	0.17	bdl	3.3	-	6270	5.33	0.21	1.63	0.10	0.47	750	46.5	11	0.16	bdl	bdl	bdl	2.22	bdl	0.07	bdl	0.66	bdl	32	0.45	6
		Py7	17	0.07	bdl	bdl	-	3100	bdl	bdl	bdl	bdl	bdl	880	33.1	bdl	bdl	bdl	bdl	bdl	0.41	bdl	0.34	bdl	0.28	bdl	65	0.52	
		Py8	17.4	0.13	bdl	0.82	-	4560	2.93	bdl	0.41	bdl	bdl	137	30.7	bdl	bdl	bdl	bdl	bdl	0.23	bdl	0.10	bdl	0.19	bdl	3	0.05	
		Py9	16.3	0.05	bdl	bdl	-	5290	11.72	bdl	0.58	bdl	bdl	191	63.3	bdl	bdl	bdl	bdl	bdl	bdl	bdl	0.07	bdl	0.27	bdl	0.02	bdl	5
		Py10	18.9	0.12	bdl	0.91	-	4770	8.2	0.95	0.63	bdl	0.46	87	70	bdl	12.3	bdl	bdl	0.34	23.4	2.39	bdl	bdl	0.20	1.51	2760	20.6	
	Cpy	Cpy1	8.7	bdl	bdl	2.23	-	0.53	7.61	339700	616	0.26	bdl	25.2	61.4	bdl	81.4	3.75	33.14	30.5	15.9	bdl	bdl	bdl	1.99	0.45	5.95	0.23	
		Cpy2	7.4	bdl	bdl	4.8	-	0.56	8.44	332200	513	0.29	0.88	25.5	76.5	0	74.5	3.29	36.6	32.7	7.7	bdl	bdl	bdl	2.06	bdl	2.62	0.08	CPY-1.1
		Cpy3	7.9	bdl	bdl	2.35	-	1.91	11.2	313000	473	bdl	bdl	21.9	58.4	0.01	57.3	4.23	28.8	22.39	15.3	bdl	bdl	0.5	1.5	0.40	220	1.3	CPY-4.1
		Cpy4	7	bdl	bdl	3.05	-	0.43	8.83	337900	497	0.34	0.68	19.2	87	bdl	60.9	2.44	34.5	26.8	2.41	bdl	bdl	0.05	1.46	0.79	2.09	0.03	CPY-3.1
	Sph	Zn1	2.86	bdl	bdl	1364	45660	20.41	0.5	5100	-	0.18	0.54	9.5	55.5	0	13.4	1969	85.06	0.79	9.9	0.37	bdl	0.13	113.6	0.13	4.66	0.15	
		Zn2	2.43	bdl	bdl	1419	41910	15.34	bdl	91	-	0.43	0.67	8.3	71.3	bdl	2.58	1879	78.37	0.25	1.72	bdl	bdl	0.09	110.7	bdl	1.23	0.03	
		Zn3	3.09	bdl	bdl	1450	47330	21.88	bdl	1570	-	0.45	0.64	12.5	73.1	bdl	5.97	2019	88.02	0.29	2.11	bdl	bdl	0.38	120.1	0.03	1.34	0.06	
		Zn4	3.04	bdl	bdl	1409	46080	19.78	0.37	2540	-	0.39	0.54	12.9	68.5	0.01	8.84	1997	77.63	0.52	8.78	bdl	bdl	0.17	110.6	0.08	4.65	0.11	
		Zn5	2.76	bdl	bdl	1525	49000	22.23	0.87	2730	-	0.37	0.64	17.9	63.1	bdl	10.2	1976	86.7	0.89	5.62	bdl	bdl	0.31	99.2	0.12	6	0.10	
		Zn6	2.9	bdl	bdl	1411	44310	17.37	bdl	176	-	0.34	0.71	14.9	72.5	bdl	4.79	1954	81.78	0.19	6.45	bdl	bdl	0.14	108.2	0.07	2.58	0.09	
		Zn7	4.7	1.99	1.92	1511	50200	24.52	0.38	2560	-	0.62	0.65	14.5	69.3	bdl	10.1	2021	83.69	0.44	4.81	bdl	bdl	0.08	117.2	bdl	8.1	0.24	
		Zn8	2.19	bdl	bdl	1444	47900	21.67	0.33	4100	-	0.28	0.66	10.2	73.1	bdl	7.2	2027	86.08	0.57	6.71	bdl	bdl	0.21	103.8	0.09	15.2	0.17	
		Zn9	3.2	0.04	bdl	1615	48320	9.31	bdl	330	-	0.43	0.65	9.8	76.3	bdl	2.54	2250	87.2	0.29	3.41	bdl	bdl	0.04	108.1	0.06	27	0.17	
	Po	Po1	5.7	0.14	0.43	3.32	-	70.3	293	bdl	0.41	bdl	0.85	378	72	bdl	0.34	bdl	bdl	bdl	0.49	bdl	bdl	bdl	0.76	0.04	2.6	0.23	
		Po2	4.6	0.07	0.54	bdl	-	71.7	328	bdl	bdl	bdl	bdl	386	54.5	bdl	2.82	bdl	bdl	bdl	0.25	bdl	bdl	bdl	0.53	bdl	3.68	1.16	
		Po3	6.4	0.36	0.79	9.6	-	65.7	463	bdl	2.4	0.09	0.88	316	65.8	bdl	0.94	bdl	bdl	bdl	290	bdl	bdl	bdl	0.96	0.10	8.4	2	
		Po4	5.2	bdl	bdl	3.54	-	59	464	2.2	bdl	bdl	bdl	308	59	0	1.39	bdl	bdl	bdl	2.46	bdl	bdl	bdl	0.81	0.08	7.7	0.79	
		Po5	4.5	bdl	bdl	1.13	-	69.5	270	bdl	bdl	bdl	1.03	329	70.6	bdl	0.05	bdl	bdl	bdl	bdl	bdl	bdl	bdl	0.99	bdl	0.22	bdl	
		Po6	4	bdl	bdl	1.51	-	72	308	bdl	bdl	bdl	0.93	282	76.5	bdl	1.83	bdl	bdl	bdl	0.49	bdl	bdl	bdl	1.56	0.05	4.94	0.7	
		Po1	4.5	bdl	bdl	bdl	-	73.1	253.2	bdl	bdl	bdl	0.8	276	66.9	bdl	0.28	bdl	bdl	bdl	bdl	bdl	bdl	bdl	0.39	bdl	bdl	0.28	
		Po2	7.4	0.14	bdl	3.8	-	71.9	285	bdl	1.9	bdl	1.1	244	76.5	bdl	0.10	bdl	bdl	bdl	1.6	bdl	bdl	bdl	0.38	bdl	2.7	0.10	

		Po3	4.6	bdl	bdl	1.54	-	72.1	311	bdl	bdl	bdl	bdl	289	56.3	bdl	2.2	bdl	bdl	bdl	1.98	bdl	bdl	bdl	0.43	0.12	12.8	1.61	
		Py1	16.3	0.04	bdl	bdl	-	5390	bdl	bdl	bdl	bdl	0.26	2037	30.6	bdl	bdl	bdl	bdl	bdl	bdl	bdl	bdl	bdl	0.44	bdl	bdl	bdl	13
		Py2	13.7	0.04	bdl	0.38	-	3380	2.54	bdl	bdl	0.04	0.26	257	26.1	bdl	bdl	bdl	bdl	bdl	bdl	bdl	bdl	bdl	0.33	bdl	0.04	bdl	12
		Py3	13.6	0.03	bdl	bdl	-	2130	2.16	bdl	0.11	bdl	bdl	268	23	bdl	bdl	bdl	bdl	bdl	bdl	bdl	bdl	0.03	bdl	0.38	bdl	0.09	bdl	1
		Py4	14.1	0.05	bdl	15.9	-	5050	55	18	250	bdl	0.62	7.8	78.5	bdl	0.84	bdl	bdl	bdl	3.8	0.4	bdl	0.55	0.33	0.2	69	0.54	5
		Py5	13.2	0.03	bdl	bdl	-	3680	bdl	bdl	bdl	bdl	0.34	22.7	29.5	bdl	bdl	bdl	bdl	0.27	bdl	bdl	bdl	bdl	0.22	bdl	bdl	bdl	9
	Py	Py6	14.4	0.03	bdl	bdl	-	3110	2.75	bdl	bdl	bdl	0.22	292	24	bdl	bdl	bdl	bdl	bdl	bdl	bdl	bdl	bdl	bdl	bdl	bdl	bdl	7
		Py7	15.1	bdl	bdl	bdl	-	3340	2.27	bdl	bdl	bdl	bdl	357	27.5	bdl	bdl	bdl	bdl	bdl	bdl	bdl	0.03	bdl	bdl	bdl	bdl	bdl	15
		Py8	14.9	0.05	bdl	bdl	-	2560	6.88	bdl	bdl	bdl	0.51	1.43	78.7	bdl	bdl	bdl	bdl	bdl	bdl	bdl	bdl	bdl	0.08	bdl	bdl	bdl	
		Py9	14.9	bdl	bdl	bdl	-	2610	2.15	bdl	bdl	bdl	bdl	264	24.5	bdl	bdl	bdl	bdl	bdl	bdl	bdl	bdl	bdl	bdl	bdl	bdl	bdl	14
		Py10	17.1	0.05	bdl	0.36	-	1962	7.26	bdl	bdl	bdl	0.68	0.62	68.2	bdl	bdl	bdl	bdl	bdl	bdl	bdl	bdl	bdl	bdl	bdl	0.03	bdl	6
		Py11	15.3	0.06	bdl	bdl	-	6600	3.18	bdl	bdl	bdl	0.31	12.9	37.2	bdl	bdl	bdl	bdl	bdl	bdl	bdl	bdl	bdl	bdl	bdl	0.04	bdl	2
	Cpy	Cpy1	9.3	bdl	bdl	2.42	-	0.46	5.96	330000	637	0.74	1.22	56.1	105.3	0.01	57.2	3.26	18.99	5.87	0.37	bdl	bdl	bdl	1.54	bdl	0.34	bdl	
		Cpy3	9.2	bdl	bdl	2.02	-	0.41	4.76	327600	511	1.38	1.33	46.9	103.4	bdl	51.8	1.45	19.58	2.04	1.76	bdl	bdl	bdl	0.68	1.02	0.73	bdl	
FCQ-06.1		Zn1	2.76	bdl	bdl	2473	54170	19.22	bdl	29.95	-	0.48	0.63	9.7	62.9	0.03	1.10	1851	52.13	0.28	bdl	bdl	bdl	0.04	76	bdl	0.12	bdl	
		Zn2	3.67	bdl	bdl	2213	51140	17.53	bdl	41.7	-	0.47	0.49	8.6	66.4	0.05	1.29	1787	53.65	bdl	0.84	bdl	bdl	0.06	73.4	0.03	0.60	bdl	
		Zn3	3.12	bdl	bdl	2307	51750	15.9	bdl	226	-	0.52	0.63	14.8	69.9	0.04	1.94	1791	50.75	0.32	1.38	bdl	bdl	0.19	71.3	bdl	1.06	0.01	
	Sph	Zn4	2.86	bdl	bdl	2348	51860	16.26	bdl	42.7	-	0.52	0.63	13.8	68.7	bdl	1.57	1748	51.49	0.36	0.10	bdl	bdl	0.1	72.7	bdl	0.20	0.00	
		Zn5	3.02	bdl	bdl	2332	51260	9.39	0.17	438	-	0.49	0.62	12.3	66.2	0.01	1.88	1763	51.76	0.26	1.03	bdl	bdl	0.14	72.8	0.09	0.72	0.01	
		Zn6	3.08	bdl	bdl	2441	52900	11.16	bdl	28.92	-	0.52	0.65	9.9	71.6	bdl	1.53	1740	50.52	0.21	0.42	bdl	bdl	0.18	71.4	bdl	0.44	bdl	
		Zn7	2.51	bdl	bdl	2433	56400	128.1	bdl	28.6	-	0.53	0.69	2.9	61.2	0.02	0.66	1719	50.11	0.24	0.11	bdl	bdl	bdl	57.6	bdl	0.74	bdl	
		Zn8	3.27	bdl	bdl	2376	52970	19.44	bdl	31	-	0.53	0.48	18.2	64.4	0.01	0.88	1843	52.9	bdl	0.33	bdl	bdl	bdl	71	0.02	0.23	bdl	
		Po1	4.4	bdl	bdl	8.42	-	46.3	384	0.63	0.3	bdl	0.97	208	82.4	bdl	0.11	bdl	bdl	bdl	0.38	bdl	bdl	bdl	0.3	bdl	1.89	bdl	
		Po2	3.4	bdl	bdl	2.24	-	49.7	362	bdl	bdl	bdl	1.01	230	93	bdl	0.62	bdl	bdl	bdl	bdl	bdl	bdl	bdl	bdl	0.10	0.47	0.03	
	Po	Po3	6.4	bdl	bdl	2.02	-	52	383	0.73	0.41	bdl	1.2	232	91.3	bdl	0.20	bdl	0.02	bdl	bdl	bdl	bdl	bdl	0.35	bdl	0.29	bdl	
		Po4	4.4	bdl	bdl	2.7	-	47.7	379	bdl	bdl	bdl	0.6	190	81.5	bdl	0.46	bdl	bdl	bdl	0.21	bdl	bdl	bdl	0.26	0.10	1.18	0.10	
		Po5	5.1	bdl	bdl	6.06	-	49.2	361	0.39	bdl	bdl	0.89	179	79.1	0.02	0.08	bdl	bdl	bdl	bdl	bdl	bdl	bdl	0.32	bdl	0.38	bdl	
		Po6	4.7	bdl	bdl	4.95	-	50.1	387	0.51	0.4	bdl	0.74	213	87.3	bdl	0.08	bdl	bdl	bdl	0.62	bdl	bdl	bdl	0.42	bdl	2.96	bdl	
		Py1	13.7	0.06	bdl	bdl	-	1115	77.9	0.24	0.20	bdl	bdl	2520	18.2	bdl	bdl	bdl	bdl	bdl	bdl	bdl	bdl	0.18	bdl	0.4	bdl	0.08	bdl	4
		Py2	12.1	bdl	bdl	bdl	-	1910	31.7	0.91	bdl	bdl	bdl	2700	18.3	bdl	0.29	bdl	bdl	bdl	0.43	bdl	0.24	0.01	0.18	bdl	41	0.25	5
		Py3	13.7	0.04	bdl	bdl	-	3.85	87	bdl	bdl	bdl	bdl	2270	12.7	bdl	0.02	bdl	bdl	bdl	bdl	bdl	bdl	bdl	0.13	bdl	2	bdl	6
		Py5	11.4	bdl	bdl	0.36	-	33.3	208	0.25	bdl	bdl	0.28	5150	39.6	bdl	4.8	0.62	bdl	bdl	4.5	0.5	bdl	0.08	bdl	bdl	910	3.4	
	Py	Py6	12.8	0.04	bdl	bdl	-	1730	31.2	bdl	bdl	bdl	bdl	3160	19.1	bdl	bdl	bdl	bdl	bdl	bdl	bdl	0.14	bdl	bdl	bdl	0.45	bdl	
		Py7	10.7	bdl	bdl	bdl	-	193	82.8	bdl	bdl	bdl	bdl	2080	17.4	bdl	bdl	bdl	bdl	bdl	bdl	bdl	bdl	bdl	bdl	bdl	bdl	bdl	9
		Py8	11.5	bdl	bdl	bdl	-	2.10	36.9	bdl	bdl	bdl	bdl	636	11.6	bdl	bdl	bdl	bdl	bdl	bdl	bdl	bdl	bdl	bdl	bdl	0.33	bdl	1
		Py9	11.1	bdl	bdl	0.31	-	24.50	24.9	bdl	bdl	bdl	bdl	513	9.2	0.18	0.03	bdl	bdl	bdl	bdl	bdl	bdl	bdl	bdl	bdl	7.5	0.04	
		Py10	11.7	bdl	bdl	bdl	-	38.8	383	bdl	bdl	bdl	0.28	4600	23.3	bdl	bdl	bdl	bdl	bdl	bdl	bdl	bdl	bdl	0.19	bdl	bdl	bdl	
		Gn1	bdl	bdl	bdl	1.67	bdl	bdl	bdl	3.44	bdl	bdl	10	43.7	1188	0	3060	174	0.28	11.87	2131	43.2	bdl	bdl	0.16	117.4	-	2415	
FCQ-1		Gn2	0.79	bdl	bdl	1.69	bdl	bdl	bdl	4.41	bdl	bdl	9.98	44.8	1171	0	3060	165.8	0.28	18.41	2034	71	bdl	0.05	0.28	116	-	2334	Ga-4
		Gn3	0.93	bdl	bdl	1.82	bdl	0	bdl	4.93	bdl	bdl	9.87	60.5	1204	0	3037	171	0.22	14.4	2082	49	bdl	0	0.21	110.4	-	2246	Ga-5
		Gn4	1.01	bdl	bdl	1.21	bdl	bdl	bdl	3.47	bdl	bdl	10.01	61.5	1167	bdl	2872	184.6	0.23	10.71	1981	108	bdl	0.02	0.18	103.7	-	2183	Ga-2
	Gn	Gn5	1.12	bdl	bdl	1.18	bdl	bdl	bdl	1.83	bdl	bdl	9.77	68	1184	0	2668	151.7	0.14	5.03	1785	24.1	bdl	0	0.12	98.8	-	2235	Ga-1
		Gn6	0.69	bdl	bdl	1.18	bdl	bdl	bdl	1.69	0.09	bdl	9.96	80.1	1187	0	2670	148.7	0.43	7	1704	63	bdl	bdl	0.15	93.8	-	2227	Ga-8
		Gn7	1.35	bdl	bdl	1.61	bdl	bdl	bdl	3.21	bdl	bdl	10.13	68	1210	0.01	2704	169	0.26	16.79	1767	60.1	bdl	bdl	0.20	95.9	-	2119	Ga-3
		Gn8	1.14	bdl	bdl	5.05	4.8	0	bdl	6.5	0.19	bdl	10.24	51.5	1201	bdl	4510	326	1.19	70	7000	158	bdl	bdl	0.40	93.7	-	2314	Ga-6
		Gn9	1.18	0.02	bdl	3.8	15.3	bdl	bdl	87	1.73	0.01	9.75	44.1	1173	bdl	3300	218	0.50	24.7	2160	98.2	bdl	bdl	0.40	96.3	-	2265	Ga-7
		Gn10	1.39	bdl	bdl	1.34	bdl	bdl	bdl	2.5	bdl	bdl	9.78	36.7	1191	0	2786	154.3	0.20	10.23	1782	48.5	bdl	bdl	0.24	96.8	-	2438	
	Aspy	Aspy1	4.09	bdl	bdl	bdl	-	274	142.4	bdl	bdl	bdl	0.76	426000	42.9	0.01	1.8	bdl	0.25	bdl	38.8	9.8	bdl	bdl	1.53	0.04	bdl	0.06	
		Aspy2	4.42	bdl	bdl	0.35	-	19.8	169.2	0.17	bdl	bdl	0.79	469000	47.9	0.00	0.24	bdl	0.27	bdl	26.5	8	bdl	0.07	2.5	bdl	38	0.08	
		2_Py1	13	bdl	bdl	bdl	-	4460	4.34	0.21	0.21	bdl	bdl	212	10	bdl	bdl	bdl	bdl	bdl	bdl	0.57	0.03	bdl	bdl	bdl	0.04	0.24	10
		2_Py2	82	5.1	9.1	8.1	-	7080	23.1	0.17	3.7	0.2	bdl	18.4	16.1	bdl	0.02	bdl	bdl	bdl	0.11	0.46	bdl	bdl	bdl	0.11	4	2.04	8
		1_Py1	16.9	3.5	3.5	14.2	-	9980	21.3	0.39	2.6	bdl	0.23	0.96	22.5	0	bdl	bdl	bdl	bdl	bdl	0.51	bdl	bdl	0.12	bdl	1.74	1.52	
FCQ-06.2	Py	1_Py3	14.2	bdl	bdl	bdl	-	7130	6.87	0.17	bdl	bdl	bdl	3.6	29.5	bdl	bdl	bdl	bdl	bdl	bdl	bdl	bdl	bdl	bdl	bdl	0.10	0.28	
		1_Py4	16.1	1.4	0.89	4.8	-	5960	12	1.09	0.59	bdl	0.34	1.49	35	bdl	0.31	bdl	bdl	bdl	0.98	0.56	bdl	bdl	bdl	1.19	31.4	12.1	
		1_Py5	13.1	bdl	bdl	bdl	-	5690	12	bdl	0.32	bdl	bdl	70.7	9.9	bdl	bdl	bdl	bdl	bdl	bdl	bdl	bdl	bdl	bdl	bdl	bdl	bdl	
		1_Py6	13.9	0.05	bdl	bdl	-	8110	16.1	bdl	0.28	bdl	bdl	12.2	11.2	bdl	bdl	bdl	bdl	bdl	bdl	bdl	0.01	bdl	bdl	bdl	0.04	bdl	1

		3_Py1	12.1	0.05	bdl	0.54	-	8130	15.1	0.42	0.34	bdl	bdl	155	23.3	bdl	0.02	bdl	bdl	bdl	0.19	0.82	0.06	0.03	0.17	bdl	1.98	4.1	5
		3_Py3	11.6	0.07	bdl	bdl	-	4860	20.9	2.52	0.14	bdl	bdl	294	12.4	0	0.03	bdl	bdl	bdl	bdl	1.85	0.11	0.03	bdl	bdl	1.12	2.2	7
		3_Py4	15.6	0.49	1.24	1.68	-	5920	16.9	0.64	0.74	bdl	bdl	278	14.4	bdl	0.03	bdl	bdl	bdl	bdl	2.28	0.08	0.07	bdl	bdl	2.8	3.91	
	Cpy	2_Cpy1	11.2	0.3	0.63	4.4	-	0.11	20	314900	480	0.16	0.81	27.1	41.3	0	10.6	6.4	2.02	bdl	0.46	bdl	bdl	0.15	0.32	0.83	10.6	5.24	
		2_Po1	7.6	0.18	bdl	1.05	-	6.61	1014	2	0.57	bdl	bdl	501	27.9	0.01	2.19	bdl	bdl	bdl	bdl	bdl	bdl	bdl	bdl	0.09	9.8	10.8	Po-2
		3_Po1	3.8	bdl	bdl	bdl	-	17.52	778	bdl	0.43	bdl	bdl	593	51.4	bdl	0.16	bdl	bdl	bdl	bdl	bdl	bdl	bdl	bdl	bdl	0.72	0.87	Po-3
		3_Po2	5.7	bdl	bdl	bdl	-	12.65	1340	bdl	0.47	bdl	0.7	495	44.7	0.01	0.21	bdl	bdl	bdl	bdl	bdl	bdl	bdl	bdl	bdl	1.58	1.31	
		3_Po3	4.7	bdl	bdl	bdl	-	174.2	193.5	0.48	0.44	bdl	bdl	507	32.1	0.01	0.06	bdl	bdl	bdl	bdl	bdl	bdl	bdl	bdl	bdl	3.6	0.18	
	Po	3_Po4	154	0.9	bdl	1.92	-	14.95	1095	bdl	0.62	bdl	bdl	552	42	0	0.42	bdl	bdl	0.86	bdl	bdl	bdl	bdl	0.17	bdl	3.29	3.9	
		1_Po1	5.8	bdl	bdl	bdl	-	1.066	896	0.43	bdl	bdl	bdl	526	23.3	0	0.4	bdl	bdl	bdl	bdl	bdl	bdl	bdl	0.14	bdl	0.92	0.58	
		1_Po2	5.5	bdl	0.31	bdl	-	4.27	1260	0.48	bdl	bdl	bdl	403	23.5	bdl	bdl	bdl	bdl	bdl	bdl	bdl	bdl	bdl	0.14	bdl	bdl	bdl	
		1_Po3	5.4	0.07	bdl	10.6	-	0.97	1253	0.69	0.57	0.23	bdl	384	25.3	0	0.33	bdl	bdl	bdl	bdl	bdl	bdl	bdl	0.17	0.05	1.69	1.48	
		1_Po4	5.3	bdl	0.42	bdl	-	1.32	696	bdl	bdl	bdl	bdl	447	32.2	bdl	0.54	bdl	bdl	bdl	bdl	bdl	bdl	bdl	0.23	bdl	1.44	1.33	
		1_Po5	4.4	bdl	0.8	2.16	-	1.43	875	bdl	bdl	bdl	bdl	444	34.4	bdl	0.23	bdl	bdl	bdl	bdl	bdl	bdl	bdl	bdl	0.06	0.48	0.28	
		Py1.1	26.3	0.09	bdl	bdl	-	2110	2.36	bdl	0.24	bdl	bdl	185.3	21.6	bdl	bdl	bdl	bdl	bdl	bdl	bdl	bdl	bdl	bdl	bdl	0.03	bdl	
		Py2.1	27.2	0.09	bdl	bdl	-	1775	3.41	bdl	0.23	bdl	bdl	3.6	19.8	bdl	bdl	bdl	bdl	bdl	bdl	bdl	bdl	bdl	bdl	bdl	0.03	bdl	2
		Py3.1	25.8	0.07	bdl	bdl	-	4160	12.79	bdl	bdl	bdl	bdl	2360	16.9	bdl	0.01	bdl	bdl	bdl	bdl	bdl	0.21	bdl	bdl	bdl	0.08	bdl	1
		Py4.1	25.2	0.09	bdl	bdl	-	841	86.1	bdl	0.29	bdl	bdl	10.1	28.6	bdl	bdl	bdl	bdl	bdl	bdl	bdl	bdl	bdl	0.07	bdl	0.03	bdl	3
	Py	Py5.1	23.8	0.07	bdl	bdl	-	2660	6.91	bdl	0.25	bdl	bdl	2270	14.3	bdl	bdl	bdl	bdl	bdl	bdl	bdl	0.10	bdl	0.22	bdl	0.07	bdl	
		Py6.1	23.8	0.07	bdl	bdl	-	6650	17.49	bdl	0.27	bdl	bdl	3920	21.1	bdl	bdl	bdl	bdl	bdl	bdl	bdl	3.41	bdl	0.15	bdl	bdl	bdl	7
		Py7.1	22.9	0.06	bdl	1.06	-	1719	9.5	0.59	140	bdl	bdl	193	15.1	bdl	0.03	0.82	bdl	bdl	0.12	bdl	bdl	bdl	0.20	bdl	0.43	bdl	
		Py8.1	22.3	0.05	bdl	bdl	-	6700	13.24	bdl	0.27	bdl	bdl	4190	18.8	bdl	bdl	bdl	bdl	bdl	bdl	bdl	0.78	bdl	0.10	bdl	0.03	bdl	5
		Py9.1	22.3	0.06	bdl	0.85	-	1260	10.2	bdl	0.19	bdl	bdl	73	18.7	bdl	0.01	bdl	bdl	bdl	0.27	bdl	bdl	bdl	0.06	bdl	0.43	0.03	
		Py10.1	21.0	0.06	bdl	bdl	-	4700	11.97	bdl	0.19	bdl	bdl	2380	17.7	bdl	bdl	bdl	bdl	0.23	bdl	bdl	0.11	bdl	0.04	bdl	0.03	bdl	
		Cpy1	10	bdl	bdl	6.55	-	0.547	7.23	338400	720	1.91	bdl	15	49	0	85.9	3.49	14.19	147.2	21.8	bdl	bdl	bdl	2.47	0.27	12.4	0.09	
	Cpy	Cpy2	7.5	bdl	bdl	170	-	2	5.91	326000	39000	2.64	bdl	15.1	59.2	bdl	76	129	16.9	154.1	13.8	bdl	bdl	0.05	15.4	0.18	6.8	0.03	
		Cpy3B	8.3	bdl	bdl	10.14	-	0.523	7.33	343400	427	1.92	bdl	13.2	49.4	bdl	75.6	1.84	14.12	137.7	9.1	bdl	bdl	bdl	3.73	0.08	3.8	bdl	
		Zn1	2.72	bdl	bdl	2859	57300	25.96	bdl	850	-	1.82	0.32	13.6	35.1	bdl	3.21	1797	36.84	0.76	3.3	bdl	bdl	0.45	48.5	0.06	48	0.08	
FC1-18.1		Zn2	2.74	bdl	bdl	2906	61110	26.71	0.223	85	-	1.8	0.23	9.4	31.3	0.01	5.1	1769	37.25	0.38	1.45	bdl	bdl	0.86	50.4	bdl	8.3	0.02	
		Zn3	2.9	bdl	bdl	2495	54900	5.85	bdl	21.98	-	1.86	0.47	15.2	40.6	bdl	1.71	1609	38.02	0.36	1.31	bdl	bdl	0.05	48.1	bdl	0.77	bdl	
		Zn4	3.1	bdl	bdl	2548	54700	4.16	bdl	22.48	-	1.78	0.35	9.9	37	0.01	1.95	1588	36.84	0.4	1.84	bdl	bdl	0.06	49.1	bdl	0.97	bdl	
		Zn5	2.98	0.02	bdl	3118	60660	18.09	bdl	43	-	2.17	0.28	7.9	35.3	0.05	1.98	1765	37.76	0.52	1.59	bdl	bdl	0.06	41.4	0.04	1.13	bdl	
	Sph	Zn6	3.06	bdl	bdl	2639	59300	19.88	bdl	960	-	1.72	0.26	11.7	32.1	0.01	1.79	1730	36.66	0.87	1.8	bdl	bdl	bdl	48.6	0.05	0.67	bdl	
		Zn7	3.26	bdl	bdl	2837	55100	11.75	0.154	450	-	1.73	0.41	14.8	37.2	0.03	2.64	1736	37.77	0.57	2.31	bdl	bdl	0.31	49.7	bdl	1.52	0.01	
		Zn8	2.21	bdl	bdl	2376	61000	11.27	bdl	20.55	-	1.92	0.41	7.4	39.4	0	0.98	1729	37.65	0.24	0.37	bdl	bdl	bdl	49.8	bdl	0.28	bdl	
		Zn9	2.25	bdl	bdl	2861	54870	19.19	bdl	2370	-	1.7	0.29	14.2	39.4	0.01	9.6	1702	37.94	2.51	10.3	bdl	bdl	0.61	50.9	0.24	4.11	0.04	
		Zn10	2.78	bdl	bdl	2876	53400	18.53	bdl	1660	-	1.94	0.41	10.2	38.4	bdl	10.5	1750	36.27	1.45	13.3	bdl	bdl	0.13	50.1	0.15	7	0.05	
		Zn11	2.45	bdl	bdl	2868	53200	18.5	0.24	2590	-	1.25	0.28	11.5	37	bdl	10.05	1761	40.25	1.54	11.7	bdl	bdl	0.51	52.7	0.18	11.8	0.05	
		Po1	6.4	bdl	bdl	bdl	-	45.9	284	bdl	bdl	bdl	0.97	349	47.9	bdl	0.17	bdl	bdl	bdl	bdl	bdl	bdl	bdl	bdl	bdl	bdl	bdl	
		Po2	5.8	bdl	bdl	5.26	-	53.6	274	bdl	0.34	bdl	bdl	418	48.4	bdl	0.38	bdl	bdl	bdl	bdl	bdl	bdl	bdl	bdl	bdl	1.01	0.09	
	Po	Po3	5.9	bdl	bdl	4.06	-	45.1	322.9	0.58	bdl	bdl	bdl	344	47.2	bdl	0.17	bdl	bdl	0.53	bdl	bdl	bdl	bdl	0.20	bdl	0.15	bdl	
		Po4	3.5	bdl	bdl	1.53	-	45	336	bdl	bdl	bdl	bdl	346	44.2	bdl	1.31	bdl	bdl	bdl	0.75	bdl	bdl	bdl	0.48	0.06	3.81	0.23	
		Po5	5.1	bdl	bdl	4.43	-	45.9	339	bdl	bdl	bdl	bdl	339	38.6	bdl	0.36	bdl	bdl	bdl	bdl	bdl	bdl	bdl	0.89	bdl	0.68	bdl	
		Po6	4.7	bdl	bdl	6.03	-	47.4	264	bdl	bdl	bdl	bdl	336	44.4	bdl	0.70	bdl	bdl	bdl	bdl	bdl	bdl	0	0.33	bdl	0.95	0.10	
		Py1	14.9	bdl	bdl	bdl	-	4540	5.73	bdl	0.22	bdl	bdl	44.7	31.4	1.5	bdl	bdl	bdl	bdl	bdl	bdl	bdl	bdl	0.09	bdl	0.06	bdl	1
		Py2	13.4	bdl	bdl	bdl	-	1710	1.44	0.19	bdl	bdl	bdl	235	21.9	bdl	bdl	bdl	bdl	bdl	bdl	bdl	bdl	bdl	0.09	bdl	bdl	bdl	2
		Py3	15.4	0.04	bdl	bdl	-	2690	2.27	0.21	bdl	0	0.25	318	25.4	bdl	bdl	bdl	bdl	bdl	bdl	bdl	0.15	bdl	0.08	bdl	0.22	bdl	3
	Py	Py4	14.2	0.05	bdl	bdl	-	2700	1.11	bdl	0.24	bdl	0.34	6.43	19.9	bdl	bdl	bdl	bdl	bdl	bdl	bdl	bdl	bdl	0.09	bdl	bdl	bdl	4
		Py5	14.5	0.04	bdl	bdl	-	3590	12.06	0.19	bdl	bdl	0.72	9.86	109.5	bdl	bdl	bdl	bdl	bdl	bdl	bdl	bdl	bdl	0.10	bdl	bdl	bdl	5
FCQ-18.2		Py6	14.7	0.04	bdl	bdl	-	2456	1.79	bdl	0.21	bdl	bdl	78.6	21.2	bdl	bdl	bdl	bdl	bdl	bdl	bdl	bdl	bdl	bdl	bdl	0.02	bdl	6
		Py7	13.6	0.03	bdl	bdl	-	4750	4.07	bdl	bdl	bdl	0.38	8.84	33.4	bdl	bdl	bdl	bdl	bdl	bdl	bdl	bdl	bdl	bdl	bdl	bdl	bdl	7
		Cpy1	6.9	bdl	bdl	4.3	-	0.31	5.17	331200	531	1.23	1.34	45.2	99	bdl	49.5	1.72	21.98	4.68	2.48	bdl	bdl	bdl	1.23	0.08	22.9	bdl	
	Cpy	Cpy2	10	bdl	bdl	440	-	8.1	17.3	294000	131000	0.86	1.17	42.1	75.8	bdl	69.3	420	31.1	3.16	24.1	2.04	bdl	bdl	27.8	2.11	380	0.96	
		Cpy4	7.3	bdl	bdl	bdl	-	0.5	5.71	342000	589	1.14	1.02	32.3	67.7	0	65.3	2.56	22.71	3.45	8.2	bdl	bdl	bdl	0.3	0.84	103	0.20	
	Sph	Zn1	2.83	bdl	bdl	2300	51600	19.26	bdl	227	-	0.53	0.71	12.7	55.8	bdl	2.3	1788	53.86	1.46	1.89	bdl	bdl	0.05	59.9	0.39	1.23	0.02	

		Zn2	2.83	bdl	bdl	2485	53400	17.03	bdl	29.6	-	0.47	0.66	19.2	61.5	bdl	1.51	1785	51.21	0.29	0.86	bdl	bdl	0.14	61.5	bdl	0.57	bdl	
		Zn3	2.38	bdl	bdl	2184	50400	5.31	bdl	35.5	-	0.53	0.53	15.7	49.5	0.02	3.4	1612	53.41	0.21	3.16	bdl	bdl	0.08	60.6	0.09	1.97	0.03	
		Zn4	2.42	bdl	bdl	2313	51700	4.19	bdl	29.8	-	0.47	0.59	18.8	64	bdl	1.11	1690	51.82	0.19	0.47	bdl	bdl	bdl	53	0.06	0.29	bdl	
		Zn5	2.97	bdl	bdl	2323	52900	2.78	0.165	28.5	-	0.52	0.54	13.1	54.6	bdl	0.98	1730	53.47	bdl	0.33	bdl	bdl	bdl	59.5	bdl	0.37	bdl	
		Zn6	2.76	bdl	bdl	2343	50840	18.02	bdl	960	-	0.45	0.67	7.5	57.3	0.03	8.5	1757	52.81	0.23	8.8	bdl	bdl	0.05	58.2	0.49	13.7	0.10	
		Zn7	2.68	bdl	bdl	2467	53240	20.04	bdl	141	-	0.55	0.64	12	58.8	0.01	2.02	1836	54.72	bdl	1.97	bdl	bdl	0.12	58.3	0.02	1.28	bdl	
		Zn8	2.59	0.16	bdl	2393	52100	17.44	bdl	520	-	0.47	0.4	12.5	44.1	0.01	6	1775	61.44	0.29	6.9	0.5	bdl	0.09	57.9	0.24	1.85	0.03	
	Po	Po1	5.3	bdl	bdl	5.64	-	50.5	396	29	0.56	0.05	1.36	270	78.9	bdl	0.41	bdl	bdl	bdl	bdl	bdl	bdl	bdl	0.25	bdl	1.25	0.11	Po-1
		Po2	5	bdl	bdl	1.1	-	53.7	354	0.69	bdl	bdl	bdl	257	70.1	bdl	0.61	bdl	bdl	bdl	0.28	bdl	bdl	bdl	bdl	bdl	1.85	0.19	Po-2
		Po3	3.8	bdl	bdl	bdl	-	49	393	0.81	bdl	bdl	0.75	235	73.2	bdl	bdl	bdl	bdl	bdl	bdl	bdl	bdl	0	bdl	bdl	bdl	bdl	
		Po4	3.9	bdl	bdl	1.29	-	51.3	346	0.94	0.32	0.01	1.18	230	72	bdl	0.07	bdl	bdl	bdl	bdl	bdl	bdl	bdl	bdl	bdl	0.16	bdl	
		Po5	6.9	bdl	bdl	1.15	-	51.6	380	0.4	bdl	bdl	0.77	233	70	bdl	2.36	bdl	bdl	bdl	bdl	bdl	bdl	bdl	bdl	0.15	0.43	bdl	
		1_Po1	5.8	bdl	bdl	7.18	-	117.3	292	bdl	0.31	bdl	1.31	214	100.6	bdl	0.59	bdl	bdl	bdl	bdl	bdl	bdl	0.01	bdl	bdl	1.28	0.07	
		Py1	19.6	0.25	bdl	bdl	-	1678	3748	20	4.95	bdl	0.46	bdl	46.5	0.02	25.6	4.64	bdl	bdl	bdl	bdl	bdl	bdl	0.29	0.14	bdl	0.27	
		Py2	11.7	0.23	bdl	bdl	-	1735	3450	32.4	1.53	bdl	bdl	bdl	bdl	bdl	16.32	10.92	bdl	bdl	bdl	bdl	bdl	bdl	0.44	0.48	0.12	0.02	Py-3
		Py3	12.6	0.20	0.15	bdl	-	1485	4100	0.77	0.31	bdl	0.24	bdl	22.1	bdl	39.8	7.88	bdl	bdl	bdl	bdl	bdl	bdl	0.30	0.51	12.3	0.04	Py-1
		Py4	11.49	0.21	bdl	0.23	-	1602	3580	30.8	23.7	bdl	1.05	bdl	141	0.11	129	10.34	0.02	bdl	bdl	bdl	bdl	0.01	0.59	0.84	4.83	0.47	
	Py	Py5	12.51	0.13	bdl	bdl	-	1403	4650	38.4	bdl	bdl	0.58	bdl	72	bdl	14.87	22.4	bdl	bdl	bdl	bdl	bdl	0.36	0.47	0.98	20.3	0.22	Py-4
		Py6	12.35	0.36	bdl	bdl	-	1598	6540	6.15	0.5	0.01	0.23	bdl	15.53	bdl	39.7	8.94	bdl	bdl	bdl	bdl	bdl	bdl	0.57	34.6	8.02	0.23	Py-2
		Py7	14.8	0.17	bdl	bdl	-	1786	3384	19.7	19.4	bdl	0.23	0.53	25.3	bdl	7.79	1.57	0	bdl	bdl	bdl	bdl	bdl	0.10	0.07	0.21	0.03	
		Py8	13.5	0.41	bdl	0.19	-	1769	3357	21.7	3.17	0.02	0.28	bdl	30.2	0.02	6.9	bdl	bdl	bdl	bdl	bdl	bdl	bdl	0.04	0.03	0.20	0.13	Py-5
		Py9	16.1	0.23	bdl	bdl	-	1784	4210	5.28	4.4	bdl	0.22	0.39	12.1	bdl	8.39	29	bdl	bdl	bdl	bdl	bdl	0.02	0.11	4.96	5.23	0.11	
FCQ-13		Py10	14.1	0.04	bdl	bdl	-	1072	2298	3.53	0.51	bdl	0.30	0.81	39.5	bdl	135.6	bdl	bdl	bdl	bdl	bdl	bdl	0.01	0.07	bdl	2.04	0.38	
		Cpy1	9.6	bdl	bdl	bdl	-	6.52	bdl	323900	665	0.55	bdl	18.3	36.8	bdl	bdl	21.2	34.06	3.98	bdl	bdl	bdl	bdl	0.68	bdl	1.24	1.56	
		Cpy2	6.9	bdl	bdl	0.63	-	7.4	0.65	338700	693	0.53	bdl	18.8	44.7	0	3.5	21.8	25.56	3.67	bdl	bdl	bdl	0.08	0.74	bdl	0.97	1.11	CPY-3.1
	Cpy	Cpy3	7.8	bdl	bdl	bdl	-	10.3	bdl	333900	547	0.39	0.97	19.3	38.5	0	1.05	15.9	22.13	4.36	bdl	bdl	bdl	bdl	0.59	bdl	bdl	1.76	CPY-4.1
		Cpy4	9.2	bdl	bdl	bdl	-	6.14	bdl	344500	1140	0.26	bdl	19.3	38.3	0	5.49	28.9	24.52	2.87	bdl	bdl	bdl	bdl	0.61	bdl	1.06	2.03	CPY-6.1
		Cpy5	9.1	bdl	bdl	bdl	-	6.37	bdl	341300	1010	0.64	bdl	14	40.8	0.01	0.69	21.9	21.38	4.46	bdl	bdl	bdl	bdl	0.71	bdl	0.65	0.64	CPY-2.1
		Cpy6	8.1	bdl	bdl	0.49	-	11	0.28	335000	636	0.20	bdl	14.5	42.7	bdl	0.79	16.8	30	4.11	bdl	bdl	bdl	bdl	0.82	0.05	1.49	0.93	
	Sph	Zn1	4.22	bdl	bdl	157.3	43900	465	0.32	92	-	0.22	0.25	20.9	25.4	bdl	0.91	8329	85.3	0.21	bdl	bdl	bdl	0.02	24.8	bdl	0.3	0.39	
		Zn2	3.07	bdl	bdl	151.3	43190	463.2	1.37	2020	-	0.12	0.35	22.9	29.6	bdl	4.63	8459	83.6	0.92	bdl	bdl	bdl	0.06	32.5	bdl	5.66	8.3	
	Po	Po1	4.9	bdl	bdl	bdl	-	724	3090	bdl	bdl	bdl	bdl	320	31.6	bdl	bdl	bdl	bdl	bdl	bdl	bdl	bdl	bdl	0.42	bdl	bdl	0.24	

Abbreviations: Py (pyrite), Po (pyrrhotite), Cpy (chalcopyrite), Gn (galena), and Sph (sphalerite).

Table 7.17. Investigation of isotopic equilibrium of sulfide mineral pairs from samples of the Fazenda Coqueiro Deposit, and their temperature of formation.

Sample	Sulfide type	Weighted mean $\delta^{34}S$ (‰)	Weighted mean $\Delta^{33}S$ (‰)	Sulfide pair	$\Delta\delta=\delta^{34}S_A-\delta^{34}S_B$	Temperature (°C)[1]	Viable temperature[2]	Isotopic Equlibrium[3]
FCQ-06.3	Pyrite	1.46	2.13	Py-Po	1.00	273	Yes	Yes
	Pyrrhotite	0.46	2.04	Py-Cpy	1.16	350	Yes	Yes
	Chalcopyrite	0.31	2.11	Po-Cpy	0.15	717	No	Yes
FCQ-1	Pyrite	1.79	2.14	Py-Gn	-1.54	N/A[4]	N/A	Yes
	Galena	3.34	2.08					
FCQ-06.2	Pyrite	2.00	2.07	Py-Po	0.85	320	Yes	Yes
	Pyrrhotite	1.15	2.08					
FCQ-18.2	Pyrite	1.51	1.96	Py-Po	0.77	353	Yes	Yes
	Pyrrhotite	0.74	1.94					
FCQ-13	Pyrite	-1.53	-0.17	Py-Cpy	0.14	1512	No	Yes
	Chalcopyrite	-1.67	-0.23					

[1]Temperatures are calculated using measured $\delta^{34}S$ values and fractionation factors from Ohmoto and Rye (1979);

[2]Based on a temperature of 200 - 400°C from modern hydrothermal systems (Petersen et al., 1998);

[3]Mineral pairs with $\Delta^{33}S$ values that overlap within the 2σ reproducibility of the measurements (±0.1‰) are consistent with isotopic equilibrium (Jamieson et al., 2006);

[4]$\Delta d < 0$ therefore temperatures cannot be calculated.

Table 7.18. Information on sample locations from the Mundo Novo Greenstone Belt.

Sample	Location	Latitude	Longitude	Note
PD-11	Pindobaçu Region	10° 43' 53.4" S	40° 22' 43.9" W	-
PD-04	Pindobaçu Region - Fumaça River	10° 39' 41.3" S	40° 21' 54.2" W	-
PD-06	Pindobaçu Region	10° 41' 28.2" S	40° 22' 07.3" W	-
PD-07	Pindobaçu Region	10° 41' 28.2" S	40° 22' 07.3" W	-
FCJ-4	Pindobaçu Region	10° 41' 49.4" S	40° 22' 04" W	-
FCQ-06.5	Fazenda Coqueiro	11° 53' 36.7" S	40° 29' 36.8" W	Drill Core FCQ-06
FCQ-06.3				
FCQ-06.1				
FCQ-1				
FCQ-06.2				
FCQ-18.1	Fazenda Coqueiro	11° 53' 31.9" S	40° 29' 38.3" W	Drill Core FCQ-18
FCQ-18.2				
FCQ-13	Fazenda Coqueiro	11° 53' 40.1" S	40° 29' 27.3" W	Drill Core FCQ-13

7.3. Uranium irradiation history of carbonado diamond; implications for Paleoarchean oxidation in the São Francisco Craton

THE GEOLOGICAL SOCIETY OF AMERICA®

Uranium irradiation history of carbonado diamond; implications for Paleoarchean oxidation in the São Francisco craton

Charles W. Magee, Jr.[1,2,3], Guilherme Teles[1,4], Edward P. Vicenzi[3,5], Wayne Taylor[1,6], and Peter Heaney[7]
[1]Research School of Earth Sciences, Australian National University, Canberra, 0200 ACT, Australia
[2]Australian Scientific Instruments, Fyshwick, 2609 ACT, Australia
[3]Smithsonian Institution, Department of Mineral Sciences, Washington DC 20013, USA
[4]Universidade de Brasilia, Brasilia 70910-900, Brazil
[5]Smithsonian Institution, Museum Conservation Institute, Suitland, Maryland 20746, USA
[6]Energy Metals Ltd., PO Box 1323, West Perth, 6005 WA, Australia
[7]Department of Geosciences, Pennsylvania State University, State College, Pennsylvania 16801, USA

ABSTRACT

Carbonado is a porous polycrystalline diamond rock found in central African and Brazilian placer deposits. It contains unsupported radiogenic isotopes of He, Ne, Kr, Xe, and Pb. Here we show that these, and the radiation-related defects introduced to the diamond structure, are a result of uranium precipitation, with no isotopic or spectroscopic evidence of Th enrichment. The daughter products are unsupported due to Proterozoic U remobilization. Combining existing carbonado Pb isotope data with recent studies of the geochronology of the tectonic evolution of the São Francisco craton (eastern South America) reveals that the most likely scenario is Paleoarchean uranium enrichment of carbonado, followed by Mesoproterozoic uranium dissolution. Under all possible scenarios, the carbonado radiation damage history requires U mobilization in the Mesoarchean or late Paleoarchean. This is consistent with recent studies of South Africa and India Mesoarchean paleosols, which also show evidence for local oxygen activity greater than that of the Archean atmosphere and ocean. While those studies rely on whole-rock trace element and transition metal stable isotope measurements, this combination of crystallographic defects, sedimentary geochronology, and radiogenic isotopes supports the same conclusions of nonmarine, near-surface Archean oxygen enhancement.

INTRODUCTION

Carbonado Irradiation Evidence

Carbonado is a gravel- to cobble-sized, porous, polycrystalline diamond aggregate found in placer deposits in Brazil and Central African Republic. Carbonado has a light carbon isotopic composition (Vinogradov et al., 1966), fissionogenic noble gas signature (Ozima et al., 1991), non-mantle secondary inclusion mineralogy (Trueb and Butterman, 1969), and distinctive microstructure (Fettke and Sturges, 1933). These unusual features have caused debates about the origin of carbonado, summarized by McCall (2009). Whatever their origin, their radiogenic $^{207}Pb/^{206}Pb$ isotopic composition of 0.38 requires them to have formed in the Archean (Ozima and Tatsumoto, 1997; Sano et al., 2002). However, further constraints on which parts of the Archean are model-dependent, and subsequent transport into younger sediments, are poorly understood. Most carbonado studies viewed epigenetic carbonado alteration as a barrier to determining formation. We take the opposite approach, ignoring carbonado genesis and instead using the epigenetic alteration to constrain the history of carbonado and the erosional and depositional cycles of the São Francisco craton (eastern South America) and Congo sediments in which this diamond is found.

Recent studies (Sautter et al., 2011; Wilson et al., 2012) show that cathodoluminescence (CL) and photoluminescence (PL) features in a few unusual coarse-grained (but still isotopically light) carbonados are related to epigenetic uranium deposition in the cracks and pores, irradiation of the diamond matrix, and subsequent dissolution of the uranium. However, the textural features of the single carbonado grains recently studied (Sautter et al., 2011; Wilson et al., 2012), while similar to each other, are different from the majority of carbonado stones. This work describes a more representative suite of carbonado samples (Table 1), characterizing the uranium precipitation, irradiation, and dissolution features in carbonado of all textural types.

Geology of the Chapada Diamantina and the Diamond Deposits

Carbonado is found in alluvial deposits in Central Africa and the Chapada Diamantina (Diamond Plateau) of Brazil (Derby and Branner, 1905). Stratigraphically, the Chapada Diamantina Group occurs as the upper section of the Espinhaço Supergroup in the Chapada Diamantina region, where the sandstones and conglomerates of the Tombador Formation crop out. These Mesoproterozoic sediments overlie a basement that was metamorphosed during the Transamazonian–Eburnean cycle (2.1–1.9 Ga).

Diamonds in the Chapada Diamantina appear to weather from the Lavras conglomerate of the Tombador Formation, because they are found in streams that drain only this unit, such as the Rio Cachorrinho, south of Lençois (Sampaio et al., 1994; Pedreira, 1997). The Tombador Formation records a significant source-area change relative to the underlying units by well-documented paleocurrent changes from eastward to westward (Pedreira, 1997). The ages of detrital zircons confirm this (Guadagnin et al., 2015). In addition, the Tombador Formation conglomerates contain green, fuchsite-bearing quartzite clasts, used by garimpeiros (independent prospectors), as an indicator for diamond prospecting; these clasts may have been derived from the pre-Transamazonian Jacobina Basin region (Pedreira, 1997).

The depositional age of the Tombador Formation is 1.436 ± 0.026 Ga, the date of tuffaceous interbeds in its paleo–fluvial plains (Guadagnin et al., 2015). Ozima and Tatsumoto (1997) gave an unsupported radiogenic $^{207}Pb/^{206}Pb$ of 0.38 for carbonado, which yields a precipitation age of between 3.8 and 2.6 Ga, depending on when the uranium dissolution occurred.

The older limit of this age range predates most of the rocks in the São Francisco craton, which are Paleoproterozoic to Neoarchean in age. These diamonds cannot have resided in a crust that had not yet formed, so a geochronologic study of carbonado-bearing streams was performed to determine whether they contained zircons as old as the Pb model age of carbonado. Pedreira (1997) suggested that the green fuchsitic extraformational quartzite clasts found in

TABLE 1. SUMMARY OF THE BASIC TEXTURES AND LUMINESCENCE FEATURES OF 21 POLISHED CARBONADOS

Sample	Texture	Color	CL features	Radiation pattern	Source
R-G6	anhedral	orange		bull's-eyes	Brazil
R-F7	microcrystal	orange and green	radiation		Brazil
R-E1	anhedral	orange			Brazil
R-E3	anhedral	orange		bull's-eyes	Brazil
R-E7	microcrystal	multicolored	microstructure		Brazil
R-G1	anhedral	orange and green	radiation	bull's-eyes	Brazil
B-1	microcrystal	multicolored	microstructure		Brazil
B-2	anhedral	orange		bull's-eyes	Brazil
L-3	microcrystal	orange green blue	both	bull's-eyes	Brazil
L-4	anhedral	orange		bull's-eyes	Brazil
L-5	megacrystal	blue growth, multicolored radiation damage	both	bull's-eyes, crack halos	Brazil
L-7	anhedral	orange		bull's-eyes	Brazil
L-9	microcrystal	multicolored	microstructure		Brazil
CAR 1	microcrystal	orange, few green grains	both	bull's-eyes	CAR
CAR 2	anhedral	orange		bull's-eyes and flow patterns	CAR
CAR 11	anhedral	orange		bull's-eyes	CAR
CAR 16	anhedral	orange and light green	radiation		CAR
CAR 17	anhedral	green, orange highlights	radiation	bull's-eyes	CAR
CAR 21	microcrystal	multicolored	microstructure		CAR
CAR 24	anhedral	orange and green	radiation		CAR
CAR 25	anhedral	green with orange highlights	radiation	bull's-eyes	CAR

Note: CAR—Central African Republic.

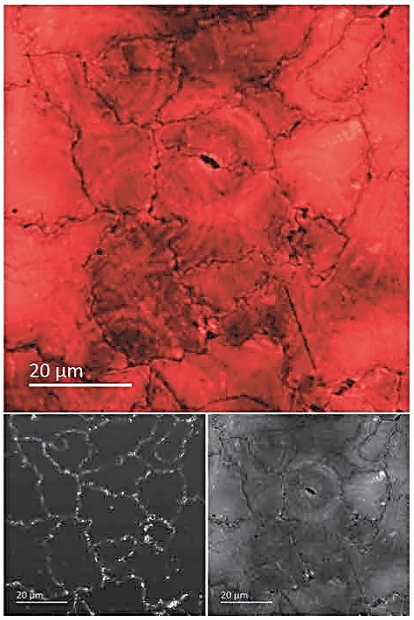

Figure 1. Scanning electron microscopy–based color cathodoluminescence (CL) image of carbonado RG-1 from Brazil, showing radiation damage halos resulting from alpha particles released during uranium series decay. Bottom left panel is an electron image showing grain boundaries; bottom right panel is a panchromatic (visible and ultraviolet) CL image showing concentric circles that represent damage zones resulting from different portions of the U decay chain that emit of alpha particles with differing characteristic energies. Images courtesy of the Smithsonian Institution (Suitland, MD, USA).

the conglomerates are related to quartzite with a green fuchsitic matrix in the Jacobina Basin (Teles et al., 2015).

METHODS

Of the 21 carbonados studied, 16 (8 from Central African Republic and 8 from Brazil) were purchased from dealers or donated by other researchers. Study of carbonado sourced from intermediaries was common in the 20th century. Samples procured this way exhibit isotopic, microstructural, and spectroscopic similarities identifying them as a single population. To better understand the sedimentary context, an additional five carbonados were bought from a garimpeiro in Lençóis, Bahia, Brazil, who had panned them from local streams. Rock and heavy mineral separates from these streams were collected using methods described in the GSA Data Repository[1].

Imaging and spectroscopic studies were done on 21 carbonado stones from Central African Republic and Brazil; of these, textural and luminescence defect information from three samples have been published. Grayscale CL images of carbonados B-1 and CAR-2, along with CL and PL spectra from B-1, were presented by Magee and Taylor (1999). Hyperspectral imagery of carbonado L-5 was presented by Wilson et al. (2012). The imaging and spectrographic techniques are detailed in the Data Repository.

In situ mass spectrometry consisted of the following: the Pb isotopic composition of the florencite minerals in Central African Republic carbonado pores was determined using the SHRIMP II (sensitive high-resolution ion microprobe) at the Research School of Earth Sciences, Australian National University (Canberra), using methods detailed in the Data Repository.

Detrital zircon U-Th-Pb geochronology was performed on zircons from the green extraformational clasts (Pedreira, 1997) of the Lavras conglomerate of the Tombador Formation, on zircons from the Rio Cachorrinho, and on one of the green Jacobina quartzites, which was correlated with the Tombado clasts (Pedreira, 1997). These zircons were reanalyzed using the SHRIMP IIe at Geoscience Australia (Symonston, Australia). Methodological details are provided in the Data Repository.

RESULTS

The carbonados show a number of textural types (see the Data Repository), and the microtextures and luminescence features are summarized in Table 1. Although previous publications have focused on texturally interesting carbonados (Magee and Taylor, 1999; Sautter et al., 2011; Wilson et al., 2012), most of these carbonados have anhedral textures. The coarse-grained texture of carbonado L-5, studied in detail using hyperspectral imagery (Wilson et al., 2012), is unique in this collection. All of the other nonanhedral grains have a microporphyritic texture. All 21 specimens show at least some change in CL response associated with pores. Despite the microtextural variations, some examples of all textural types show bull's-eye halos, and extensive radiation damage along cracks or on outside surfaces (Fig. 1; Figs. DR3–DR7 in the Data Repository). No features are consistent with Th irradiation.

The Pb isotopic composition for the florencite in Central African Republic carbonado is both modern and common (Fig. 2). This is similar to the Pb isotopic compositions of the acid washes from carbonado combustion experiments (Ozima and Tatsumoto, 1997), and yields additional evidence that the pores of carbonado are open to exchange with the environment.

The detrital zircon geochronology data of the sediments from the Rio Cachorrinho, which drains the Lavras conglomerate of the Tombador Formation near Lençóis, show significant zircon populations from the 2.1 Ga Transamazonian–Eburnean cycle, with a smaller Neoarchean population and occasional Paleoarchean to Mesoarchean grains present in the zircon population (Fig. DR11; Table DR3).

The detrital zircon patterns from the extraformational green quartzite clasts and the Jacobina quartzites are strikingly different from the stream sediments, because all of those zircons are Paleoarchean, and the Paleoproterozoic and Neoarchean grains that dominate the entire stream population are absent (Fig. 3; Tables DR6 and DR7).

[1]GSA Data Repository item 2016176, methods, carbonado additional textural and spectral details, pore mineral Chemistry, radiation damage, Raman and photoluminescence, and detrital zircon ages, is available online at www.geosociety.org/pubs/ft2016.htm, or on request from editing@geosociety.org or Documents Secretary, GSA, P.O. Box 9140, Boulder, CO 80301, USA.

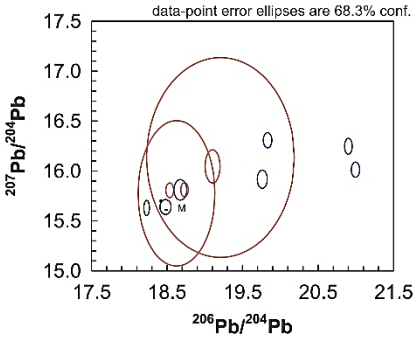

Figure 2. Isotopic composition of florencite Pb (black) compared to the previously reported isotopic composition of Pb leached from carbonado (red), and the Pb isotopic composition of bulk carbonado (blue) (Ozima and Tatsumoto, 1997).

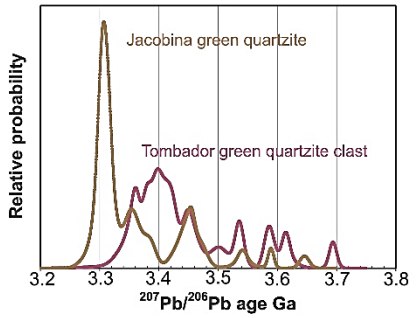

Figure 3. SHRIMP (sensitive high resolution ion microprobe) detrital zircon $^{207}Pb/^{206}Pb$ ages for the green clasts from the Lavras conglomerate of the Tombador Formation (Brazil) (purple) and a fuchsitic quartzite from the Jacobina Group (tan).

DISCUSSION

The luminescence and textural data show that the carbonados with anhedral microtextures, although previously reported (Kagi et al., 2007; Yokochi et al., 2008), have been underrepresented in more recent defect-related luminescence studies (Rondeau et al., 2008; Sautter et al., 2011; Wilson et al., 2012). All carbonado samples studied here show the same U-related defect luminescence features seen in detailed studies of coarsely crystalline carbonado grains. The radiation patterns are consistent with U precipitation in the pores and cracks of carbonado. The modern common Pb composition of florencite shows that carbonado pores are still open to pore-water exchange with the environment, confirming previous textural observations (Trueb and Butterman, 1969).

The Rio Cachorrinho stream detrital zircon geochronology is similar to published lower Tombador sandstone data (Guadagnin et al., 2015), for which age clusters represent the main tectonic cycles of the Chapada Diamantina basement. The Jacobina quartzite and Tombador green clast detrital zircon data are similar to each other in that the youngest zircons are Paleoarchean, almost 2 b.y. older than the Tombador deposition age. However, the Tombador data lack the large 3.308 ± 0.003 Ga population that dominates the Jacobina data, and the broad 3.420–3.380 Ga Tombador zircon population is smaller in the Jacobina quartzite. The Jacobina data are consistent with recent work from this region (Teles et al., 2015).

Implications for Carbonado Geochronology

The best constraint on the unsupported Pb, He, Kr, and Xe radiogenic isotopes is the $^{207}Pb/^{206}Pb$ isotope ratio of 0.38 (Ozima et al., 1991; Ozima and Tatsumoto, 1997). Unlike the closed system $^{207}Pb/^{206}Pb$ equation, which has a unique answer for a given $^{207}Pb/^{206}Pb$ ratio, the equation for a system with U loss consists of paired precipitation times (t_p) and dissolution times (t_d):

$$\frac{^{207}Pb}{^{206}Pb} = \frac{1}{137.8}\frac{e^{^{235}\lambda t_p} - e^{^{235}\lambda t_d}}{e^{^{238}\lambda t_p} - e^{^{238}\lambda t_d}}. \quad (1)$$

When $t_d = 0$, this equation simplifies to the closed system $^{207}Pb/^{206}Pb$ age equation commonly used in geochronology ($e^0 = 1$). For each t_d between t_p and 0, there is a corresponding residence time ($t_p - t_d$), and a unique pair of t_d and t_p. For a $^{207}Pb/^{206}Pb$ of 0.38, varying t_d from 0 to t_p varies t_p from 2.56 and 3.83 Ga. It is important to note that despite some misunderstanding in the literature (Haggerty, 2014), this is not an uncertainty envelope. Rather, it is a range of model outputs, which depend on the time of uranium dissolution (t_d). Figure 4 shows the paired t_p and t_d curves, with various potential geologic triggers on the y-axis. The red line at a radiation duration of 0.2 b.y. (Fig. 4) indicates the minimum time required to accumulate the implanted helium (Ozima et al., 1991), assuming all pore space is filled with uraninite. This represents the shortest physically plausible U residence time.

As seen in Figure 4, the precipitation age required for U dissolution at the 1.436 ± 0.026 Ga time of the Tombador Formation is 3.322 ± 0.013 Ga. This corresponds well with the maximum deposition age of the Tombador green quartzite clasts (Fig. 3). Thus the most parsimonious explanation for the implanted Pb isotopic value is uranium precipitation in the pores and cracks of carbonado at ca. 3.322 Ga, a reasonable deposition age for the source rock of the Tombador green sandstone clasts. The U then dissolves in the next sedimentary cycle at the ca. 1.436 Ga time of Tombador Formation deposition. These calculations do not include any uncertainty component on the 0.38 model $^{207}Pb/^{206}Pb$ ratio (Ozima and Tatsumoto, 1997); changing the $^{207}Pb/^{206}Pb$ ratio by 0.01 changes the modeled ages by ~0.045 b.y.

The isotopic similarity of radiogenic Pb in Central African Republic and Brazilian carbonados (Ozima and Tatsumoto, 1997; Sano et al., 2002) suggests that they shared a common history between t_p and t_d. The erosion event that produced the detritus that formed the Tombador sediments may have also transported carbonado to the Congo portion of the craton. Alternatively, an additional cycle of uplift and erosion prior to the opening of the Atlantic Ocean (such as the Brasiliano orogeny) could have remobilized and transported carbonado from the Mesoproterozoic Brazilian sediments to Africa.

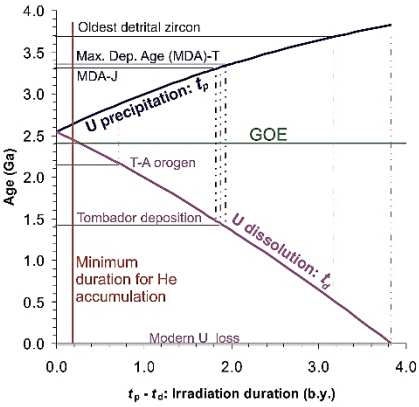

Figure 4. Uranium precipitation and dissolution age curves required to yield the Ozima and Tatsumoto (1997) $^{207}Pb/^{206}Pb$ ratio of 0.38 (precipitation time is t_p; dissolution time is t_d). The minimum accumulation time from unsupported noble gases (Ozima et al., 1991) is shown as a red line. The great oxidation event (GOE) is shown as a green line. Various geological events that could trigger U precipitation or dissolution are shown on the left; tie lines show when the associated dissolution or precipitation must have occurred to yield the observed $^{207}Pb/^{206}Pb$ ratio. The oldest detrital zircon and maximum deposition (Max. Dep.) age for the Tombador (T) green quartzite clasts and correlated Jacobina (J) quartzites are from this study. The Transamazonian (T-A) orogen is from the ca. 2.1 Ga sedimentary zircon peak in these sediments. The Tombador deposition age is from Guadagnin et al. (2015). The temporal pairing of the maximum deposition age of the Tombador green quartzite clasts and the deposition age of the Tombador Formation represents the simplest model for when uranium was precipitated in and dissolved from carbonado.

Implications for Archean Oxygen

The Archean atmosphere is traditionally regarded as too reducing to mobilize U through oxidation, and pyrite and Au mineralization in the Jacobina conglomerates on a large scale supports this suggestion (Teles et al., 2015). However, recent studies have indicated the presence of transient whiffs of oxygen in the Archean, particularly in terrestrial settings (Anbar et al., 2007; Crowe et al., 2013; Mukhopadhyay et al., 2014). Furthermore, the benthic hypothesis (Lalonde and Konhauser, 2015), backed up with a modern example (Sumner et

al., 2015), suggests that oxygen produced in the near subsurface could react with multivalent matrix or groundwater elements without ever interacting with the atmosphere. The Pb isotopic constraints for carbonado require it to have gained its uranium in the Archean. Our preferred ca. 3.323 Ga precipitation age is somewhat older than the oldest oxidized paleosol (3.29–3.02 Ga) and 3.22 Ga evidence for pore-dwelling microfossils (Mukhopadhyay et al., 2014; Homann et al., 2016).

Due to the relative scarcity of diamonds in the bulk sedimentary rock, only a tiny proportion of the bulk-rock U needs to be mobilized to account for the U enrichment in these diamonds. Because diamond surfaces (including the grain boundaries of individual diamond crystallites in carbonado) are oleophilic, the carbonado can trap hydrocarbons to reduce dissolved, oxidized U, precipitating the U along carbonado grain boundaries where the radiation damage features show it must have resided.

The oxygen activity required to mobilize U as UO_2^{2+} is lower (Takeno, 2005) than what is required for the Ce oxidation (Mukhopadhyay et al., 2014) or Cr oxidation (Crowe et al., 2013) reported in Mesoarchean paleosols. So, oxygen production in the late Paleoarchean need not have been as high as in the Mesoarchean. Uranium mobilization is enhanced by low pH, while Cr mobilization and Ce immobilization are facilitated by high pH, suggesting different or variable aqueous conditions.

Our preferred deposition age is close to the transition time between the large $\Delta^{33}S$ deviations of the Eoarchean and the modest $\Delta^{33}S$ deviations of the Mesoarchean (Farquhar et al., 2010). A study of the sulfur isotope systematics of the Jacobina sediments might yield further insight into the global redox systems operating at that time.

CONCLUSIONS

The Pb systematics of carbonado require precipitation of uranium in carbonado pores and cracks in the Archean. The benthic perspective (Lalonde and Konhauser, 2015) allows this, and constraints on the timing of Tombador deposition (Guadagnin et al., 2015) imply late Paleoarchean U precipitation. Unlike previous studies of paleosols and black shales (Anbar et al., 2007; Crowe et al., 2013; Mukhopadhyay et al., 2014; Stüeken et al., 2015), which identified oxidation via bulk-rock techniques of trace element geochemistry and stable isotopic fractionation, this study comes to the same conclusions using detrital minerals and radiogenic isotopes. While most carbonado research of the past 20 years has focused on determining the origin of carbonado, it may be that studying its epigenetic history reveals evidence for the earliest traces of oxygen in Earth's crust.

ACKNOWLEDGMENTS

We thank A. Pedreira, R. Conçeicão, M.M. Marinho, H. Conçeicão, the Universidade Federal da Bahia, and Companhia Baiana de Pesquisa Mineral for assistance in planning and carrying out field work; T. Mernagh, P. Monroe, and K. Nugent for help with Raman, cathodoluminescence, and photoluminescence work; and I. Williams, D. Rubatto, M. Palin, and M. Shelley for assistance with SHRIMP and LA-ICP-MS. This research was made possible with an A. E. Ringwood scholarship from the Research School of Earth Science, Australian National University, and an OPRS (Overseas Postgraduate Research Scholarship) from the Commonwealth Government of Australia. Multispectral CL imaging support was provided by the Smithsonian's Museum Conservation Institute (Maryland, USA). We thank R. Wirth, F. Kaminsky, and an anonymous reviewer for constructive comments.

REFERENCES CITED

Anbar, A.D., et al., 2007, A whiff of oxygen before the Great Oxidation Event?: Science, v. 317, p. 1903–1906, doi:10.1126/science.1140325.

Crowe, S.A., Døssing, L.N., Beukes, N.J., Bau, M., Kruger, S.J., Frei, R., and Canfield, D.E., 2013, Atmospheric oxygenation three billion years ago: Nature, v. 501, p. 535–538, doi:10.1038/nature12426.

Derby, O., and Branner, J., 1905, The geology of the diamond and carbonado washings of Bahia, Brazil: Economic Geology and the Bulletin of the Society of Economic Geologists, v. 1, p. 134–142, doi:10.2113/gsecongeo.1.2.134.

Farquhar, J., Wu, N., Canfield, D.E., and Oduro, H., 2010, Connections between sulfur cycle evolution, sulfur isotopes, sediments, and base metal sulfide deposits: Economic Geology and the Bulletin of the Society of Economic Geologists, v. 105, p. 509–533, doi:10.2113/gsecongeo.105.3.509.

Fettke, C.R., and Sturges, F.C., 1933, Structure of carbonado or black diamond: American Mineralogist, v. 18, p. 172–174.

Guadagnin, F., Chemale, F., Jr., Magalhães, A.J.C., Santana, A., Dussin, I., and Takehara, L., 2015, Age constraints on crystal-tuff from the Espinhaço Supergroup—Insight into the Paleoproterozoic to Mesoproterozoic intracratonic basin cycles of the Congo–São Francisco Craton: Gondwana Research, v. 27, p. 363–376, doi:10.1016/j.gr.2013.10.009.

Haggerty, S.E., 2014, Carbonado: Physical and chemical properties, a critical evaluation of proposed origins, and a revised genetic model: Earth-Science Reviews, v. 130, p. 49–72, doi:10.1016/j.earscirev.2013.12.008.

Homann, M., Heubeck, C., Bontognali, T.R.R., Bouvier, A.-S., Baumgartner, L.P., and Airo, A., 2016, Evidence for cavity-dwelling microbial life in 3.22 Ga tidal deposits: Geology, v. 44, p. 51–54, doi:10.1130/G37272.1.

Kagi, H., Sato, S., Akagi, T., and Kanda, H., 2007, Generation history of carbonado inferred from photoluminescence spectra, cathodoluminescence imaging, and carbon-isotopic composition: American Mineralogist, v. 92, p. 217–224, doi:10.2138/am.2007.1957.

Lalonde, S.V., and Konhauser, K.O., 2015, Benthic perspective on Earth's oldest evidence for oxygenic photosynthesis: National Academy of Sciences Proceedings, v. 112, p. 995–1000, doi:10.1073/pnas.1415718112.

Magee, C.W., and Taylor, W.R., 1999, Constraints from luminescence on the history and origin of carbonado, *in* Gurney, J.J., et al., eds., Proceedings of the International Kimberlite Conference 7: Cape Town, South Africa, Red Roof Design, p. 529–532.

McCall, G.J.H., 2009, The carbonado diamond conundrum: Earth-Science Reviews, v. 93, p. 85–91, doi:10.1016/j.earscirev.2009.01.002.

Mukhopadhyay, J., Crowley, Q.G., Ghosh, S., Ghosh, G., Chakrabarti, K., Misra, B., Heron, K., and Bose, S., 2014, Oxygenation of the Archean atmosphere: New paleosol constraints from eastern India: Geology, v. 42, p. 923–926, doi:10.1130/G36091.1.

Ozima, M., and Tatsumoto, M., 1997, Radiation-induced diamond crystallization: Origin of carbonados and its implications on meteorite nanodiamonds: Geochimica et Cosmochimica Acta, v. 61, p. 369–376, doi:10.1016/S0016-7037(96)00346-8.

Ozima, M., Zashu, S., Tomura, K., and Matsuhisa, Y., 1991, Constraints from noble-gas contents on the origin of carbonado diamonds: Nature, v. 351, p. 472–474, doi:10.1038/351472a0.

Pedreira, A.J., 1997, Sistemas deposicionais da Chapada Diamantina Centro-oriental, Bahia: Brazilian Journal of Geology, v. 27, p. 229–240.

Rondeau, B., Sautter, V., and Barjon, J., 2008, New columnar texture of carbonado: Cathodoluminescence study: Diamond and Related Materials, v. 17, p. 1897–1901, doi:10.1016/j.diamond.2008.04.006.

Sampaio, D.R., Costa, E.D.A.d., and Neto, M.C.A., 1994, Diamantes e carbonados do alto Rio Paraguaçu: Geologia e potencialidade econômica: Arquivos Abertos, p. 1–23.

Sano, Y., Yokochi, R., Terada, K., Chaves, M.L., and Ozima, M., 2002, Ion microprobe Pb-Pb dating of carbonado, polycrystalline diamond: Precambrian Research, v. 113, p. 155–168, doi:10.1016/S0301-9268(01)00208-X.

Sautter, V., Lorand, J.-P., Cordier, P., Rondeau, B., Leroux, H., Ferraris, C., and Pont, S., 2011, Petrogenesis of mineral micro-inclusions in an uncommon carbonado: European Journal of Mineralogy, v. 23, p. 721–729, doi:10.1127/0935-1221/2011/0023-2154.

Stüeken, E.E., Buick, R., and Anbar, A.D., 2015, Selenium isotopes support free O_2 in the latest Archean: Geology, v. 43, p. 259–262, doi:10.1130/G36218.1.

Sumner, D.Y., Hawes, I., Mackey, T.J., Jungblut, A.D., and Doran, P.T., 2015, Antarctic microbial mats: A modern analog for Archean lacustrine oxygen oases: Geology, v. 43, p. 887–890, doi:10.1130/G36966.1.

Takeno, N., 2005, Atlas of Eh-pH diagrams: Intercomparison of thermodynamic databases: Geological Survey of Japan Open File Report 419, 285 p.

Teles, G., Chemale, F., Jr., and de Oliveira, C.G., 2015, Paleoarchean record of the detrital pyrite-bearing, Jacobina Au-U deposits, Bahia, Brazil: Precambrian Research, v. 256, p. 289–313, doi:10.1016/j.precamres.2014.11.004.

Trueb, L., and Butterman, W.C., 1969, Carbonado: A microstructural study: American Mineralogist, v. 54, p. 412–425.

Vinogradov, A.P., Kropotova, O.I., Orlov, Y.L., and Grinenko, V.A., 1966, Isotopic composition of diamond crystals and carbonado: Geokhimiya, v. 12, p. 1395–1397.

Wilson, N.C., MacRae, C.M., Torpy, A., Davidson, C.J., and Vicenzi, E.P., 2012, Hyperspectral cathodoluminescence examination of defects in a carbonado diamond: Microscopy and Microanalysis, v. 18, p. 1303–1312, doi:10.1017/S1431927612013578.

Yokochi, R., Ohnenstetter, D., and Sano, Y., 2008, Intragrain variation in $\delta^{13}C$ and nitrogen concentration associated with textural heterogeneities of carbonado: Canadian Mineralogist, v. 46, p. 1283–1296, doi:10.3749/canmin.46.5.1283.

Manuscript received 1 February 2016
Revised manuscript received 10 May 2016
Manuscript accepted 16 May 2016

Printed in USA